4D offline PET-based treatment verification in ion beam therapy: experimental and clinical evaluation

Christopher Kurz

München 2014

4D offline PET-based treatment verification in ion beam therapy: experimental and clinical evaluation

Christopher Kurz

Dissertation
an der Fakultät für Physik
der Ludwig–Maximilians–Universität
München

vorgelegt von
Christopher Kurz
aus Neuwied

München, den 12.06.2014

Erstgutachter: Prof. Dr. Katia Parodi
Zweitgutachter: Prof. Dr. Jan Wilkens
Tag der mündlichen Prüfung: 29.08.2014

Contents

List of Figures

List of Tables

List of Abbreviations

3D	3 dimensional
4D	4 dimensional (space and time)
AC	Attenuation correction
ADP	Activity depth profile
AP	Anterior-posterior
BEV	Beam's eye view
BP	Bragg-peak
cps	Counts per second
CSDA	Continuous slowing down approximation
CT	Computed tomography
CTV	Clinical target volume
DIR	Deformable image registration
DNA	Deoxyribonucleic acid
DOI	Depth-of-interaction
FBP	Filtered back-projection
FDG	^{18}F-Fludeoxyglucose
FOV	Field of view
FWHM	Full-width-at-half-maximum
GSI	Gesellschaft für Schwerionenforschung
GTV	Gross tumour volume
GW	Gating window
HCC	Hepato-cellular carcinoma
HEBT	High energy beam transfer line
HIT	Heidelberg Ion-Beam Therapy Center
HLUT	Hounsfield look-up table
HU	Hounsfield unit
IC	Ionisation chamber
ICRU	International Commission on Radiation Units and Measurements
IMRT	Intensity-modulated radiation therapy
ITV	Internal target volume

LBL	Lawrence Berkeley Laboratory
LEM	Local effect model
LET	Linear energy transfer
LINAC	Linear accelerator
LLUMC	Loma Linda University Medical Center
LM	List-mode
LOR	Line of response
LR	Left-right
LSO	Lutetium oxyorthosilicate
MBR	Machine beam record
MC	Monte-Carlo
MLEM	Maximum likelihood expectation maximisation
MWPC	Multi-wire proportional chamber
NIRS	National Institute of Radiological Sciences
NXP	Next-point signal
OP	Ordinary Poisson
OSEM	Ordered subset expectation maximisation
PET	Positron emission tomography
PMMA	Polymethyl-methacrylate
PSF	Point-spread function
PTCOG	Particle Therapy Co-Operative Group
PTV	Planning target volume
RBE	Relative biological effectiveness
RF	Random fraction
ROI	Region-of-interest
RPTC	Rinecker Proton Therapy Center
RT	Radiotherapy
SI	Superior-inferior
SiPM	Silicon photomultiplier
SOBP	Spread-out Bragg-peak
TOF	Time-of-flight
TP	Treatment planning
TPS	Treatment planning system
TRiP	TReatment plannIng for Particles
US	Ultrasound
VMAT	Volumetric intensity modulated arc therapy
VOI	Volume-of-interest
WEPL	Water equivalent path-length

Zusammenfassung

In der Strahlentherapie mit Protonen und schwereren Ionen ist durch die erreichbaren steilen Dosisgradienten eine hochkonforme Anpassung der applizierten Strahlendosis an beliebig geformte Zielvolumina möglich. Diese geht allerdings mit einer erhöhten Empfindlichkeit gegenüber potenziellen Unsicherheiten, etwa durch Veränderungen in der Patientenanatomie, einher. Zusätzliche Herausforderungen entstehen durch Atembewegungen, welche nicht nur zu schnellen anatomischen Veränderungen, sondern, im Falle gescannter Ionenstrahlen, auch zur Ausprägung von Dosisinhomogenitäten führen können. Daher ist es unbedingt wünschenswert, die Applikation der Bestrahlung genau zu verifizieren und mögliche Abweichungen von der geplanten Bestrahlung zu detektieren. Das einzige derzeit klinisch eingesetzte Verfahren, welches die zeitnahe Verifizierung einzelner Bestrahlungsfraktionen erlaubt, basiert auf der Messung der während der Bestrahlung gebildeten β^+-Emitter mittels Positronen-Emissions-Tomographie (PET). Am Heidelberger Ionenstrahl-Therapiezentrum (HIT) wurde speziell hierzu ein kommerzieller PET/CT (Computer-Tomographie)-Scanner direkt neben den Bestrahlungsräumen installiert. Bis heute ist die Anwendung dieses Verfahrens jedoch klinisch auf statische Zielvolumina beschränkt.

Ziel dieser Dissertation war es, die Möglichkeiten der Anwendung PET-basierter Bestrahlungsverifikation unter Berücksichtigung von Organbewegungen zu untersuchen. In einer experimentellen Bestrahlungsstudie mit bewegten Phantomen konnte nicht nur erstmals die Machbarkeit einer PET-basierten Bestrahlungsüberwachung bewegter Objekte mittels eines kommerziellen PET/CT-Scanners gezeigt werden, sondern auch das hohe Potenzial dieser Methode, Abweichungen von der geplanten Bestrahlung durch Bewegungen im Sub-Millimeter Bereich zu detektieren. Auch die erste Anwendung unter erheblich schwierigeren, klinischen Bedingungen auf vier exemplarische Leberzellkarzinom-Patienten zeigte mögliche Verbesserungen durch Berücksichtigung der Tumorbewegung, speziell für Patienten mit einer Bewegungsamplitude von über 1 cm, bei denen eine hinreichende Zahl von Koinzidenzen während des PET-Scans gemessen wurde. Trotz Anwendung der in einer detaillierten Phantom-Bildgebungsstudie im Rahmen dieser Arbeit ermittelten optimalen PET Rekonstruktions-Parameter, erwies sich jedoch eine zu niedrige Anzahl gemessener Koinzidenzen und das daraus resultierende Bildrauschen als ein entscheidender limitierender Faktor für den Nachweis von Dosisinhomogenitäten im Patienten. Auch die Modellierung der biologischen Auswaschung der induzierten Radio-Isotope erwies sich als nicht hinreichend genau und erschwert bislang eine quantitative Analyse der gemessenen und simulierten Daten unter Berücksichtigung der Organbewegung. Zukünftig sind Verbesserungen durch rauschärmere, zeitaufgelöste Rekonstrucktionsalgorithmen, eine verbesserte Bewegungsüberwachung, z.B. mittels Ultraschallbildgebung, welche im Rahmen dieser Arbeit erstmals in die zeitaufgelöste PET-Bildgebung integriert wurde, sowie einer patienten-spezifischen Modellierung der Aktivitäts-Auswaschung zu erwarten.

Abstract

Due to the accessible sharp dose gradients, external beam radiotherapy with protons and heavier ions enables a highly conformal adaptation of the delivered dose to arbitrarily shaped tumour volumes. However, this high conformity is accompanied by an increased sensitivity to potential uncertainties, e.g., due to changes in the patient anatomy. Additional challenges are imposed by respiratory motion which does not only lead to rapid changes of the patient anatomy, but, in the cased of actively scanned ions beams, also to the formation of dose inhomogeneities. Therefore, it is highly desirable to verify the actual application of the treatment and to detect possible deviations with respect to the planned irradiation. At present, the only clinically implemented approach for a close-in-time verification of single treatment fractions is based on detecting the distribution of β^+-emitter formed in nuclear fragmentation reactions during the irradiation by means of positron emission tomography (PET). For this purpose, a commercial PET/CT (computed tomography) scanner has been installed directly next to the treatment rooms at the Heidelberg Ion-Beam Therapy Center (HIT). Up to present, the application of this treatment verification technique is, however, still limited to static target volumes.

This thesis aimed at investigating the feasibility and performance of PET-based treatment verification under consideration of organ motion. In experimental irradiation studies with moving phantoms, not only the practicability of PET-based treatment monitoring for moving targets, using a commercial PET/CT device, could be shown for the first time, but also the potential of this technique to detect motion-related deviations from the planned treatment with sub-millimetre accuracy. The first application to four exemplary hepato-cellular carcinoma patient cases under substantially more challenging clinical conditions indicated potential for improvement by taking organ motion into consideration, particularly for patients exhibiting motion amplitudes of above 1 cm and a sufficiently large number of detected true coincidences during their post-irradiation PET scan. Despite the application of an optimised PET image reconstruction scheme, as retrieved from a dedicated phantom imaging study in the scope of this work, the small number of counts and the resulting high level of image noise were identified as a major limiting factor for the detection of motion-induced dose inhomogeneities within the patient. Moreover, the biological washout modelling of the irradiation-induced isotopes proved to be not sufficiently accurate and thereby impede a quantitative analysis of measured and simulated data under consideration of target motion. In future, improvements are particularly foreseen through dedicated noise-robust time-resolved (4D) image reconstruction algorithms, an improved tracking of the organ motion, e.g., by ultrasound (US) imaging, as implemented for the first time in 4D PET imaging in the scope of this work, as well as by patient-specific washout models.

Chapter 1

Introduction

According to the Eurostat database, cancer is the second leading cause of death in Germany and the European Union. In 2010, there have been $480,000$ new cancer cases and $220,000$ cancer-related deaths in Germany [Kaatsch et al., 2013]. Due to the ageing population, cancer incidences are expected to increase further over the next years. Surgery, chemotherapy, radiotherapy and combinations of these constitute the main treatment options for cancer patients. Radiotherapy is a particularly suitable option for patients with a cancer diagnosis at the stage of a localised primary tumour. In total, about 50% of all cancer patients undergo radiotherapy during their course of treatment.

The goal of radiotherapy is the inactivation of cancer cells by irradiation-induced ionisation processes. As similar mechanisms occur in non-tumour cells as well, the radiation burden to adjacent healthy structures has to be kept as low as reasonably possible. Consequently, radiotherapy aims at delivering a highly conformal lethal dose to the defined target volume, while not exceeding the toxic dose in the surrounding normal tissue. As a promising alternative to the conventional radiotherapy with photons, which has been used for tumour treatment since the end of the 19 th century, ion beam therapy with protons and heavier ions, such as ^{12}C, has been investigated by several research facilities since the 1950s and integrated into clinical environments since the 1990s. Recent studies have shown that the superior dose conformity, which is feasible due to the favourable physical properties of ion beams with respect to photon beams, can result in an improved tumour control rate for particular cancer indications [Schulz-Ertner et al., 2007; Tsujii et al., 2007; Durante and Löffler, 2010].

At the same time, however, the accessible sharp dose gradients make ion beam therapy prone to uncertainties, introduced e.g., by changes in the patient anatomy or deviations in the patient positioning. In order to fully exploit the potential of ion beam therapy, it is therefore highly desirable to verify the correct application of the planned treatment. Up to date, the only clinically implemented approach for in-vivo monitoring of single treatment fractions during or shortly after ion beam irradiation is based on positron emission tomography (PET) imaging of the irradiation-induced β^+-emitter within the patient, which are produced as a by-product in nuclear fragmentation reactions during the treatment. This method is, e.g., applied at the Heidelberg Ion-Beam Therapy Center (HIT), where the patient activation is measured directly after the irradiation with a commercial full-ring PET/CT (computed tomography) scanner installed next to the treatment rooms (offline).

Considerable challenges are additionally imposed to ion beam therapy if the target volume is affected by organ motion, e.g., due to respiration. Motion does not only result in a changing anatomy of the target region during the actual beam application, but can also lead to dose inhomogeneities in the target volume due to an interplay of the organ motion and the dynamic beam delivery in the case of scanned ion beams. Despite the additionally introduced uncertainties, the treatment of moving tumours is of high clinical interest: for hepato-cellular carcinoma (HCC) patients, e.g., for which the 5-year survival rate in Germany was found to be below 10% in 2010 [Kaatsch et al., 2013], studies at the National Institute of Radiological Sciences (NIRS) in Chiba (Japan) showed a clearly improved outcome by hypo-fractionated irradiation with carbon ions [Kato et al., 2004; Tsujii et al., 2007]. The increased level of uncertainty in the treatment of moving targets, however, strongly demands for a thorough monitoring of the actually applied treatment.

Aim of this thesis is to expand the already clinically integrated offline PET-based treatment verification at HIT from stationary to moving target volumes by considering the organ motion during the irradiation, as well as during the subsequent PET/CT acquisition. Up to present, the applicability of PET-based treatment monitoring to moving targets has only been investigated in few irradiation studies with mobile phantoms, using dedicated dual-head in-beam PET cameras [Parodi et al., 2009; Stützer et al., 2013]. In the scope of this work, the first moving phantom study on the feasibility and potential of time-resolved (4D) offline PET-based treatment verification with a commercial PET/CT scanner will be presented, as well as the first application of this monitoring technique to clinical cases.

The thesis is organised as follows: chapter 2 introduces the physical and biological fundamentals of ion beam therapy, together with its technical and clinical implementation, and reviews the role of uncertainties and organ motion in particle therapy. In chapter 3 the approach of PET-based treatment verification is explained in detail, with a special focus on the offline implementation at HIT. The following chapter 4 presents a first detailed study on the feasibility and potential of 4D offline PET monitoring after ^{12}C ion irradiation with a commercial full-ring PET/CT scanner in a high statistics moving phantom scenario. Moreover, a first integration of ultrasound (US) based motion tracking into 4D PET imaging, which is foreseen as a future option to enhance the accuracy of 4D patient PET imaging, will be covered. Chapter 5 deals with a detailed analysis of the performance of the used PET/CT scanner under extremely low counting statistics, which are generally considered as a main challenge in PET-based treatment verification, but particularly impede 4D PET imaging at typically even reduced count numbers. This chapter also aims at identifying the optimal reconstruction scheme to be applied under the particular statistical conditions in post-irradiation PET imaging and discusses the impact of the high radiation background emerging from the radioactive Lutetium-based PET detectors on the acquired images. Eventually, chapter 6 introduces the first clinical application of 4D PET-based treatment verification to four exemplary HCC patients treated with scanned ^{12}C ion beams at HIT and evaluates the potential, as well as the current limitations of post-irradiation PET imaging for monitoring the treatment of moving tumours. Chapter 7 concludes this thesis and discusses future perspectives and possible improvements of 4D PET-based treatment monitoring in ion beam therapy.

Chapter 2

Fundamentals of ion beam therapy

2.1 A brief introduction to ion beam therapy

In general, radiotherapy aims at sterilising cancer cells by irradiation-induced ionisation processes. The most sensitive target of the cell is represented by the Deoxyribonucleic acid (DNA). Single, double and, even more effectively, complex clustered strand breaks of the DNA molecule can lead to the inactivation of single cells and result in a local control or even shrinkage of the tumour [Goodhead, 1994]. Similar processes, however, also occur in the surrounding healthy tissue and close-by organs at risk, leading to side-effects during the irradiation or even inducing secondary cancer on a time-scale of months to years. Consequently, a highly conformal dose delivery to the tumour and best-possible sparing of the adjacent healthy structures has to be the aim of radiation therapy.

Although the conformity of conventional external beam radiotherapy with photons could be further increased over the last years by modern beam application techniques like intensity-modulated radiation therapy (IMRT) [Webb, 2003] or volumetric intensity-modulated arc therapy (VMAT) [Rao et al., 2010], it is still intrinsically limited by the physical properties of high-energy (MeV) photon beams: the shallow maximum of the energy and herewith dose deposition of a photon beam can be found few centimetres away from the patient surface and is followed by an exponential decay with increasing depth. As an alternative to photon irradiation, the application of proton or heavier ion beams had already been envisioned by Robert R. Wilson in 1946 [Wilson, 1946]: these beams show an "inverse" depth dose profile, exhibiting a sharp dose maximum, known as the Bragg-peak (BP) [Bragg and Kleeman, 1905], close to the end of the primary ions range, while the dose deposited in the entrance channel is comparably small (see figure 2.1). The position of this BP is directly correlated with the energy of the incident ion beam and can thus be adjusted with millimetre accuracy to the given target structure. Even extended deep-seated tumours can be covered by the superposition of ion beams of different energies to a so-called *spread-out Bragg-peak* (SOBP) at a still comparably low entrance dose, as also shown in figure 2.1. Moreover, ions heavier than protons show a reduced lateral scattering, as well as an enhanced biological effectiveness in comparison to photons, making them particularly interesting for the treatment of hypoxic and radio-resistant tumours with poor response to conventional radiotherapy. A detailed description of the underlying processes will be given in the following sections. Making optimal use of these properties, the integral dose given to the patient can

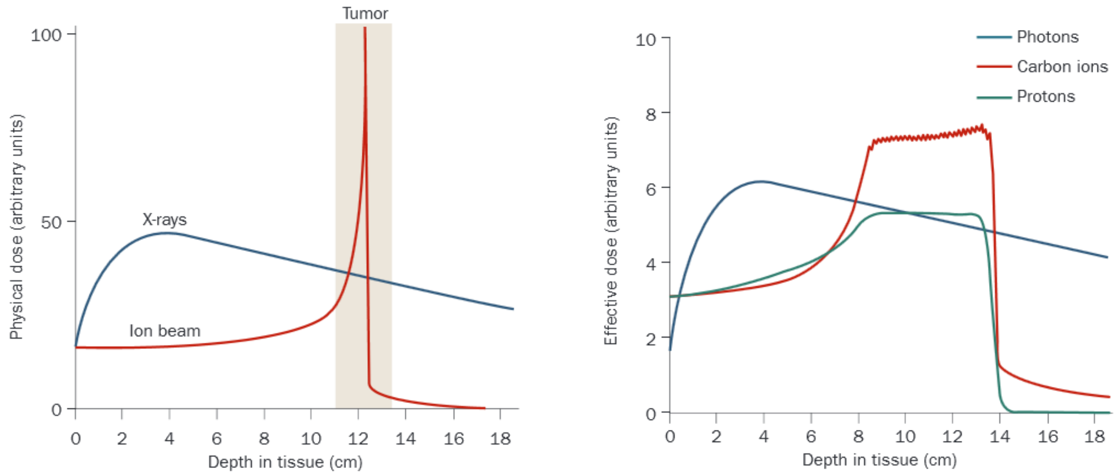

Figure 2.1: Comparison of photon and ion beam depth dose distributions. While photons exhibit a shallow dose maximum close to the entrance region, ion beams show a distinct dose maximum, known as the Bragg-peak, close to the end of the particles range (left). In order to cover a deep-seated extended tumour volume with a homogeneous dose, ion beams of different energies are super-imposed to a spread-out Bragg-peak (right). Figure from [Durante and Löffler, 2010].

be significantly reduced and a higher conformity to arbitrarily shaped target volumes can be achieved, as shown for the case of a head tumour in figure 2.2.

Following the investigations of R. Wilson, first patients have been treated with protons in 1954 at the Lawrence Berkeley Laboratory (LBL) in Berkeley, USA [Tobias et al., 1958]. First irradiations with Helium ions started in 1957, followed by first treatments with heavier ions like Carbon and Neon at the same institution in 1975 [Castro et al., 1980]. Still, it took until 1990 before the first dedicated ion beam therapy facility, embedding proton therapy in a clinical environment, opened at the Loma Linda University Medical Center (LLUMC). Up to date, more than $100,000$ patients have been treated with protons and heavy ions world-wide. More than 40 ion beam therapy facilities are currently in operation and more than 30 centres are in the planning or construction phase [PTCOG, 2013].

In Germany, first patients have been treated with carbon ions at the GSI Helmholtzzentrum für Schwerionenforschung at Darmstadt in 1997 [Debus et al., 2000]. Until the shut-down in 2008, over 400 patients, mostly suffering from tumours in the brain and the skull-base, have been treated. The promising clinical results achieved in the GSI pilot project [Schulz-Ertner et al., 2004, 2007] motivated the building of a dedicated, hospital-based proton and carbon ion treatment facility, the Heidelberg Ion-Beam Therapy Center [Haberer et al., 2004]. Starting patient treatment in 2009, nearly 2000 patients have been treated at HIT until the end of 2013.

2.2 Physical properties of ion beams

The above-mentioned favourable physical properties of proton and heavy ion beams, namely the inverse depth dose profile and the reduced lateral scattering in the case of heavier ions, are directly related to the underlying physical interactions of ions in matter, which will be reviewed in this

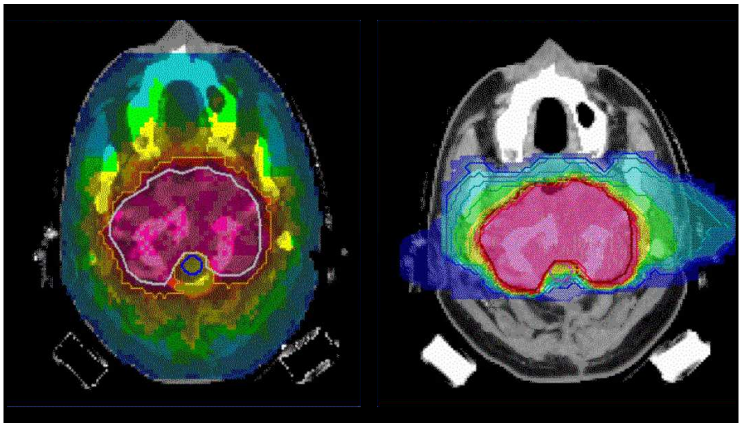

Figure 2.2: Comparison of the 2D dose distributions (color wash) achieved with 9 intensity-modulated photon fields (left) and 2 opposing carbon ion fields (right). As can be seen, a higher dose conformity and a lower integral dose outside the target volume can be achieved by the heavy ion beams. Coutesy of O. Jäkel, Heidelberg University Hospital.

---

section.

The central physical quantity in external beam radiotherapy with photons and ion beams is the dose deposited in a medium. According to [ICRU, 1993b] it is defined as the mean energy $\mathrm{d}\epsilon$ deposited by the directly- or indirectly-ionising radiation in a mass element $\mathrm{d}m$ and is measured in Gray (Gy):

$$D = \frac{\mathrm{d}\epsilon}{\mathrm{d}m} \qquad [1\mathrm{Gy} = 1\mathrm{J/kg}]\,. \tag{2.1}$$

For a mono-energetic parallel beam, the dose absorbed in a thin layer of an absorber material with mass density ρ is given by:

$$D[Gy] = 1.6 \times 10^{-9} \times \frac{\mathrm{d}E}{\mathrm{d}x}\left[\frac{\mathrm{keV}}{\mu\mathrm{m}}\right] \times \Phi\left[\mathrm{cm}^{-2}\right] \times \frac{1}{\rho}\left[\frac{\mathrm{cm}^3}{\mathrm{g}}\right]\,, \tag{2.2}$$

where Φ is fluence of the incident particle beam, i.e. , the number of particles per area, and $\mathrm{d}E/\mathrm{d}x$ is the particles energy-loss per unit path-length, the so-called *electronic stopping power* S.

2.2.1 Energy-loss of ions in matter

Three different mechanisms contribute to the energy-loss of ion beams in matter. The inelastic scattering of the ions on the target electrons, leading to the electronic stopping power, the elastic scattering of the ions on the target nuclei, known as nuclear stopping power, and the energy-loss by radiative processes.

In ion beam therapy, the initial beam energies are adapted to the requirement that deep seated tumours in a water-equivalent depth of up to 30 cm within the patient can be reached by the Bragg-peak. Therefore energies of up to 220 MeV for protons and up to 430 MeV/u for ^{12}C ions are of need, corresponding to velocities of up to $0.7 \cdot c$, where c is the speed of light. In this medium-relativistic energy regime, energy-loss is dominated by the electronic stopping

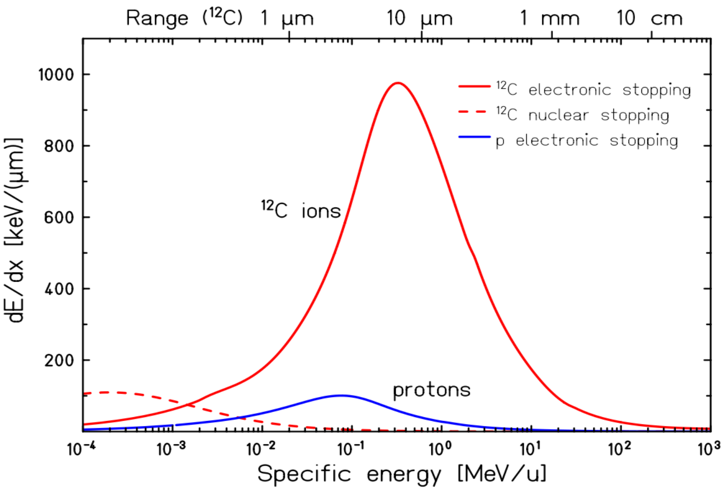

Figure 2.3: Stopping power of protons and ^{12}C ions in water. The residual ranges of ^{12}C ions corresponding to the specific energies (energy per atomic mass unit u) on the x-axis are shown at the top. Figure from [Schardt et al., 2010].

---

power [Schardt et al., 2010], which can be well described by the Bethe-Bloch formula [Bethe, 1930; Bloch, 1933; Fano, 1963] down to energies of about 1 MeV/u:

$$-\frac{\mathrm{d}E}{\mathrm{d}x} = 2\pi r_e^2 m_e c^2 N_e \frac{Z_p^2}{\beta^2}\left[\ln\left(\frac{2m_e c^2\beta^2\gamma^2 T_{max}}{\langle I\rangle^2}\right) - 2\beta^2 - 2\frac{C}{Z_t} - \delta\right] . \tag{2.3}$$

Here, T_{max} is the largest possible energy transfer in a single collision with a free electron, r_e the classical electron radius, m_e the electron rest mass, β the projectile velocity in units of c, $\gamma = 1/\sqrt{1-\beta^2}$ and Z_p the projectile electric charge. $2C/Z_t$ and δ describe the shell and density effect correction, respectively. The absorber medium itself is characterised by its electron density N_e and its mean ionisation potential $\langle I\rangle$. For water, e.g., an ionisation potential of 75 eV was recommended by the ICRU [ICRU, 1994] in the case of protons, but proposals for higher values (for protons as well as heavy ions), ranging from 75 to 80 eV, have been made in the literature [Bichsel et al., 2000; Kumazaki et al., 2007; Schardt et al., 2008; Parodi et al., 2012; Kurz et al., 2012].

The electronic stopping power of protons and ^{12}C ions in water are shown in figure 2.3 as as a function of the particle energy and the residual particle range. For incident ions at therapeutic energies in the order of 10^2 MeV/u, the stopping power, and herewith the local dose deposition will increase with decreasing energy due to the dominant $1/\beta^2$ dependence in equation 2.3. The maximum energy-loss will occur shortly before the particles stop and their energy falls below 1 MeV/u, giving rise to the above-mentioned Bragg-peak. At even lower energies, the stopping power finally decreases due to recombination processes in the media, which reduce the effective charge of the projectiles. This can be incorporated in the Bethe-Bloch formula by replacing the projectile charge Z_p by the effective charge Z_{eff}, given by empirical formula [Barkas, 1963]:

$$Z_{eff} = Z_p\left[1 - exp(-125\beta Z_p^{-2/3})\right] . \tag{2.4}$$

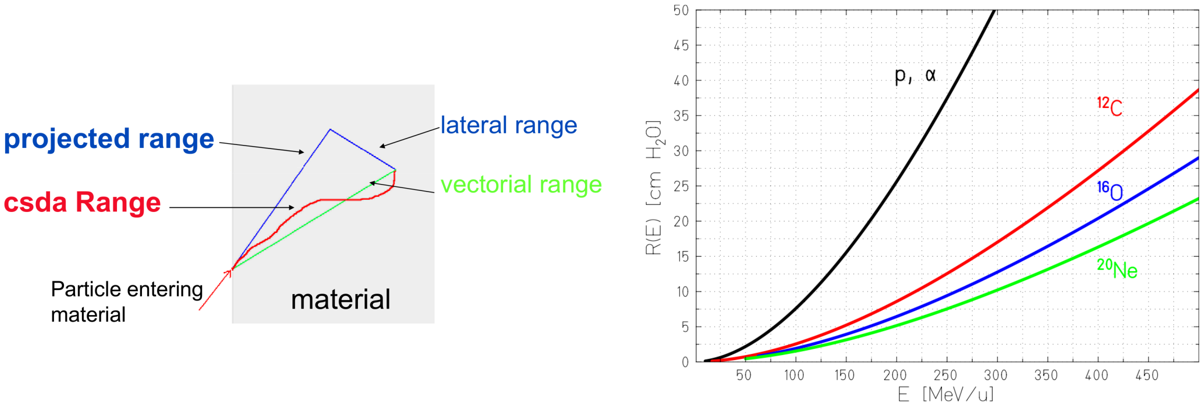

Figure 2.4: Illustration of different range definitions (left, courtesy of O. Jäkel) and mean ranges of different ion species as a function of their initial energy in water (right) [Schardt et al., 2010].

At energies below about 10 keV/u, the contribution of the nuclear stopping power starts to increase (see figure 2.3), but the contribution to the deposited dose is very small and generally neglected in radiotherapy applications [Elsässer et al., 2009], just as contributions from the radiative energy-loss processes at therapeutic energies.

The finite path-length R_{CSDA} of a particle in an absorber until it comes to rest is given by:

$$R_{CSDA}(E) = \int_0^E \left(\frac{\mathrm{d}E'}{\mathrm{d}x}\right)^{-1} \mathrm{d}E'. \tag{2.5}$$

in the so-called *continuous slowing down approximation* (CSDA). For heavy charged particles, which experience little lateral scattering, the average depth of penetration in the absorber, called mean or projected particle range R, is very similar to the CSDA range R_{CSDA}. An illustration of the different range definitions, as well as the mean range in water of different therapeutically used ion species as a function of their initial energy is given in figure 2.4. Taking into account the main Z_p^2 and $1/\beta^2$ dependencies of the stopping power in the Bethe-Bloch formula, one can find that the range for the same velocity β approximately scales with A/Z_p^2.

The Bethe-Bloch equation, however, only describes the mean energy-loss per unit path-length, as the energy-loss in matter is affected by statistical fluctuations. These fluctuations, known as energy-loss straggling, lead to a broadening of the energy spectrum of an incident ion beam, consisting of a large number of particles, with increasing depth. In the limit of a large absorber or many collisions, the broadened energy distribution can be approximated by a Gaussian of width σ_E [Bohr, 1940; Ahlen, 1980]. The energy straggling directly translates into a straggling of the residual range with width σ_R and leads to a broadening of the Bragg-peak, as well as to a decrease of the peak-to-plateau dose ratio. The straggling width σ_R can by approximated by:

$$\sigma_R = \frac{R}{\sqrt{M}} f\left(\frac{E}{Mc^2}\right)_{med}, \tag{2.6}$$

where f is a nearly constant function depending on the absorber material [Schardt et al., 2010]. Consequently, range straggling, and herewith Bragg-peak width and entrance-to-peak dose ratio, will increase with increasing particle range and decrease with increasing particle mass M.

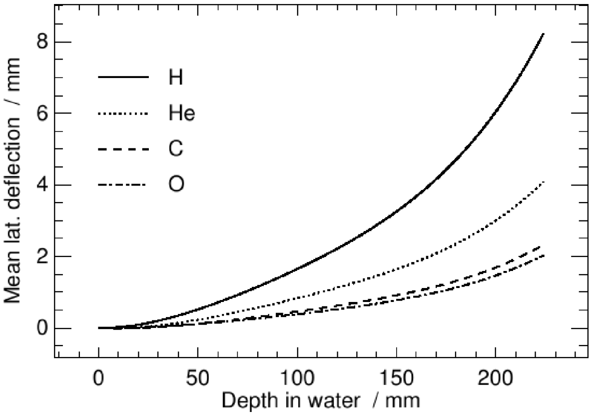

Figure 2.5: Mean lateral deflection of protons and different heavy ion species as a function of their penetration depth in water. At the same depth, scattering of protons is clearly enhanced [Parodi, 2004].

2.2.2 Lateral scattering

Besides the discussed inverse depth dose profile, ions heavier than protons offer the advantage of a reduced lateral scattering in comparison to MeV photon beams. The lateral scattering of ion beams in a medium can mainly be attributed to the elastic Coulomb scattering of incident ions on the target nuclei, deflecting them by an angle Θ from their original path. In order to obtain the distribution of the scattering angle Θ, a Boltzmann transport equation [Arkeryd, 1972] has to be solved. The analytical solution has been presented by Molière [Molière, 1948] and can be approximated for small scattering angles by a Gaussian distribution with a standard deviation given by the Highland formula [Highland, 1975]:

$$\sigma_\Theta[\mathrm{rad}] = \frac{14.1MeV}{\beta pc} Z_p \sqrt{\frac{d}{L_{rad}}} \left[1 + \frac{1}{9} \log_{10}\left(\frac{d}{L_{rad}}\right)\right] , \tag{2.7}$$

In this equation, the absorber material is characterised by its thickness d and its radiation length L_{rad} (for water, e.g.,$L_{rad} = 36\,\mathrm{cm}$). Due to the $1/\beta pc$ factor, lateral scattering will increase for low energies and will be reduced for heavier ions in comparison to protons at the same penetration depth, as shown in figure 2.5.

2.2.3 Nuclear interactions

Besides the electromagnetic interactions discussed in the two previous sections, heavy ions can interact with the target nuclei via the strong nuclear force. These interactions lead to an exponential attenuation of the primary heavy ion fluence Φ in depth according to:

$$\Phi(z) = \Phi_0 \exp\left(-N\sigma_{Reac} z\right) , \tag{2.8}$$

where Φ_0 is the initial ion beam fluence, σ_{Reac} the total reaction cross-section and N the density of target nuclei.

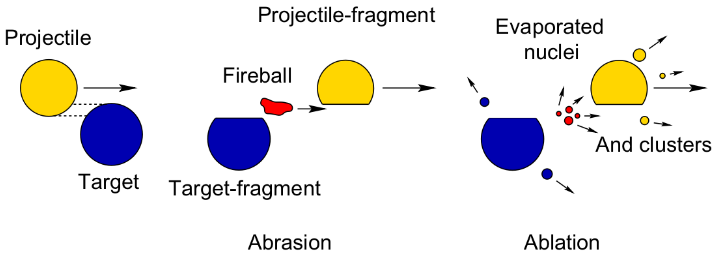

Figure 2.6: Illustration of the abrasion-ablation model to describe peripheral nucleus-nucleus collisions at therapeutic energies. After few nucleons are abraded in a small overlapping zone ("fireball"), the generated projectile and target fragment, as well as the fireball de-excite in the so-called ablation process. Taken from [Gunzert-Marx et al., 2008].

For geometrical reason, peripheral collisions of heavy ions in which only few nucleons of the projectile and the target nuclei participate are much more common than central collision, which could result in a complete disintegration of both particles. These peripheral nucleus-nucleus collisions are described as a two step process in the so-called abrasion-ablation model [Serber, 1947], which is schematically shown in figure 2.6. In a first step, nucleons are abraded in a small overlapping zone ("fireball"), while the remaining outer nucleons, having a Fermi-energy comparably low to the projectile energy, are only slightly affected. In a second step, the newly build projectile and target fragment, as well as the fireball de-excite in the so-called ablation process, emitting prompt-γ radiation, protons, neutrons or nucleon clusters. According to the collision kinematics, the target fragment almost stays at rest, while the projectile fragment proceeds at nearly the same velocity as the incident nuclei. Further details on nuclear fragmentation reactions can, e.g., be found in [Goldhaber and Heckman, 1978; Hüfner, 1985].

The reduced fluence of incident particles (according to equation 2.8) directly translates into a reduced peak-to-entrance dose ratio since the Bragg-peak is produced by only a reduced number of primary heavy ions. Moreover, the on-going nuclear interactions lead to the build up of a secondary particle spectrum. While the energy deposited by the target fragments, nearly at rest, can be neglected, the dose deposited by the further penetrating projectile fragments has to be considered in the dose calculation. Due to the A/Z_p^2 dependence of the ion range, fragments with charge $Z < Z_p$, travelling at about the same velocity as the incident heavy ions, have typically larger ranges in the media with respect to the primary ions and deposit dose behind the actual Bragg-peak, where the primary particles are stopped. The contributions of various projectile fragments produced by a ^{12}C ion beam in water to the integrated depth dose distribution are shown in figure 2.7. Although the reaction cross-section σ_{Reac} is nearly constant down to energies of about 100 MeV/u, ion beams of higher energies show a more pronounced dose tail and an enhanced decrease of the dose in the plateau region due to the longer path-length travelled by the primary particles.

The secondary particles produced in the nuclear fragmentation reactions not only affect the depth dose distribution of heavy ion beams in matter, but also the lateral dose profiles. Although the produced secondary particles are clearly forward peaked, their lateral distribution is broader if compared to that of the primary ions, also due to the enhanced scattering of lighter particles (cf. equation 2.7). Consequently, the lateral dose profile has to be described not only by one

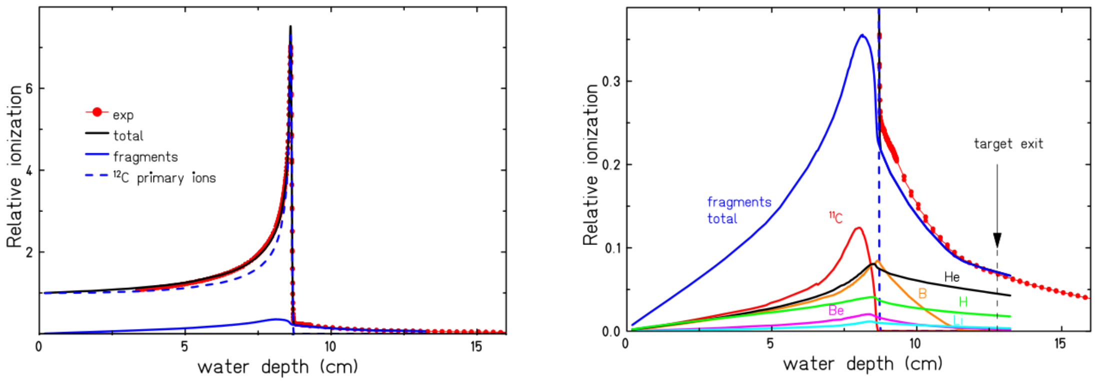

Figure 2.7: Simulation of the dose contributions of projectile fragments to the total depth dose distribution of a 200 MeV/u ^{12}C ion beam in water (right). While the generated carbon fragments (mainly ^{11}C) are stopped shortly before the Bragg-peak, projectile fragments with lower Z have typically increased ranges and give rise to the exit dose behind the peak (left). Figure from [Gunzert-Marx et al., 2008].

Gaussian (related to the multiple scattering of the primary beam according to section 2.2.2), but a linear combination of at least two [Schwaab et al., 2011; Parodi et al., 2013] or even three [Inaniwa et al., 2009].

Although nuclear processes have been described for the case of heavy ions up to this point, protons will undergo nuclear interactions with the target nuclei, as well, resulting in a decrease of the primary proton fluence according to equation 2.8 with increasing depth. These nuclear reactions lead to the formation of target fragments, nearly staying at rest in the much more likely peripheral collisions, and to the production of secondary protons, as well as other light secondary particles evaporated from the excited target nuclei (e.g., deuterons, tritons and Helium isotopes) [Paganetti, 2002]. In contrast to the previously discussed nucleus-nucleus interactions, however, dose contributions by secondary particles are orders of magnitude lower. Moreover, no projectile fragments and no fireball at the abrasion stage are generated in the case of incident proton beams.

Despite the fact that nuclear fragmentation reactions affect the spatial dose deposition pattern in an unfavourable manner by reducing the number of primary ions reaching the Bragg-peak, giving rise to an exit dose distal to the dose maximum (only in the case of heavy ions) and enhancing the lateral spread of the dose distribution, they can be of clinical benefit: nuclear interactions lead to the formation of neutron-deficient β^+-emitting fragments, which can be used for non-invasive, in-vivo ion beam treatment verification by PET imaging, as will be explained in detail in chapter 3. At a pre-clinical stage, also the imaging of prompt gammas and secondary ions emerging from the nuclear interactions is currently being investigated in the context of ion beam therapy monitoring [Min et al., 2006; Gwosch et al., 2013; Knopf and Lomax, 2013].

2.3 Biological aspects of heavy ion beams

Besides the physical advantages covered in the previous section, ions heavier than protons might also yield an enhanced biological selectivity with respect to photons. The quantity relating the efficiency of ions to those of photons is the relative biological effectiveness (RBE), defined as the

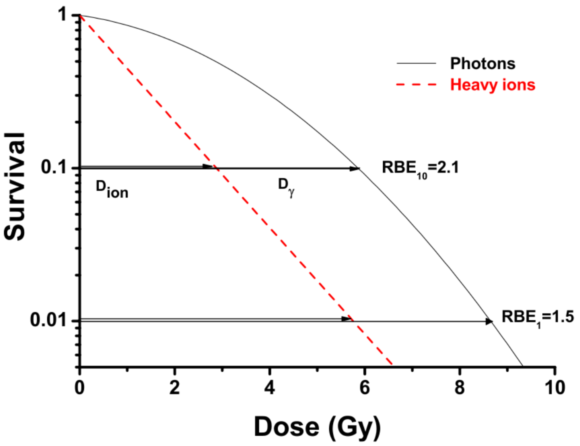

Figure 2.8: Illustration of the RBE definition for heavy ions from experimental cell-survival curves. It can be seen that the RBE depends on the regarded iso-effect, here the 10% and 1% survival, respectively. From[Schardt et al., 2010].

---

ratio of the physical dose by a reference radiation, typically ^{60}Co γ-radiation, and the physical dose by the ion radiation, both resulting in the same biological effect [Scholz, 2003] (see figure 2.8).

$$\mathrm{RBE} = \left.\frac{D_{ref}}{D_{ion}}\right|_{iso-effect} . \tag{2.9}$$

By weighting the physical ion dose with the RBE, the so-called *biological dose* of the ion radiation can be obtained and directly compared to an equivalent photon dose. By this, the experience gained in photon therapy, e.g., the dose required for local tumour control, can directly be translated into the field of ion therapy.

The RBE itself is a complex quantity depending on a variety of parameter like the regarded iso-effect in equation 2.9 (typically the 10% or 1% cell-survival, see figure 2.8), the cell-type under investigation, the charge Z of the heavy ion species and the linear energy transfer (LET) of the incident radiation [Weyrather et al., 1999]. The latter quantity is defined as:

$$LET_\Delta = \frac{\mathrm{d}E_\Delta}{\mathrm{d}x}, \tag{2.10}$$

where $\mathrm{d}E_\Delta$ is the energy locally transferred to charged secondary particles of the stopping medium, not accounting for secondary particles with an energy above a given threshold Δ, as these are not absorbed locally. Setting Δ to infinity, one obtains the “unrestricted stopping power”, which is equal to the electronic stopping power given by equation 2.3.

The dependence of the RBE on the LET is displayed in figure 2.9. As can be seen, heavy ions provide an increasing RBE towards higher LET and smaller residual ranges. Consequently, when approaching the Bragg-peak, positioned within the tumour, the LET and herewith the RBE of the heavy ion beam will increase. At the same time, the RBE will be comparably low in the beam entrance region, despite the lower dose level at which a higher RBE could be expected (cf., figure 2.8). In the end, this differential effect between entrance and Bragg-peak region leads to a superior biological selectivity of heavy ions with respect to photons. In the case of protons

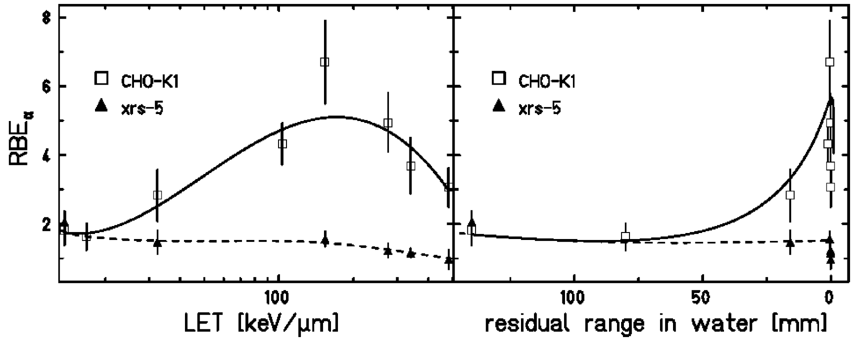

Figure 2.9: The RBE of ^{12}C ions as a function of the LET (left) and the residual range (right) for CHO-K1 chinese hamster cells and their repair deficient mutant xrs-5. Figure from [Weyrather et al., 1999].

on the other hand, the increase of LET and herewith RBE towards the Bragg-peak is much less pronounced due to the Z_p^2 dependence of the LET, and it was shown to be sufficient to apply a constant RBE of 1.1 in the whole treatment field [Paganetti et al., 2002]. An enhanced biological selectivity with respect to conventional photon therapy is thus not given in proton therapy, as there is no differential effect between the entrance and the target region.

For a deeper understanding of the LET dependence of the RBE, the local dose deposition pattern and track-structure of heavy ions has to be considered. In general, heavy ions with high LET show an increasingly inhomogeneous local dose deposition, leading to more complex DNA damages and herewith an increased biological efficiency [Krämer et al., 2003].

2.4 Clinical implementation of ion beam therapy

2.4.1 Ion beam delivery

Up to present, most of the operating ion beam therapy facilities use a so-called *passive beam delivery*: a narrow, almost mono-energetic ion beam is widened up in the lateral direction by several scattering systems and in depth by a range modulator or binary range shifters, yielding a homogeneous 3D dose-cube. This cube is then adapted to the patient-specific target anatomy by a collimator (lateral shaping) and a patient-specific bolus (distal edge shaping) [Chu et al., 1993]. Besides the need for patient-individual hardware, this method has limitations in adapting the dose to the proximal edge of the tumour and shows a comparably high yield of fragments and secondary particles like neutrons due to interactions in the passively beam shaping elements.

In order to overcome these drawbacks, most of the planned or recently built centres use a *3D active scanning beam delivery system* [Haberer et al., 1993; Pedroni et al., 1995]. The idea is as follows (cf. figure 2.10): the tumour is sub-divided into slices corresponding to the same ion beam energy in beam's eye view (BEV). In each of these slices, the tumour volume is covered with a grid of so-called *raster-spots* which are subsequently irradiated with a prescribed number of particles by deflecting the ion beam with a set of two dipole magnets in the horizontal and vertical direction. If all spots of one energy layer are irradiated to the given particle number, the

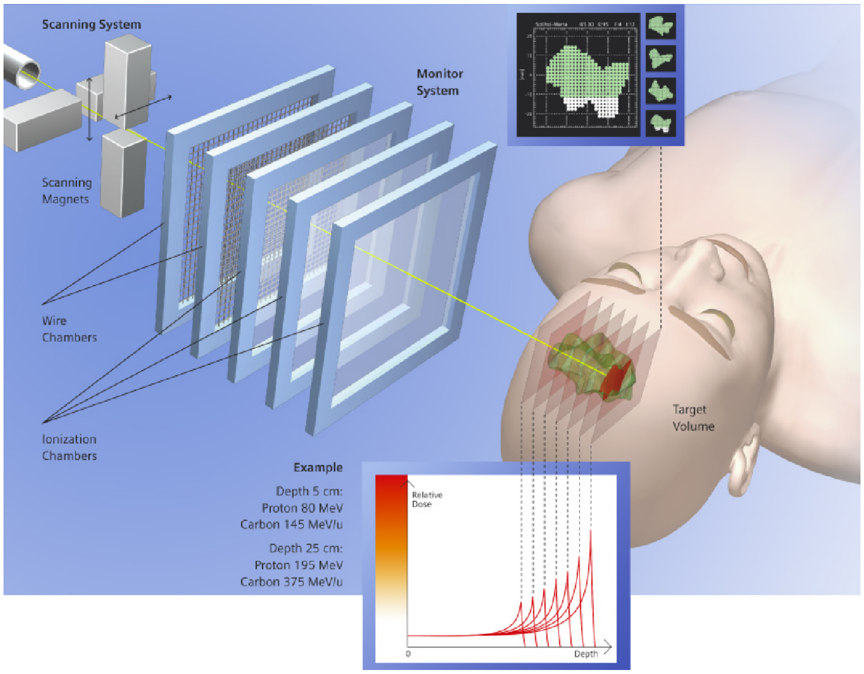

Figure 2.10: Illustration of the 3-D Raster Scanning technique at HIT. The presently irradiated iso-energy layer is selected by tuning the ion beam energy directly at the synchrotron. A double magnet system accomplishes the lateral beam deflection to the individual raster-spots within each layer. Moreover, the beam application monitoring system (BAMS) in front of the patient is depicted. (Source: Siemens Healthcare, Particle Therapy).

energy of the beam is changed to the next adjacent energy slice.

These active beam delivery systems enable sub-millimetre accuracy and, as the intensity is varied from spot to spot in order to achieve a homogeneous dose within the tumour, inherently offer intensity-modulation and best-possible dose conformity to the target volume, including the proximal edge. Moreover, if the energy variation from slice to slice is applied directly at the accelerator level, passively shaping elements can be avoided completely. On the other hand, active scanning techniques are technically much more challenging: the position and intensity of the beam needs to be verified in real-time for each single raster-spot, as small deviations can already lead to remarkable changes in the dose distribution because of the sharp dose gradients of the single pencil beams. Hence, beam application monitoring systems need to be installed. They typically consist of a redundant set of ionisation chambers (IC) and position sensitive detectors (e.g., multi-wire proportional chambers (MWPC) or strip chambers) for fluence and position verification, respectively. Feedback-loops then have to enable the regulation of deviations or, in critical cases, the abortion of the beam application within μs.

2.4.2 The Heidelberg Ion-Beam Therapy Center

At HIT, 3D intensity-modulated raster-scanning is applied, using active energy variation at the synchrotron accelerator level. In order to optimise patient care, the accelerator system offers a comprehensive library of possible beam settings, which can be used in the treatment planning

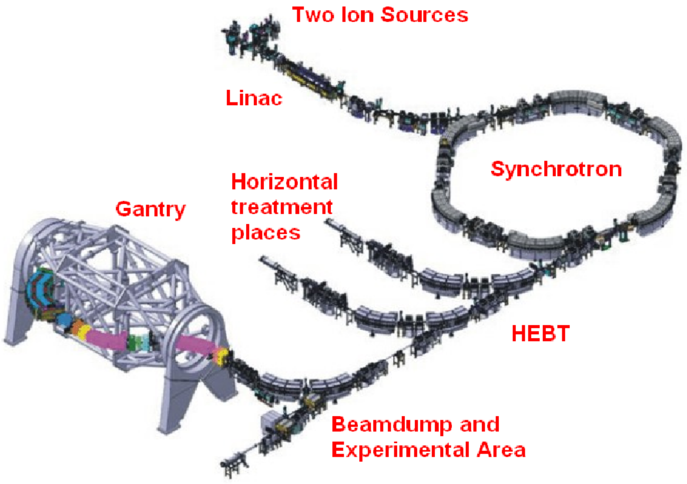

Figure 2.11: The main components of HIT: ions are produced at the ion sources and accelerated stepwise in the linear accelerator (LINAC) and the synchroton. The high energy beam transfer line (HEBT) guides the ions to the two horizontal treatment places, the gantry and the experimental area. [Winkelmann et al., 2010].

process (see next subsection): 255 energy steps, corresponding to particle ranges between 2 and 30 cm in water, can be combined with 4 different foci (lateral beam widths) and ten different intensity levels [Haberer et al., 2004; Parodi et al., 2012].

A sketch of the Heidelberg ion beam facility is shown in figure 2.11. Patients are irradiated in three different treatment rooms: two with a fixed horizontal beam line and one with the world-wide first 360°-rotating heavy ion gantry. Up to date, patients have only been treated using protons and ^{12}C ions, but the synchrotron is also able to deliver ^{4}He, as well as ^{16}O ion beams [Kurz et al., 2012], which might become a future treatment alternative.

2.4.3 Treatment planning

Besides the complex technical implementation, the approach of an actively scanned ion beam delivery poses great demands on the treatment planning system (TPS). The TPS has the complex task of overlapping between about $20,000$ and $50,000$ pencil beams, each corresponding to a single raster-spot in the given target volume, to the optimal dose pattern within the patient. For this, an objective function taking into account, among others, the dose coverage of the target volume, the dose homogeneity in the target volume and the dose given to the surrounding normal tissue and organs at risk, has to be minimised. The settings for a single pencil beam can be retrieved from the above-mentioned library of available beam parameter settings (energy, spot-size, intensity). As a result of the optimisation process, the TPS yields a number of particles to be applied to each of the raster-spots, which is later controlled by the beam monitoring system during the actual patient irradiation.

At HIT, a TPS similar to the dedicated planning software TRiP (TReatment plannIng for Particles) [Krämer et al., 2000], developed for the GSI pilot project in Darmstadt, is used. Dose calculation within the software (Siemens Syngo PT Planning System) is accomplished by a so-called *pencil beam algorithm*, in which the total dose is composed as the sum of the individual pencil beams dose per primary ion, weighted by their specific particle number N_{PB}:

$$D_{tot}(\vec{x}) = \sum_{PB} D_{PB}(\vec{x}) \times N_{PB}\,, \tag{2.11}$$

with

$$D_{PB}(E_{beam}, \vec{x}) = d(E_{beam}, z) \times L(r, z), . \tag{2.12}$$

Here, $d(E_{beam}, z)$ is the laterally integrated depth dose profile, and $L(r, z)$ the normalized (to one) lateral dose distribution of a pencil beam of energy E_{beam} in depth z. $L(r, z)$ is described by a combination of two Gaussian distributions (cf. section 2.2.2) with depth dependent widths $\sigma_i(z)$ and weights $w(z)$ and $1 - w(z)$ [Parodi et al., 2013]. The widths $\sigma_i(z)$ and the weight $w(z)$ of the pencil beam lateral dose profiles at each available beam foci, as well as the integrated depth dose distributions for all available pencil beam energies are generated by dedicated Monte-Carlo (MC) simulations. These are tuned such that dosimetric measurements of lateral and depth dose distributions at a limited number of beam settings can be reproduced precisely, as described in detail in [Parodi et al., 2012, 2013]. All MC-generated profiles are stored in a database and can directly be accessed by the TPS for dose calculation.

The steps for dose calculation described up to this points, as well as the MC generation of the basic TPS input data, are performed in water as a reference medium. When calculating the dose to a patient, however, the depth dose profiles need to be scaled in depth in order to account for the patient-specific anatomy and herewith tissue composition. For this, the depth in a given tissue is translated into the corresponding equivalent depth in water. The conversion factor is called water equivalent path-length (WEPL) and can be derived from the patient CT Hounsfield number by using a so-called *Hounsfield look-up table* (HLUT), as shown in figure 2.12 [Jäkel et al., 2001a; Rietzel et al., 2007]. This table is usually based on a piecewise-linear interpolation of a set of measurements with tissue-equivalent media, in which their WEPL as well as their Hounsfield unit (HU) in a CT scan are determined (see data points in figure 2.12). The TPS then translates the patient anatomy into a water equivalent frame, on which the dose can be calculated as previously described.

In the case of radiation therapy with heavy ions, their biological effectiveness has to be included in the optimisation process as well: after having found a clinically acceptable physical dose distribution, the biological dose within the patient has to be optimised in a non-trivial final step. As the RBE is a complex quantity depending on a wide range of parameters (cf. section 2.3), a bio-physical model within the TPS is of need. At HIT, the so called local effect model (LEM) is used [Scholz and Kraft, 1994, 1996; Scholz and Elsässer, 2007]: it considers the highly inhomogeneous local dose deposition pattern of heavy ions and establishes the relationship between the response of the cells to this distribution and the corresponding response to a homogeneous photon dose, as measured in previous cell experiments or retrieved from clinical photon experience. It assumes that locally, there is no fundamental difference in the response of cells to heavy ions and photons and that differences in the biological efficiency solely arise from the different characteristics of the local dose distribution.

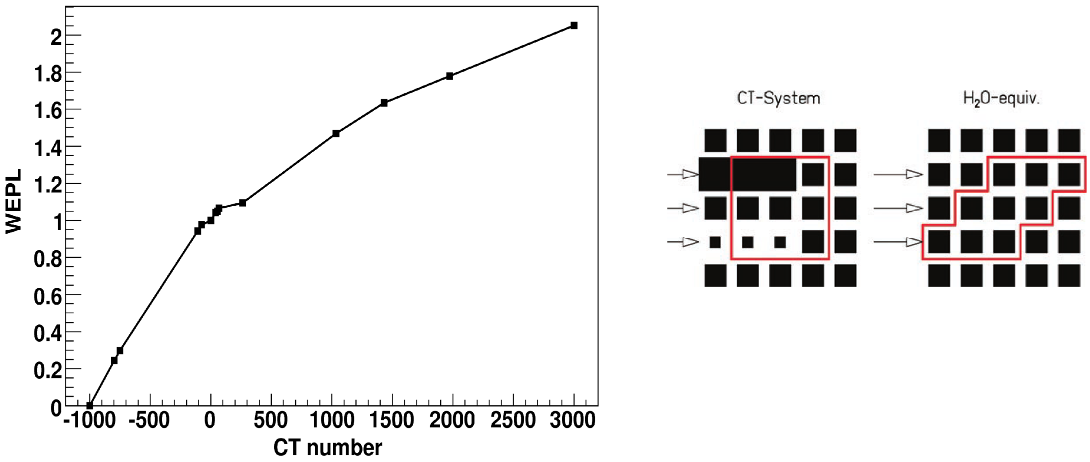

Figure 2.12: For translation of the patient CT into a water equivalent frame, CT numbers are converted into WEPL using a piecewise-linear interpolation of a set of WEPL and CT HU measurements of tissue equivalent materials. The TPS will calculate the optimal dose on a water equivalent system, right side. (Adapted from [Krämer et al., 2000]).

2.5 Uncertainties in ion beam therapy

By making optimal use of the physical, as well as biological properties of proton and heavy ion beams and by applying modern 3D active beam scanning techniques, treatment planning systems can achieve highly conformal dose distributions. The accessible sharp dose gradients allow for an increase of the tumour dose with respect to conventional photon therapy, while not increasing or even reducing the radiation burden to adjacent healthy structures and organs at risk.

On the other hand, the high degree of conformity makes ion beam therapy prone to uncertainties in the radio-therapeutic treatment chain. Small changes in the patient anatomy on the day of the actual irradiation with respect to the treatment planning CT can immediately result in a dose pattern which considerably deviates from the planned one. This is illustrated in figure 2.13 for a hypothetical patient case, where a 1 cm wide air gap is filled up with water during the actual treatment. While there is only a slight impact on the shallow photon dose profile, a serious degradation of the of the ^{12}C ion SOBP dose pattern can be observed: the distal tumour part receives a significantly lower dose, whereas the normal tissue proximal to the tumour is exposed to a remarkably higher dose. In a similar way, deviations in the patient set-up and immobilisation can diminish the anticipated superiority of ion beam dose distributions.

In order to minimise the impact of anatomical changes and patient miss-alignments, modern radiotherapy implements image guidance in the treatment course. Typically, 2D orthogonal X-ray imaging in treatment position for the matching of bony landmarks or implanted markers is performed right before the actual beam application and minimises set-up uncertainties to about 1.5 mm [Jäkel et al., 2001b]. These systems, however, only provide 2D projections and poor soft-tissue contrast. For this reason, the use of 3D X-ray CTs (conventional or cone-beam CT) for image guidance is more and more spreading, particularly in modern photon therapy, although it is accompanied by an additional radiation burden on the patient.

Still, image guidance cannot account for uncertainties in the imaging process itself, where

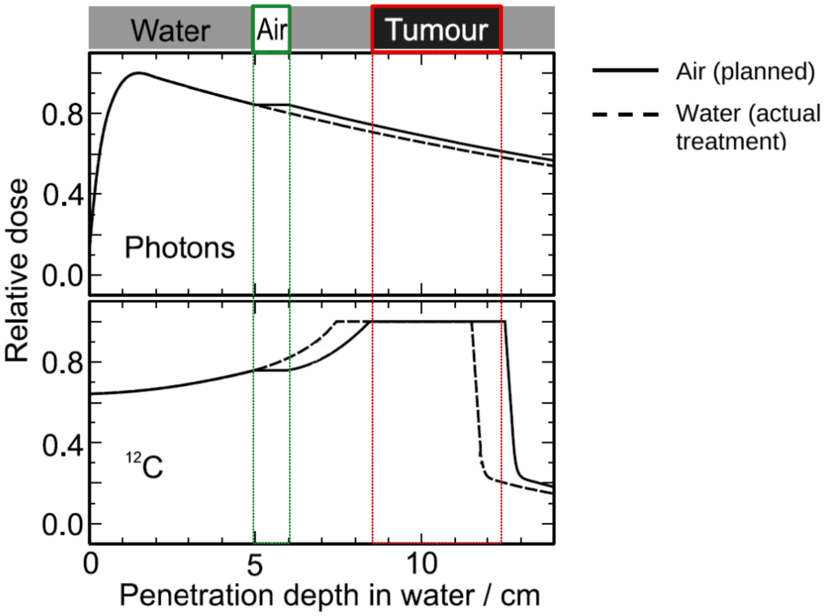

Figure 2.13: Impact of anatomical changes on the depth dose distributions of a 6 MeV photon beam (top) and a ^{12}C SOBP (bottom), assuming the filling of a 1 cm wide air gap with water during the actual treatment. While the impact on the photon dose profile is rather small, the induced shift of the SOPB leads to a significant under-dosage of the distal tumour part and a critical over-dosage in the normal tissue proximal to the tumour. (Adapted from [Enghardt, 2005]).

errors can e.g., be introduced by partial volume effects, metal implants, beam hardening effects, image noise or the CT number dependence on the object size. Due to these intrinsic CT inaccuracies and errors in the WEPL measurements, the HLUT which connects the CT numbers to corresponding WEPLs is affected by uncertainties, as well. They directly translate into uncertainties of the beam range within the patient, as calculated by the TPS [Rietzel et al., 2007]. Further errors can be introduced, if materials of different stopping power cannot be distinguished by their Hounsfield number. A deep investigation of numerous sources of range uncertainties in proton therapy can be found in [Paganetti, 2012]. Here, the total range accuracy for the proton beams has been determined to be in the order of $2-5\%+1.2$ mm, depending on the complexity of tissue inhomogeneities. A similar estimate of $1-3\%$ for carbon ion beam ranges can be found in [Jäkel et al., 2001b]. For a deep-seated tumour at about 20 cm depth in water, this corresponds to an uncertainty of approximately $4-10$ mm.

The simplest way to account for the underlying uncertainties in ion beam therapy is to extend the identified tumour volume by a safety margin at the stage of treatment planning on the basis of the treatment planning patient CT [ICRU, 1993a, 1999]. This enlargement of the irradiated volume might, however, lead to conflicts with close-by organs at risk, generally increases the dose given to adjacent healthy tissue and thereby degrades the conformity of ion beam therapy. Moreover, when selecting the incident beam directions during the treatment planning stage, it is typically avoided to place the distal dose fall-off in front of critical structures. Instead, the less sharp but more reliable lateral dose gradients are used, sacrificing the best possible dose distribution for the sake of safety. In future, progress in treatment planning is foreseen by dedicated robust planning techniques, which inherently consider possible uncertainties at the stage of plan optimisation, but are not yet established in clinical routine [Unkelbach et al., 2009; Chen et al., 2012].

2.6 Organ motion in ion beam therapy

Besides the uncertainties covered in the previous section, severe errors can be introduced by organ motion for specific treatment sites, like the prostate, the lung or the liver.

2.6.1 Introduction to organ motion

Depending on the time-scale on which changes of the patient anatomy occur, organ motion is typically divided into inter-fractional motion (i.e., changes from fraction to fraction on a time-scale of days) and intra-fractional motion (i.e., changes during the treatment application on a time-scale of seconds to minutes).

The sources of inter-fractional motion are diverse. Tumour shrinkage, e.g., can occur for a wide range of tumours and particularly affects the treatment at locations where large density gradients between target volume and surrounding tissue can be found, like in the lung [Mori et al., 2009b]. Lung tumours are moreover sensitive to base-line drifts of the patients respiratory motion [Sonke et al., 2008] from fraction to fraction. Other tumour localisations, like the prostate and the pancreas are strongly effected by inter-fractional motion due to variations in bladder and gut filling [van Herk et al., 1995; Whitfield et al., 2012].

Intra-fractional motion [1] on the other hand can be mainly attributed to heart beat and respiration. Respiratory motion does not only affect tumours in the lung, but also in many other organs, like the pancreas [Mori et al., 2009a], the liver or even the prostate [Malone et al., 2000]. For tumours in the lung, a large variation of the motion trajectory from patient to patient is typically found. Even for an individual patient, trajectories might change from fraction to fraction [Seppenwoolde et al., 2002]. In general, it was found that motion amplitudes depend, among others, on the location of the lesion within the lung, and that amplitudes are on average larger in the superior-inferior (SI) direction than in the anterior-posterior (AP) and left-right (LR) directions [Shirato et al., 2004]. About 40% of the lung tumour patients investigated in [Liu et al., 2007] showed a SI motion amplitude of above 5 mm, while the motion amplitude did not exceed 13.4 mm in 95% of the patients. For tumours in the liver, which are of main interest in the scope of this work, a pronounced motion in the SI direction was found, as well. In [Case et al., 2010] a mean motion of 8 mm in this direction was found, ranging from about 0 to 19 mm. Changes of the motion amplitude within the individual treatment fractions and from fraction to fraction were found to be small (below 2 mm). Similar results have been reported in [Kitamura et al., 2003], where beyond that a dependence of the motion amplitude on the location of the lesion within the liver was observed.

---

[1] In the context of this work, the term organ motion will from now on be used synonymously for intra-fractional motion.

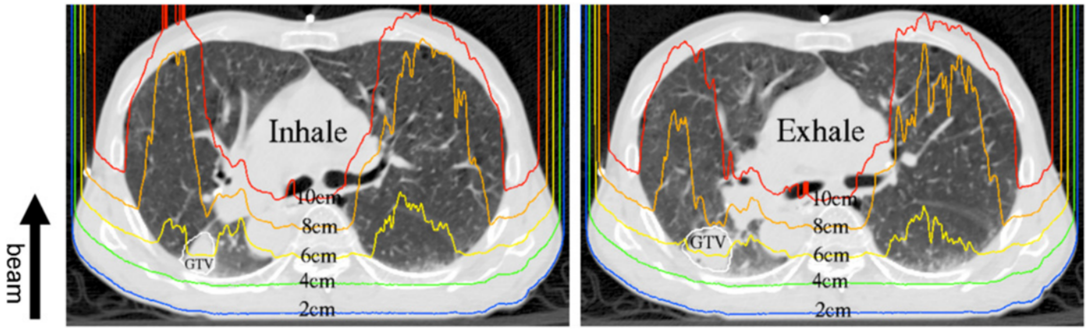

Figure 2.14: In the presence of respiratory motion, significant differences in the WEPL, corresponding to the depicted iso-range lines, can appear between different motion states (here inhale (left) and exhale (right)). In this case, the changes can be mainly attributed to the movement of the *gross tumour volume* (GTV) with respect to the treatment field. Figure from [Bert and Durante, 2011].

2.6.2 Implications of organ motion for ion beam therapy

In the presence of organ motion, the patient anatomy can undergo changes within seconds. As discussed in section 2.5, these anatomical changes can have a significant impact on the actually applied dose to the patient due to changes in the WEPL traversed by the beam particles, as shown for the case of a lung tumour in figure 2.14. In this case, the relatively large density gradients between the lung tissue and the tumour result in a significant shift of the iso-range lines. If density gradients are smaller, e.g., for central lesions in the liver, changes of the iso-range lines are generally smaller, but the amount of dose deposited outside the actual target volume can still be significant.

Besides compromising the dose distribution by anatomical changes, organ motion can lead to so-called *interplay effects* in the case of an active scanning beam delivery. Here, irradiation times are typically in the order of minutes, i.e. , much larger than the typical respiratory period, and the spot-wise beam delivery sequence interferes with the organ motion [Phillips et al., 1992]. This can lead to areas of severe under- and over-dosage within the target volume, as well as to unwanted exposure of healthy structures, as shown in figure 2.15 for the case of three liver tumour patients. The magnitude of interplay effects depends, among others, on the tumour motion amplitude and the direction of the motion with respect to the scanning direction and the incident beam direction [Lambert et al., 2005; Grözinger et al., 2006; Bert et al., 2008].

2.6.3 Organ motion management in ion beam therapy

In order to minimise the negative impact of organ motion on the treatment outcome, a wide range of techniques have been developed over the last years. Considering inter-fractional motion, the approach of image guided radiotherapy, as mentioned in section 2.5, is very promising: the current location of the target volume on the treatment day is retrieved and can directly be used for a correction of the patient position or an adaptation of the planned treatment. Determination of the target volume position can e.g., be based on 3D cone-beam CT imaging, 2D Xray imaging of implanted fiducial markers or ultrasound imaging [Kupelian et al., 2008]. Up to present, image guidance techniques are, however, predominantly applied to modern photon therapy. The

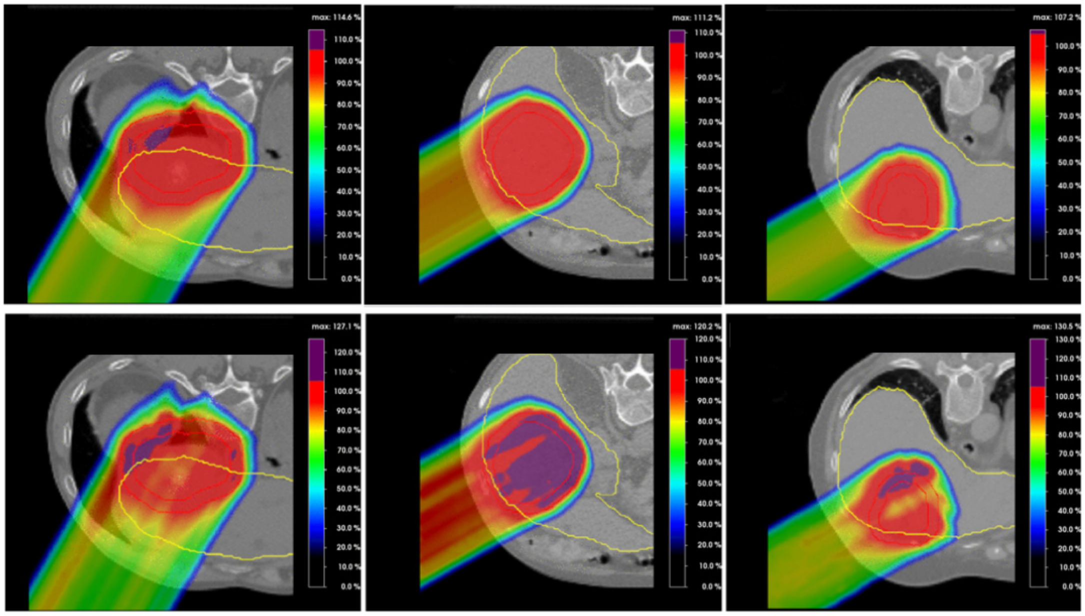

Figure 2.15: Study of interplay effects in three different liver tumour patients treated with scanned proton beam therapy (bottom row). In all cases, the dose conformity and uniformity within the target volume is clearly diminished, while the dose to particular areas of the normal tissue is significantly enhanced with respect to the static reference study (top row). Adapted from [Zhang et al., 2012].

---

most frequently applied approach in ion beam therapy still is to include potential inter-fractional changes in the treatment planning process by an increase of the applied safety margins. Yet, this generally leads to a degradation of the dose conformity and possibly to an increase of the radiation exposure to close-by organs at risk, like the rectum in the case of prostate radiotherapy.

The approach of increased margins can also be applied to account for respiration-related inter-fractional motion [Nihei et al., 2006; Bush et al., 2004]. Although range changes due to respiratory motion of the target volume can be included in the definition of the so-called *internal target volume* (ITV) [Graeff et al., 2012], consisting of the gross tumour volume and a set of margins accounting for all expected uncertainties, the increase of margins still leads to an increased radiation burden on healthy tissues and cannot reduce interplay effects in the case of a scanned beam delivery. Consequently, a variety of motion mitigation techniques have been developed to foster ion beam therapy of moving tumours.

One straightforward approach is the reduction of the amplitude of organ motion. This can be accomplished, e.g., by breath-hold techniques [Remouchamps et al., 2003], apnoea [RPTC, 2012], the so-called *jet-ventilation* [Hof et al., 2003] or abdominal compression systems [Negoro et al., 2001; Wunderink et al., 2008]. The latter have shown to reduce the SI motion amplitude of liver tumours on average by more than 50%. Besides these motion suppression techniques, special beam application techniques for motion mitigation have been developed: beam gating, rescanning and beam tracking.

In beam gating, the target volume is only irradiated in a predefined part of the breathing cycle, the *gating window* (GW) [Minohara et al., 2000]. This is schematically shown in figure 2.16: the tumour motion is detected by a motion monitoring system (see section 2.6.4), which creates

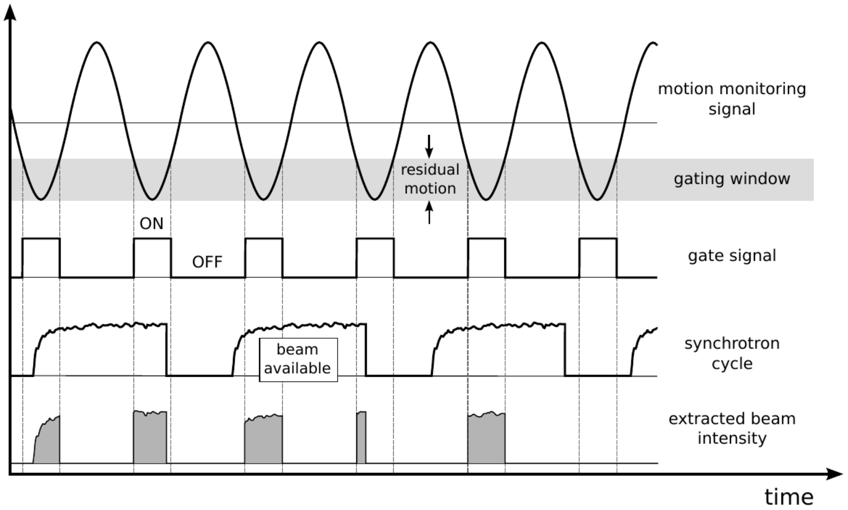

Figure 2.16: Illustration of the beam gating technique for a synchrotron accelerator. The target volume motion is detected by a motion monitoring system, which creates a logical gate signal according to the predefined GW. If the tumour motion coincides with the GW and beam is available from the synchrotron, the beam is extracted and delivered to the target. Figure from [Richter, 2013].

---

a logical gate signal based on the pre-defined gating window, typically arranged symmetrically around the comparably stable end-exhale position. If the gate is open, i.e., the tumour is in the desired position, and beam is available from the accelerator, beam extraction starts. If the tumour moves out of the gating window, beam application is aborted immediately. Beam gating has already been implemented for patient treatment at several facilities, like NIRS [Miyamoto et al., 2007], the Proton Medical Research Center at Tsukuba University, Japan [Hashimoto et al., 2006] or the Heidelberg ion beam facility [Richter, 2013]. The effectiveness of beam gating, however, strongly depends on the size of the gating window, which defines the residual motion of the tumour during the gated beam delivery. Particularly in the case of an active beam delivery, residual motion can still cause a notable interplay pattern in the target region. Increasing the lateral width of the single raster-spots was found to reduce the impact of residual motion on the dose homogeneity, but only at the expense of a decreased dose conformity [Bert et al., 2009; Richter, 2013]. In addition, beam gating relies on a accurate tracking of the target motion by the monitoring system.

This is not the case for the approach of rescanning, which is based on a statistical averaging effect by repeated irradiation of the target volume with a certain fraction of the total dose in each scan [Phillips et al., 1992]. Rescanning can be applied in different ways: in volumetric rescanning, the whole target volume is rescanned, while in slice-by-slice rescanning the single iso-energy slices are rescanned to the total dose one after the other. Rescanning can efficiently diminish interplay patterns by the averaging effect (provided that there are no synchronisation effects between the respiratory motion and the beam delivery [Furukawa et al., 2010]), but still requires safety margins covering the whole range of the target motion, thus decreasing dose conformity and increasing dose to normal tissue [Bert and Durante, 2011]. A promising approach, which is planned to be implemented in the near future at several centres using actively scanned ion beams, is therefore the combination of gating and rescanning: gating restricts the tumour motion amplitude and herewith the applied margins to the residual target motion within the GW, rescanning mitigates residual interplay effects by repeated scanning [Furukawa et al., 2007; Zenklusen et al., 2010].

A completely different approach is pursued with the technique of beam tracking in scanned particle therapy: here, the applied ion beam follows the tumour movement, as detected by a motion monitoring system. Lateral tracking is accomplished by the scanning magnets, while possible range changes are accounted for by fast energy modulation of the beam, e.g., by a mechanical passive energy degrader. The parameters for correction of the beam position and energy in each motion state are pre-calculated on the basis of the time-resolved 4D planning CT, stored in a look-up table and applied online according to the presently detected motion phase [Bert et al., 2007; Saito et al., 2009; Bert et al., 2010]. Theoretically, an increase of safety margins is not necessary in beam tracking, but as neither the target motion is reduced, nor the applied dose smoothed by repeated scans, this technique is highly sensitive to errors in the tracking of the tumour motion, and to changes in the respiratory motion of the patient with respect to the treatment planning 4D CT. As a consequence, beam tracking in ion beam therapy is still at a pre-clinical stage.

2.6.4 Motion monitoring

As already stressed in the previous section 2.6.3, motion monitoring systems play an important role in the field of 4D radiotherapy with ion beams. Accurate and precise determination of the target position in real-time is, however, not only important in the context of the beam delivery (gating, tracking), but also in the context of patient imaging during the treatment planning process, e.g., in order to adapt safety margins to the target motion. The latter is usually determined on the basis of a 4D CT image, for which projection data are acquired in such a way that for each image slice, data in each respiratory state are available. These data are then split into the single motion phases (either before or after reconstruction) according to the simultaneously recorded respiratory motion signal [Vedam et al., 2003a; Pan et al., 2004].

Inaccuracies in the detection of the target motion can result in severe imaging artefacts [Wood and Henkelman, 1984; Vedam et al., 2003a; Liu et al., 2009], leading to an incorrect delineation of the tumour volume during treatment planning and consequently to significant deviations of the applied treatment from the intended one, particularly in the case of gating or tracking.

Up to date, most clinically available motion monitoring systems infer the actual target position from an external motion surrogate, which is supposed to be well-correlated to the actual internal organ motion [Vedam et al., 2003b]. This external motion signal can be deduced in various ways, e.g., by optical tracking of surface markers (Varian RPM system, Varian Medical Systems, Palo Alto, USA) or by measuring the expansion of the patient chest-wall either with a laser distance sensor or with a pressure sensor attached around the patient with a dedicated belt (ANZAI AZ-733V, ANZAI Medical, Tokyo, Japan). The assumption of a reliable and stable correlation between internal and external motion has, however, been found to be questionable in particular cases, especially if the target motion is undergoing phase-shifts or base-line drifts [Chen et al., 2001; Zhang et al., 2003; Ionascu et al., 2003; Koch et al., 2004; Hoisak et al., 2004]. Consequently, it is highly desirable to detect the actual internal target movement directly, e.g., by magnetic tracking of implanted radio-frequency marker [Seiler et al., 2000] or by fluoroscopic imaging of implanted high density fiducials [Shirato et al., 2000]. These techniques are however invasive [Bhagat et al., 2010] and, in the case of fluoroscopic tracking, put additional dose burden on the patient [Shirato et al., 2004]. A promising approach to avoid these side-effects could be motion tracking by real-time ultrasound imaging. A first implementation of this technique for 4D PET imaging will be presented later in this work.

2.6.5 Treatment of moving targets at HIT

At HIT, the treatment of moving tumours is up to date limited to HCC patients with respiration-affected target volumes in the liver. Until the end of 2013, in total 16 HCC patients have been irradiated. In order to reduce the tumour motion amplitude and diminish possible interplay effects by the scanned beam delivery, 15 of those patients were treated with an abdominal compression system. Typically, SI motion amplitudes could be reduced to below 1 cm. In two critical cases, as well as in the single case without compression, a gated beam delivery has been applied. In addition, the lateral beam width has been increased from the standard size of 6 mm to 10 mm full-width-at-half-maximum (FWHM), using a 2 mm lateral raster grid spacing [Richter et al., 2014].

Treatment planning for these patients has been performed with the Siemens Syngo PT TPS, either on a free-breathing 3D CT for patients irradiated with the abdominal compression system, or on a breath-hold 3D CT in the end-exhale position for the pure gating patient. Motion has, nevertheless, been considered in the treatment planning step as well, namely by an increased ITV margin around the *clinical target volume* (CTV, region of visible malignant growth and surrounding subclinical microscopic malignant disease [ICRU, 1993a, 1999]), covering the entire tumour motion trajectory, as retrieved from a contrast enhanced 4D CT scan. On top, safety margins of 5 mm in the lateral and 7 mm in the longitudinal direction were added to form the planning target volume (PTV). All patients have been treated by a single right-lateral carbon ion field to a total biologically effective PTV dose of 32.4 Gy(RBE) in four treatment fractions, following the fractionation scheme of [Tsujii et al., 2007]. During the 4D CT imaging, as well as during the actual beam application, the patient respiratory motion has been monitored by the pressure sensor of the ANZAI AZ-733V respiratory gating system [Combs et al., 2011; Habermehl et al., 2013].

In order to minimise set-up uncertainties and to avoid unfavourable consequences by inter-fractional motion (particularly due to variations in gut filling), all patients underwent a 3D position verification CT in treatment position right before the actual irradiation. Moreover, treatment verification by means of post-irradiation PET imaging has been carried out (see chapters 3 and 6 for details).

2.7 Summary

In this chapter, the most important physical and biological rationale of ion beam therapy have been introduced. The favourable physical and, in the case of heavy ions, biological properties of ion beams in combination with modern beam application techniques allow for an increased dose conformity to the target volume and a reduced dose burden on healthy tissues with respect to conventional photon therapy.

This chapter, however, also pointed out that the accessible sharp dose gradients make ion beam therapy prone to uncertainties. The sources of uncertainty are manifold. Usually, they are taken into account by a cautious increase of the applied safety margins around the actual target volume and careful selection of the incident beam directions at the expense of a less conformal dose distribution within the patient. In order to fully exploit the promised potential of ion beam therapy, it is therefore indispensable to control uncertainties in the treatment chain and to verify the actually applied treatment in-situ and in 3D. The only clinically implemented approach for an independent verification of the entire treatment chain shortly after single irradiation fractions is based on 3D PET imaging of the radiation induced β^+-emitter within the patient, as introduced in detail in the following chapter.

Additional challenges and uncertainties arise in the presence of organ motion. A variety of different motion mitigation techniques have been developed. Approaches like beam gating or tracking can theoretically achieve results close to static reference cases, but they heavily rely on the validity of the underlying patient 4D CT data and an accurate detection of the target motion during beam delivery. Variations in the shape or the baseline of the respiratory trajectory of the target volume, or the practically unavoidable residual motion in the case of gating can still lead to severe deviations of the applied treatment with respect to the planned one. Due to the increased level of uncertainty in the treatment of moving targets, especially in the case of a scanned beam delivery, a time-resolved (4D) verification of the actually applied treatment is highly desirable. In the scope of this work, the extension of the PET-based treatment verification approach, presently being restricted to clinical applications with static target volumes, to moving tumour entities will be investigated under clinical conditions for the first time.

Chapter 3

PET-based treatment verification in ion beam therapy

This chapter will review in detail the concept of PET-based treatment verification in ion beam therapy. First, the physical rationale behind PET-based treatment monitoring and the basics of PET imaging will be introduced. Then, the clinical implementation, with a focus on the approach pursued at HIT, will be discussed.

3.1 Production of β^+-emitter

As has been mentioned in section 2.2.3, nuclear fragmentation reactions of incident projectile nuclei in the penetrated tissue can lead to the formation of neutron-deficient positron emitters, which can be detected by PET imaging systems [Enghardt et al., 1999, 2004a; Parodi et al., 2008a].

While in the case of carbon ions, projectile and target nuclei can fragment, incident proton beams can only form target fragments, as the protons themselves cannot fragment (cf. figure 3.1). An overview of the irradiation-induced β^+-emitter which contribute most significantly to the detectable activity signal in the target volume is given in table 3.1 [Parodi et al., 2008b]. Thereof, the most important isotopes are ^{11}C and ^{15}O, with half-life times of about 20 and 2 min, respectively.

The cross-sections of the main production channels of these two β^+ emitter are depicted in figure 3.2, once for the case of protons and once for the case of carbon ions. For protons and carbon ions, the reaction cross-sections are almost constant down to about 100 MeV and 10 MeV/u, respectively. Below this energy, the β^+-emitter production cross-sections will increase, until

Table 3.1: Overview of the most important β^+-emitter in PET-based ion beam therapy monitoring and their corresponding half-lives.

Isotope	^{11}C	^{15}O	^{13}N	^{30}P	^{34}Cl	^{38}K
Half-life [min]	20.38	2.04	9.97	2.50	32.00	7.63

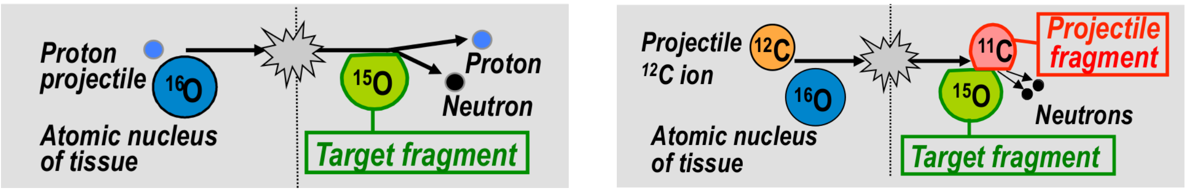

Figure 3.1: Illustration of the formation of positron emitter in proton (left) and carbon ion (right) therapy. While in the case of protons only positron emitting target fragments can be generated, β^+-active projectile fragments can additionally be produced in the case of carbon ions.

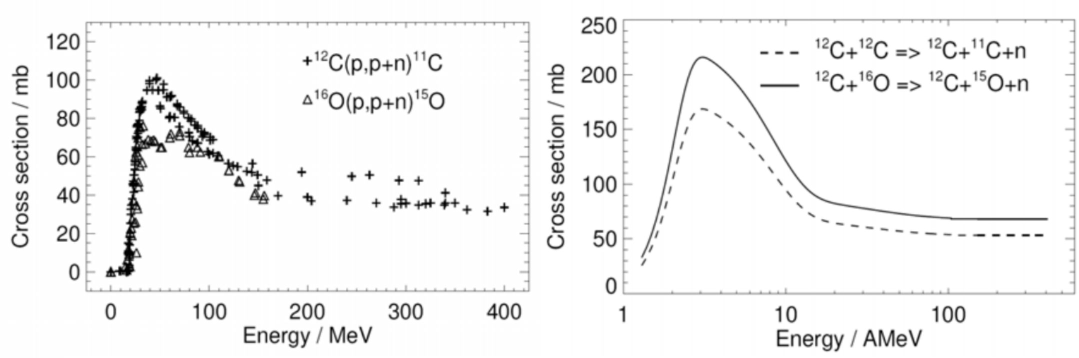

Figure 3.2: Cross-sections of the main reaction channels for the formation of ^{11}C and ^{15}O β^+-emitter by protons (left, measured data) and carbon ions (right, calculated data). Taken from [Parodi, 2004].

the projectile energy falls below the threshold of the regarded nuclear reaction. These energies typically correspond to just a few millimetre residual range of the incident particles in soft tissue. In the case of protons, where only target fragments nearly staying at rest are produced in the nuclear interactions (cf. section 2.2.3), this results in a rather flat or slightly increasing activity profile as a function of depth. Right in front of the Bragg-peak, the projectile energy falls below the reaction threshold and the activity profile shows a substantial fall-off which follows the shape of the decrease of the underlying dominant cross-sections. This is exemplarily shown in figure 3.3 for a proton beam in a Polymethyl-methacrylate (PMMA) target.

In the case of carbon ions, this flat distribution of target fragments is superimposed by the activity distribution originating from the produced projectile fragments, mostly ^{11}C. The latter are produced at nearly the same velocity as the incident projectile (cf. section 2.2.3) and, due to the A/Z^2 dependence of the ion stopping power, have a comparable range. This gives rise to a characteristic maximum in the activity distribution shortly before the Bragg-peak, where the primary ions are stopped (see figure 3.3). One should also notice that target fragments can still be produced distal to the Bragg-peak by long-penetrating secondary particles, like protons.

3.2 Positron emission tomography imaging

The irradiation-induced activity pattern within the target volume can be assessed in 3D by PET imaging techniques. These rely on the coincidence detection of two 511 keV photons [Phelps et al.,

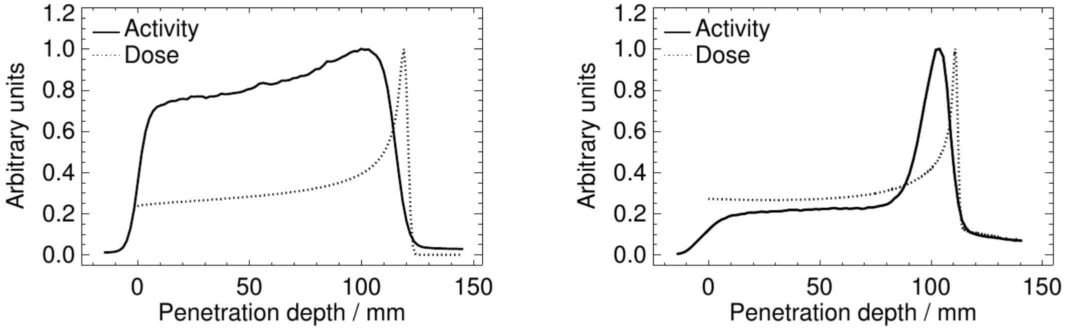

Figure 3.3: Measured activity depth profiles (solid line) and calculated depth dose distributions (dashed line) of 140 MeV protons (left) and 259.5 MeV/u ^{12}C ions in Polymethyl-methacrylate (PMMA), normalised to the maximum. While the activity profile is rather shallow in the case of protons, a distinct peak, formed by the projectile ^{11}C fragments, can be noticed in the case of carbon ions. Figure from [Parodi, 2004].

1975; Ter-Pogossian et al., 1975], which originate from the annihilation of the positron generated in the radio-active decay of a β^+-emitter $A(Z,N)$, with mass number A, atomic number Z, and neutron number N according to:

$$A(Z,N) \quad \longrightarrow \quad A(Z-1,N+1)+e^{+}+\nu_{e}\,. \tag{3.1}$$

The positron is emitted with a continuous energy spectra and slows down over a few millimetres in the surrounding tissue. Here, it can suffer from direct annihilation under the emission of two anti-parallel gammas or it can form the unstable e^+e^- bound state positronium with an electron of the tissue before annihilating into either two or three gammas. As described in detail in [Harpen, 2004], the decay into two gammas is, however, much more likely. Due to momentum conservation, the two gammas are emitted in anti-parallel directions (if neglecting the small residual motion of the positron) with an energy of the e^+ and e^- rest mass of 511 keV, each. The anti-parallel gammas are detected in coincidence by an opposed detector pair, and attributed to a decay along the line connecting the two detectors, the so-called *line of response* (LOR), as schematically shown in figure 3.4.

Besides coincidences ascribed to the two primary gammas emitted by a single β^+-decay ("true coincidence"), coincidences of two gammas from independent decays might be detected by chance ("random coincidence"). Moreover, one, or even both, of the emitted gammas might undergo scattering before reaching the detector, leading to an incorrectly projected LOR, not containing the actual location of the annihilation ("scattered coincidence"). This is illustrated in figure 3.5.

In PET imaging, only true coincidences contain valuable information for the recovery of the underlying β^+-activity distribution. Hence, scattered and random coincidences need to be corrected for, when processing the acquired coincidence data, as described e.g., in [Ollinger, 1996; Watson et al., 1996; Brasse et al., 2005]. Moreover, the attenuation of gammas along each LOR needs to be considered in the case of quantitative imaging [deKemp and Nahmias, 1994; Kinahan et al., 1998], as well as the efficiency of the single detectors and the geometrical detection probability for each emission position.

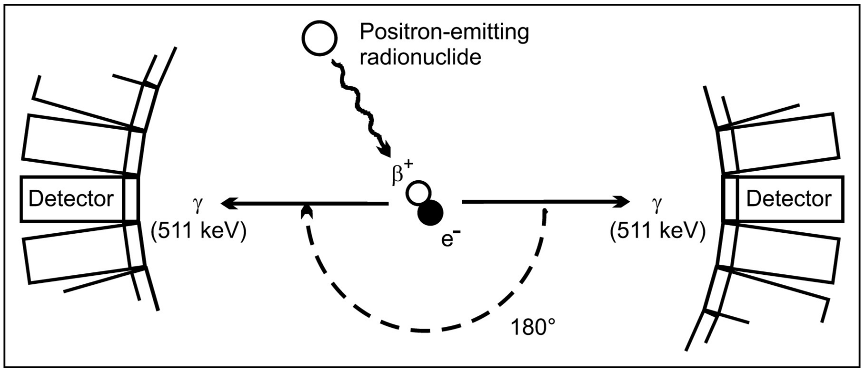

Figure 3.4: Illustration of PET imaging: the β^+-active nucleus emits a positron which is stopped in the close-by medium and annihilates with an electron into two anti-parallel gammas of 511 keV, each. These are detected in coincidence by a detector pair and attributed to a decay along the line of response, connecting the two opposed detectors. Figure from [Verel et al., 2005].

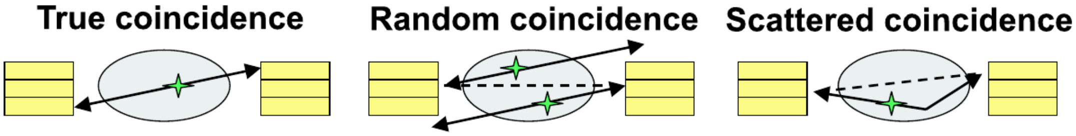

Figure 3.5: Sketch of the different coincidence types in PET imaging. In a true coincidence, the original gammas are detected and the LOR (dashed line) contains the spot of annihilation. In scattered coincidences, at least one of the emitted gammas is scattered before detection and in random coincidences, two independent gammas are accidentally attributed to the same event, leading to an incorrectly projected LOR in both cases. Taken from [Parodi, 2004].

The corrected true coincidence data represents a projection of the underlying activity distribution, which can thus be recovered by tomographic reconstruction algorithms like a filtered back-projection (FBP) [Brooks and Di Chiro, 1975; Ollinger and Fessler, 1997], or by so-called *iterative reconstruction algorithms*. The latter are based on the statistical nature of radio-active decay (Poisson statistics) and solve the problem of finding the most likely activity distribution that would yield the measured projection data [Qi and Leahy, 2006]. The most widely used iterative algorithms are the so-called *maximum likelihood expectation maximisation* (MLEM) [Shepp and Vardi, 1982] and the *ordered subset expectation maximisation* (OSEM) [Hudson and Larkin, 1994], which differs from the MLEM in the fact that the projection data is subdivided into a user-defined number of subsets during the reconstruction process for faster convergence.

Iterative reconstruction algorithms are particularly suitable in low counting statistics scenarios and are thus of particular interest in PET-based treatment verification, where the amount of irradiation-induced activity in the subject of investigation is significantly lower than in diagnostic PET imaging with injected radio-tracers: in diagnostic PET imaging, activity densities in the order of $10 - 100$ kBq/ml are typically found, while PET-based treatment verification has to struggle with activities in the order of $0.05 - 10$ kBq/ml, depending on the specific implementation [Enghardt et al., 2004a; Parodi et al., 2007a; Bauer et al., 2013b] (as briefly reviewed in the subsequent section).

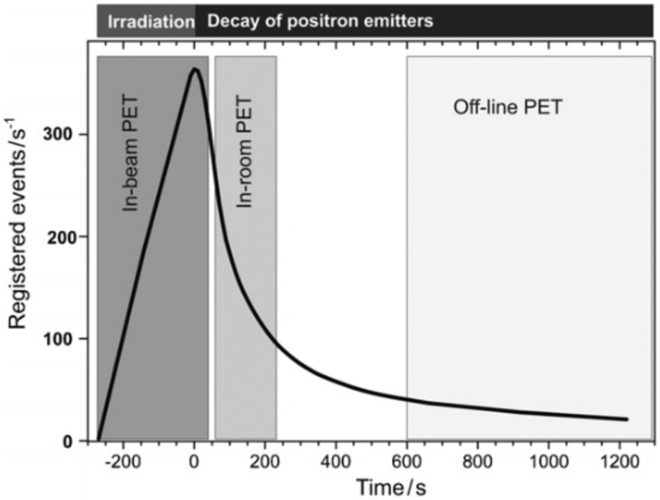

Figure 3.6: Illustration of the different time regimes in PET-based treatment verification. In-beam acquisition starts during the treatment and can be prolonged shorty after. In-room and offline applications can start with a delay of $1-3$ and $5-10\,\mathrm{min}$, respectively. Consequently, the number of detectable counts, is highest for in-beam and lowest for offline PET monitoring, thus calling for a prolonged measurement time. Taken from [Shakirin et al., 2011].

The achievable intrinsic spatial resolution in whole-body PET imaging is about $3-5\,\mathrm{mm}$ FWHM. It is mainly limited by the non-perfect co-linearity of the two coincidentally detected gammas, the residual range of the emitted positron (approximately $1-3\,\mathrm{mm}$ FWHM) and the detector granularity [Moses, 2011]. This limited resolution leads to an overall blurring of the reconstructed images, but does not prevent millimetre accuracy in the detection of activity gradients, as desired in PET-based treatment verification and demonstrated in dedicated phantom experiments [Parodi et al., 2005b].

3.3 Clinical implementation of PET-based treatment verification

PET-based monitoring of ion beam therapy has already been implemented at several facilities worldwide. The different approaches which are being pursued can be classified into three categories: in-beam, in-room and offline (cf. figure 3.6). In in-beam treatment verification, PET data is acquired during the actual irradiation (typically during the synchrotron spill pauses to avoid high random rates by irradiation-induced prompt gammas [Parodi et al., 2005a]) and might be prolonged up to few minutes after the treatment [Enghardt et al., 2004b; Parodi et al., 2008a; Nishio et al., 2010]. This technique yields a comparably high number of counts (depending on the length of the spill pauses used for data acquisition) and is less sensitive to washout processes of the induced activity, e.g., due to blood perfusion [Shakirin et al., 2011; Helmbrecht et al., 2013]. On the other hand, this approach is up to present limited to the application of dedicated PET-detectors in dual-head or partial-ring geometries with high integration costs in order to not obstruct the movement of the patient couch. These geometries provide a reduced detection efficiency and suffer from limited-angle artefacts in the reconstructed images [Crespo et al., 2006]. Improvements are, however, foreseen by further evolved PET detectors with high time-of-flight (TOF) resolution [Crespo et al., 2007] or by dedicated open-ring PET geometries [Yamaya et al., 2008; Tashima et al., 2012], which are presently being investigated at a pre-clinical stage.

The latter limitations are overcome in in-room and offline PET-based treatment verification by the usage of commercial full-ring PET or PET/CT scanner. The two approaches only differ in the localisation of the used PET imaging device, being installed either directly in the treatment room [Zhu et al., 2011; Min et al., 2013] or at a separate site [Parodi et al., 2007c; Bauer et al., 2013b]. In both cases, however, data is acquired with some delay after the actual irradiation. Consequently, part of the detectable amount of irradiation-induced activity has already decayed at the time of data acquisition, and the number of detected true coincidences might be reduced with respect to in-beam PET, hence calling for an increased data recording time [Shakirin et al., 2011]. In the offline approach, where delay times between irradiation and imaging are typically in the order of $5 - 15\,\mathrm{min}$, the residual signal by the fast-decaying ^{15}O isotopes is almost negligible and the residual activity can predominantly be ascribed to ^{11}C [Parodi et al., 2008b]. The in-room approach offers remarkably shorter delay times, even allowing for the imaging of ^{15}O [Zhu et al., 2011], but is much less practicable in terms of clinical workflow and cost-effectiveness, as the treatment room cannot be used during the time of data acquisition and as the PET scanner might not be used for clinical applications besides treatment monitoring [Shakirin et al., 2011]. Both approaches, the in-room and the offline verification, are also remarkably affected by washout effects in the irradiated tissue [Parodi et al., 2007c]. These processes lead to a further decrease of the detectable activity, as well as to a distortion of the induced activity pattern and were found to be described only with limited accuracy by the currently applied washout models [Zhu et al., 2011; Bauer et al., 2013b].

Regardless of the time regime of PET data acquisition, the approach of in-vivo PET-based treatment verification requires modelling of the expected irradiation-induced activity distribution, possibly including washout effects, since a direct comparison of PET measurement and planned dose is not feasible: activity and dose distributions are correlated but not equal, as can be seen in figure 3.3. The quality of the actually applied treatment, consequently, has to be deduced from a comparison of the expected activity distribution within the patient, calculated on the basis of the treatment plan and the time course of irradiation and imaging, to the actual PET measurement. This will be described in detail for the implementation chosen at HIT in the next section. Without an adequate modelling of the induced activity to be expected, only an inter-fractional treatment comparison by means of measured PET images would be feasible, as implemented by [Nishio et al., 2010].

Despite the above-mentioned challenges, an accuracy in the order of $1.5 - 5\,\mathrm{mm}$, depending on the actual treatment site, has been reported to be achievable in PET-based treatment verification [Parodi et al., 2007c; Knopf et al., 2011].

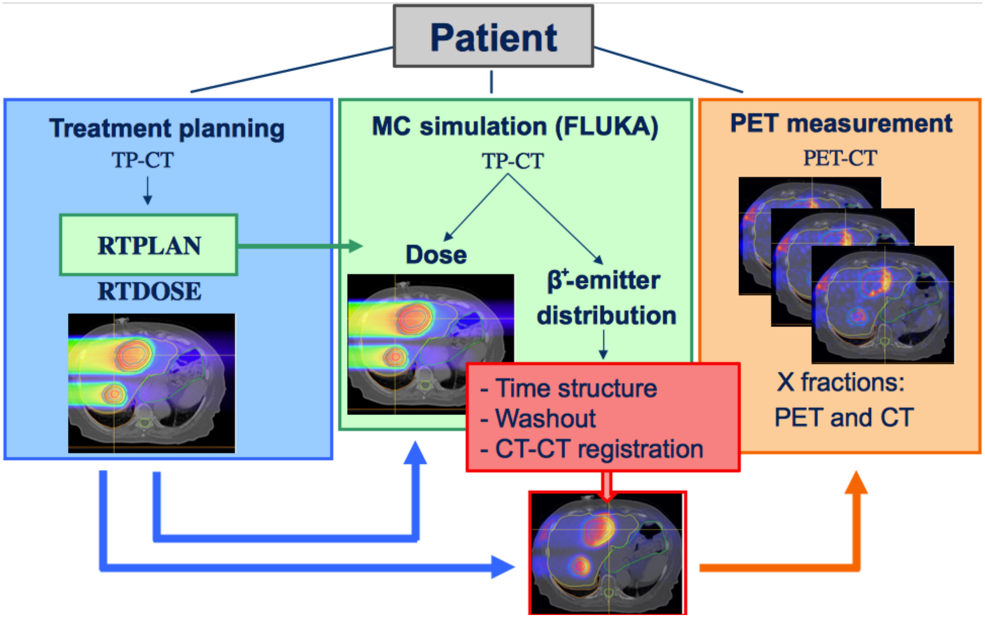

Figure 3.7: Depiction of the offline PET-based treatment verification workflow at HIT. Patient treatment planning (TP) data is used as input for a Monte-Carlo simulation of the β^+-emitter distribution in the patient. This raw distribution is corrected for the time structure of the irradiation and the data acquisition of the given fraction, as well as for the biological washout. The resulting reference activity pattern within the patient is then aligned (CT-CT registration of TP-CT and PET-CT) and compared to the actually measured PET data of the fraction in order to verify the treatment.

3.4 Implementation of offline PET-based treatment verification at HIT

At the Heidelberg ion beam facility, a commercial PET/CT scanner (Siemens Biograph mCT, Siemens Molecular Imaging, Knoxville TN, USA [Jakoby et al., 2011]) for treatment verification is installed next to the patient treatment rooms (offline). The workflow is depicted in figure 3.7: starting from the treatment planning (TP) data, i.e., the irradiation plan (RTplan) and the TP-CT, β^+-emitter distributions for all relevant isotopes are calculated within the patient. The obtained β^+-emitter pattern is converted to an activity distribution by accounting for the fraction-specific time course of the irradiation, transportation and imaging, as well as for the biological washout. The calculated activity is then registered to the actual PET/CT measurement on the basis of a manual rigid registration of the PET-CT (acquired for attenuation correction of the measured coincidence data at the PET/CT scanner) and the TP-CT. As a result, the activity to be expected within the patient under assumption of a correct dose application is retrieved and can be compared directly to the actual PET measurement of the given fraction in order to verify the correct application of the irradiation. The single steps are explained in detail in the following sections.

Up to present, the treatment of more than 120 patients has been monitored by means of post-irradiation PET imaging at HIT. About 2/3 of these patients have been irradiated with carbon ions, 1/3 with protons. The most frequent tumour location is the head and neck region, contributing about 50% of all patients, followed by the prostate (≈ 20%) and the liver (≈ 10%).

3.4.1 MC simulation of the β^+-emitter distribution

The expected β^+-emitter distribution within the patient is calculated using the FLUKA MC code [Battistoni et al., 2007; Ferrari et al., 2005]. FLUKA is a general purpose MC code for the modelling of particle transport and interaction in matter. It explicitly simulates the electromagnetic and nuclear interactions of the incident ion beams within the patient. The properties of the incident beam, i.e., energy, focus, lateral position and number of particles for each raster-spot of the scanned beam delivery, are retrieved from the treatment plan and converted to the required beam properties within the simulation by a dedicated source routine. The patient anatomy is described by the underlying TP-CT data, which is segmented into 33 materials of different elemental composition and nominal physical properties (density, ionisation potential) on the basis of the retrieved Hounsfield units according to the approach of [Schneider et al., 2000; Parodi et al., 2007c]. For a continuous scaling of the physical properties (nuclear and electromagnetic) as a function of the HU, additional correction factors are applied within each of the 33 segmented HU intervals. This scaling is chosen such that it further ensures FLUKA to follow the same the HU-WEPL calibration curve as used in the TPS (cf. section 2.4.3) in order to enable a consistent beam range verification [Parodi et al., 2007a, c; Bauer et al., 2013b].

As a result of the FLUKA simulation, the yield of the most important β^+-emitter, as listed in table 3.1, and the 3D physical and biological dose deposition pattern within the patient per incident primary particle is obtained. Typically about $10^7 - 10^8$ primary particles are simulated, corresponding to about 1% of the total amount of particles in the treatment plan and requiring about $6-8$ h of CPU time when using $40-60$ parallel executions on a high performance computer cluster.

3.4.2 Calculation of the irradiation-induced activity

Starting from the results of the FLUKA simulation, i.e., the spatial distribution of the irradiation-induced β^+-emitter, the activity which is expected to be measured within the patient during the post-irradiation PET scan needs to be determined.

In this post-processing step, the decay of the activity during the actual irradiation time t_{irr}, the delay between the end of the irradiation and the start of the PET measurement Δt and during the PET data acquisition time t_{frame} has to be determined. In addition to the physical decay, the amount of irradiation-induced radio-isotopes is reduced by biological washout effects. According to [Mizuno et al., 2003], a fast (half-life $T_{1/2f} = 2 - 10\,\text{s}$), a medium ($T_{1/2m} = 100 - 200\,\text{s}$) and a slow ($T_{1/2s} = 3000 - 10000\,\text{s}$) component of biological decay exist. In the pursued offline PET monitoring approach, Δt is typically in the order of $6 - 12\,\text{min}$ at HIT, so that the fast and medium component have already decayed and only the slow biological decay component is typically considered. On the basis of the CT Hounsfield numbers, the irradiated tissue is segmented into regions of low, intermediate and normal perfusion. Each of these regions is characterised by its specific relative fraction of the slow decay component M_s and its biological decay constant λ^s_{bio} ($\lambda^s_{\text{bio}} = ln(2)/T_{1/2s}$). The intervals of the HU segmentation, as well as the applied values for M_s and λ^s_{bio} are reported in [Parodi et al., 2007c]. Finally, the expected average activity within the patient $\langle A(\mathbf{r}) \rangle$ can be calculated as:

$$\langle A(\mathbf{r}) \rangle = G(\mathbf{r}) * \left\{ \sum_i n_i \cdot \sum_j \left[M_s(\mathbf{r}) N_{ij}(\mathbf{r}) \cdot \frac{[1 - exp(-\lambda_j t_{\mathrm{irr},i})]}{t_{\mathrm{irr},i}} \cdot \right.\right.$$
$$\left.\left. exp(-\lambda_{\mathrm{tot},j}(\mathbf{r}) \Delta t_i) \cdot \frac{[1 - exp(-\lambda_{\mathrm{tot},j}(\mathbf{r}) t_{\mathrm{frame}})]}{\lambda_{\mathrm{tot},j}(\mathbf{r}) t_{\mathrm{frame}}} \right] \right\} \quad (3.2)$$

where N_{ij} is the amount of isotopes j formed by irradiation field i as calculated by the FLUKA simulation, n_i the total number of particles of each individual field and λ_j and $\lambda_{\mathrm{tot},j}$ the physical and total ($\lambda_{\mathrm{tot},j}(\mathbf{r}) = \lambda_j + \lambda^s_{\mathrm{bio}}(\mathbf{r})$) decay constants. In order to enable a direct comparison of the simulated expectation to the measured PET data, the limited resolution of the PET scanner is modelled by a 3D convolution of the post-processed simulation data with a Gaussian kernel $G(\mathbf{r})$.

3.4.3 Data acquisition and the Biograph mCT scanner

For acquiring the post-irradiation PET data to be compared to the simulation on the basis of the treatment planning data, patients are either walked over or transported by a dedicated shuttle system (PatLog by ONCOlog, Medical QA AB, Uppsala, Sweden) to the PET/CT room immediately after their irradiation. Before starting the PET/CT scan, they are re-immobilised using the same equipment, e.g., thermo-plastic masks in the case of head patients, that have been used for fixation during the beam application. In the case of liver patients, which will be investigated in depth in the scope of this work (cf. chapter 6), however, immobilisation is much more complex, including a vacuum mattress, head and arm holder and in most cases an abdominal compression system. Hence, a re-immobilisation would be too cumbersome and time-consuming. Instead, these patients are immobilised only once at the PET/CT room before the actual treatment and transported to the treatment site with the shuttle system. This also enables the acquisition of a 3D position verification CT at the PET/CT scanner before the patients are irradiated. After having completed the beam application, the shuttle transfers the patients back to the PET/CT room for acquiring the verification PET data.

In all cases, data is acquired in list-mode (LM) format by the Biograph mCT scanner at one single bed-position within the scanner field of view (FOV), which has a size of 21.8 cm (axial) × 60.5 cm (transaxial). The PET scanner consists of four detector rings, each containing 48 detector blocks with 13×13 crystals having a dimension of $4 \times 4 \times 20\,\mathrm{mm}^3$ each. At the coincidence processor level, a time window of 4.1 ns and an energy window of $435 - 650\,\mathrm{keV}$ are applied.

Moreover, the use of lutetium oxyorthosilicate (LSO) detector crystals with high scintillation light yield and fast scintillation light decay [Melcher and Schweitzer, 1992] enables the application of time-of-flight PET techniques: the time difference t_d between the two detected events of a single coincidence can be used to attribute the origin of the underlying annihilation to a distinct distance $x = ct_d/2$ from the central axis of the scanner. The achievable TOF resolution Δt directly translated into a resolution Δx in space for the origin of the positron annihilation. The probability density for the origin of a detected coincidence is no longer constant over the corresponding LOR within the imaged object, but has a Gaussian shape with a maximum at position x and FWHM Δx, as depicted in figure 3.8. The utilisation of TOF information in the image reconstruction algorithm mainly leads to a faster convergences to the final image and an

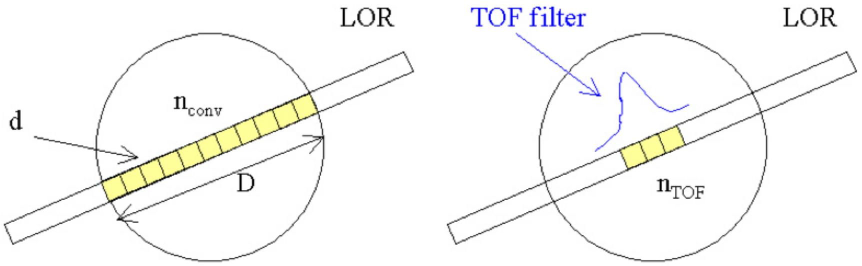

Figure 3.8: Scheme of TOF PET. While in conventional PET the probability of the localisation of the positron annihilation is equally distributed among all image elements $\mathrm{n_{conv}}$ along the LOR within the object of size D (left), it follows a Gaussian shape (TOF filter) covering a reduced number of image elements $\mathrm{n_{TOF}}$ if TOF information is available (right). Taken from [Conti et al., 2005].

---

improvement of the signal to noise ratio (SNR) with respect to conventional (conv) PET imaging, which can be approximated by [Surti et al., 2002]:

$$\mathrm{SNR_{TOF}} = \sqrt{\frac{\mathrm{D}}{\Delta x}} \cdot \mathrm{SNR_{conv}}, \tag{3.3}$$

where D is the diameter of the imaged object. The Biograph mCT scanner allows for a TOF resolution Δt of about 530 ps [Jakoby et al., 2011], resulting in more than two times higher SNRs for an average transaxial patient size of 40 cm.

A certain drawback is, however, given by the intrinsic radioactivity of the LSO crystals, since natural lutetium consists to about 2.6% of the radioactive isotope ^{176}Lu. The latter emits β^- particles with a mean energy of 420 keV, as well as three gammas with energies of 307, 202 and 88 keV [Goertzen et al., 2007], which leads to a significant increase of the single and herewith of the random count rates [Yamamoto et al., 2005]. In [Parodi et al., 2007b], a random background of about 1000 counts per second (cps) was determined for a comparable scanner as used at HIT. At the same time, the background of true events from LSO was reported to be negligible. A detailed analysis of the LSO-induced random background and its impact on the reconstructed images for the Biograph mCT scanner has been carried out in the scope of this work and will be presented in chapter 5.

The acquired post-irradiation LM data of a patient scan are reconstructed iteratively by a fully 3D *ordinary-Poisson*-OSEM (OP-OSEM) algorithm [Comtat et al., 2004], taking into account not only the available TOF information, but also the space dependent resolution within the FOV by means of a point-spread function (PSF) [Casey, 2007, 2008]. During reconstruction, the acquired coincidence data are corrected for attenuation on the basis of an attenuation correction CT with extended FOV and for scatter coincidences on the basis of a single scatter simulation [Watson, 2000], which is additionally scaled to the measured emission sinogram data in order to account for scatter contributions from outside the axial PET FOV [Watson et al., 2004]. By selecting ^{22}Na with a half-life of 2.6 years as imaged radio-tracer, the mandatory decay correction can be avoided and the mean activity during the scan can be retrieved if the branching ratio of 0.9 for the β^+-decay of ^{22}Na is considered in the data analysis [Bauer et al., 2013b].

The Biograph mCT scanner also allows for 4D PET and CT imaging in the presence of organ motion, e.g., in the case of liver patients which will be investigated in depth in the course of this

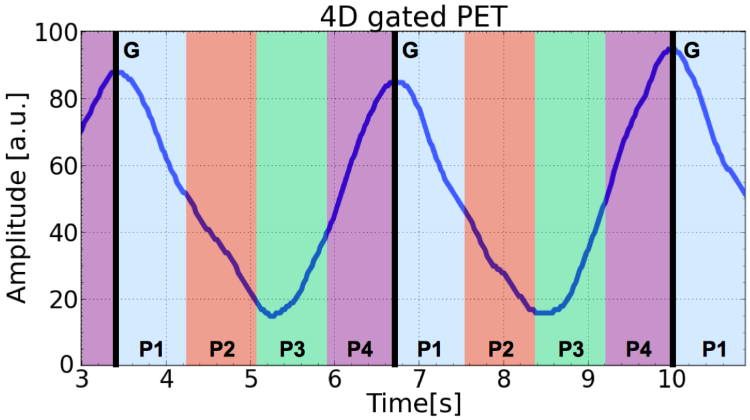

Figure 3.9: Illustration of phase-sorting in 4D gated PET imaging. The continuously acquired LM data is subdivided between each two inhale peaks (here marked as gates 'G') into a user-defined number of equally sized bins in time which correspond to the single motion phases (in the depicted case P1 to P4). The data within each respiratory phase is then reconstructed separately.

work. Motion is monitored by the ANZAI pressure sensor and recorded in parallel to the CT or PET scan. In the case of 4D CT imaging, the continuously (helical mode) acquired CT data, which needs to cover each image position along the scanner axis in each respiratory phase [Keall et al., 2004], is sorted into a set of user-defined phases on the basis of the relative breathing amplitude (relative amplitude-sorting): each respiratory cycle is split into an inspiration and expiration part, which is then scaled to $0 - 100\%$. The data within each of the user-defined respiratory states, corresponding to a certain relative amplitude of the inspiration or the expiration part, is then reconstructed separately in order to retrieve a time-resolved CT image. In the case of 4D PET imaging, the data is split into a user-defined number of equally sized time bins between every two inspiration peaks (phase-sorting, see figure 3.9). These inspiration peaks are the only information which is written into the acquired LM data stream by the motion monitoring system as so-called *gate-tags*. For reconstructing the 4D PET image, the data within each of the defined time bins is reconstructed separately (4D gated PET [Nehmeh et al., 2002]). This leads to a significantly reduced residual motion within each motion state, but also to a reduced number of counts and herewith a reduced SNR, which is approximately proportional to the square root of the number of true coincidences.

3.4.4 The SimInterface

For the analysis and comparison of planned, simulated and measured data, a dedicated software framework, called *SimInterface*, has been developed at HIT on the basis of the *MeVisLab* (Fraunhofer MeVis, Bremen, Germany) development environment [Unholtz et al., 2011]. The SimInterface also serves as a management system of patient data (TP, PET/CT, MC simulation) and accomplishes several tasks within the workflow of PET-based treatment verification. These tasks include the preparation of patient data for input to the FLUKA MC simulation (see section 3.4.1), the running and monitoring of the automated MC calculations on the connected computer cluster, the post-processing of the calculated β^+-emitter pattern (cf. section 3.4.2) and the visualisation of multi-modal image data (CT, PET, TPS dose, RT structure sets etc) and corresponding simulation output data. Moreover, the SimInterface provides an environment for manual rigid registration of CT data-sets, as required, e.g., for the comparison of expected and measured activity distributions, based on the TP-CT and the PET-CT, respectively.

Making use of the above-mentioned capabilities of the SimInterface, a patient-specific simulation of the irradiation-induced activity can be prepared, run and post-processed within a few steps, and can directly be compared to the measured post-irradiation PET/CT data to asses the quality of the applied treatment. The SimInterface is, however, not restricted to the analysis and comparison of PET or activity data. It can also be used for comparing, e.g., TPS dose (physical and biological) to MC calculated dose, or MC calculated dose distributions on the TP-CT and the fraction-specific PET-CT.

Besides the ability to compare planned, simulated and measured data-sets by a 2D-synchronised visualisation of multi-modal images and 1D profiles, the SimInterface contains a module for preparing the required input data to a dedicated range verification tool. Verification of the beam range is of particular interest in ion beam therapy monitoring, because uncertainties in the beam range are typically larger than those in the lateral direction, which are e.g., not affected by errors in the HU-WEPL calibration curve. In this context, the SimInterface is used to align the reference data-set, as well as the data-set being investigated for range deviations, to the incident beam direction. The aligned data, usually consisting of two PET data-sets and the corresponding CTs, are then analysed within an additional range verification module: it determines the most-likely shift between two given 1D profiles (typically simulated and measured activity) along the beam axis at each lateral position within the irradiation field. This yields a 2D map of range deviations in beam's eye view. The corresponding CT data are also analysed in terms of inhomogeneities (variance) and WEPL along each profile, as well as in terms of the CT contour position, which might hint on a patient mis-positioning. Details on the implementation of the range verification for PET-based treatment verification can be found in [Frey et al., 2014]. Basically, the implemented algorithm normalises both of the compared activity profiles to their maximum, then determines the shift $\delta_z^{\min}$ at which the absolute difference between both profiles in a properly chosen interval I_k along the beam axis is minimal. $\delta_z^{\min}$ is referred to as most-likely shift.

The SimInterface is used as standard tool in clinical applications of 3D PET-based treatment verification at HIT for stationary target volumes. In the scope of this work, the extension of the established PET monitoring workflow to moving tumour entities has been investigated and the SimInterface capabilities had to be extended in order to enable the handling of 4D TP data (4D TP-CT and a set of state RTplans) and to yield an expectation of the irradiation-induced activity within the patient under consideration of the respiratory motion during the beam application. The necessary extensions of the SimInterface performed in this thesis will be described in detail in chapter 6 in the context of the first application of 4D offline PET-based treatment verification to clinical cases, after a thorough report on the feasibility and potential of this approach, as assessed in dedicated experimental campaigns with phantoms, in the following chapters.

Chapter 4

On the feasibility of 4D PET-based treatment verification: moving phantom studies

This chapter deals with comprehensive moving phantom studies on (1) post-irradiation 4D offline PET-based treatment verification and (2) the implementation of a novel motion monitoring system, based on ultrasound imaging, for time-resolved PET imaging. In the first part, a moving phantom irradiation campaign will be discussed and analysed with the aim to infer the feasibility and potential of 4D treatment monitoring by means of time-resolved post-irradiation PET imaging with a commercial PET/CT scanner. The presented experiments serve as a controlled simplified scenario with high counting statistics, paving the way towards a first application to clinical cases, as discussed in chapter 6. The second part will cover a first implementation of ultrasound motion tracking in 4D PET imaging and compare this novel approach to the performance of the standard ANZAI motion monitoring system. Ultrasound tracking promises accurate, dose-free and real-time tracking of internal structures and might result in an improved sorting of the acquired data into the single motion phases and herewith in an improved 4D image quality.

4.1 Moving phantom irradiation studies on 4D offline PET-based treatment verification

4.1.1 Material and methods

4.1.1.1 Phantom irradiation

In order to investigate the feasibility of 4D offline PET-based treatment verification, PMMA phantoms have been set up in three different geometries, referred to as *Square*, *Line Mono* and *Line Mult*, and irradiated once under static (reference) and once under moving conditions by a scanned ^{12}C ion beam. The experimental set-up for the *Line Mult* study is shown in figure 4.1: the beam passes through a PMMA fence with a thickness of 1.5, 2.25, 2.75 or 3.25 cm, depending on the lateral beam position, and is stopped in a PMMA block phantom with a dimension of $9 \times 9 \times 30\,\mathrm{cm}^3$. The phantom itself has been positioned on the QUASAR respiratory motion

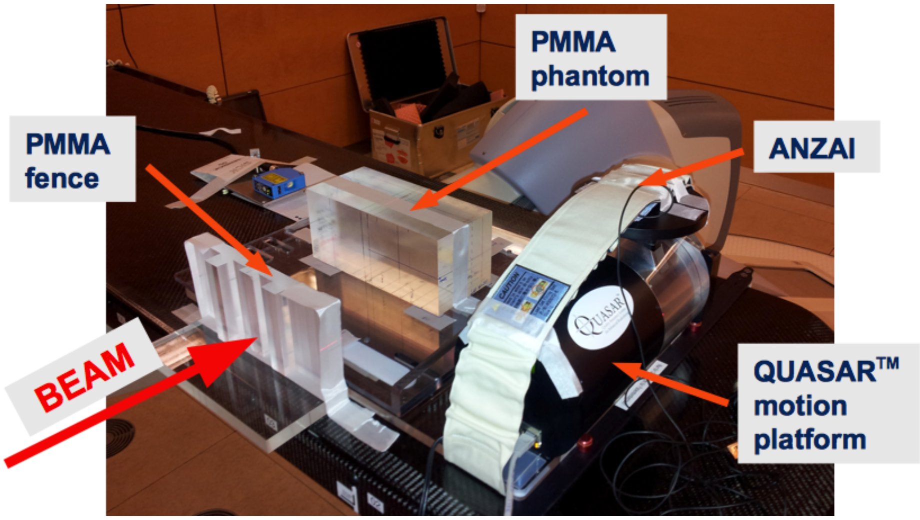

Figure 4.1: Experimental set-up of the *Line Mult* moving phantom irradiation study: the ^{12}C ion beam was entering from the left (along the depicted red arrow) and reached the PMMA phantom through a PMMA fence of laterally varying thickness. The PMMA phantom was positioned on the QUASAR motion platform, which performed a cos^4-shaped motion perpendicular to the beam axis. Motion was monitored during the irradiation and the subsequent PET/CT acquisition by the pressure sensor of the ANZAI respiratory gating system, which had been attached directly to the QUASAR platform.

platform (Modus Medical, London, Canada), while the fence was put stationary on the patient table. In the *Line Mono* case, the geometry was modified in so far that the PMMA fence was positioned directly next to the PMMA block on the QUASAR motion platform. For the *Square* study, the fence has been removed, and the PMMA phantom rotated by 90° on the platform in order to align the long axis of the phantom to the incident beam direction.

Except for the static reference measurements, the QUASAR motion platform moved the phantom (and the PMMA fence in the *Line Mono* study) perpendicular to the incident beam with a cos^4-shaped motion of $A = 2\,\text{cm}$ amplitude and $T = 3\,\text{s}$ period, imitating a regular patient-like breathing pattern [Lujan et al., 1999]. The displacement of the phantom during the actual beam application, as well as during the subsequent PET/CT scan, has been monitored by the pressure sensor of the ANZAI respiratory gating system. In order to account for the phantom motion during the irradiation, a gated beam delivery in combination with rescanning has been applied. The gating window covered the shallow minimum of the cos^4-shaped motion, corresponding to the stable end-exhale position of a patient, plus another 20% or 50% of the respiratory cycle amplitude around this position, limiting the residual motion amplitude to 4 or 10 mm, respectively. Rescanning has been applied in addition in order to deliver a high total number of particles, while keeping the number of particles irradiated within one rescan to each of the raster-spots in a patient-like range.

An overview of the chosen irradiation parameters for each of the three investigated geometries is given in table 4.1. In the *Line Mult* case, four different energies have been applied in order to correct for the different thicknesses of the PMMA fence and to gain a constant residual range within the PMMA block downstream the fence. In the *Line Mono* case, on the other hand, the fence was used to induce a range modulation of the beam, stopping within the phantom, in order to investigate the accuracy of the PET-based treatment monitoring approach under stationary and moving conditions.

4.1.1.2 Post-irradiation PET imaging

Right after the irradiation, the activated PMMA phantoms were transported to the adjacent PET/CT room. An overview of the irradiation times t_{irr}, the number of applied beam spills N_{spill}, the average spill times t_{spill}, the average beam extraction times $t_{\mathrm{extr}} = t_{\mathrm{irr}}/N_{\mathrm{spill}}$ and the delay times between irradiation and PET acquisition Δt are given in table 4.2. The phantoms were kept in exactly the same position on the motion platform and the same cos^4-shaped motion ($A = 2\,\mathrm{cm}$, $T = 3\,\mathrm{s}$) was applied during the PET LM data acquisition (not for the static reference measurements). The PET scan time was set to 30 min, in order to collect a reasonable number of true coincidences, which is also given in table 4.2. In comparison, a typical 4D patient examination will provide between $400,000$ and $900,000$ true coincidences at a comparable number of randoms.

The acquired LM data have been reconstructed in 3D by an OP-OSEM algorithm using 3 iterations with 24 subsets (3i24s) and a 5 mm (FWHM) post-reconstruction Gaussian filter (gf5) on a voxel grid of $2 \times 2 \times 3\,\mathrm{mm}^3$, corresponding to the standard settings for phantom data analysis

Table 4.1: Irradiation parameters for the different phantom set-ups *Square*, *Line Mono* and *Line Mult*. The depicted gating windows (GW) only apply to the moving phantom cases.

Study	Lateral field size [cm] (horizontal × vertical)	Beam energy [MeV/u]	Total number of particles	GWs [%]	Number of rescans
Square	4.8 × 4.8	200.28	$7.45620 \cdot 10^9$	20&50	60
Line Mono	14.1 × 1.5	200.28	$7.51680 \cdot 10^9$	50	60
Line Mult	14.1 × 1.5	200.28, 212.12 219.79, 227.29	$2.00448 \cdot 10^9$	20&50	16

Table 4.2: Overview of the time course of the beam delivery and subsequent PET acquisition as well as the number of detected true and random coincidences for the eight investigated phantom irradiation. Gated irradiation are labeled by *G20* or *G50* for an applied gating window of 20 or 50%, respectively.

Study	t_{irr} [s]	N_{spill}	t_{spill} [s]	t_{extr} [s]	Δt [s]	$\mathrm{N}_{\mathrm{true}}$	$\mathrm{N}_{\mathrm{rand}}$
Square	400	60	2.50	6.66	330	3,623,600	1,913,121
Square G50	546	60	4.33	9.10	422	3,262,937	1,872,870
Square G20	541	60	3.93	9.02	412	3,163,861	2,112,582
Line Mono	410	60	2.55	6.83	274	3,478,959	1,858,254
Line Mono G50	483	60	3.76	8.05	371	3,128,771	1,993,110
Line Mult	356	64	1.30	5.56	284	935,421	2,034,819
Line Mult G50	453	65	1.90	6.97	357	846,933	2,108,005
Line Mult G20	514	64	1.80	8.03	340	848,264	2,189,409

at HIT [Bauer et al., 2013a]. In the case of moving phantoms, the ANZAI system, used for monitoring of the phantom motion, enabled an additional 4D gated PET image reconstruction with phase-sorting, as described in section 3.4.3. In all considered cases, eight motion phases have been reconstructed with the above-mentioned settings (OP-OSEM, 3i24s, gf5). All image reconstructions included scatter coincidence correction as well as attenuation correction on the basis of a *free-breathing* 3D CT. The use of an averaged 4D CT or a phase-specific 3D CT of each individually reconstructed PET phase is, up to present, not implemented on the Biograph mCT scanner.

In order to obtain one single motion-compensated 4D PET image for further analysis, the images of the single motion phases were registered to a common reference phase, here chosen as the first phase after the inhale peak, by a manual rigid transformation, summed up and divided by the number of phases. The accuracy of the manual registration was retrieved as 0.1 ± 0.1 mm from the ability to recover an artificially introduced 3D shift of various regarded single-phase PET images. Moreover, the precision of the registration procedure was determined by multiple registrations of various image pairs and found to be in the order of 0.5 mm. Thus, when performing eight registrations to retrieve the motion-compensated 4D PET image, the combined registration error decreases to $0.5/\sqrt{8}\,\mathrm{mm} \approx 0.2\,\mathrm{mm}$, which was ensured to not significantly affect the outcome of the image data analysis discussed later in this section.

4.1.1.3 Calculation of the irradiation-induced activity pattern

The corresponding MC calculations of the expected irradiation-induced activity patterns within the phantoms were performed on the basis of the analytical phantom geometry and the applied treatment plans, using FLUKA 2011.2b. The not precisely known material stopping properties of PMMA (density and ionisation potential) were tuned such that the simulation reproduces the measured position of the activity peak within the phantom for the static *Square* irradiation (see figure 4.3 in section 4.1.2.1).

In the case of moving phantoms, the motion-cycle has been divided into 20 equally-sized phases on the basis of the relative motion amplitude (cf. section 3.4.3). This means the in- and exhale motion were subdivided into 10% steps with a residual motion of 2 mm. For each of these motion states, the average displacement of the phantom has been calculated under consideration of the cos^4-shaped motion and a phase-specific FLUKA simulation has been set-up. This phase-specific simulation also requires a set of so-called *state raster files*. These files are equivalent to treatment plan files for each considered motion state: they contain the number of particles that have been irradiated to each raster-spot in each of the regarded motion states. The state raster files used for the simulation of the moving phantom irradiation in this work have been retrieved by the TRiP4D software, developed at GSI, Darmstadt and extensively validated in dedicated experiments [Richter et al., 2013]. The procedure of generating the required set of state raster files for the 20 chosen motion states on the basis of relative amplitude-sorting is described in detail in [Richter, 2013]. In principle, the ANZAI motion signal acquired during the phantom irradiation is synchronised to the corresponding machine beam record, which contains time stamps after the irradiation of each single raster-spot has been finished, the so-called *next-point signal* (NXP). Then, by using the latter information and the time-correlated motion signal, the number of particles that have been applied to a single spot in a particular motion state can be retrieved. The number of simulated primaries was set to about 0.5% of the irradiated particles in each motion state in order to assure a similar level of statistics in the single simulations.

As a result of these calculations, the yield of ^{11}C, ^{15}O and ^{13}N in the PMMA phantoms per incident ^{12}C primary ion has been obtained. According to [Parodi et al., 2008b], the mean activity to be expected in the acquired post-irradiation PET scan has then been calculated as:

$$\langle A(\mathbf{r})\rangle = G(\mathbf{r}) * \Bigg\{ \sum_i n_i \cdot \sum_j \Bigg[N_{ji}(\mathbf{r}-\Delta_i) \cdot \frac{[1-exp(-\lambda_j t_{\text{spill}})]}{t_{\text{spill}} \cdot N_{\text{spill}}} \cdot exp(-\lambda_j \Delta t) \cdot \frac{[1-exp(-\lambda_j t_{\text{frame}})]}{\lambda_j t_{\text{frame}}} \cdot \sum_{k=0}^{N_{\text{spill}}} exp(-k\lambda_j t_{\text{extr}}) \Bigg] \Bigg\}. \quad (4.1)$$

Here, n_i is the number of irradiated particles according to the (motion state i specific) treatment plan, N_{ji} the output of the FLUKA simulation in motion state i for isotope j, Δ_i the calculated phantom displacement in state i and λ_j the physical decay constant of isotope j. Compared to equation 3.2, the spill structure of the synchrotron beam delivery has been explicitly taken into account and the isotope washout omitted. Following equation 4.1, the time-resolved or 4D activity pattern within the phantom has been retrieved by summing up the mean activities of each single motion state i, shifted according to the determined average displacement Δ_i. The width σ of the applied Gaussian filter $G(\mathbf{r})$ was optimised by comparing the shape of the activity at the entrance of the PMMA phantom in the simulated and the measured data and set to 3.5 mm.

For a direct comparison to the measured data, the post-processed simulation data was registered by a manual rigid registration to the static reference measurement of the regarded geometrical set-up. Along the beam axis, the data-sets were matched on the activity increase at the phantom entrance in order to enable a thorough range analysis and comparison.

4.1.2 Irradiation specific data analysis and results

4.1.2.1 *Square* irradiation

Data analysis The collected data, consisting of the 3D and 4D (motion-compensated) reconstructed images of the three *Square* irradiation studies (static, *G50* and *G20*) and the post-processed MC data for each of the three investigated cases, have been analysed by dedicated python (version 2.6.5) routines. The properties of main interest in the analysis were the PET-based ion beam range, the lateral width and the lateral penumbra of the irradiation-induced square-shaped activity distribution.

The PET-based range $\mathrm{R}_{\mathrm{PET}}$ of a regarded activity depth profile (ADP) has been defined as the distance between the position of the maximum activity of the 1D profile, interpolated by a cubic spline, and a fixed proximal reference position A_5 (cf. figure 4.2). Here, A_5 has been defined as the proximal position at which 5% of the maximum activity is reached in the laterally integrated (i.e., summed up over both directions perpendicular to the beam axis) ADP of the static *Square* reference measurement. For a thorough range evaluation, all 1D profiles along the beam direction which exhibit a maximum activity of at least 50% of the overall maximum activity value in the investigated 3D activity distribution have been included in the analysis.

The width of the induced activity pattern has been determined for both lateral directions as the FWHM on the basis of the profile specific *averaged maximum activity* $\langle A_{95}\rangle$, defined as the mean of all activity values above 95% of the activity maximum of the regarded profile. All 1D lateral profiles along the given axis exhibiting a maximum activity of at least 50% of the

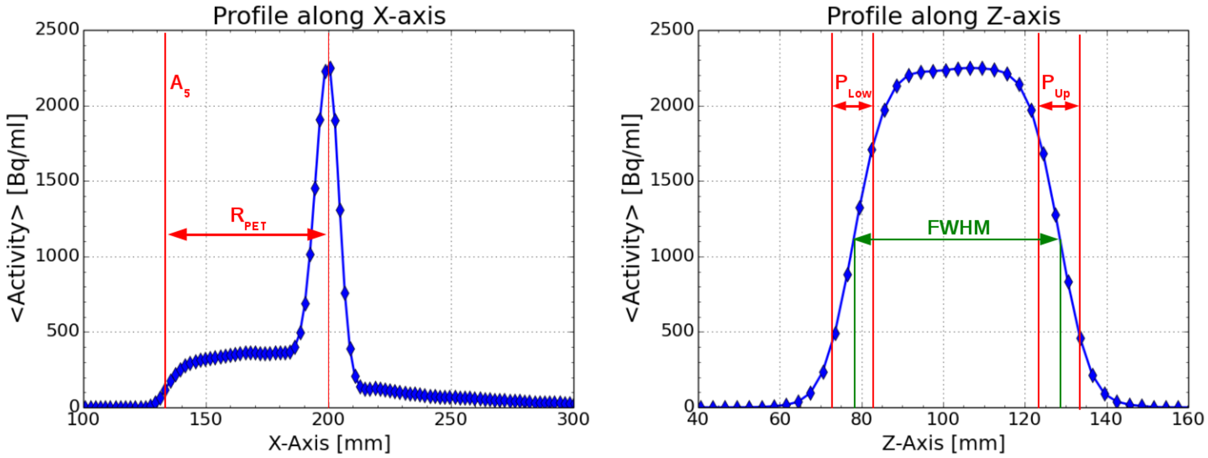

Figure 4.2: Illustration of the PET profile data analysis. The PET range $\mathrm{R_{PET}}$ has been determined as the distance between the maximum of the interpolated ADP and A_5 (left). The upper and lower penumbra have been defined as the distances of the positions of the 20 and 80% activity thresholds with respect to $\langle A_{95} \rangle$, on which also the FWHM has been based (right).

global maximum activity have been taken into account in the analysis. Moreover, the *lower* and *upper* penumbra $\mathrm{P_{low/up}}$ of the lateral profiles have been retrieved as the distance between the 20% and 80% activity increase or decrease, respectively, as shown in figure 4.2. All data have been analysed in the PET coordinate system: the beam enters parallel to the positive x-axis, the y-axis corresponds to the vertical lateral direction and the z-axis, being parallel to the scanner axis, coincides with the horizontal lateral direction and the direction of the phantom motion (left-right in BEV). Consequently, profiles along the x- and y-axis exhibit a 2 mm pixel spacing, while profiles along the z-axis have a 3 mm spacing.

In order to measure the similarity of the 2D activity distributions of different data-sets, a 2D γ-index analysis (3%, 3 mm) has additionally been carried out [Low et al., 1998]. The γ-index analysis has been performed in all planes perpendicular to the incident beam direction with an integrated activity of at least 90% of the maximum activity of the laterally integrated ADP. The lateral region for analysis was restricted to the area exhibiting activities of more than 20% of the plane maximum activity, plus a 2 cm margin. In order to enable the comparison of data-sets with different time structures, the compared 2D data-sets have been normalised to the integral activity in the analysed part of the regarded lateral plane.

Results An overview of the results retrieved for the PET-based range and the lateral FWHM and penumbra is given in table 4.3 for the static *Square* irradiation, the two moving phantom studies *G20* and *G50* (reconstructed in 3D and 4D) and for the corresponding MC calculations. For all depicted quantities, the mean value and standard deviation σ over of all analysed 1D profiles are presented.

In terms of the PET-based range $\mathrm{R_{PET}}$, an agreement within 0.6 mm between all considered data-sets has been found. For most cases, this corresponds to an agreement within 1σ, thus demonstrating the feasibility of sub-millimetre precision in offline PET-based range verification. In the comparison of simulated and measured ADPs, a generally good agreement has been found in terms of the shape and quantification, with some remaining differences (below 5% of the maximum activity) in the shallow plateau region proximal to the activity peak (see figure 4.3). These deviations can be attributed to inaccuracies in the MC modelling of the underlying nuclear interactions, to the simplified modelling (by a Gaussian filter) of the PET imaging process when calculating the expected activity (see equation 4.1) and to uncertainties in the activity quantification in the reconstructed PET images (cf. chapter 5). As expected, the motion of the homogeneous phantom perpendicular to the beam direction was found to have a negligible impact on the determined beam range and ADP shape. With respect to these quantities, no significant differences between 3D and 4D image reconstruction have been observed.

A similar finding has been made for the profile analysis in the vertical lateral direction, perpendicular to the actual phantom movement. Neither the FWHM_y, nor the P_y have been found to be affected significantly by the target motion and a generally good agreement (within 1σ) of the different measured data-sets, reconstructed in 3D or in 4D, and the simulated data has been observed. Differences in the amount of induced activity between measurement and simulation were confirmed to not exceed 5% of $\langle A_{95} \rangle$ in the analysed y-profiles. The simulated data, however, exhibits an enhanced symmetry of the lateral activity profiles along the y- and z-axis, as shown for the integrated (summed up over the two respective perpendicular axis) lateral profiles of the static *Square* irradiation study in figure 4.4. This can mainly be attributed to differences in the PET scanner resolution along the two regarded axes, once being parallel to the scanner axis and once perpendicular to the latter, as well as to a space dependent resolution along each of the axes, which is neglected in the MC data post-processing. Still, with respect to the application of dual-head PET detector systems, the achieved symmetry is considerably improved.

In contrast to the previously discussed results for the two axis perpendicular to the actual phantom movement, the investigated quantities along the z-axis are significantly affected by the target motion (cf. bold entries in table 4.3). The main impact was found to be a $45 \pm 9\,\%$ enhanced

Table 4.3: Results of the *Square* irradiation study. PET-based range, FWHM and penumbra are shown for the static reference measurement, the 3D and 4D reconstructions of the two gated irradiation (*G50* and *G20*) and the corresponding FLUKA simulations. The penumbra is given as the mean value of $\mathrm{P}_{\mathrm{low}}$ and P_{up} for the analysed lateral profiles along the y- and z-axis. Considerable deviations with respect to the static reference are given in bold.

Study	$\mathrm{R}_{\mathrm{PET}}$[mm]	FWHM_y[mm]	FWHM_z[mm]	P_y[mm]	P_z[mm]
Square, static	65.9 ± 0.3	50.7 ± 0.6	49.9 ± 0.4	10.0 ± 0.5	10.5 ± 0.4
Square G50, 3D	65.7 ± 0.2	50.9 ± 1.2	49.1 ± 0.6	10.6 ± 0.8	$\mathbf{15.1 \pm 0.8}$
Square G50, 4D	65.8 ± 0.2	50.7 ± 0.9	$\mathbf{48.0 \pm 0.4}$	10.6 ± 0.7	$\mathbf{11.3 \pm 0.5}$
Square G20, 3D	66.1 ± 0.2	51.1 ± 0.3	50.5 ± 1.0	10.1 ± 0.4	$\mathbf{16.3 \pm 0.8}$
Square G20, 4D	65.8 ± 0.2	51.1 ± 0.6	49.7 ± 0.5	10.0 ± 0.5	10.5 ± 0.6
FLUKA, static	65.7 ± 0.1	50.5 ± 0.1	50.5 ± 0.1	9.9 ± 0.1	10.0 ± 0.1
FLUKA G50, 4D	65.7 ± 0.1	50.0 ± 1.3	50.6 ± 0.2	10.5 ± 1.1	$\mathbf{11.0 \pm 0.3}$
FLUKA G20, 4D	65.5 ± 0.1	50.5 ± 0.4	50.8 ± 0.2	10.0 ± 0.3	10.2 ± 0.1

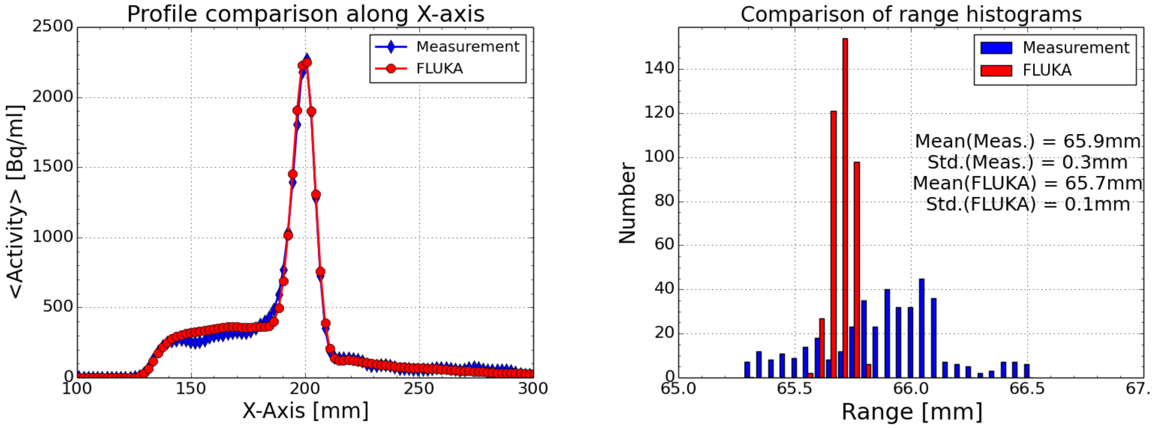

Figure 4.3: Comparison of measured (blue) and simulated (red) ADP (left) and of the determined range histograms containing all analysed 1D profiles along the x-axis (right) for the static *Square* study. A high agreement has been observed in terms of shape and amount of irradiation-induced activity. The mean PET-based ranges agree well within 1σ, as the unknown material stopping properties of PMMA used in the simulation have been tuned to this measurement. Due to the underlying PET image noise, the standard deviation is enhanced for the measured data.

---

penumbra P_z, if performing a stationary (3D) PET image reconstruction under phantom motion. Similar results have been reported in [Parodi et al., 2009] and [Stützer et al., 2013] for moving phantom activation studies with a dedicated in-beam dual-head PET camera at GSI, Darmstadt. For the *Square G20* study, this enhancement of the penumbra is illustrated for a central 1D profile along the z-axis in figure 4.5 and for the entire population of analysed z-profiles in figure 4.6. If the target motion is, however, considered by a motion-compensated 4D gated PET image reconstruction, the penumbra has been found to be substantially reduced and results similar to the static reference study could be achieved (see figures 4.5 and 4.6). In the *Square G50* study, though, a slight enhancement of the penumbra with respect to the static reference measurement has been observed in the 4D reconstruction of the measured data and could be confirmed by the 4D MC simulation, where this enhancement even exceeds 1σ. The observed difference with respect to the static reference can be attributed to the residual motion within the applied gating window during the irradiation and indicates a high sensitivity of 4D offline PET-based treatment verification, being able to detect these small alterations. If applying the smaller gating window, no significant difference to the static reference can be found in the simulation as well as in the 4D reconstruction of the measured data due to the reduced residual motion.

Besides the enhanced penumbra, a significantly reduced lateral width in the direction of motion has been observed in the 4D gated PET image of the *Square G50* study. This, however, could not be reproduced by the performed 4D FLUKA simulation and has thus been attributed to the inaccurate attenuation correction due to motion-induced artefacts in the underlying attenuation correction CT (AC CT), in which the width of the phantom is reduced from 9 to 7.5 cm along the direction of motion. A reconstruction on the basis of an averaged 4D CT would be beneficial, but is not feasible on the used commercial PET/CT machine. Nevertheless, the observed deviation to the static reference case and to the corresponding 4D MC simulation is still below the dimension

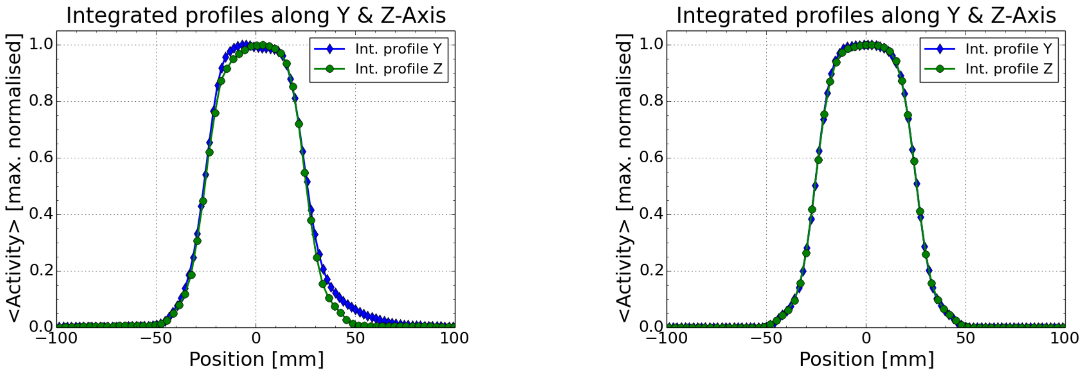

Figure 4.4: Comparison of the integrated lateral profiles, normalised to the maximum activity, along y- and z-axis (blue and green) for the static *Square* study. The measured data (left), shows an overall reduced symmetry in the two lateral axis with respect to the simulated data (right).

of a single image pixel (3 mm).

In addition to the discussed range and lateral profile analysis, the obtained 2D activity distributions have been investigated by means of a 2D γ-index analysis, as previously mentioned. All the regarded 2D activity patterns are shown in the lateral (y-z) plane of maximum activity in figure 4.7. For the static (3D) reconstructions of the two considered gated irradiation studies, the previously analysed blurring in the direction of motion (z-axis) is clearly visible. An additional effect of the target motion, which has not been observed in the previous profile analysis, was found to be a distortion of the square-shaped activity within the phantom along the z-axis, particularly in the *Square G50* study. This distortion, although corresponding to a lateral displacement of the 50% activity thresholds of the 1D lateral profiles along the direction of motion by only 3 mm, has clearly been detected in the corresponding 4D PET image and could be reproduced by the corresponding 4D MC calculation with an agreement of less than 1 mm (see figure 4.8). The observed deformation of the activity pattern can be attributed to the residual motion of the phantom within the gating window and the synchronisation of the irradiation with the periodic phantom trajectory. Irradiation was performed by scanning line after line along the z-axis (horizontally), such that, effectively, horizontal scanning was significantly faster than vertical scanning (along the y-axis). Consequently, the phantom was moving continuously, with a residual motion amplitude of approximately 1 cm, during the slow vertical beam scanning, leading to the observed distortion of the induced activity. This effect could not be diminished by the 60 times rescanning, as the irradiation of each spill started at almost the same respiratory phase. If, however, the gating window is reduced (G20), the observed deformation is notably smaller. This has been confirmed by the γ-index analysis: the γ-index of the *Square G20* 4D study is significantly smaller than the one of the *Square G50* 4D study if compared to the static reference case, as shown in table 4.4. Moreover, the analysis confirmed the enhanced agreement of the 4D reconstructions to the static reference measurement compared to the blurred 3D PET images of the moving phantoms.

Concerning the agreement of measured and simulated data, it has been found that the 4D simulations yield a comparable similarity (γ-index in the order of 90%) to the motion-compensated reconstruction of the measured data, as has been observed in the static reference study. For the

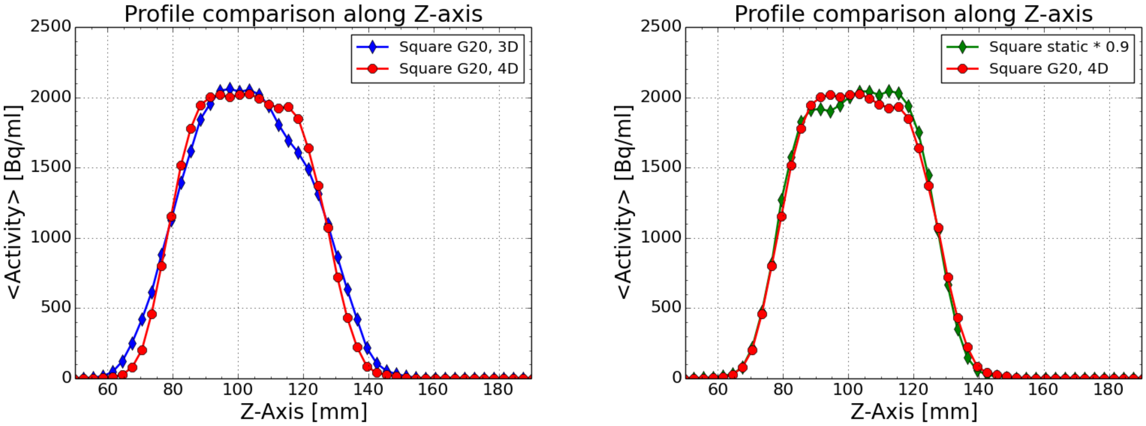

Figure 4.5: Comparison of central lateral profiles in the direction of motion for the *Square G20* study. The 3D reconstruction (blue) of the acquired PET data shows a significantly increased penumbra with respect to the 4D reconstruction (red, left plot), which can achieve results similar to the static reference measurement (green, right plot). The static reference has been normalised by a factor of 0.9 to account for the different time structures of the two studies.

Square G20 study, it could also be confirmed that including the phantom motion in the MC calculation leads to an enhanced agreement with the measured data, although differences between stationary and moving phantom data are generally small. In the *Square G50* study, the retrieved γ-index was found to be slightly smaller than in the two other *Square* studies due to the reduced lateral width of the 4D PET image, as previously discussed. This particularly limits the similarity of the 4D simulation to the 4D image. Still, on the basis of the underlying experimental results, a comparable performance of PET-based treatment verification under stationary and moving conditions has been found if phantom motion is considered properly by a 4D simulation and a

Table 4.4: Results of the γ-index analysis of the *Square* irradiation study. Mean value and standard deviation of the analysed y-z-planes are presented in each case.

Study 1	Study 2	γ-index
Square, static	FLUKA, static	$90.9\% \pm 0.6\%$
Square, static	*Square G50*, 3D	$79.2\% \pm 0.3\%$
Square, static	*Square G50*, 4D	$86.9\% \pm 0.1\%$
Square, static	*Square G20*, 3D	$75.4\% \pm 0.1\%$
Square, static	*Square G20*, 4D	$89.3\% \pm 1.3\%$
Square G50, 4D	FLUKA, static	$87.4\% \pm 0.2\%$
Square G50, 4D	FLUKA G50, 4D	$87.2\% \pm 0.2\%$
Square G20, 4D	FLUKA, static	$90.5\% \pm 0.5\%$
Square G20, 4D	FLUKA G20, 4D	$93.3\% \pm 0.9\%$

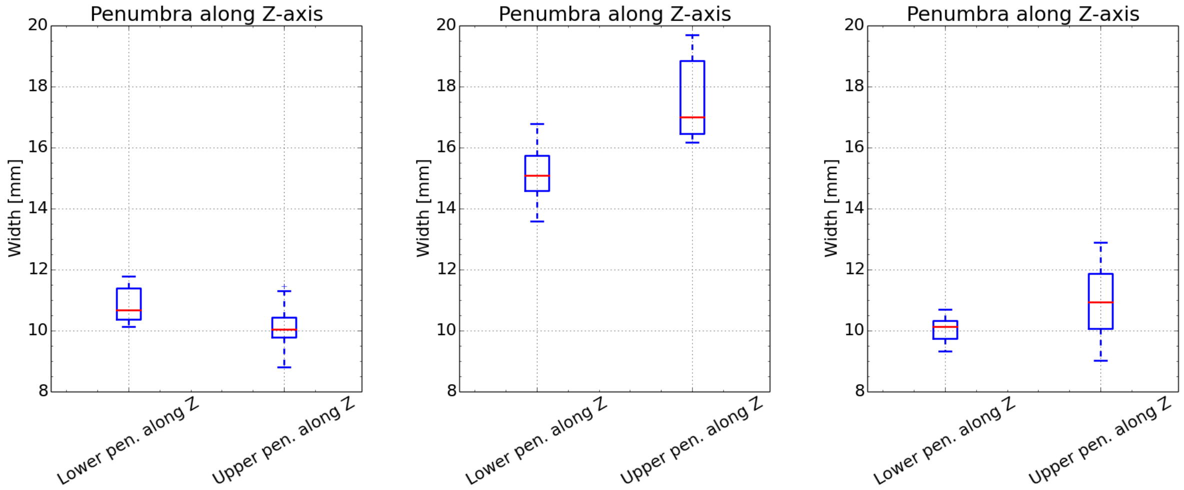

(a) *Square* static (b) *Square G20*, 3D recon. (c) *Square G20*, 4D recon.

Figure 4.6: Box-plots of the penumbra determined for the 1D profiles along the direction of target motion in the *Square G20* irradiation study. A significant enhancement in the 3D reconstruction (middle), with respect to the static reference (left) has been observed. The 4D gated PET image reconstruction (right) yields results similar to the static reference case.

motion-compensated image reconstruction.

4.1.2.2 *Line Mono* irradiation

Data analysis The 3D and 4D reconstructions of the acquired post-irradiation PET data and the corresponding FLUKA MC calculations of the *Line Mono* static and *G50* studies have been analysed in terms of the PET-based range $\mathrm{R}_{\mathrm{PET}}$ by the same approach used in the *Square* irradiation analysis. Due to the range modulation introduced by the PMMA fence placed in front of the phantom, different ranges with respect to the fixed proximal position A_5 could be found in the PMMA block and have been compared to the known geometrical shape of the fence in order to infer the accessible accuracy of PET-based range verification under static and under moving conditions. Moreover, the lateral (perpendicular to the incident beam) profiles of the activity distributions have been analysed by means of their FWHM and penumbra, following the description in the previous section. To measure the similarity of the retrieved data-sets, a 2D γ-index analysis has been performed in all x-z-planes, which exceed an integral activity of 90% of the maximum activity of the integrated profile along the vertical y-axis. The choice of transaxial planes, as was the case in the *Square* data analysis, has been avoided since the shape of the activity distribution is expected to change significantly as a function of depth within the phantom due to the given range modulation, while it is rather constant along the vertical y-axis. In addition, the similarity of the detected range deviations, being the central issue of the *Line Mono* irradiation study, can only be evaluated in planes parallel to the incident beam direction.

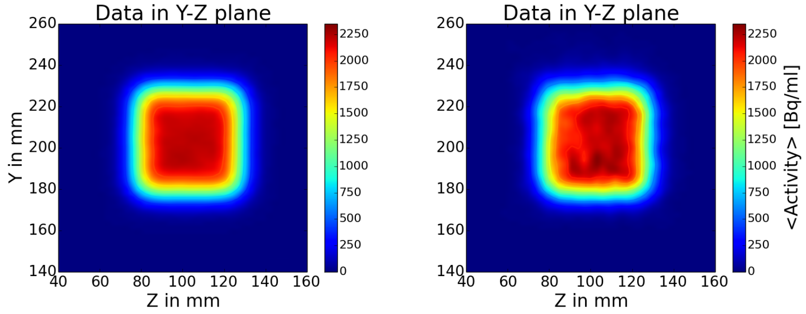

(a) *Square* static, FLUKA (b) *Square* static

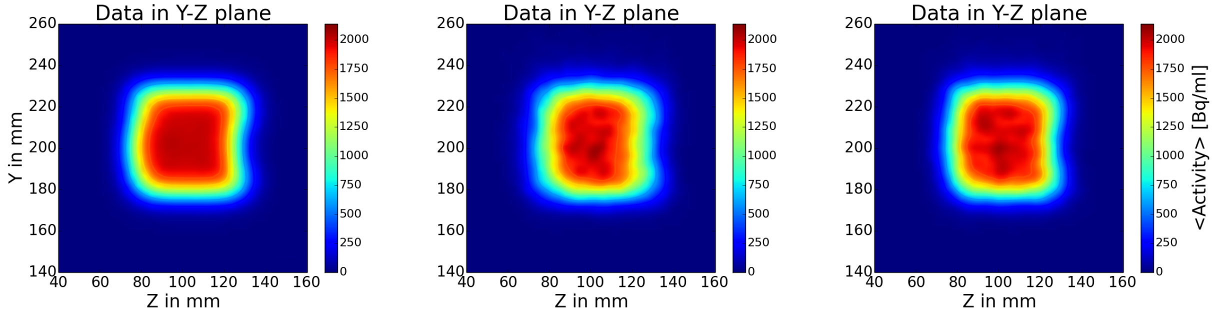

(c) *Square G50*, 4D FLUKA. (d) *Square G50*, 3D recon (e) *Square G50*, 4D recon

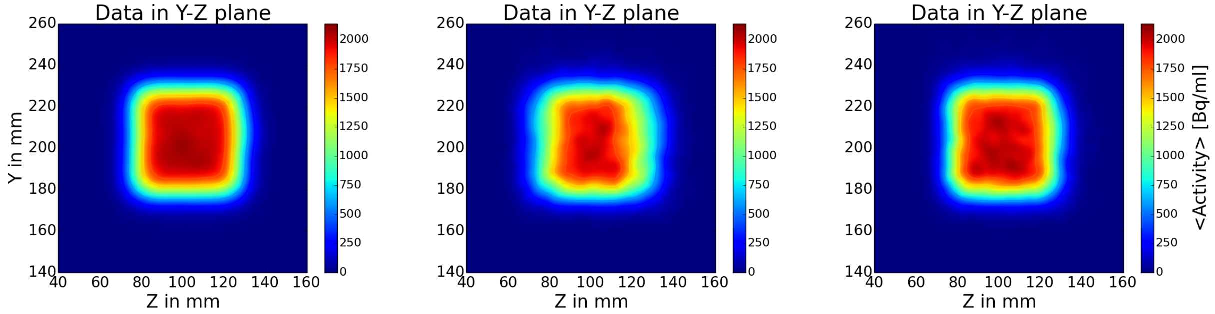

(f) *Square G20*, 4D FLUKA. (g) *Square G20*, 3D recon (h) *Square G20*, 4D recon

Figure 4.7: 2D activity distributions in the y-z-plane, i.e., perpendicular to the incident beam, for the investigated square irradiation studies. The simulation data is shown in the left column, the 3D reconstructed images in the middle column and the 4D reconstructions (only for the gated irradiation) are depicted in the right column. The images of the moving phantom studies are significantly blurred along the direction of motion, if not considering the movement in the reconstruction process. Due to the residual motion in the *G50* study, the square-shaped activity pattern is distorted along the direction of motion, as can be seen in the simulated and the 4D reconstructed data. This effect is notably reduced for the smaller gating window G20, in the simulation as well as in the measurement.

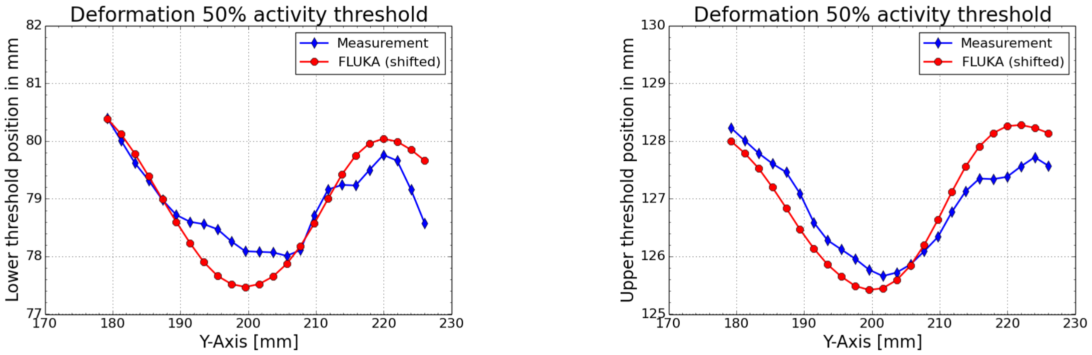

Figure 4.8: Illustration of the motion-induced *Square G50* activity distortion, corresponding to a displacement of the 50% activity thresholds in the direction of motion. For the lower (left) and the upper (right) 50% threshold, the displacement in measurement (blue) and simulation (red) agree within about 1 mm. The threshold positions of the simulated data have been shifted in order to compensate the different FWHMs (cf. table 4.3) in simulation and measurement for easier comparison.

Results An overview of the results obtained from the analysis of the different mono-energetic line irradiation studies is given in table 4.5, addressing the lateral properties of the considered activity distributions in the direction of motion, as well as the PET-based verification of the induced particle beam range deviations. These have theoretical dimensions of $\mathrm{DR}_1 = 7.5\,\mathrm{mm}$, $\mathrm{DR}_2 = 12.5\,\mathrm{mm}$ and $\mathrm{DR}_3 = 17.5\,\mathrm{mm}$. The range differences have been determined on the basis of the four different *absolute* PET-based ranges found within the PMMA phantom, as exemplarily shown for the measured data in figure 4.9. The retrieved absolute PET-ranges are depicted in appendix A.1 and have been found to agree within 0.9 mm for all investigated data-sets.

In terms of the determined range deviations DR_i, the theoretical shape of the PMMA fence could be reproduced with an accuracy better than 1 mm for all investigated data-sets, with the exception of the 3D PET reconstruction of the gated irradiation. Here, especially the smallest range difference DR_1 could not be accurately recovered. The presented results prove the ability to detect range deviations with sub-millimetre accuracy and precision (1σ) under static and moving

Table 4.5: Results of the *Line Mono* irradiation study. The FWHM and penumbra (mean of upper and lower) in the direction of the phantom motion are presented, together with the determined range differences induced by the PMMA fence. Notable deviations with respect to the static reference are given in bold.

Study	DR_1[mm]	DR_2[mm]	DR_3[mm]	FWHM_z[mm]	P_z[mm]
Line Mono, static	6.8 ± 0.9	12.5 ± 0.6	17.2 ± 0.5	143.9 ± 0.7	10.1 ± 0.3
Line Mono G50, 3D	$\mathbf{5.9 \pm 1.3}$	11.7 ± 1.1	17.2 ± 1.1	$\mathbf{148.3 \pm 1.2}$	$\mathbf{13.9 \pm 1.0}$
Line Mono G50, 4D	6.8 ± 0.7	12.1 ± 0.6	17.6 ± 0.5	143.2 ± 0.4	$\mathbf{11.9 \pm 0.5}$
FLUKA, static	6.8 ± 0.7	12.3 ± 0.4	17.3 ± 0.4	144.1 ± 0.2	9.9 ± 0.2
FLUKA G50, 4D	6.7 ± 1.0	12.2 ± 0.7	17.3 ± 0.6	144.3 ± 0.1	$\mathbf{11.1 \pm 0.1}$

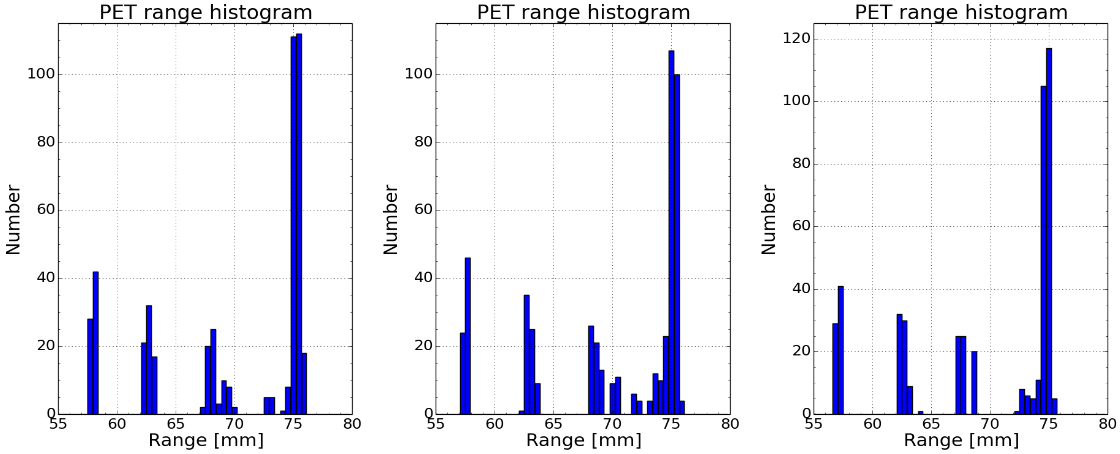

(a) *Line Mono*, static (b) *Line Mono G50*, 3D recon. (c) *Line Mono G50*, 4D recon.

Figure 4.9: Range histograms of the *Line Mono* static and *Line Mono G50* measurements. In the stationary image reconstruction of the moving target (middle), the range distribution shows an increased spread, which results in a less precise and accurate range verification, particularly for the smallest induced range difference. If performing a 4D motion-compensated reconstruction (right), results similar to the static reference case (left) can be achieved.

conditions by offline PET-imaging of the irradiation-induced activity. But, they also show that neglecting the target motion in the PET image reconstruction process can lead to a remarkable degradation of the retrieved results in terms of accuracy and precision (see figure 4.9 and table 4.5). By applying a motion-compensated 4D gated PET image reconstruction, however, results similar to the static reference measurement could be achieved, in agreement with the findings of the *Square* study. With respect to the simulated data, a comparable accuracy and an only slightly reduced precision has been observed in the analysis of the measured PET images of the static and the moving case, thus indicating the high reliability of the acquired post-irradiation PET data at the considered high statistics scenario.

The increased level of uncertainty in the quantification of the introduced range deviations determined for the 3D reconstruction of the *Line Mono G50* PET data is directly related to a remarkable blurring of the induced activity pattern along the direction of motion. The blurring is characterized by a significant increase of $\mathrm{FWHM_z}$ and $\mathrm{P_z}$ with respect to the static reference and can clearly be seen in the 2D activity distribution in the x-z-plane, as shown together with the other investigated data-sets in figure 4.10, and in the exemplary 1D lateral profiles depicted in figure 4.11. Both figures also show the notably reduced smearing and apparently improved agreement to the static reference measurement for the motion-compensated image reconstruction of the acquired 4D PET LM data. Still, with respect to the static reference, a significantly enhanced penumbra has been detected in the 4D reconstruction, but could be confirmed by the corresponding MC simulation and thus be attributed to the residual motion within the GW. Moreover, it has been found that the residual motion of the phantom leads to a shift of the two central activity maxima in the regarded lateral profiles by approximately 2 mm and to a slight distortion of the peak on the right. Both observations could be reproduced with sub-millimetre

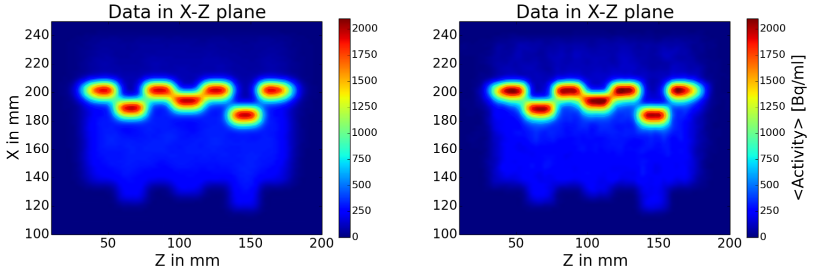

(a) *Line Mono* static, FLUKA (b) *Line Mono* static

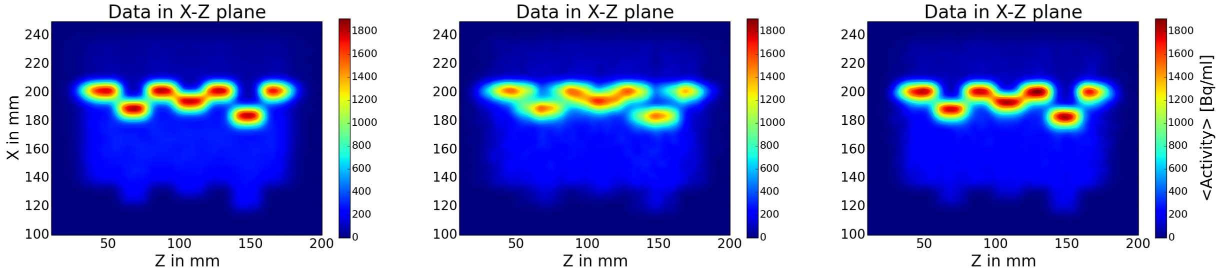

(c) *Line Mono G50*, 4D FLUKA. (d) *Line Mono G50*, 3D recon (e) *Line Mono G50*, 4D recon

Figure 4.10: 2D activity distributions in the x-z-plane of maximum activity for all investigated *Line Mono* data-sets. The 3D PET reconstruction of the moving phantom study *G50* shows a significant blurring along the axis of motion compared to the static reference and the motion-compensated 4D PET image. In general, a high agreement of simulation and measurement for the 3D and the 4D (motion-compensated) study has been found.

agreement by the corresponding 3D and 4D FLUKA calculations, which are displayed in figure 4.11, as well.

Concerning the quantification of the irradiation-induced activity an agreement within about $5-10\%$ of $\langle A_{95} \rangle$ between measurement and simulation has been achieved. Compared to the *Square* irradiation study, the agreement is slightly reduced, which can be attributed to the spatially more inhomogeneous activity pattern and the more condensed activity spots (see figure 4.10) leading to an overall increased level of uncertainty in simulation and measurement.

In the analysis of the lateral profiles along the vertical axis, i.e., perpendicular to the phantom movement, a high agreement (within 1σ) in terms of $\mathrm{FWHM_y}$ and $\mathrm{P_y}$ of all the five considered data-sets has been found and an impact of the target motion could not be identified, as expected.

Additionally, the similarity of the different data-sets quantified by the 2D γ-index is summarised in table 4.6. Compared to the *Square* irradiation study, an overall reduced agreement between different data pairs has been identified, which can be attributed to the overall higher complexity of the induced activity pattern with respect to the simple, shallow square shape, as well. Nevertheless, the γ-index analysis could indicate a significantly enhanced agreement between the 4D image reconstruction of the gated irradiation and the static reference measurement with respect to the 3D PET reconstruction of the gating case, proving the importance of incorporating the target motion to the reconstruction process. In agreement with the *Square*

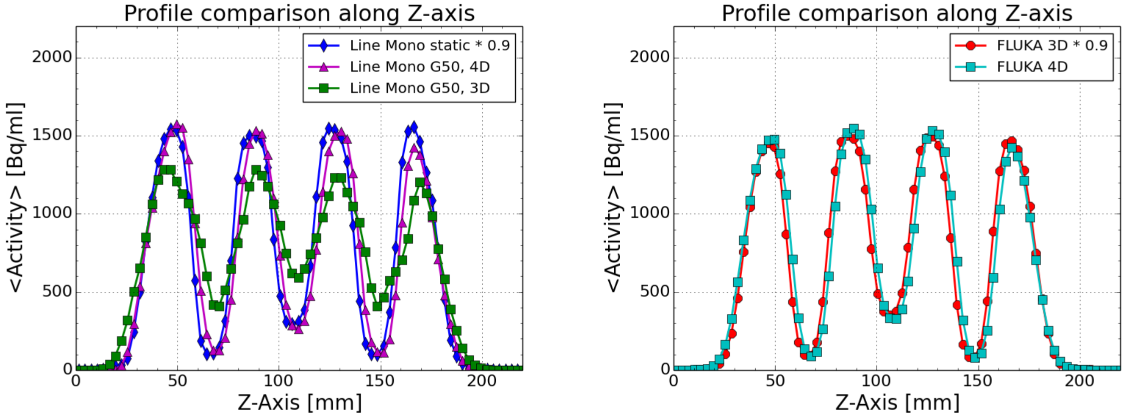

(a) Measurement (b) Simulation

Figure 4.11: Comparison of the lateral profiles along the direction of motion for the measured (left) and simulated (right) activity distributions. The 3D image reconstruction of the moving target (green) shows a significant blurring and an enhanced penumbra. Besides, a 2 mm shift of the two central activity maxima has been noticed in the 4D image (magenta) and the 4D simulation data (cyan) with respect to the corresponding static reference (blue, red). The 3D data-sets have been normalised to account for the different time structure of the two measurements.

irradiation study, a comparable similarity of the 4D FLUKA simulation to the corresponding 4D motion-compensated reconstruction and of the static FLUKA simulation to the static reference measurement has been found, which reflects the reliability of the performed 4D PET-based irradiation verification. Even the small influence of the residual motion on the induced activity pattern could be reproduced accurately, as also confirmed by the enhanced gamma index of 4D simulation and 4D PET with respect to 3D simulation and 4D PET.

4.1.2.3 *Line Mult* irradiation

Data analysis The available data-sets, consisting of the post-irradiation PET measurements of the static reference case and the irradiation with 20 and 50% GWs, together with the cor-

Table 4.6: Results of the γ-index analysis of the *Line Mono* irradiation study. In each case, mean value and standard deviation of the analysed x-z-planes are given.

Study 1	Study 2	γ-index
Line Mono, static	FLUKA, static	$85.6\% \pm 1.9\%$
Line Mono, static	*Line Mono G50*, 3D	$81.2\% \pm 0.4\%$
Line Mono, static	*Line Mono G50*, 4D	$87.0\% \pm 0.6\%$
Line Mono G50, 4D	FLUKA, static	$79.4\% \pm 0.5\%$
Line Mono G50, 4D	FLUKA G50, 4D	$83.8\% \pm 0.7\%$

responding FLUKA MC calculations, have been analysed in a similar way as the previously discussed *Square* study, using the same thresholds for the lateral profile and range analysis, but a study-specific fixed value of A_5, based on the static *Line Mult* reference measurement. Additionally, a 2D γ-index analysis has been performed within a dedicated region of y-z-planes that have been selected according to the same parameters used in the *Square* data analysis. The y-z-planes were chosen as the alteration of the qualitative shape of the underlying activity pattern with depth is small due to the range-compensated irradiation of the phantom through the PMMA fence.

Results An overview of the results of the profile-based analysis of the *Line Mult* studies is given in appendix A.2. The PET-based range of all investigated data-sets was found to agree within 0.7 mm. A deviation of less than 1σ has been identified between measured and simulated data for all investigated cases. A comparable, sub-millimetre precision has also been observed for the width and the penumbra of the analysed 1D profiles in the vertical lateral direction, perpendicular to the phantom motion, which has been found not to affect the quantities discussed up to here, as expected. In terms of absolute activity quantification, a similar agreement between measurement and simulation as reported in the *Line Mono* data analysis has been determined (about $5-10\%$ of $\langle A_{95} \rangle$).

In contrast to the depth and vertical lateral profiles, the properties of the horizontal lateral profiles along the direction of the phantom movement, were identified to be significantly affected by the target motion, particularly in the case of the larger gating window. Here, especially the lateral penumbra and its uncertainty were found to be considerably enhanced in the measurement as well as in the simulation. This observation could be attributed to a notable distortion of the induced horizontal lateral activity profiles with respect to the static reference measurement, as can be seen from the 2D activity distributions depicted in figure 4.12: particularly the 50% GW study is affected by significant interplay effects of the ion beam delivery and the residual phantom motion. When applying a reduced GW of 20%, the shape of the static reference distribution could be largely recovered and a FWHM and penumbra comparable to the static case have been observed. For all moving irradiation, an enhanced blurring of the induced activity pattern has been noticed in the stationary PET image reconstructions.

The 2D distributions shown in figure 4.12 have also been analysed by means of their 2D γ-index, yielding the results presented in table 4.7. The enhanced similarity of the *G20* study to the static reference with respect to the *G50* study could be confirmed and a significantly enhanced agreement of the 4D simulations to the corresponding 4D image reconstructions compared to the 3D MC calculations has been found. As observed in the *Square* and *Line Mono* studies, the 4D simulations and corresponding measurements were found to show a correlation comparable to those of the static reference, hinting on the reliability but also on the necessity of a 4D simulation under consideration of the phantom motion during the beam application.

Still, in the particular case of the *Line Mult* irradiation, which provides a remarkably more complex interplay pattern with respect to the *Square* and *Line Mono* studies, remaining differences between 4D measurements and 4D simulations concerning the particular shape of the underlying activity distributions have been observed (cf. figure 4.12). One major source of uncertainty within the 4D simulation workflow was identified in the temporal co-registration of the logged ANZAI motion signal and the NXP signals of the corresponding machine beam records (MBR). Slight changes of the temporal offset between motion and beam signal, corresponding to

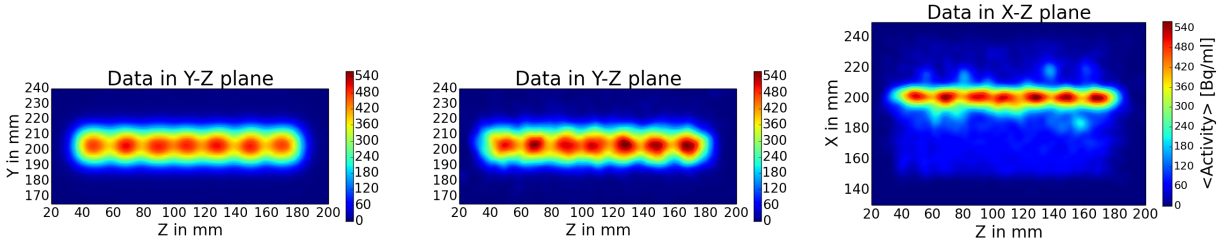

(a) *Line Mult* static, FLUKA (b) *Line Mult* static (c) *Line Mult* static

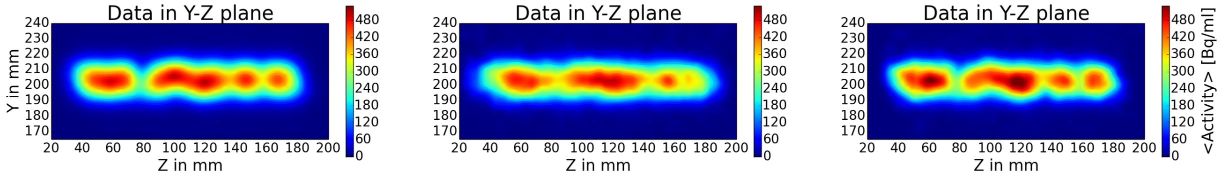

(d) *Line Mult G50*, 4D FLUKA (e) *Line Mult G50*, 3D recon (f) *Line Mult G50*, 4D recon

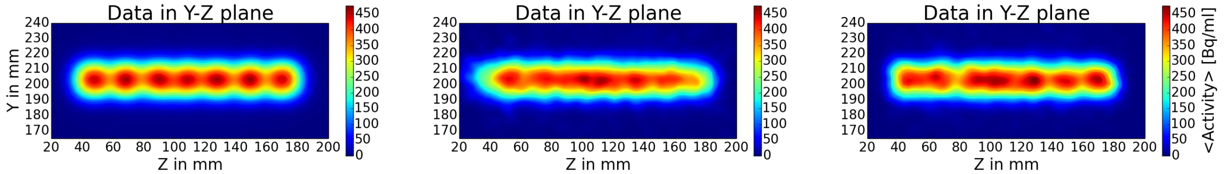

(g) *Line Mult G20*, 4D FLUKA (h) *Line Mult G20*, 3D recon (i) *Line Mult G20*, 4D recon

Figure 4.12: 2D activity distributions of the analysed *Line Mult* irradiation study data. By adapting the beam energy to the shape of the PMMA fence, range deviations are largely avoided (see top-right). Due to the finite beam size and the sharp edges of the PMMA fence, regions of over- and under-shoot in the PMMA block have, however, been found and lead to a pattern of 7 single spots in the lateral (y-z) image planes of maximum activity. The *G50* study (middle row) is significantly affected by interplay effects, while the *G20* study (bottom row) yields results close to the static reference (top row) if performing a gated 4D PET reconstruction (bottom-right).

a phase shift of the target motion, can immediately result in significant changes of the determined state raster files and herewith of the irradiation-induced activity. All 4D FLUKA calculations presented up to this point have been performed using a synchronisation of the end of the first spill according to the ANZAI beam status (directly retrieved from the accelerator) and the last NXP of the first spill within the MBR. Although the ANZAI system provides a sampling rate of 25 ms (the MBR provides 1 μs) deviations between the ANZAI beam signal and the NXP signals in the MBR of up to ±75 ms during the course of irradiation have been found. In addition, delays in the logging and processing of the acquired motion data within the ANZAI system had been observed in dedicated experiments at the Heidelberg facility, just as a non-constant offset between the system times of the ANZAI and the accelerator system [Richter, 2014]. Consequently, phase shifts between 0 (ph000, 4D FLUKA data presented up to here) and 300 ms (ph300) have been introduced when generating the state-raster files in order to carefully investigate the impact of a

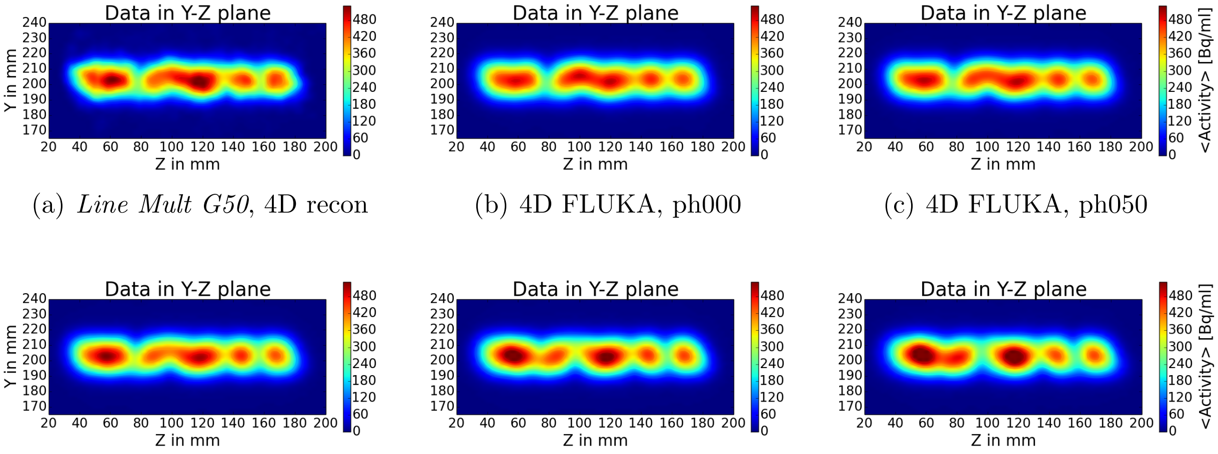

(a) *Line Mult G50*, 4D recon (b) 4D FLUKA, ph000 (c) 4D FLUKA, ph050

(d) 4D FLUKA, ph100 (e) 4D FLUKA, ph200 (f) 4D FLUKA, ph300

Figure 4.13: Investigation of phase shifts between the ANZAI motion data and the beam delivery sequence for the *Line Mult G50* study. An enhanced agreement to the measurement was found for phase shifts of 50 and 100 ms, while the similarity decreased for larger offsets.

possible temporal mismatch of the motion signal and the beam delivery sequence. The obtained results are shown for the *Line Mult G50* study in figure 4.13 and compared to the corresponding motion-compensated PET image. It can be seen that an overall enhanced agreement to the measurement has already been achieved by applying a phase shift of 50 ms: the determined γ-index was found to increase significantly from $86.9\% \pm 0.2\%$ to $89.2\% \pm 0.2\%$. For a phase shift of 100 ms, a slightly enhanced γ-index of $87.2\% \pm 0.3\%$ could still be found, while for larger, as well as for negative shifts, a decreasing similarity has been observed.

For the *Line Mult* study with a 20% GW, a slight visual improvement by applying a 100 ms phase shift has been achieved without, however, increasing the determined γ-index. As expected, the *G20* simulation is more robust against phase-shifts compared to the G50 study due to the

Table 4.7: Results of the γ-index analysis of the *Line Mult* irradiation study. Mean value and standard deviation of all analysed lateral planes are given.

Study 1	Study 2	γ-index
Line Mult, static	FLUKA, static	$88.4\% \pm 0.9\%$
Line Mult, static	*Line Mult G50*, 4D	$79.9\% \pm 0.9\%$
Line Mult, static	*Line Mult G20*, 4D	$85.0\% \pm 0.1\%$
Line Mult G50, 4D	FLUKA, static	$81.0\% \pm 0.5\%$
Line Mult G50, 4D	FLUKA G50, 4D	$86.9\% \pm 0.2\%$
Line Mult G20, 4D	FLUKA, static	$84.5\% \pm 0.8\%$
Line Mult G20, 4D	FLUKA G20, 4D	$86.3\% \pm 0.9\%$

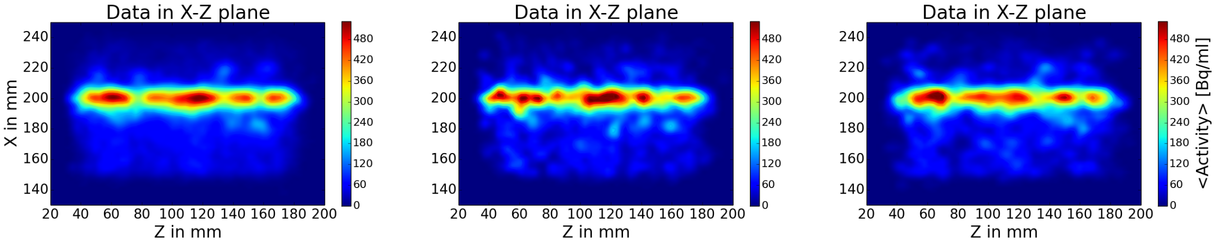

(a) G20, 4D recon (b) G20, 4D recon, phase 0 (c) G20, 4D recon, phase 5

Figure 4.14: Comparison of the motion-compensated 4D PET image (left) and two exemplary single PET phases (middle and right). The single phases are clearly suffering from severe image noise, leading to notable deviations in the amount and shape of the reconstructed activity. The motion-compensated image is smoother due to the summation of all phases, registered to the reference phase 0.

reduced residual motion and interplay effects. Similar findings have been made when investigating the impact of a possible phase shift on the *Square* and *Line Mono* gating studies: due to the lack of a prominent interplay pattern, the impact of the initial motion phase on the calculated activity pattern was found to be notably smaller than in the *Line Mult G50* study. Nevertheless, the latter study clearly demonstrated the potential of 4D PET-based treatment verification: it has been demonstrated to be feasible to determine the initial motion phase of the moving phantom with a precision of about 50 ms and to achieve an equivalent agreement of simulation and measurement as found for the static reference case.

The high accuracy of the results retrieved within the moving *Line Mult* studies becomes even more remarkable if considering the low counting statistics of the acquired PET data. According to table 4.2, each of the eight reconstructed motion states contains only about $100,000$ true counts, leading to a substantial noise in each of the reconstructed phases, as shown for two exemplary phases in comparison to the 4D motion-compensated PET image in figure 4.14. The latter image is considerably smoothed by the registration and subsequent summation of the eight single phases in the chosen reference phase. With respect to the static reference measurement, the number of counts within each phase is about a factor of nine lower, leading to a SNR reduced by a factor of three. As a consequence, the results retrieved in the profile analysis of single-phase PET images are significantly less precise and a sub-millimetre accuracy cannot be ensured, as shown for two exemplary motion phases of the *Line Mult G50* and *G20* study in table A.3 in appendix A.2. Moreover, remarkable differences between the PET images in different motion phases have been observed: for the two phases 0 and 5 shown in figure 4.14, e.g., a γ-index of just $78.0\% \pm 0.5\%$ has been determined. Despite these findings, a comparable accuracy and precision with respect to the static reference could still be achieved when analysing the smoothed motion-compensated 4D gated PET image, although only providing a comparable number of true coincidences ($\approx 850,000$ in total, i.e., $\approx 100,000$ in each of the eight gated PET phase) as in the clinical patient cases discussed in chapter 6.

4.1.3 Discussion and conclusion

The moving phantom irradiation studies presented in the first section of this chapter contribute a first thorough experimental investigation on the applicability of offline PET-based treatment verification, using a commercial full-ring PET/CT scanner, to moving targets. Besides an in-depth comparison of the results retrieved once in static reference measurements and once in measurements with moving phantoms (applying a motion-compensated beam delivery by gating and rescanning), the performance of corresponding 4D FLUKA MC simulations under consideration of the target movement during the irradiation has been studied.

In general, it could be found that in the given comparably high statistics scenario ($850,000 - 3,600,000$ true coincidences) an accuracy and precision of below one millimetre can be achieved in terms of the beam range as well as in terms of the lateral profile properties, namely the profile width and its penumbra. Similar results in terms of the accessible precision and accuracy have been reported in [Parodi et al., 2005b] for static and in [Parodi et al., 2009] and [Stützer et al., 2013] for moving phantom irradiation studies, using a dedicated dual-head in-beam PET detector. In contrast to these studies, however, the use of a commercial PET/CT system allowed for an absolute quantification of the irradiation-induced activity. Here, differences between simulation and measurement were typically found to be in the order of $5 - 10\%$ and can be attributed to uncertainties in the modelling of nuclear interactions within the FLUKA MC code, to inaccuracies by the approximate modelling of the image acquisition and reconstruction process in the activity calculation by only a post-simulation Gaussian filter, as well as to intrinsic uncertainties in the activity quantification by the PET/CT scanner (cf. chapter 5) and the limited accuracy of the applied attenuation correction on the basis of the free-breathing 3D CT during 4D gated PET image reconstruction.

For all three investigated geometries, namely the *Square*, *Line Mono* and *Line Mult* study, the importance of 4D motion-compensated PET imaging in the case of moving phantoms has clearly been demonstrated. The applied 4D gated PET image reconstruction, currently being the only available option for 4D PET imaging on the Biograph mCT scanner, clearly out-performed the additionally performed 3D PET image reconstruction without taking the motion into account. In the case of the *Square* irradiation study, target motion lead to a significantly enhanced lateral profile penumbra in the 3D reconstructed images, similar to the observations presented in [Parodi et al., 2009; Stützer et al., 2013]. The shape of the lateral profiles was, however, found be recovered by the 4D image reconstruction, yielding results comparable to the static reference measurement. Similar observations have been made for the *Line Mono* study, where motion also remarkably impeded the precision and accuracy of determining the induced range deviations in the static reconstruction under target motion. The 4D reconstruction, however, enabled an equivalent performance, i.e., sub-millimetre accuracy in the detection of range differences, compared to the static reference, in agreement with the observation in [Stützer et al., 2013]. In the case of the *Line Mult* study, the considerable blurring along the direction of motion in the 3D reconstruction of the moving phantom hindered the identification of the irradiation-induced interplay effects, introduced by the residual motion of the phantom within the applied GW, thus further indicating the need of a motion-compensated 4D PET image reconstruction in order to fully exploit the potential of 4D PET-based treatment monitoring.

In the *Square* and *Line Mono* irradiation study, slight distortions of the detected activity due to the residual phantom motion have been identified as well, although typically not exceeding a scale of few millimetres. In the case of the *Square* irradiation, a slight distortion of the square-shaped activity in the vertical lateral direction has been observed due to the unavoidable synchronisation of the synchrotron duty cycle and the phantom motion. In this particular case, the enhanced symmetry of the used full-ring detector geometry with respect to the dual-head set-up used in previous studies promises considerable advantages due the lack of limited angle artefacts, which lead to a significant degradation of the resolution along the lateral direction connecting the two detector heads [Crespo et al., 2006].

Concerning the corresponding 4D FLUKA calculations, an equivalent agreement of static reference measurements with static FLUKA calculations and of 4D motion-compensated PET images with 4D FLUKA simulations has been found for all studies, based on a 2D γ-index analysis. The FLUKA simulations particularly confirmed the observed alterations due to the residual phantom motion within the GW and herewith the high sensitivity of 4D offline PET-based treatment verification. One critical issue in this context was spotted in the synchronisation of the ANZAI-detected motion trajectory and the beam delivery sequence, having an uncertainty in the order of about $100-200\,\mathrm{ms}$. A dedicated simulation study for the *Line Mult* geometry, exhibiting the most prominent interplay pattern, showed the sensitivity of the calculated expected activity distribution in the phantom to the actual motion phase at the start of the beam application. The study, however, also showed the high potential of 4D PET monitoring: by comparing the simulated data to the motion-compensated 4D PET image, the time offset could be determined with a precision of about 50 ms. Future studies will benefit from a dedicated EtherCAT system which has been installed in the mean time and allows for a synchronous detection of ANZAI and beam status signals, thus eliminating uncertainties in the synchronisation and enhancing the achievable precision of the performed 4D MC calculations [Richter et al., 2014].

In conclusion, the conducted studies not only proved the feasibility of 4D offline PET-based treatment verification by means of a commercial full-ring PET/CT scanner, but also indicated the high potential of this approach. In the considered simplified experimental scenario (comparably high counting statistics, no washout, regular phantom movement), motion-induced interplay effects, leading to a distortion of the induced activity pattern with respect to the static reference, could be monitored with high (sub-millimetre) accuracy, yielding an equivalent similarity of measurement and simulation as observed in the static reference cases. Interplay effects are one main hazard in the treatment of moving tumours with scanned ion beams, and an accurate identification is consequently highly desirable. 4D PET-based treatment verification has been shown to have the potential of significantly contributing to control these risks and herewith to contribute to an improved treatment of patients with mobile tumours.

A first application of 4D offline PET-based treatment monitoring to motion affected patient irradiation will be presented in chapter 6, in order to investigate in detail the potential of this method under clinical conditions. One main challenge is anticipated to be the further reduced number of detected true coincidences, being in the order of $400,000 - 900,000$. As reported in [Parodi et al., 2009] and [Stützer et al., 2013], reduced counting statistics will lead to a degradation of the retrieved results, typically hindering a sub-millimetre precision and accuracy. A similar finding has been made in this work when analysing single phases of the gated 4D PET reconstruction of the *Line Mult* study, where each phase contained only about $100,000$ true counts. Moreover, a thorough identification of the induced interplay pattern in these single phases was found to be considerably more challenging due to the strongly enhanced image noise.

The issue of low counting statistics, and herewith high image noise, is one of the major challenges in PET-based treatment monitoring in general, but is of particular interest for the 4D offline treatment verification approach pursued in this work due to the used gated 4D PET image reconstruction, which further reduces the number of true coincidences within each single motion state. Consequently, in the following chapter 5, an in-depth analysis of the noise properties and geometrical fidelity of the Biograph mCT scanner over a wide range of counting statistics (also covering the patient-relevant regime) will be carried out. Moreover, the accuracy of activity quantification and the often-debated impact of the high random background due to the intrinsic radio-activity of the LSO detectors will be addressed in detail.

4.2 A first implementation of ultrasound-based motion tracking in 4D PET imaging

In the previous section, the importance of the motion monitoring system in the context of 4D PET-based treatment verification has been pointed out: an accurate tracking of the target motion is necessary for the generation of the state-raster files, which are used in the 4D simulation of the irradiation-induced activity, and it is also essential for motion mitigation during the post-irradiation PET acquisition. The sensitivity of the induced activity pattern to the underlying state-raster files has been shown particularly in the *Line Mult G50* study (see section 4.1.2.3), where slight phase shifts of the detected motion with respect to the beam delivery sequence were found to have a remarkable impact on the calculated activity pattern. In a similar way, a mis-identification of the actual motion state during the irradiation, e.g., due to a lack of correlation between an external motion surrogate and the actual internal organ motion (cf. section 2.6.4), can lead to significant differences between calculated and actually applied dose or induced activity. Moreover, the previous moving phantom irradiation studies showed a remarkable degradation of the quality of the retrieved PET images if motion is not accounted for in the PET image reconstruction. Neglecting motion can lead to a significantly degraded accuracy and precision of the determined ion beam range, as shown for the *Line Mono* study (see section 4.1.2.2), and a substantial blurring along the direction of motion, hindering e.g., a thorough identification of irradiation-induced interplay patterns. Similar to the generation of the state raster files, accurate 4D imaging requires an accurate identification of the current patient motion state during data acquisition. As a consequence an enhanced 4D imaging performance by advanced motion tracking techniques is foreseen, particularly in the presence of breathing irregularities, as typically encountered during the prolonged 4D post-irradiation patient PET acquisition.

Aim of the study discussed in this section is to investigate the feasibility of implementing an advanced ultrasound-based tracking system in time-resolved PET and to compare its performance to the reference monitoring system at HIT, namely the ANZAI respiratory gating system, within a 4D PET imaging study with moving ^{22}Na point sources.

4.2.1 Material and methods

4.2.1.1 US tracking device

For US-based motion monitoring, the prototype US tracking system Sonoplan II (mediri GmbH, Heidelberg, Germany) was used. It is based on the Digital Phased Array System (DiPhAS, Fraunhofer IBMT, St. Ingbert, Germany) in combination with an US T-probe which includes two perpendicular 5.5 MHz, 64 element phased array transducers, allowing for simultaneous imaging

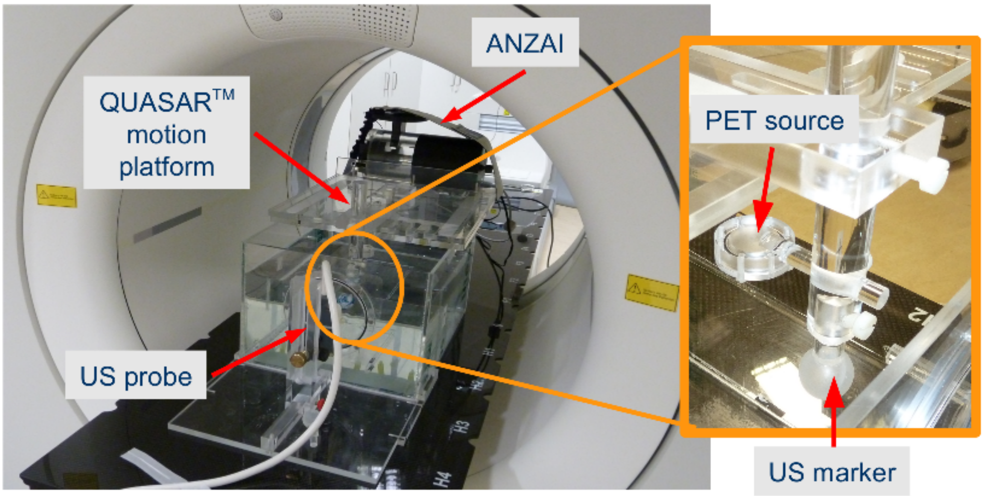

Figure 4.15: Image of the experimental set-up for investigating the feasibility of US-based 4D PET imaging. The US marker and the rigidly attached ^{22}Na PET point source were moved parallel to the scanner axis by the QUASAR motion platform. Movement was synchronously detected by the ANZAI system and the US probe, which has been coupled to the water tank through a Mylar-foil window.

in two perpendicular planes. The captured US images are post-processed and evaluated by the US tracking software which includes a probabilistic algorithm for real-time tracking of user-defined structures in the acquired images [Zhang et al., 2010]. Target motion can be described by up to five parameters (translation and scaling in x and y, plus a rotation) in each of the two considered planes at a frame-rate of approximately 5 Hz with a precision of below 1 mm [Prall et al., 2014].

In comparison, the certified ANZAI respiratory gating system only provides a one dimensional external signal, the patient chest-wall expansion, from which the actual internal motion has to be inferred. Consequently, due to the questionable correlation of internal and external motion, particularly in the case of irregular breathing patterns (cf. section 2.6.4), a superiority of real-time internal motion tracking, as potentially provided by the US-system, is anticipated.

4.2.1.2 Experimental set-up

An image of the used experimental set-up for investigating the feasibility of US tracking based 4D PET imaging is shown in figure 4.15. The used ^{22}Na point source has been moved along the PET/CT scanner axis (z-axis) by the QUASAR respiratory motion platform and rigidly attached to an US marker, represented by a rubber ball. In order to be able to monitor this marker, it has been placed in a water-filled tank, to which the US transducer was coupled through a window covered with a thin Mylar-foil. Motion was simultaneously detected by the ANZAI system, directly connected to the motion platform as a standard reference (similar to the previously discussed moving phantom irradiation study), and by the US system, tracking the contour of the US marker. The whole set-up has then been placed in the bore of the Biograph mCT scanner. Regular motion patterns (sinusoidal- and $\cos^4$-shaped) with different amplitudes A and periods T have been investigated, as well as a real patient motion trajectory recorded during a 4D post-irradiation patient PET scan.

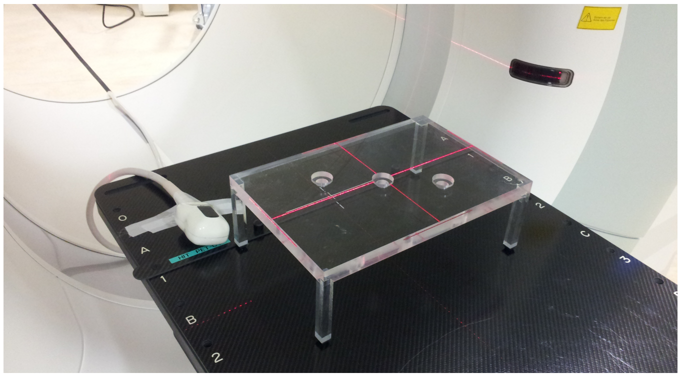

Figure 4.16: Image of the experimental set-up used to investigate the impact of the US probe on the acquired PET images. The three ^{22}Na point sources have been positioned in a diagonal line within the Plexiglass frame, aligned to the PET/CT laser system. In the depicted case, the US probe has been placed beside the source holder.

In addition, the impact of the US probe, placed in different positions within the FOV of the PET detector ring, on the acquired PET images has been analysed in terms of activity quantification and geometrical fidelity in order to exclude undesirable image artefacts due to the application of US tracking. For this purpose, three ^{22}Na point sources have been placed in a diagonal line within a fixed Plexiglass source holder. The middle source was positioned at the iso-centre of the scanner, while the two other sources were positioned with an offset of ±4 cm along the scanner axis and ±6 cm in the radial direction. One reference scan and four scans with the US probe fixated at different positions within the FOV have been acquired. The probe has been positioned (1) beside the Plexiglass holder (see figure 4.16), (2) on the short edge of the source holder, (3) under the source holder, about 6 cm below the middle source, and (4) right on top of the central source on the source holder.

4.2.1.3 Data acquisition, processing and analysis

In all cases, PET data have been acquired in LM format with time tags every ms. In order to enable a 4D image reconstruction in the moving phantom study, the positions in time of the inhale peaks are provided by the ANZAI respiratory gating system within the acquired LM data stream as gate-tags. For the 4D gated PET image reconstruction, the LM data has been subdivided into eight motion phases, as typically done in 4D patient examinations, and reconstructed by a filtered back-projection (FBP). The single respiratory phases have then been registered manually to the maximum inhale phase, chosen as a reference.

In contrast to the standard ANZAI motion surrogate, the US tracking device cannot be coupled directly to the PET/CT scanner. Instead, the US motion signal has been acquired in parallel on a separate computer system and fed back to the acquired LM data retrospectively. For this purpose, the inhale peaks in the the US tracking signal, considering only the displacement parameter along the scanner axis, have been determined, corrected for the time offset between the two computer systems and used to replace the ANZAI gate-tags within the acquired LM data. The retrieved modified LM stream, now containing US-based gate-tags, has then been fed back to the PET/CT scanner and reconstructed in the same way as the original LM data with ANZAI

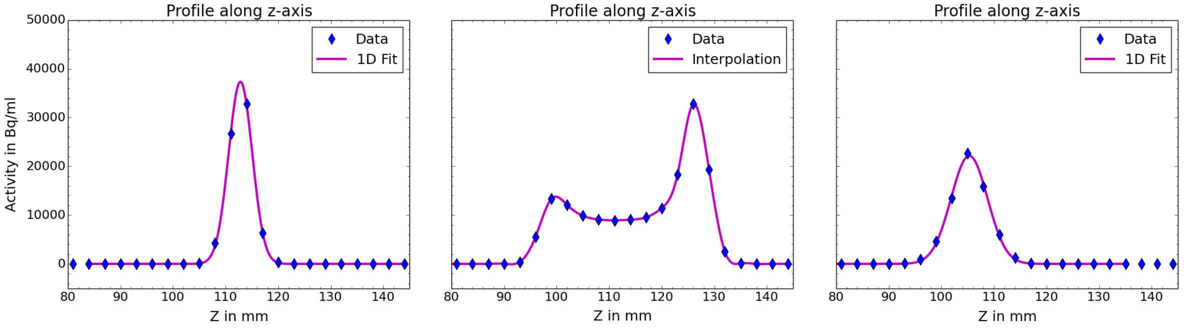

(a) Static reference (b) cos^4, $A = 3\,\text{cm}$, 3D recon. (c) cos^4, $A = 3\,\text{cm}$, 4D recon.

Figure 4.17: Comparison of static (left) and moving point source PET images. The activity of the source is smeared over the whole motion amplitude (here 3 cm) if not corrected for (middle). Using the standard ANZAI-based 4D gated image reconstruction, the Gaussian shape of the point source can be recovered (right).

gate-tags. This enabled a direct comparison of 4D gated PET based once on the new US tracking device and once on the reference ANZAI system. The quantity of interest in this comparison was the width of the point source in the direction of motion (along the scanner z-axis) in the reconstructed images, as determined by a Gaussian fit at the x-y position of maximum activity.

To quantify the impact of the US probe on the statically reconstructed PET images of the second experiment, the integral activity within a generous volume-of-interest (VOI) around each of the three imaged sources has been determined, as well as the position of the three sources in x, y and z. The latter have been retrieved from 1D Gaussian fits along the three scanner axis through the maximum activity of each single point source. As a measure for possible image distortions, the relative positions of the individual sources with respect to the reference measurement without US transducer in the FOV have been analysed.

4.2.2 Results

4.2.2.1 4D PET image reconstruction and comparison of tracking data

As shown in figure 4.17 for a cos^4-shaped breathing pattern, motion of the point source leads to a remarkable smearing and distortion of the point-like activity in the direction of motion, as observed in the previously discussed moving phantom irradiation study, and to a notably larger integral activity if not performing a motion-compensated image reconstruction. By applying a 4D gated PET image reconstruction (here based on the reference ANZAI gate-tags), however, the original Gaussian shape of the point source, as well as the correct integral activity, can be recovered. Still, with respect to the static reference measurement, the FWHM along the direction of motion was found to increase from 5.2 mm to 9.6 mm in the depicted case due to the residual motion within the eight considered motion states.

Following the aim of this study, namely to investigate the feasibility and performance of an ultrasound-based motion-mitigated image reconstruction, the acquired tracking data of the US system and the ANZAI reference surrogate, on which the gate-tags written into the PET LM

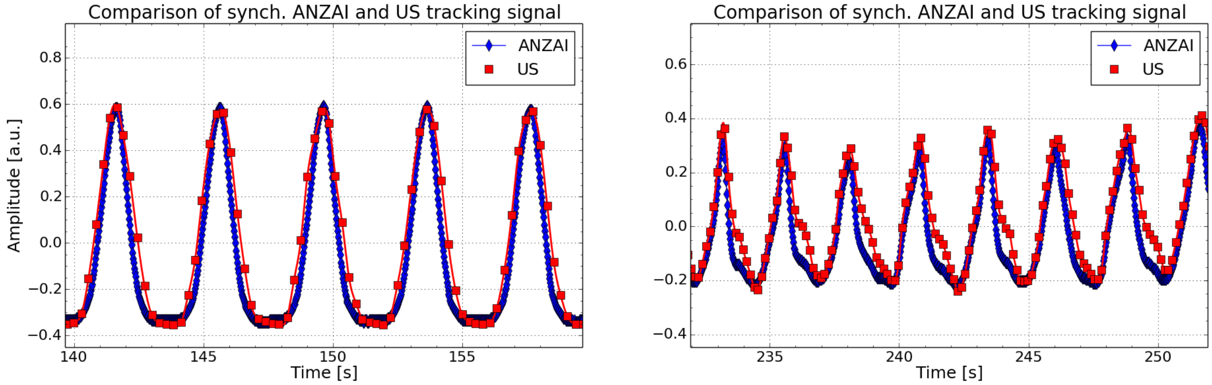

(a) $cos^4, A = 3\,\mathrm{cm}, T = 4\,\mathrm{s}$ (b) Patient, $A_{max} = 3\,\mathrm{cm}$

Figure 4.18: Comparison of synchronised US (red) and ANZAI (blue) tracking data for a regular cos^4-shaped motion (left) and an original patient trajectory (right). As the US system provides a considerably lower frame rate, the acquired data have been interpolated. In general, a good agreement between the two data-sets has been found. Particularly the positions in time of the inhale peaks agree quite well, typically within less than 100 ms.

data are based, have been compared. Out of the ten available tracking parameters delivered by the US device, only the displacement in the direction of motion, used in the retrospective LM data manipulation, has been considered. All further US tracking parameters were found to be constant in time for the selected one-dimensional motion aligned to the perpendicular US planes and could thus be neglected. As shown in figure 4.18 for the cos^4-shaped motion, with $T = 4\,\mathrm{s}$ and $A = 3\,\mathrm{cm}$, and for a real patient breathing pattern with a maximum peak-to-peak amplitude of 3 cm, a good agreement between the two tracking systems has been found. Minor deviations have typically been identified in the exhale part of the trajectory. In the performed 4D gated PET image reconstruction, however, only the positions of the inhale peaks are of importance: here, a standard deviation in time of less than 100 ms has been found for all investigated breathing patterns (cf. table 4.8), hinting on a comparable performance of both tracking systems in terms of motion-mitigated 4D PET imaging. It should be noticed that the mean time difference of the inhale peak positions has been set to zero by the prior synchronisation of the two tracking data-streams.

4.2.2.2 Performance of US-based 4D PET

An overview of the FWHMs obtained by the 1D Gaussian fit along the direction of motion (z-axis) in the 4D-reconstructed motion-mitigated PET images, based once on the ANZAI and once on the US tracking signal, is presented in table 4.8, together with the standard deviation of the above-mentioned time differences between ANZAI- and US-detected inhale peaks (corresponding to the LM data gate-tags), $\Delta t_{\mathrm{US}}^{\mathrm{ANZAI}}$. The depicted FWHM values have an uncertainty of 0.2 mm originating from the manual registration of the reconstructed phases to the chosen reference phase and the uncertainty of the performed fit. An error of 0.2 mm in the manual registration process was estimated by multiple registrations of the same data-set and comparison of the determined

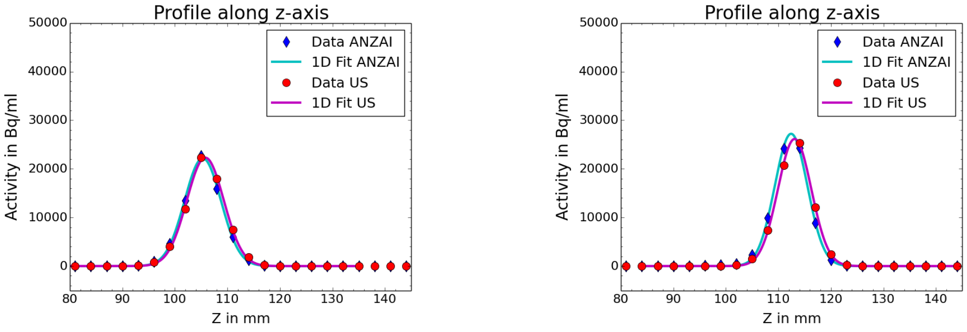

(a) $cos^4, A = 3\,\mathrm{cm}, T = 4\,\mathrm{s}$ (b) Patient, $A_{max} = 3\,\mathrm{cm}$

Figure 4.19: Comparison of profiles along the direction of movement for the $\cos^4$-shaped motion with $A = 3\,\mathrm{cm}$ and $T = 4\,\mathrm{s}$ (left) and the real patient trajectory (right). The ANZAI-based (blue, cyan) and the US-based (red, magenta) 4D gated PET images agree within less then 0.8 mm in terms of the point source position and show an equal FWHM in the direction of motion.

FWHMs. The error in the 1D Gaussian fitting was typically found to be below 0.1 mm.

Taking these uncertainties into account, an equivalent performance of the clinically used ANZAI gating system and the prototype US tracking device has been identified in terms of motion mitigation in 4D PET imaging under the given experimental conditions. The profiles along the direction of motion, as retrieved with the two investigated tracking devices, are compared for the $\cos^4$-shaped motion with $A = 3\,\mathrm{cm}$ and $T = 4\,\mathrm{s}$, as well as for the investigated patient motion trajectory in figure 4.19. In both cases, the FWHM agrees within 0.2 mm and the position of the point source, corresponding to the mean value of the fitted Gaussian, agrees within 0.8 mm. In general, for all investigated motion patterns of table 4.8, the position of the point source has been observed to agree within less than 5% of the case-specific motion amplitude in the ANZAI-

Table 4.8: Overview of the determined point source FWHMs along the scanner axis and the standard deviations of the inhale peak time differences. The combined error of the manual registration and the Gaussian fit in the FWHMs has been determined as 0.2 mm in all cases.

Motion Shape	Sinusoidal T = 4 s A = 4 cm	Cos^4 T = 4 s A = 3 cm	Cos^4 T = 4 s A = 2 cm	Cos^4 T = 2.5 s A = 3 cm	Patient $\mathrm{A_{max}} = 3\,\mathrm{cm}$
$\mathrm{FWHM_z}$[mm] ANZAI	9.6	8.2	7.2	8.3	7.3
$\mathrm{FWHM_z}$[mm] US	9.6	8.3	7.4	8.3	7.5
$\mathrm{STD}(\Delta t_{\mathrm{US}}^{\mathrm{ANZAI}})$ [ms]	50.0	32.3	41.4	33.6	81.1

and US-based 4D motion-compensated images.

The retrieved results (cf. table 4.8) moreover confirmed that a higher motion amplitude results in a larger FWHM due to an enhanced residual motion in the single PET phases. Concerning the patient-like data-set, it must be considered that the average breathing amplitude was about 2 cm, i.e., smaller than the maximum peak-to-peak amplitude of 3 cm. The breathing period, on the other hand, was found to not affect the results because of the used phase-based sorting of the LM data.

In general, the method of retrospectively replacing the ANZAI gate-tags in the acquired LM PET data by the determined US gate-tags has proven to work reliably during the data preparation process. However, a prior synchronisation of each independent data-set has been found to be necessary, in order to correct for an observed, non-constant time offset between the two different operating systems on which the tracking routines were run, and which consequently had to be determined at the beginning of each single PET acquisition. This problem can likely be solved by running the US tracking software directly on the ANZAI computer, which was not feasible in the context of this study as the ANZAI computer is in clinical use and additional software installation not allowed. Further efforts on an improved synchronisation of both devices are, however, not of need if pursuing the approach of retrospective introduction of the US gate-tags into the acquired LM data, but would be required for future prospective gated PET acquisitions on the basis of US motion tracking.

In the presented results, the anticipated superiority of the US tracking system could not be shown due to the chosen set-up with a regular 1D motion and the only available gated 4D PET image reconstruction, which solely relies on the position of the inhale peaks and not on the actual source position. In order to demonstrate the promised advantages of US tracking, a more detailed investigation with a more complex, uncorrelated 3D point source motion and a more sophisticated way of sorting the acquired LM data into the different motion phases, making use of all the ten US tracking parameters, would be of need. A realisation within the restricted environment of a clinically used PET/CT device is, however, expected to be too elaborated and beyond the scope of this work, which focused on a first proof-of-principle study on the feasibility of US-based 4D PET.

4.2.2.3 Artefact effects by the US probe

The results of the investigations on possible imaging artefacts induced by the ultrasound probe being positioned within the PET FOV are presented in tables 4.9 and 4.10. Table 4.9 presents the impact of the US transducer on the quantification of the point source activity. Repeated measurements of a single point source showed a quantification uncertainty of about 1%. The alterations caused by the US probe are typically in the same order of magnitude, not exceeding a value of 3.5% with respect to the reference measurement without US probe. The only exception has been found for the probe positioned directly next to the central source S2. Here, artefacts in the underlying AC CT lead to an over-correction of the point source activity by about 20%, thus surpassing a clinically acceptable limit. This extreme situation will, however, rarely appear in clinical cases where the activity of main interest is usually not positioned directly at the patients skin. Particularly in the context of PET-based verification of the applied ion beam range, the distal activity fall-off, which is of main interest in the data analysis, is typically located several centimetres below the patient skin.

Concerning the spatial distortion introduced by the US probe, similar conclusions could be drawn: the impact of the transducer on the determined positions of the three imaged point sources has been found to be smaller than one single image pixel, having a size of 2 mm perpendicular and 3 mm parallel to the scanner axis (see table 4.10). Considering the point source resolution of the scanner, which has been determined as 4.4 mm in [Jakoby et al., 2011], the retrieved alterations are not expected to significantly impact the quality of clinical PET data-sets. In this context, it should also be mentioned that the chosen experimental set-up represents an extreme case, being highly sensitive to imaging artefacts. In a patient scenario, the contribution of the ultrasound probe to the attenuation of the emitted gamma rays will be significantly smaller and the more shallow activity pattern with respect to the investigated sub-millimetre point sources will be notably less prone to image distortions.

Consequently, clinical US-based 4D PET imaging will not be significantly impeded by artefacts introduced by the used US transducer if keeping a distance of a few centimetres between the US probe and the investigated activity distribution within the patient.

4.2.3 Discussion and conclusion

In the second part of this chapter, a first implementation of US-based motion tracking in 4D PET imaging has been performed and compared in terms of motion mitigation to the presently used standard motion monitoring device at HIT, namely the certified ANZAI pressure sensor, in dedicated phantom imaging studies. US-tacking is a promising technique which enables non-invasive, dose-free and real-time tracking of the internal target movement, thus not relying on the questionable correlation of external and internal motion in contrast to the ANZAI system. This capability is important for an advanced sorting of the acquired image data to the single motion phases for an improved, artefact-free 4D imaging, as well as for an improved sorting of the irradiated beam spots to the single motion phases when retrieving the 4D state-raster files. Both applications have been shown to be of utmost importance for 4D offline PET-based treatment verification in the discussed moving phantom irradiation studies (cf. section 4.1.3).

The conducted 4D PET imaging study showed that 4D gated PET imaging based on US motion tracking is feasible and that results equivalent (differences on the sub-millimetre scale) to the clinically used ANZAI respiratory gating system can be achieved. The standard deviations of time differences between the required gate-tags in the acquired LM data were found to be

Table 4.9: Impact of the US probe on the point source quantification. The determined integral VOI activities A are given for each of the three imaged point sources S_i, together with the deviation to the reference measurement without US probe (in brackets). All determined activities have an uncertainty of 1.0%.

	A_{S1} [10^8Bq/ml]	A_{S2} [10^7Bq/ml]	A_{S3} [10^8Bq/ml]
Reference	2.95	8.25	2.93
Beside source holder	2.89(−2.0%)	8.23(−0.2%)	2.91(−0.7%)
Edge of source holder	3.01(+2.0%)	8.17(−1.0%)	2.83(−3.4%)
Below source holder	2.99(+1.4%)	8.23(−0.2%)	2.88(−1.7%)
Top of source holder	3.01(+2.0%)	9.96(+20.7%)	2.93(+0.0%)

below 100 ms and the investigated FWHMs along the direction of motion were observed to agree within 0.2 mm for all investigated cases when comparing the 4D data-sets retrieved with the two monitoring systems. Moreover, the positions of the moving point-source in the 4D motion-compensated images were found to agree within less than 5% of the respective motion amplitude. In line with these findings, a sub-millimetre agreement between the US tracking device and a high-precision laser distance sensor has also been reported by [Prall et al., 2014].

Moreover, a study with a fixed point-source set-up proved that quantification and geometrical fidelity of the scanner are not significantly degraded when positioning the US-transducer in the PET FOV, as long as a minimum distance of few centimetres between the imaged activity pattern and the US probe is kept. This will be the case in most clinical scenarios, where the relevant activity is very rarely to be found close to the patient skin. Another challenge that might be encountered in clinical scenarios is the motion of the US probe, attached to the patient surface, during respiratory motion. This problem, however, can be solved by additional optical tracking of the US probe motion, which enables US tracking in absolute coordinates within the PET/CT coordinate system, as shown in [Schwaab et al., 2014].

Further studies with more complex motion patterns, particularly with uncorrelated motions in more than one dimension, and with an advanced way of sorting the acquired LM data into the different reconstructed motion states should aim at showing the anticipated benefits from US motion tracking in 4D PET imaging under conditions closer to clinical scenarios. Moreover, these investigations should clarify the issue of timing synchronisation between the two tracking systems, also considering possible delays in the US tracking system which have been described in [Schwaab et al., 2014; Prall et al., 2014]. Although these delays are not of concern for the presented retrospectively gated US-based PET imaging with prior synchronisation of the motion data-streams, they become a crucial issue for prospective gating in 4D PET imaging and real-time motion monitoring during irradiation, as being of need for generating the state-raster files for 4D dose and activity calculations. As has been shown for regular target movement in [Prall et al., 2014], motion prediction by an artificial neural network, might be one possible solution to this complication.

Table 4.10: Image distortions induced by the US transducer. The depicted values show the spatial deviations determined along all three axes for each of the three point sources with respect to the reference image without US transducer in the PET FOV. The error in the fitted positions and in the retrieved deviations is below 0.1 mm.

	$(\Delta x_{\mathrm{S1}}, \Delta y_{\mathrm{S1}}, \Delta z_{\mathrm{S1}})$ [mm]	$(\Delta x_{\mathrm{S2}}, \Delta y_{\mathrm{S2}}, \Delta z_{\mathrm{S2}})$ [mm]	$(\Delta x_{\mathrm{S3}}, \Delta y_{\mathrm{S3}}, \Delta z_{\mathrm{S3}})$ [mm]
Beside source holder	$(-0.3, -0.1, +0.9)$	$(-0.2, -0.1, +1.7)$	$(-0.2, -0.1, +0.7)$
Edge of source holder	$(+0.0, -1.5, +1.0)$	$(-0.0, -0.0, +1.8)$	$(+0.1, +1.0, +1.5)$
Below source holder	$(-0.3, -0.1, +0.7)$	$(-0.3, -0.1, +0.8)$	$(-0.2, -0.1, +0.2)$
Top of source holder	$(-0.3, -0.1, +1.1)$	$(-0.2, +0.0, +1.9)$	$(-0.2, -0.1, +1.6)$

Chapter 5

Investigations on the performance of the Biograph mCT PET/CT scanner at very low true count rates

In the post-irradiation PET/CT studies of moving phantoms discussed in the previous chapter, analysis of the retrieved PET images has been found to be challenged by a decreasing number of true coincidences. In particular, when analysing the single motion state PET images obtained from the 4D gated image reconstruction in the *Line Mult* study, sub-millimetre precision in the depth and lateral profile analysis could no longer be provided, and a proper identification of the residual motion-related interplay pattern was found to be considerably undermined (cf. section 4.1.2.3). Similar observations have been made for comparable moving phantom studies at low counting statistics with a dedicated BGO(Bismuth germanate)-crystal based in-beam PET camera in [Parodi et al., 2009; Stützer et al., 2013].

In the same way, the small amount of irradiation-induced activity and the directly related high level of noise in the reconstructed PET images has been reported to be one of the major challenges of in-vivo PET-based treatment verification under clinical conditions [Parodi et al., 2008a; Shakirin et al., 2011; Bauer et al., 2013b]. The numbers of detected coincidences for carbon-ion post-irradiation PET acquisitions at HIT are presented in table 5.1 for several exemplary patient cases with various tumour indications. The given random fraction (RF) is calculated as the number of random coincidences divided by the number of prompt (sum of random and true) coincidences. As can be seen, the acquired clinical data provides between about $80,000$ and $1,200,000$ true coincidences for image reconstruction, which is about $1-3$ orders of magnitude less than in standard nuclear medicine imaging with injected radio-tracers like ^{18}F-Fludeoxyglucose (FDG) [Nagaki et al., 2011]. The number of random coincidences has been found to be almost constant, as predominantly attributed to the intrinsic LSO-related random background (cf. section 3.4.3). The latter has been determined as 1032 ± 27 cps by a fit of the measured random rates in 18 different patient scans by an exponential decay plus a constant background term according to equation (3) in [Parodi et al., 2007b]. Due to this constant background, RFs range from about 60 to 96% in the taken data-sets. In the case of 4D gated PET image reconstruction, which is of particular interest in the scope of this work and where the acquired data are reconstructed separately within each motion phase, the number of available true coincidences is even further reduced (at constant RF) by the number of considered motion states. For the depicted liver patients in table 5.1, e.g., which will be studied in depth in chapter 6 with respect to the applicability of 4D offline PET-based treatment monitoring, the number of true counts per phase will be decreased to 100,000 or less if reconstructing a set of eight individual motion states, as done in the previous moving phantom irradiation study (cf. chapter 4).

The investigations presented in this chapter address in detail the reliability and accuracy of the activity quantification, as well as the geometrical fidelity of the Biograph mCT scanner, under these particular statistical conditions of small numbers of true counts and high RFs for different image reconstruction methods and settings, with the aim of identifying the best-performing algorithm and its optimal configurations for PET-based treatment verification. Moreover, the impact of the exceptionally high random background on the reconstructed PET images is thoroughly investigated.

5.1 Material and methods

5.1.1 Phantom imaging and simulation study

In order to investigate the performance of the Biograph mCT scanner over a wide range of counting statistics, a dedicated imaging study with a cylindrical water phantom has been performed (see figure 5.1). A cylindrical insert with a diameter of 46 mm within the phantom, emulating a patient-like activity distribution for verification of the geometrical fidelity and range-like assessment power, has been filled to an activity of 2007 ± 22 Bq/ml with FDG and aligned parallel to the PET/CT scanner axis. 30 subsequent PET scans with a duration of 30 min each have been acquired, collecting between 8,000,000 and 40,000 true coincidences at RFs between 21 and 98%, thus covering the whole patient-like counting regime in terms of true counts and RFs, as depicted in figure 5.1. The retrieved data have been reconstructed by 4 different reconstruction algorithms: the standard 3D OP-OSEM (in the following referred to as OSEM), 3D OP-OSEM with implementation of TOF information (OSEMTOF), 3D OP-OSEM with PSF modelling (PSF) and 3D

Table 5.1: Counting statistics of exemplary post-irradiation PET scans acquired after ^{12}C irradiation at HIT for various tumour locations. The presented liver tumour cases will be analysed in depth with respect to the applicability of 4D offline PET-based treatment verification in chapter 6.

Location	True counts	Random counts	Random fraction
Head	75,346	1,981,590	96.3%
Head/Neck	121,712	1,881,088	93.9%
Sacrum	1,190,642	1,822,141	60.5%
Prostate	588,401	1,774,623	75.1%
Liver (L1)	891,871	1,850,903	67.5%
Liver (L2)	693,686	1,922,683	73.5%
Liver (L3)	379,308	1,873,157	83.2%
Liver (L4)	703,576	1,941,071	73.4%

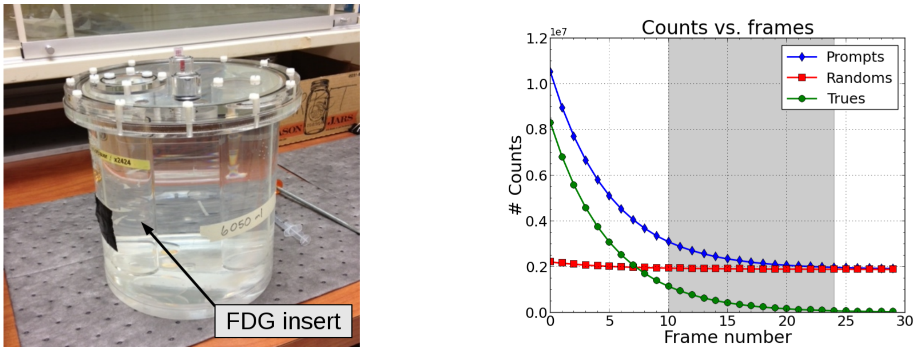

Figure 5.1: Image of the used cylindrical phantom including the FDG insert (left) and the number of counts acquired in the 30 subsequent PET frames (right). The patient-like counting regime is indicated by the grey shaded area and completely covered by the performed measurements.

OP-OSEM with TOF and PSF information (PSFTOF). For each algorithm, a variety of reconstruction parameters (number of iterations, number of subsets, post-reconstruction filter size) has been investigated in order to identify the optimal reconstruction approach for PET-based treatment verification. The voxel-size was kept constant at the available maximum value of $4 \times 4 \times 2\,\mathrm{mm}^3$ in order to optimise the number of counts per voxel under the given poor statistical conditions. In all cases, attenuation correction, on the basis of an AC CT, and scatter correction, on the basis of a single scatter simulation [Watson, 2000], scaled to the measured emission sinogram data in a region outside of the phantom (in order to account for scatter contributions from outside the axial PET FOV [Watson et al., 2004]), have been applied. All reconstructions have been performed at the Siemens Molecular Imaging headquarters in Knoxville, USA, using directly the basic reconstruction routines of the Biograph mCT scanner, which cannot be accessed by the standard end-user of the device, who is restricted to steer them via the Syngo user-interface. For the presented study, the direct usage of the underlying basic routines enabled the investigation of a wider range of reconstruction parameters than provided by the Syngo interface, concerning not only the number of iterations and subsets, but also the underlying scatter correction algorithms.

The precision and accuracy of the activity quantification, as well as the image noise, have been analysed for each reconstruction of each acquired PET frame in 16 equally spaced planes along the scanner axis in a circular region-of-interest (ROI) with a diameter of 32 mm, placed within the cylindrical FDG insert (see figure 5.2). The geometrical performance of the different reconstruction settings has moreover been inferred from the determination of the FWHM and penumbra ($80\% - 20\%$ fall-off) of the 1D activity profiles along the transaxial scanner coordinates through the centre of the 16 evaluated ROIs, as also shown in figure 5.2. The correct recovery of the two edges in each of the profiles resembles the detection of the distal fall-off of the irradiation-induced activity within a patient, as requested for analysing the particle beam range.

The impact of the high LSO-related random background on the reconstructed images has been addressed by truncating the acquired LM data of the different PET frames to fixed numbers of true coincidences and herewith yielding LM data-sets containing a constant number of true coincidences at different random fractions. This also enabled to separate the impact of low true count rates and of the high random fractions on PET imaging.

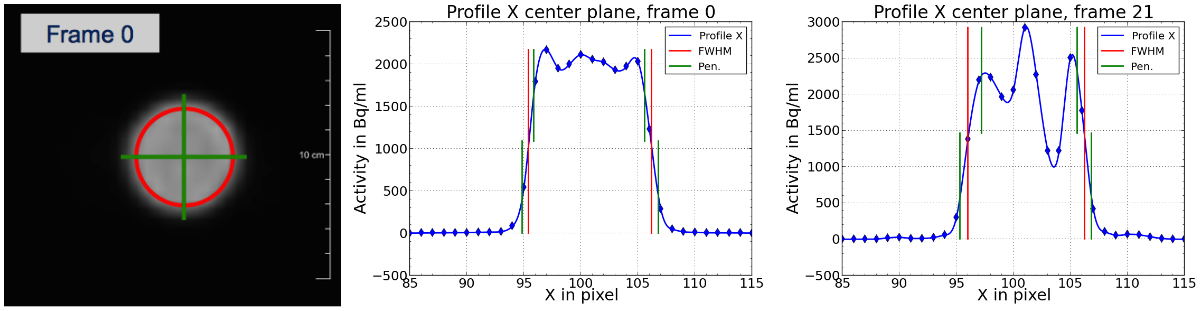

Figure 5.2: Sketch of the data analysis for the phantom experiment. Activity quantification and noise have been evaluated on the basis of 16 circular ROIs within the FDG activity insert (red, left plot) in each of the 30 PET scans. The geometrical performance was inferred from the analysis of FWHM and penumbra (middle and right plot) of the 1D profiles along the transaxial coordinates of the scanner through the centre of the ROIs (green, left plot). In frame 21 (140,000 trues) noise is considerably impeding the geometrical accuracy and precision (right plot).

In order to confirm the experimental findings and extend them to an even wider range of counting statistics, a dedicated simulation study of the experiment has additionally been performed. Within this simulation, sinogram files have been generated by the forward projection of an artificially generated image of the well-known experimental set-up under consideration of the detector sensitivity of the mCT scanner and the attenuation correction, as described by the AC-CT. Additionally, simulated scatter coincidences and random coincidences in a user-defined amount, as well as Poisson-noise could be added to the simulated sinogram data, thus enabling to separately investigate the influence of scatter coincidences in the presence and absence of random noise. The retrieved sinograms have been reconstructed by exactly the same algorithms as the measured data. The data analysis has, however, been extended by additionally analysing the amount of activity outside the FDG insert (in this case covered by a circular ROI of 56 mm), outside the water phantom and in the summed-up image.

5.1.2 Application to clinical cases

Based on the results retrieved from the phantom imaging study and the corresponding simulation, the applicability of the proposed optimal reconstruction settings to clinical cases has been investigated for four original post-irradiation patient PET data-sets: two head patients, representing the most frequent indication for PET-based treatment verification, and two liver patients (L1 and L2) which will also be discussed in chapter 6. The analysis focused on the activity quantification and image noise within a user-defined set of ROIs in planes perpendicular to the incident beam, where a rather constant activity pattern has been expected. Moreover, the optimised reconstruction strategy has been compared to the previously used standard reconstruction scheme at HIT, namely PSFTOF with 3 iterations, 21 subsets and a 5 mm post-reconstruction Gaussian filter (PSFTOF, 3i21s, gf5, inspired by the typical settings in conventional nuclear medicine imaging), in terms of beam range verification (following the most-likely shift approach described in section 3.4.4 and [Frey et al., 2014]) in order to carefully ensure an equal sensitivity to range deviations from the planned treatment application, which is of utmost importance in PET-based treatment

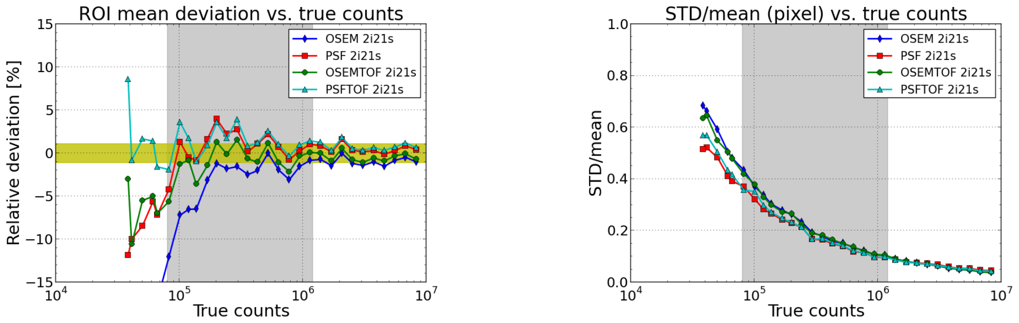

Figure 5.3: Relative deviation of the mean activity within the ROIs with respect to the injected activity (yellow bar, left plot) and image noise (right) for the OSEM (blue), PSF (red), OSEMTOF (green) and PSFTOF (cyan) reconstruction algorithms at 2i21s (cf. text). The patient-like counting regime is indicated by the grey shaded area. OSEM cannot recover the correct activity below about 200, 000 trues. PSF and TOF information can help to overcome this limitation. In terms of noise, slight advantages have been found for reconstructions including PSF information at small true numbers.

monitoring.

5.2 Results

5.2.1 Phantom data: activity quantification, noise and geometrical fidelity

The relative deviation of the mean activity determined in the 16 circular ROIs with respect to the injected activity of $2007 \pm 22\,\mathrm{Bq/ml}$ as a function of the number of detected true coincidences is shown in figure 5.3 for the different investigated reconstruction algorithms at 2 iterations with 21 subsets (2i21s) [1]. It has been found that below about 200, 000 true counts, the OSEM reconstruction can no longer recover the correct activity and is thus not suitable for low statistics patient imaging. Including PSF and TOF information has been observed to help overcoming this limitation. If applying both information (i.e., PSFTOF), the activity could be determined correctly down to about 60, 000 true counts at a RF of 98%. In terms of the image noise, here defined as the standard deviation divided by the mean value of all pixels within the 16 ROIs, a slight decrease has been identified for reconstructions with PSF-modelling at very few true counts (below about 100, 000), if not exceeding 3 iterations at 21 subsets (see figure 5.3).

The impact of the number of iterations on the activity quantification and image noise is illustrated in figure 5.4 for the PSFTOF algorithm: a small number (below 50) of MLEM-like iterations (calculated as the number of subsets times the number of OSEM iterations) has been found to lead to a slight overestimation of the determined target volume activity by up to 5%, as the reconstructed activity converges from higher to lower values. On the other hand, a significantly reduced noise-level in the reconstructed images has been observed for less iterations, particularly at small true numbers. Similar findings have been made for the other reconstruction

---

[1] If not differently stated, a post-reconstruction Gaussian filter of 5 mm has been applied to all data

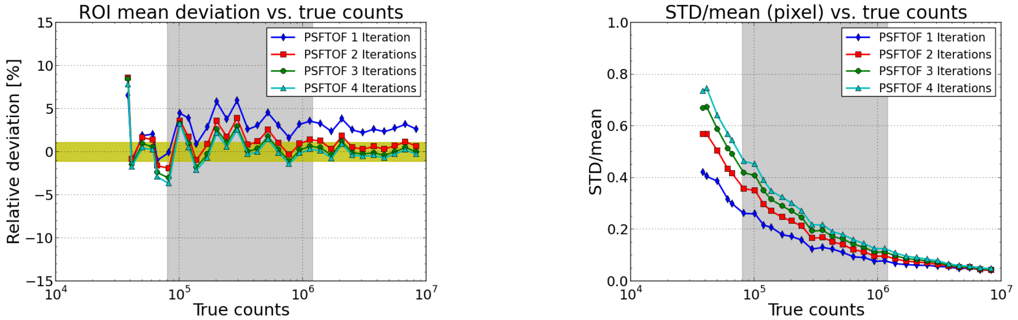

Figure 5.4: Relative deviations in activity quantification (left) and assessment of image noise (right) for 1 (blue), 2 (red), 3 (green) and 4 (cyan) iterations of the PSFTOF reconstruction. Fewer iterations tend to overestimate the activity by up to 5%, but were found to result in a significantly reduced image noise.

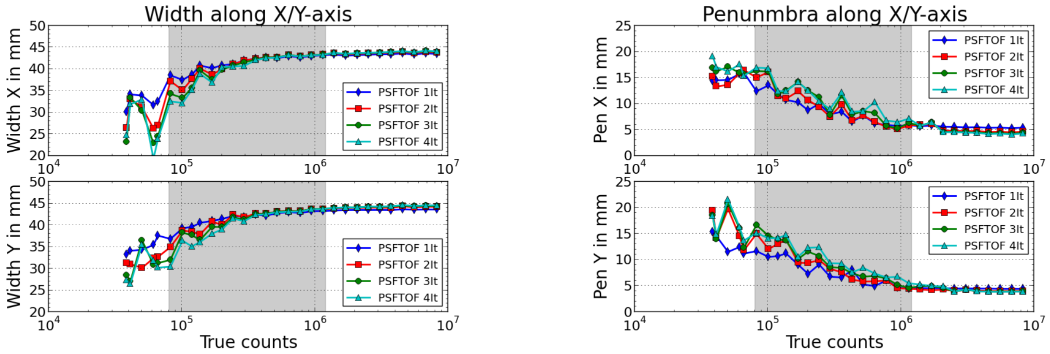

Figure 5.5: Geometrical performance for different numbers of iterations. The FWHM of the phantom can be recovered more accurately for less iterations (left). At the same time, less iterations provide a reduced lateral penumbra at low true count numbers.

algorithms and different numbers of subsets (14 and 24). Consequently, if accepting a potential overestimation of the activity by typically less than 5%, the image noise can be reduced by more than 30% below 100,000 true counts for 1 OSEM iteration of PSFTOF with respect to the currently used standard setting with 3 iterations.

In terms of geometrical fidelity, the best results could be obtained with the PSFTOF algorithm. Compared to the other reconstructions, PSFTOF was found to obtain a slightly more accurate and precise recovery of the FWHM of the imaged FDG insert as well as a smaller lateral penumbra at a reduced variance. As depicted in figure 5.5, an improved geometrical accuracy and precision has also been observed for a reduced number of iterations. This can directly be related to the reduced image noise, which generally makes the definition of thresholds (20, 50 and 80% fall-off) more prone to uncertainties (cf. figure 5.2, right plot). Similar thresholds are also used in PET-based range verification [Knopf et al., 2011; Helmbrecht et al., 2012; Frey et al., 2014], which could consequently gain in robustness by reducing the image noise level, as well. In this context,

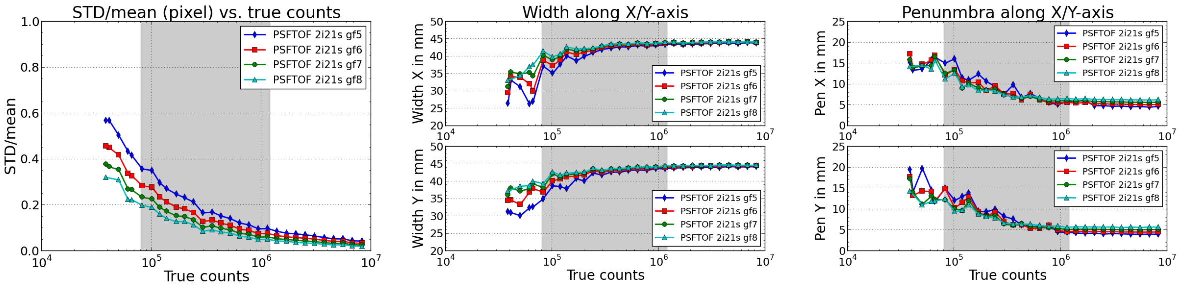

(a) Image noise (b) FWHM fidelity (c) Penumbra

Figure 5.6: Impact of the post-reconstruction filter size. As expected, larger filters result in a reduced image noise (left). This also leads to an improved recovery of the FWHM of the cylindrical insert for low true rates (middle), without increasing the lateral penumbra (right).

---

improvements have also been found by the application of larger Gaussian post-reconstruction filters, as shown in figure 5.6: larger filters result in a reduced image noise level and consequently an improved recovery of the FWHM of the cylindrical insert at small true numbers, without significantly affecting the activity quantification or the lateral penumbra. Still, enhanced Gaussian filters should be handled with care, since they reduce the granularity of the reconstructed images. Therefore, an equivalent sensitivity to detect potential range deviations has been tested for real clinical cases, as will be discussed in section 5.2.3.

5.2.2 Impact of the LSO random background

Under consideration of the results discussed in the previous section, the analysis of the truncated phantom LM data at fixed true counts and varying random fractions particularly aimed at separating the impact of small true numbers, high random fractions and the scatter coincidences on the acquired low statistics PET data.

The quantification of the ROI mean activity retrieved by the standard OSEM reconstruction is shown in figure 5.7 for different fixed numbers of true coincidences ($\text{T1} = 1,200,000$, $\text{T2} = 650,000$, $\text{T3} = 190,000$ and $\text{T4} = 80,000$) as a function of the random/true count rate for the measured, as well as for the simulated data. The previously observed failure of the OSEM to recover the correct activity in the acquired late PET frames has been confirmed in the truncated LM data: for only $80,000$ true coincidences, the determined activity decreases with increasing random background, as encountered during these late frames. It could, however, be found that the small number of true coincidences alone does not cause this inaccuracy, as quantification holds for $80,000$ true counts at RFs below about 60%. However, also a high random fraction itself has been found to not necessarily lead to a decreasing activity in the additional analysis of the simulated data: at reasonably high true count numbers, quantification is stable up to more than 95% RF. Besides, it has been observed that activity quantification will not fail under all investigated statistical conditions, if no scatter coincidences are simulated. Consequently, the OSEM failure in the late PET frames has to be attributed to inaccuracies in the scatter estimate which arise at very small true numbers and a high random background. Indeed, this explanation was confirmed by a significant increase in the amount of estimated scatter coincidences in the

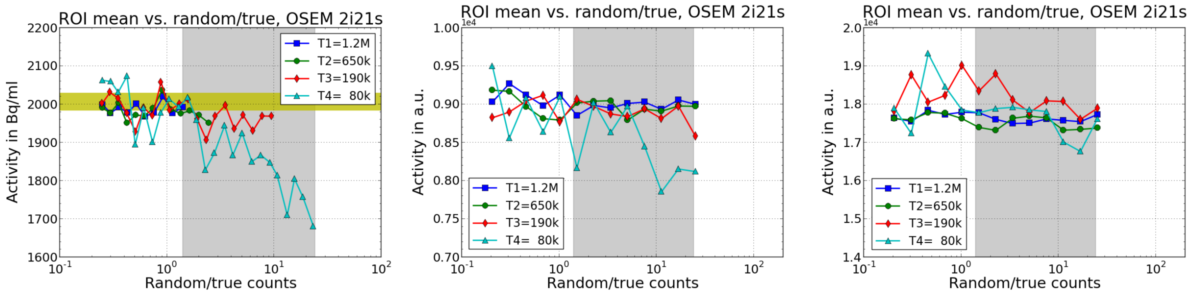

(a) Measurement (b) Simulation, with scatter (c) Simulation, no scatter

Figure 5.7: Quantification of the ROI mean activity by the OSEM algorithm at fixed true counts (T1 = 1.2M (blue), T2 = 650k (green), T3 = 190k (red), T4 = 80k (cyan)) and varying RFs. Below 100,000 trues, absolute quantification fails for the measured data at high RFs (left, injected activity indicated by the yellow bar). The decrease in the determined amount of activity has also been observed in the simulation with scatter (middle), but was not present if scatter coincidences have not been simulated (right). For simplicity, the simulated data have not been scaled to absolute activities and are given in arbitrary units.

---

late frames, which then directly leads to a decrease in the determined scatter-corrected activity. Further reconstruction attempts including a scatter correction without scaling of the simulated scatter estimate to the measured emission data and/or with an increased number of iterations of the underlying single scatter simulation have been investigated, but could not improve the quantification. Similar observations have been made for the PSF and OSEMTOF reconstructions, though at an overall reduced level of inaccuracy in the determined activity.

The PSFTOF reconstruction algorithm, on the other hand, has been found to be considerably less sensitive to this inaccurate scatter estimate and to enable a correct quantification, even under very challenging statistical conditions (see figure 5.8). The reproducibility of the mean activity value, corresponding to the standard error of the ROI mean activity (calculated as the standard deviation of the 16 determined ROI mean values), has been found to be in the order of 10%, even at only 80,000 true coincidences, and to be determined by the number of acquired true coincidences, while being independent of the actual RF. Similar observations have been made in terms of the image noise and the geometrical performance (considering accuracy and precision of the FWHM and penumbra) for the PSFTOF reconstruction algorithm: the main limitation under clinical-like counting statistics has been identified in the small number of true coincidences, not the comparably high LSO-related random background (cf. figure 5.8). This result was confirmed by the corresponding simulations with and without scatter coincidences over an even wider range of counting statistics than accessible in the measured data, as shown in figure 5.9. For the other regarded algorithms, i.e., OSEM, OSEMTOF and PSF, the true count rate has been determined as the crucial point, too, although for these methods a slight degradation of the geometrical fidelity has been observed due to high RFs, even in the absence of scatter coincidences, in the corresponding simulations.

Although neither undermining the activity quantification, nor the image noise in the regarded ROIs or the geometrical performance of the PSFTOF algorithm, it has, however, been noticed that higher random fractions lead to an increased integral image activity (sum of all image voxel)

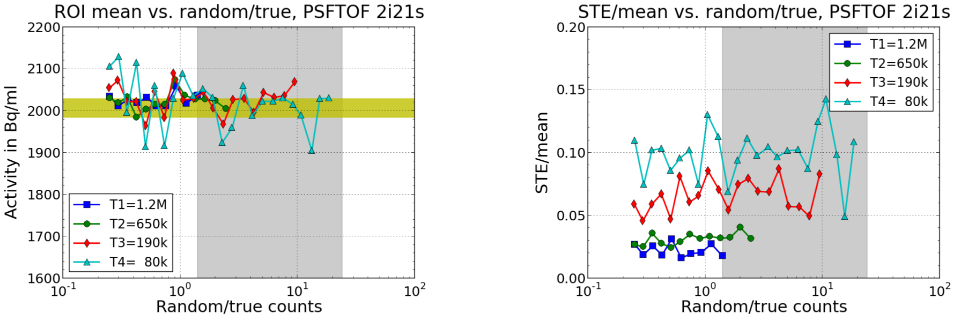

(a) Quantification (b) Reproducibility

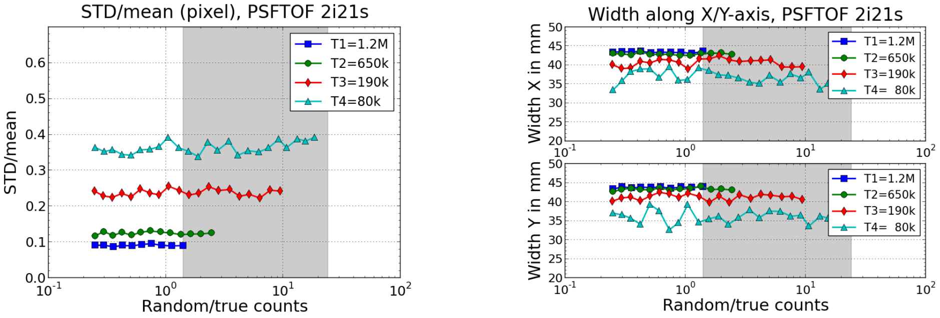

(c) Image noise (d) FWHM fidelity

Figure 5.8: Performance of the PSFTOF algorithm at fixed true counts and varying RF (truncated measured data). Absolute quantification is neither hampered by small true numbers, nor by high RFs (top left). The reproducibility (standard error of the ROI mean activity, top right), image noise (bottom left) and geometrical fidelity (here represented by the FWHM, bottom right) are mainly limited by the small number of true counts, not by high random fractions.

and to spurious, clumped activity within the whole PET FOV (see figure 5.10), even outside the actual water phantom. By analysing the truncated measured data at fixed true counts, the spurious activity throughout the FOV could be solely attributed to the high RF, as not being present at arbitrary true numbers for small RFs. Still, investigation of the simulated data showed that the increase of the integral activity towards higher RFs is more pronounced for smaller numbers of true coincidences. The observed effect can be explained by the positive bias which is being introduced to the underlying OSEM algorithm by the non-negativity bound in image space under the assumed Poisson-statistics. This bias is enhanced for small numbers of true coincidences and high RFs. In the acquired original measurement data, an increase in the total image activity between about 20 and 50% with respect to the first acquired frame has been observed below $100,000$ true counts, depending on the applied reconstruction algorithm and the number of iterations: the smallest increase of the integral activity has been identified for the PSFTOF algorithm and a small number of iterations.

Another effect that has been encountered in the analysis of the activity in the different ROIs shown in figure 5.10 is the build up of an activity halo, spatially restricted to the water phantom, outside the actual FDG insert (cf. figure 5.10 (left plot)). This halo has only been observed for

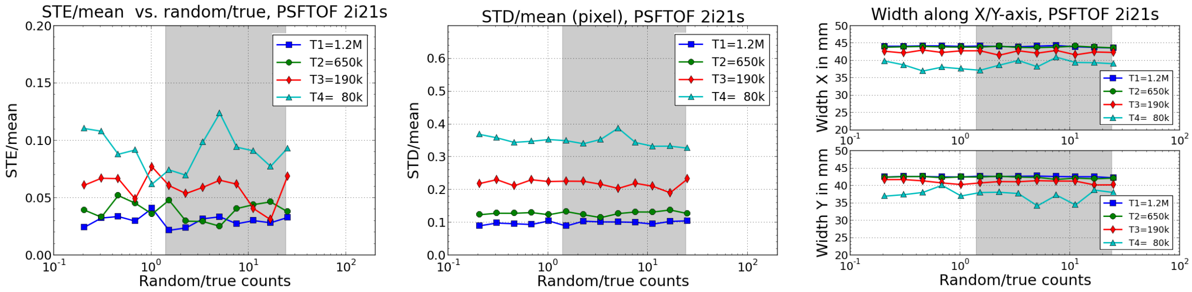

(a) Reproducibility (b) Image noise (c) FWHM fidelity

Figure 5.9: PSFTOF performance under varying statistical conditions in the simulated data without scatter contribution. Reproducibility (left), image noise (middle) and geometrical fidelity (right) are ruled by the number of true coincidences, but independent of the RF. Similar results have been retrieved for simulated data including scatter coincidences.

---

very small numbers (in the order of $100,000$) of true coincidences in the truncated measured data and appears over the whole range of investigated RFs, down to about 20%. Nevertheless, an enhancement of this halo with increasing RF at a fixed number of true counts has been found, as shown in figure 5.11. In the corresponding simulations with and without scatter coincidences, the activity halo at small RFs ($\approx$ 20%) was found to appear only in the presence of scatter. Consequently, the origin of this halo could be partially attributed to inaccuracies in the scatter correction, leading to a positive bias that is restricted to the volume of the water phantom and already appears at comparably small RFs. At high RFs, this bias will increase, such that also in the simulation without scatter coincidences the halo could be observed, although at a notably reduced level with respect to the simulation with scatter. Under the statistical conditions encountered in the original PET data (without truncation) of the late measurement frames, the observed halo thus has to be mainly attributed to the small number of true coincidences, but will be enhanced by the high random background. As shown in figure 5.11 a more pronounced halo has been observed for the OSEM algorithm compared to the PSFTOF reconstruction, while the activity build-up in the FOV outside the water tank has been found at a similar level. This can directly be explained by the previously observed higher sensitivity of the OSEM to an inaccurate scatter estimate, which translates to an increased positive bias within the water phantom, but not in the background where no scattering appears. For all investigated reconstruction algorithms, it has also been found that a larger number of iterations will result in an enhanced (larger mean value and standard deviation) halo within the water tank and in an enhanced background activity outside the phantom due to an increased bias by repeated iteration. The application of an absolute scatter correction (without scaling of the scatter simulation to the measured emission data) and/or more iterations of the underlying single scatter simulation could not reduce the observed halo within the phantom.

In terms of PET-based treatment verification, the spurious activity building up throughout the FOV can generally be neglected as the approximate position of the beam is a-priori known and the quantification in the irradiated area not affected. Also the observed activity halo in direct proximity to the actual activity distribution did not negatively affect the geometrical performance within this phantom study. For real patient data, however, the influence of scatter coincidences is

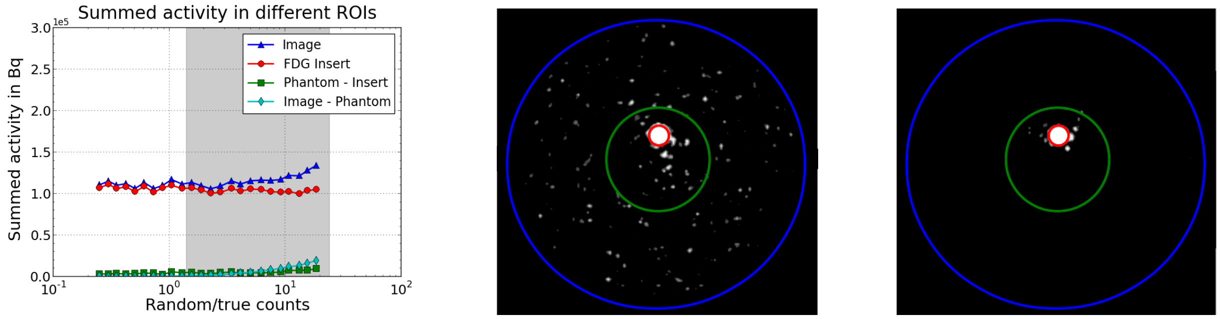

(a) T4 = 80k (b) T4 = 80k, RF = 0.94 (c) T4 = 80k, RF = 0.2

Figure 5.10: Summed up activity within different ROIs for the PSFTOF algorithm (2i21s). The integral image activity (blue ROI) increases with increasing RF at fixed true counts (left) and leads to spurious activity in the whole FOV (middle). This effect is not present at small RFs for the same number of true coincidences (right). Still, at small true numbers an activity halo builds up around the FDG insert (red ROI), but is restricted to the area of the water phantom (green ROI).

---

expected to be enhanced and single activity hot-spots within the halo might impede a thorough treatment verification if their activity level exceeds a certain threshold, e.g., used for beam range verification. Consequently, it is highly desirable to keep this halo as small as possible, which can be realised by applying the PSFTOF algorithm and only a small number of iterations.

5.2.3 Patient data: activity quantification, noise and range verification

In agreement with the observations made in the phantom imaging study, the mean activity within the selected ROIs was typically found to converge from higher to lower activity values when increasing the number of iterations in the reconstructions of the post-irradiation patient PET data. This is shown for one exemplary patient case (L2) in figure 5.12. It should be noticed that in the patient data analysis 24 subsets have been used for OSEM and PSF reconstruction, but 21 for the PSFTOF algorithm, as a consistent number of subsets (21 or 24) cannot be selected within the Syngo user-interface on the Biograph mCT scanner. In the phantom study, a consistent analysis was only allowed by direct usage of the underlying basic routines which are, however, not accessible for the standard user.

Figure 5.12 moreover illustrates that noise within the ROIs can significantly be reduced by performing less iterations and by including PSF modelling for less than 3 OSEM iterations, as observed in the previous phantom study. With respect to the currently clinically used setting with 3 iterations of the PSFTOF algorithm, it has been found that image noise can be reduced by $15-30\%$ in the investigated cases if performing only 1 iteration. The additional application of a larger post-reconstruction Gaussian filter could further reduce the noise by $10-25\%$. Comparing the originally used PET reconstruction settings (PSFTOF, 3i21s, gf5) with the proposed optimal settings (PSFTOF, 1i21s, gf8), an overall noise reduction by $25-50\%$ has been achieved. Figure 5.13 clearly illustrates the reduced image noise level for the exemplary patient case L2. At the same time, the patient data analysis proved that the overestimation of the irradiation-induced

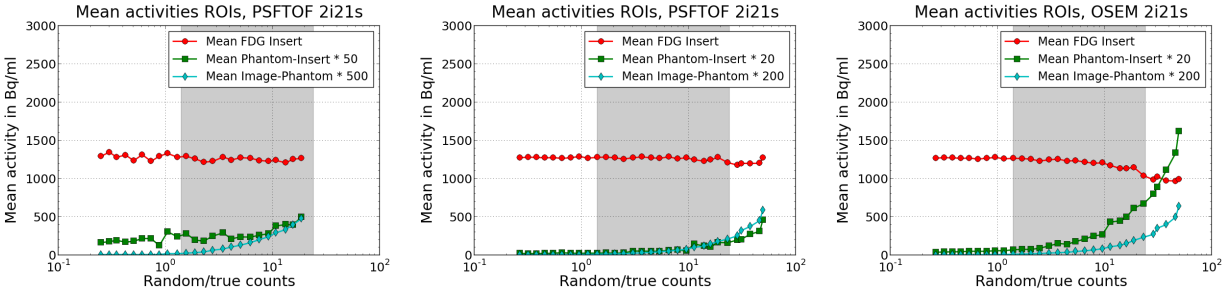

(a) Fixed true counts, PSFTOF (b) Original data, PSFTOF (c) Original data, OSEM

Figure 5.11: Analysis of the activity outside the FDG insert. An activity halo within the phantom, outside the FDG insert (green) is present down to small RFs in the truncated measured data at a fixed number of 80,000 true counts. The halo is enhanced by high RFs (left, note the higher scaling factors in the legend). In the original measured data, the halo is increased for the OSEM (right) with respect to the PSFTOF (middle), due to the higher sensitivity of the OSEM to inaccurate scatter estimates. Activity throughout the FOV, even outside the water tank (cyan), builds up additionally at high RFs at a similar level for different reconstruction algorithms.

---

activity at 1 iteration is typically smaller than $3-4\%$ with respect to the values retrieved after 10 iterations, similar to the findings of the phantom study. For the PSFTOF algorithm in particular, a variability of the mean ROI activity within the first 10 iterations between only 0.3 and 2.0% has been determined for the studied clinical cases, thus being even smaller than observed in the phantom imaging study. Considering the overall reproducibility of the determined mean activity (in the order of $2-10\%$ according to the phantom data analysis), the deviations between the different reconstruction algorithms (in the order of $1-9\%$) and the inaccuracies encountered by the washout modelling (estimated in the order of about $10-40\%$), the observed variability over different numbers of iterations is deemed to not be critical in the context of PET-based treatment verification.

A more important aspect for PET monitoring than absolute quantification is the verification of the particle beam range within the patient. Consequently, the most-likely-shift beam range verification algorithm, as described in section 3.4.4 and used for PET-based treatment verification at HIT, has been utilised to compare the original and the proposed optimal reconstruction scheme in terms of their geometrical performance in the four investigated patient cases. In particular, the enhanced Gaussian filter which reduces the image noise, but also the image granularity, has been verified to not impact the results of the range verification. Indeed, the enhanced filter (from 5 to 8 mm FWHM), as well as the reduced number of iterations (1 instead of 3), were found to lead to a small positive bias in the determined PET ranges with respect to the original settings. However, the mean range shifts were found to be in the same order as the corresponding uncertainties, not exceeding a size of 1.6 mm.

For verifying the correct application of the treatment, the reconstructed images need to be compared to an expectation, simulated on the basis of the TP-CT. In this context, the enhanced smoothing due to the proposed new reconstruction scheme had to be considered by an adaptation of the Gaussian filter applied to the calculated activity distribution according to equation 3.2. The size of the updated filter for post-processing of the simulation data has been retrieved on

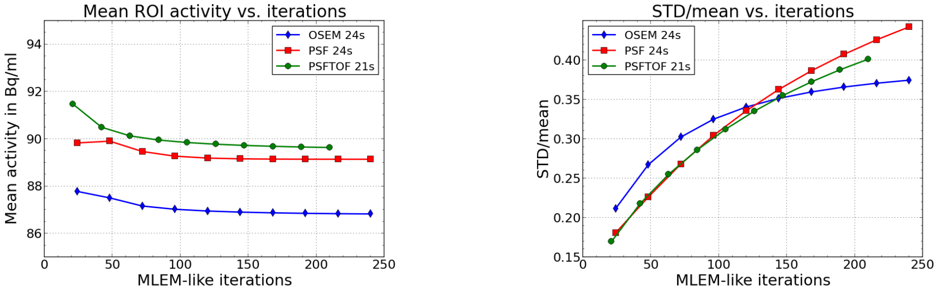

Figure 5.12: Activity quantification (left) and image noise (right) as a function of MLEM-like iterations for patient L2 and different reconstruction algorithms (OSEM (blue), PSF (red), PSFTOF (green)). The ROI mean activity only varies slightly for one algorithm (less than 2.0%), while the noise is significantly reduced for less iterations and when including PSF modelling.

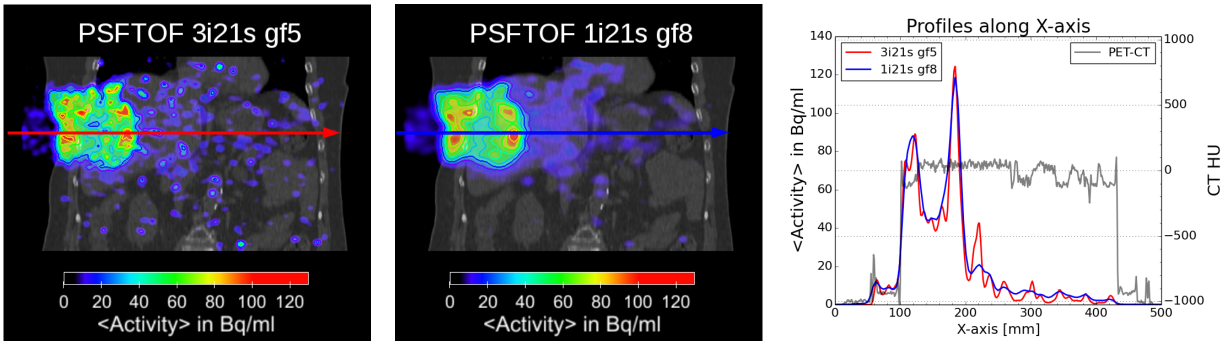

Figure 5.13: Comparison of original (left) and proposed optimised reconstruction settings (middle) applied to patient L2. While the structure of the activity pattern and the beam range is preserved, noise is considerably reduced by the new settings. This is confirmed in the profiles along the depicted red (original) and blue (optimised) arrows parallel to the beam direction (right).

the basis of high-statistics post-irradiation phantom data: it has been chosen such that it models the proximal increase of the activity at the edge of the irradiated phantom as retrieved by the regarded PET reconstruction. For the proposed new reconstruction scheme, the post-simulation Gaussian filter had to be increased from 7.1 to 8.5 mm FWHM. By this, the observed positive range bias due to the new reconstruction settings has been found to be partially compensated in the comparison of simulated and reconstructed measured data. Eventually, as depicted in figure 5.14 for patient L2, the most striking impact of the new reconstruction settings on the patient range verification has been identified as a considerable smoothing of the 2D range deviation maps. In all investigated cases, the determined mean range deviations between simulation and reconstruction agreed well within 1 standard deviation when comparing the old and optimised reconstruction scheme. All observed deviations with respect to the simulated expectation could be reliably detected, despite the reduced granularity. In two of the four cases, the reduced image noise could even lead to an enhanced agreement with the observed proximal CT contour differences, determined according to [Frey et al., 2014] (cf. figure 5.14).

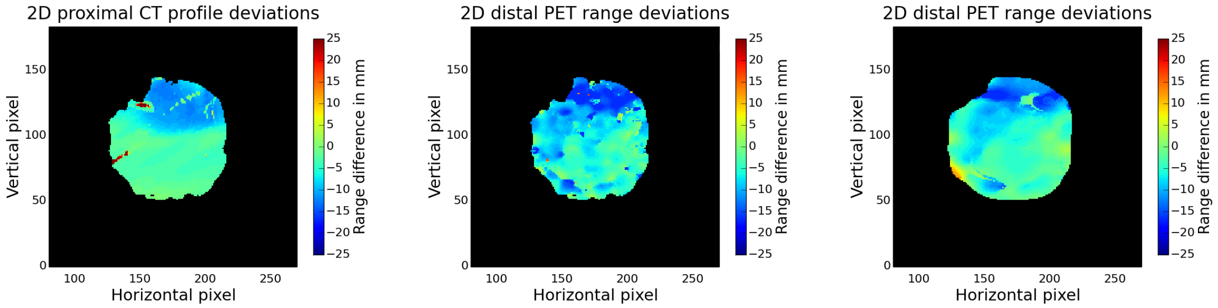

(a) TP-CT vs. PET-CT (b) Simu vs. measurement, old (c) Simu vs. measurement, new

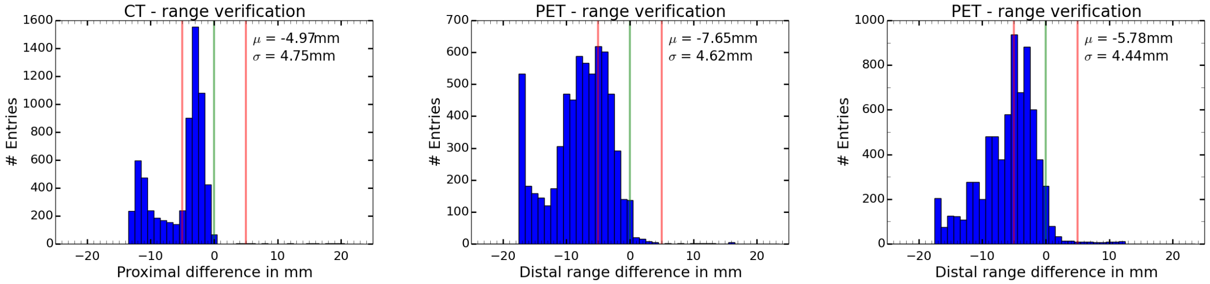

Figure 5.14: Comparison of the range verification for the old and the new reconstruction settings, as proposed in this work. The upper row depicts the proximal CT contour deviations (TP-CT vs. PET-CT, left) and the distal PET-based range deviations (simulation vs. measurement) in BEV as 2D colourmap (old settings: middle, new settings: right). The bottom row shows the corresponding range difference histograms, including their mean values and standard deviations. With respect to the old settings, the deviation map is considerably smoothed by the optimised settings and shows an overall enhanced agreement to the proximal CT shifts.

In conclusion, the applicability of the new reconstruction scheme (PSFTOF, 1i21s, gf8) to post-irradiation patient data could be demonstrated and has been found to enable a significant reduction of the image noise, representing one of the main challenges in PET-based treatment verification, while preserving activity quantification and ion beam range verification results. Moreover, the activity halo around the actual irradiation-induced activity pattern, which has been observed to be even more pronounced in clinical cases due to the more demanding scatter correction, has been found to be considerably reduced. In particular, activity hotspots outside the actual activity pattern that could potentially impede the beam range analysis can effectively be suppressed by the new reconstruction scheme (see figure 5.13).

5.3 Discussion and conclusion

Under the particular statistical conditions encountered in post-irradiation PET imaging, i.e., small numbers of true coincidences and high LSO-related RFs, the PSFTOF algorithm has been found to be the most suitable reconstruction option that is presently available on the Biograph mCT scanner. The algorithm enables accurate (less than 5% deviation from true value) and reasonably precise (mean error below 10%) PET imaging for PET-based treatment monitoring down to about 80, 000 true coincidences at 96% RF. Similar observations in terms of activity quantification at low counting scenarios with a Philips TOF PET/CT scanner have been reported in [Murray et al., 2010]. The standard OSEM approach, on the other hand, was found to fail below about 200, 000 true coincidences, which could be attributed to an overestimation in the scatter correction which appears at very small true numbers (in the order of 100, 000) and high random fractions (above 85%). Comparable conclusions have been drawn in [Cheng et al., 2010], though at different counting statistics for a different experimental set-up and PET scanner. Inclusion of TOF and PSF information makes the reconstruction less sensitive to inaccurate scatter estimates, and thereby results in an improved quantification under high RFs and small true numbers.

In the scope of the phantom study, it has also been shown that less iterations result in a small overestimation of the activity ($< 5\%$), but a significant reduction of the image noise and herewith an enhanced geometrical fidelity at small true counts rates. In the investigated clinical post-irradiation PET data-sets, the inaccuracy in activity quantification by using only 1 iteration was even found to be below 2%, which is not of concern for clinical applications as absolute quantification in PET-based treatment verification is challenged by larger uncertainties, e.g., in the modelling of the biological clearance. With respect to the originally used reconstruction settings at HIT (PSFTOF, 3i21s, gf5), which had been inspired from the typical nuclear medicine imaging settings, the proposed new reconstruction scheme (PSFTOF, 1i21s, gf8) enabled a reduction of the image noise by up to 50%. Despite the reduced image granularity due to the enhanced GF, the results obtained in the patient data range verification, and correspondingly the sensitivity to unexpected range deviations, were found to be preserved (except from the expected smoothing in the 2D range difference maps) or to be even improved in terms of an enhanced agreement to the observed differences in the patient anatomical contour due to the reduced image noise level and the more robust definition of relative activity thresholds in the range verification algorithm. As a consequence, the proposed new reconstruction settings have entered the clinical routine of PET-based treatment verification and are presently applied for the reconstruction of all post-irradiation PET data-sets at HIT, including those discussed in the context of 4D offline PET-based treatment verification in the following chapter.

In general, the main limitation in PET-based treatment verification has been identified in the small number of true coincidences, rather than in the high LSO random background. The phantom study clearly proved that image noise, reproducibility of the activity quantification and geometrical fidelity are determined by the number of true coincidences and only marginally affected by the amount of random background, if using the PSFTOF algorithm. Still, the high random background has been found to lead to the build-up of spurious activity clumped within the whole PET FOV, and herewith to an increasing integral image activity. This observation can be explained by the positive constraint in the underlying OP-OSEM algorithm, which does not allow for negative image values and thus leads to a positive bias in the reconstructed images [van Velden et al., 2009]. Further improvements in this aspect are foreseen by dedicated reconstruction algorithms, such as Negative(NEG)-ML [Nuyts et al., 2002; Grezes-Besset et al., 2007] and AB-OSEM [Byrne, 1998; Verhaeghe and Reader, 2010], which both allow for negative image values. Besides the build-up of spurious activity throughout the FOV, the encountered high RFs were found to slightly enhance the activity halo which has been observed within the water phantom for small true numbers (below about 100, 000). This halo was, however, found to be present even at small RFs and could thus be mainly attributed to an inaccurate scatter estimate at small true numbers, introducing the observed positive bias. While the comparably small background activity within the FOV can be neglected in PET-based treatment verification, where the approximate beam position is a-priori known, this halo in direct proximity to the irradiation-induced activity distribution might impact the patient data analysis if exceeding certain activity thresholds. In patient cases, inaccuracies in the scatter correction are even enhanced, thus requiring to keep the observed positive bias due to the inaccurate scatter estimate as small as possible (in terms of mean value and standard deviation). A reduction of this bias due to intra-reconstruction smoothing by implementing a scanner resolution model (PSF modelling) has already been reported in [Walker et al., 2011] and could be confirmed in the presented phantom imaging study. Moreover, it could be shown that a further decrease of the encountered halo is feasible by additionally including TOF information, which make the reconstruction more robust against inaccurate scatter estimates [Conti, 2011]. An unfavourable impact of the positive bias, once due to the inaccurate scatter correction within the phantom and once due to the high RF throughout the FOV, on the activity quantification in the analysed phantom geometry, emulating a typical patient-like activity pattern, has, however, not been observed for the PSFTOF algorithm.

In the scope of the thesis, the results retrieved in this chapter are of particular interest due to the generally reduced number of true coincidences in the pursued 4D gated PET image reconstruction with respect to 3D offline PET monitoring, which demands for a cautious characterisation of the PET scanner performance under extremely low numbers of true counts and high random fractions. Nevertheless, the obtained results are not only limited to the application of PET-based treatment verification in ion beam therapy, but might be translated to other emerging PET imaging fields at low counting statistics, such as dynamic PET imaging or PET-based ^{90}Y radio-embolisation treatment monitoring [Lhommel et al., 2010; Gates et al., 2011].

Chapter 6

First study on the feasibility of 4D offline PET-based treatment verification for HCC patients at HIT

After having studied the feasibility and potential of 4D offline PET-based treatment verification in dedicated moving phantom experiments under simplified conditions (regular motion, no washout, relatively high counting statistics) in chapter 4, this chapter will present the first application of 4D PET-based treatment monitoring to clinical cases. As a prerequisite, the studies described in chapter 5 showed that reasonably accurate PET imaging down to very low numbers of true coincidences at high random fractions is feasible with the used commercial full-ring TOF PET/CT scanner, and identified the reconstruction algorithm and parameters which are ideally suited to these statistical scenarios. Aim of this chapter is to infer the feasibility and potential advantages of considering organ motion in offline PET-based treatment monitoring under clinical conditions.

6.1 Material and methods

6.1.1 Patient cohort and data acquisition

In total, four different HCC patients, L1 to L4, with respiratory-motion affected target volumes in the liver have been investigated for this purpose. All patients have been included in the clinical trial *PROMETHEUS* [Combs et al., 2011] and treated according to the strategy described in section 2.6.5 (irradiation in four fractions of 8.1 Gy(RBE) on the basis of a 3D TP-CT with increased ITV margins derived from a contrast-enhanced 4D CT scan). For patients L1 to L3 motion has been mitigated by an abdominal compression system, for patient L4 by a gated beam delivery. The mean motion amplitudes within the CTVs, as retrieved from a deformable image registration (DIR) of the end-exhale and the end-inhale 4D CT phases, are given in table 6.1. In all cases, motion was found to be pronounced in the SI direction, with a mean amplitude between about 2 and 14 mm. For the gating patient L4, a reduced SI motion amplitude of 5.2 ± 1.4 mm within the applied 50% gating window around end-exhale has been determined.

Moreover, table 6.1 depicts the irradiation times and time delays between the end of the irradiation and the start of the subsequent PET scan for the treatment fractions that have been investigated in the scope of this chapter. The specific workflow for HCC patient post-irradiation PET monitoring follows the description in section 3.4.3: patients have first been immobilised including vacuum mattress, arm holder and abdominal compression at the PET/CT room prior to the irradiation (see figure 6.1). After a 3D position verification CT, patients have been transferred to the treatment room by a dedicated shuttle system, irradiated and transported back to the PET/CT room without re-positioning. During the subsequent 30 min PET LM data acquisition, as well as during the irradiation, the patient respiratory motion has continuously been monitored by the ANZAI respiratory gating system, thus enabling a first coherent verification of the applied treatment under consideration of the target movement. For patients L1 and L2, an additional 4D CT, in the following referred to as 4D PET-CT, has been acquired after the irradiation at the PET/CT scanner for clinical comparison to the 4D treatment planning CT (4D TP-CT).

6.1.2 PET image reconstruction

The acquired PET LM data, containing between 400, 000 and 900, 000 true coincidences (see table 5.1), have been reconstructed statically (3D) with the PSFTOF algorithm, using 1 iteration with 21 subsets and an 8 mm post-reconstruction Gaussian filter, following the findings of chapter 5. In addition, based on the ANZAI gate-tags in the recorded LM files, 4D gated PET images with 8 motion states have been reconstructed using the same parameters. In all cases, the recorded PET data has been corrected for attenuation on the basis of a free-breathing 3D AC CT and for scatter coincidences.

In order to obtain one single, motion-compensated PET image in a user-defined reference phase, a dedicated workflow had to be established, as the Biograph mCT scanner, up to present, does not allow for such a procedure. First, a phase-correlation between the phase-sorted 4D gated PET and the relative-amplitude-sorted 4D PET-CT (cf. section 3.4.3) had to be established. For this, an average breathing cycle of the patient on the basis of the acquired ANZAI signal during the 30 min PET acquisition has been calculated (see figure 6.1), and was used to determine the mean

Table 6.1: Overview of the investigated HCC patient cohort. The motion amplitudes in SI, AP and LR direction are given as mean value within the patient-specific CTVs. Moreover, the irradiation times and time delays between the end of the irradiation and the start of the PET scan (t_{irr} and Δt) for the analysed treatment fractions (Fx) of each patient are shown.

Patient	CTV	SI [mm]	AP [mm]	LR [mm]	Fx	t_{irr}[min:sec]	Δt[min:sec]
L1	1	1.8 ± 0.9	0.3 ± 0.2	0.0 ± 0.1	2	29:03	12:03
	2	9.1 ± 1.1	2.2 ± 0.3	0.2 ± 0.1			
L2	1	9.4 ± 3.7	3.2 ± 1.2	1.2 ± 0.6	3	05:48	08:09
L3	1	13.7 ± 3.3	7.5 ± 2.8	4.0 ± 1.4	1	07:17	11:39
					3	08:03	10:10
L4	1	7.4 ± 1.9	3.4 ± 0.8	0.4 ± 0.5	1	43:50	13:17
Within GW		5.2 ± 1.4	3.0 ± 0.8	0.7 ± 0.5			

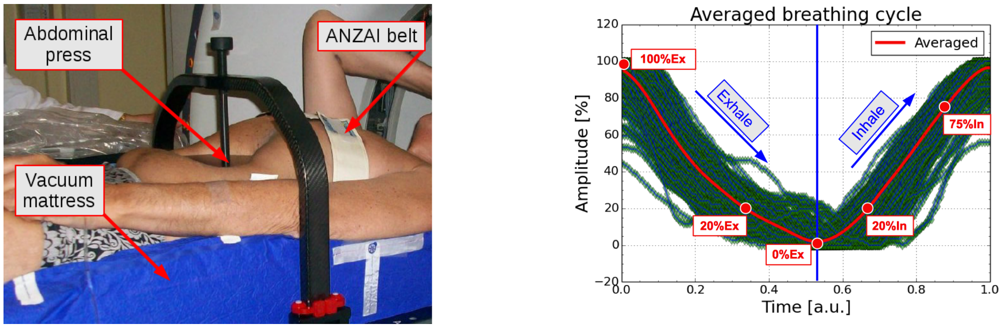

Figure 6.1: Patient set-up (left) and calculation of the average breathing cycle (right). All patients have been fixated in a vacuum mattress and motion has been mitigated by an abdominal press for patients L1 to L3. During the irradiation and the subsequent PET acquisition, motion has been monitored by the ANZAI gating system. The signal acquired during the 30 min PET scan (right, green) has been used for calculating the patient-specific averaged breathing curve (right, red), required for generating the motion-compensated 4D PET image. The reference motion states used in the analysis of the four investigated liver patients are moreover depicted by the red circles. Maximum inhalation corresponds to 100%, maximum exhalation to 0% relative amplitude.

relative motion amplitudes within each of the 8 reconstructed PET phases. The corresponding 4D PET-CT has been reconstructed at exactly the same amplitudes, thus yielding two coherent 4D data-sets. The single phases of the 4D PET-CT have then been registered to a chosen reference phase by a DIR with the open-source registration code *Plastimatch* [Shackleford et al., 2010], which has also been used for determination of the mean CTV motion amplitudes in table 6.1. The result of the DIR is a motion vector containing the 3D displacement for each individual image voxel between the two registered images. The retrieved motion vectors could thus be used to warp the single PET phases to the chosen reference phase, where they have eventually been summed up and divided by the number of phases in order to form the aimed motion-compensated 4D PET image. Using the corresponding 4D PET-CT and the DIR-based *motion-model* of the patient, the retrieved motion-compensated 4D PET image might be warped to any other motion state, as well.

An indispensable prerequisite for creating the motion-compensated 4D PET image is, however, the availability of the 4D PET-CT raw data in order to enable the reconstruction of the 4D PET-CT at exactly the same amplitudes as the phase-based 4D gated PET. Hence, the generation of a 4D motion compensated PET image has not been feasible for patients L3 and L4.

6.1.3 4D dose and activity calculation

Besides the reconstructed PET images, PET-based treatment monitoring demands a prediction of the expected irradiation-induced activity within the patient for comparison. Up to present, the SimInterface environment (cf. , section 3.4.4) only allows for calculating 3D dose and activity distributions on the basis of a 3D CT (either the 3D TP-CT or the registered 3D PET-CT) and the patient-specific RTplan file. Consequently, the SimInterface capabilities had to be extended in the scope of this work in order to enable the handling of 4D CT and 4D RTplan data and to calculate

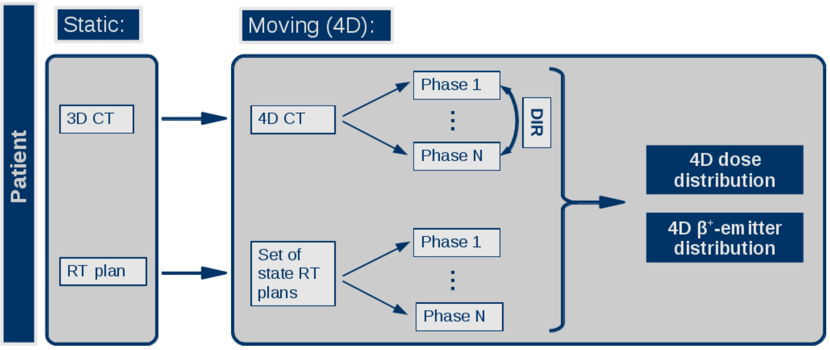

Figure 6.2: Illustration of the 4D extension of the SimInterface. Instead of a 3D RTplan and a 3D CT image, a 4D CT with N motion states and a set of N corresponding state RTplan files have to be used for dose and activity calculation. The different motion states are connected by a DIR, which eventually allows for calculating a prediction of 4D dose and β^+-emitter distribution in the patient.

---

the expected physical dose and activity distributions within the patient under consideration of the organ motion. This is schematically illustrated in figure 6.2: instead of a single 3D CT and the corresponding RTplan, the 4D activity and dose simulations have to be based on a series of N phases from a 4D CT, representing the different motion states of the patient, and the corresponding set of state RTplans covering each of the considered 4D CT phases.

The required set of state RTplan files has been generated in the same way as described in section 4.1.1.3, namely by the TRiP4D software on the basis of the synchronised beam delivery sequence and the recorded respiratory motion signal during the patient irradiation. For coherence with the underlying 4D CT data of the performed calculations, the generation of the state RTplan files had to be based on relative amplitude-sorting (cf. section 3.4.3), as well.

In analogy to the approach followed by [Richter et al., 2013] for analytical 4D dose calculations, the physical dose, as well as the β^+-emitter distribution, have been simulated for each single motion state on the basis of the corresponding 4D CT phase and state RTplan, using the FLUKA MC code. In order to calculate the total 4D physical dose in a user-defined reference motion state, chosen such that it exhibits approximately the same respiratory amplitude as the 3D TP-CT, the physical dose of all single phases have been warped to the reference phase and summed up. The warping is based on a DIR of all regarded 4D CT phases and the chosen 4D CT reference phase. Quality and accuracy of the required DIR have been investigated in [Richter et al., 2014] for exactly the same registration settings of the *plastimatch* software that have been used in this work. Based on the *inverse consistency error*, an accuracy of few millimetres for the applied DIR has been reported. Due to the non-linear dependence of the biological dose on the physical dose, 4D biological dose distributions could not be obtained by warping and summing up the single-phase biological dose. Instead, the additionally simulated α and β values [Mairani et al., 2010], characterising the biological response of the tissue to the incident irradiation, would have to be used in a future extension of the SimInterface to allow for 4D biological dose calculations. However, this was deemed beyond the scope of this work, where calculations of the 4D activity distributions to be expected within the patient are of main interest. For this, the simulated β^+-emitter distributions in each of the considered single motion phases have been post-processed according to equation 3.2. In particular, this means that the washout modelling has been calculated individually for each motion phase on the basis of the corresponding 4D CT phase in order to avoid inaccuracies introduced by a previous warping to the reference phase. Due to the comparably short respiratory period, typically in the order of about $3-4\,\mathrm{s}$, with respect to the irradiation and transportation time, all phases have been post-processed by exactly the same time parameters (cf. table 6.1), introducing an error of below 0.5% in the calculated amount of activity for all investigated cases. The readily post-processed activity distributions of the single phases have eventually been warped to the given reference phase, using the 4D CT-based DIRs, and summed up to form the 4D activity distribution expected to be measured within the patient. This expectation has then directly been compared to the post irradiation PET image reconstruction (static, or motion-compensated) of the measured data in order to infer the quality of the applied treatment under consideration of the target motion.

Within the implemented extension of the SimInterface, the described 4D physical dose and activity calculations can be carried out on the basis of 4D TP-CT data, as well as of post-irradiation 4D PET-CT data, which, however, need to be registered rigidly to the reference 3D TP-CT prior to the simulation. In analogy to the patient alignment by orthogonal X-ray imaging prior to irradiation in the treatment room, this registration has to aim at matching the bony patient anatomy in the TP-CT and PET-CT data, rather than the surrounding soft tissues or patient contours.

For comparison of 3D as well as 4D calculated and measured activities, synchronous 2D visualisation of CT and PET data, 1D profile comparison along the beam axis and 2D verification of the beam range in BEV by the most-likely shift approach [Frey et al., 2014], as described in section 3.4.4, have been utilised.

6.2 Results

6.2.1 Patient L1

The results of the activity calculations for patient L1 in 3D, using the static RTplan and the 3D TP-CT, as well as in 4D, using the generated set of state RTplans and the 4D TP-CT, are compared to the static (3D) reconstruction of the recorded PET LM data after the second treatment fraction in figure 6.3. The 4D simulation is given in the reference phase of 0% exhale (cf. figure 6.1), being closest to the respiratory phase of the 3D TP-CT.

For calculated and measured activity distributions, a characteristic crescent shape close to the distal edge of the irradiated PTV has been noticed. This observation can be explained by the subsequent irradiation of iso-energy layers with increasing energies, the typically larger number of particles applied to the most-distal slices and to the characteristic shape of the dominating ^{11}C activity depth profile, which exhibits a maximum close to the primary beam range. Altogether, this leads to an enhancement of the irradiation-induced activity at the distal edge. The sequential irradiation of iso-energy layers also explains the observed lower activity within the smaller CTV 2 in the measurement with respect to the simulation: due to the more proximal position, the smaller CTV 2 had been irradiated several minutes before the irradiation of the second, larger CTV 1 has been completed. Consequently, by assuming the same delay time between irradiation and PET imaging for both, the activity in CTV 1 is overestimated in the expectation. Future extensions of the underlying PET simulation workflow might account for this by taking into

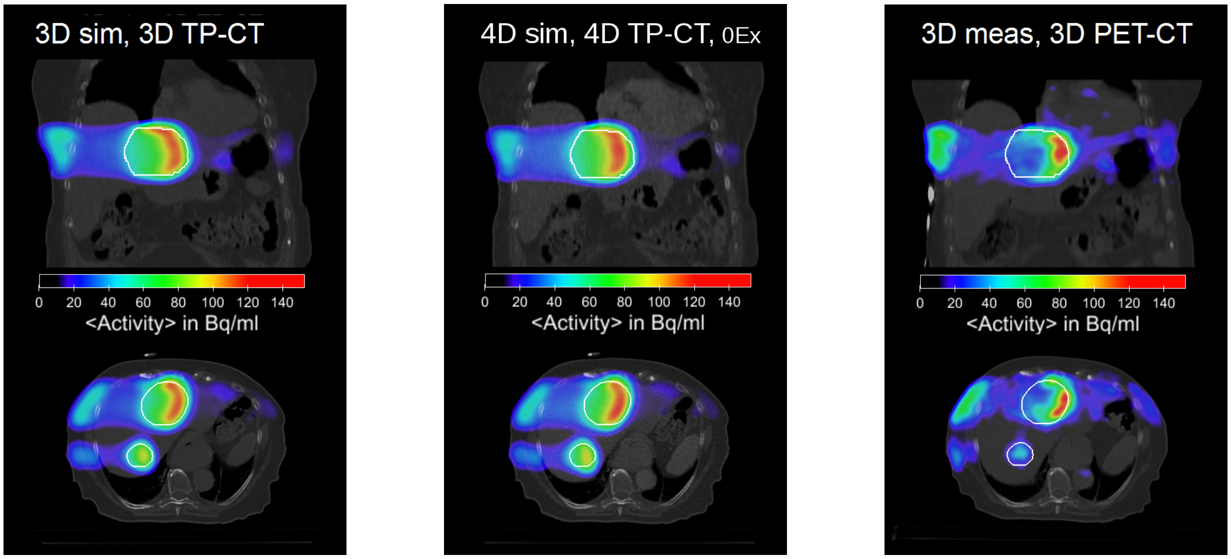

Figure 6.3: 2D activity distributions (colour-wash), corresponding CTs (grey-scale) and PTVs (white contours) for patient L1. The static simulation (i.e., 3D RTplan on 3D TP-CT) is shown on the left and compared to the 4D simulation (state RTplans on 4D TP-CT, reference phase 0% exhale) in the middle and to the static reconstruction of the acquired PET data on the right. An overall good agreement of simulated and measured data has been found. The relatively small SI motion amplitude (1.8 mm for the larger CTV 1) was found to result in only a slight distortion of the calculated activity.

consideration the exact irradiation and delay times for each individual energy slice, but have not been available at the time of this work.

Still, an overall good agreement of 3D calculated expectation and 3D measurement has been found for patient L1. The observed remaining differences can mainly be attributed to inaccuracies in the washout modelling of the irradiation-induced activity, to the considerable image noise, even in the 3D PET reconstruction using the optimised parameters, and to possible inaccuracies in the PET scatter correction, which might lead to an enhanced activity outside the PTV as has been observed in the phantom imaging study presented in chapter 5. In terms of the PET-based range verification, on average only a small, clinically not relevant, deviation between 3D measurement and 3D simulation of below 2 mm has been found. Still, in some part of the irradiation field, an over-range of about $5 - 20$ mm in the measurement has been observed. This was attributed to similar deviations in the proximal CT contour due to a slight mis-positioning of the patient (see figures 6.4 (a) and (b)).

When comparing the 3D and 4D calculated activity distributions, only a slight distortion of the induced activity has been identified, mainly visible in the coronal plane. With respect to the measured data, an improved agreement of 3D or 4D simulation has not been observed. Particularly in terms of the PET-based range assessment, deviations between 3D and 4D simulation were found to be not significant, exhibiting only an almost constant shift by about 1.4 mm of the 4D simulation towards smaller depths, due to the applied contrast agent, which leads to globally enhanced HU values in the 4D CT images (cf. figure 6.4 (c)). The overall negligible impact of the tumour motion for this patient is directly related to the very small motion amplitude of only

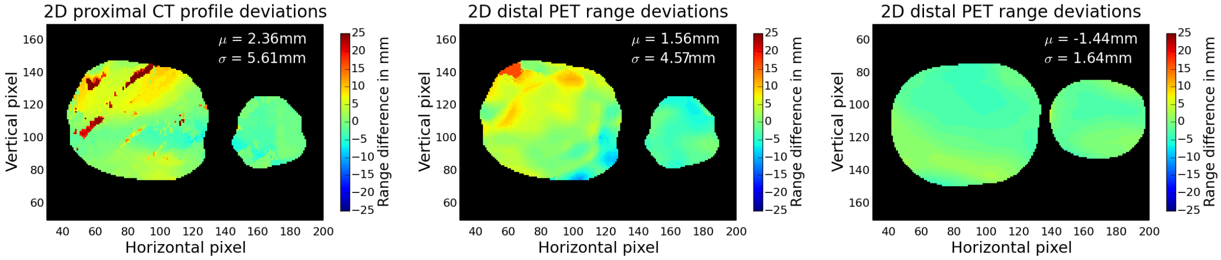

(a) 3D TP-CT vs. 3D PET-CT (b) 3D sim vs. 3D meas. (c) 3D sim vs. 4D sim

Figure 6.4: Results of the range verification for patient L1. The observed distal PET range deviations between 3D reconstruction of the measured data and 3D simulation (middle) were found in relatively good agreement with the deviations between TP-CT and PET-CT in the proximal patient contour (left). Range differences between 3D and 4D activity prediction (right) were found to be minor. The systematically smaller range in the 4D simulation is attributed to the applied contrast agent, resulting in overall increased HUs in the 4D CT images with respect to the native 3D CT.

about 2 mm in the SI direction for the larger CTV 1. This was additionally confirmed by the 4D physical dose calculations on the basis of the 4D TP-CT, as well as by additional 4D physical dose and activity simulations on the basis of the 4D PET-CT acquired after the discussed treatment fraction. None of these data showed a considerable influence of the small target motion, such that it can be concluded that a 3D post-irradiation verification is sufficient for this kind of patient. A gain of knowledge by including organ motion to the post-irradiation treatment monitoring workflow could not be found.

Nevertheless, it should be remarked that interplay patterns have been found in the 4D physical dose calculation within the smaller CTV 2, which is subject to a considerably larger motion amplitude (cf. table 6.1). In the 4D activity simulation, however, the observed interplay pattern has been observed to be smeared for the most part by the limited PET resolution, modelled by a post-simulation Gaussian filter, and thus to be not detectable in the reconstructed image of the measured data, which is moreover significantly obstructed by the extremely low amount of activity within CTV 2, as can be seen in figure 6.3.

6.2.2 Patient L2

The investigated activity distributions for the second liver patient, L2, are shown in figure 6.5: besides the 3D simulation on the 3D TP-CT and the 4D simulation on the 4D TP-CT, the 3D and 4D simulations of the irradiation-induced activity distributions on the 3D and 4D PET-CT, respectively, are depicted as well as the 3D (static) and 4D (motion-compensated) reconstructed PET images. All 4D data-sets are displayed in the 75% inhale phase (cf. figure 6.1), which has been found to best match the respiratory state of the 3D TP-CT.

As can be seen in the comparison of 3D and 4D simulation data, the considerable SI motion amplitude of above 9 mm for this patient leads to the formation of a clearly visible interplay pattern, namely two separate activity hotspots in the distal region of the homogeneously irradiated PTV (cf. red arrow in figure 6.5). This pattern could clearly be identified in the corresponding PET measurement after the second treatment fraction, as well. Although the induced

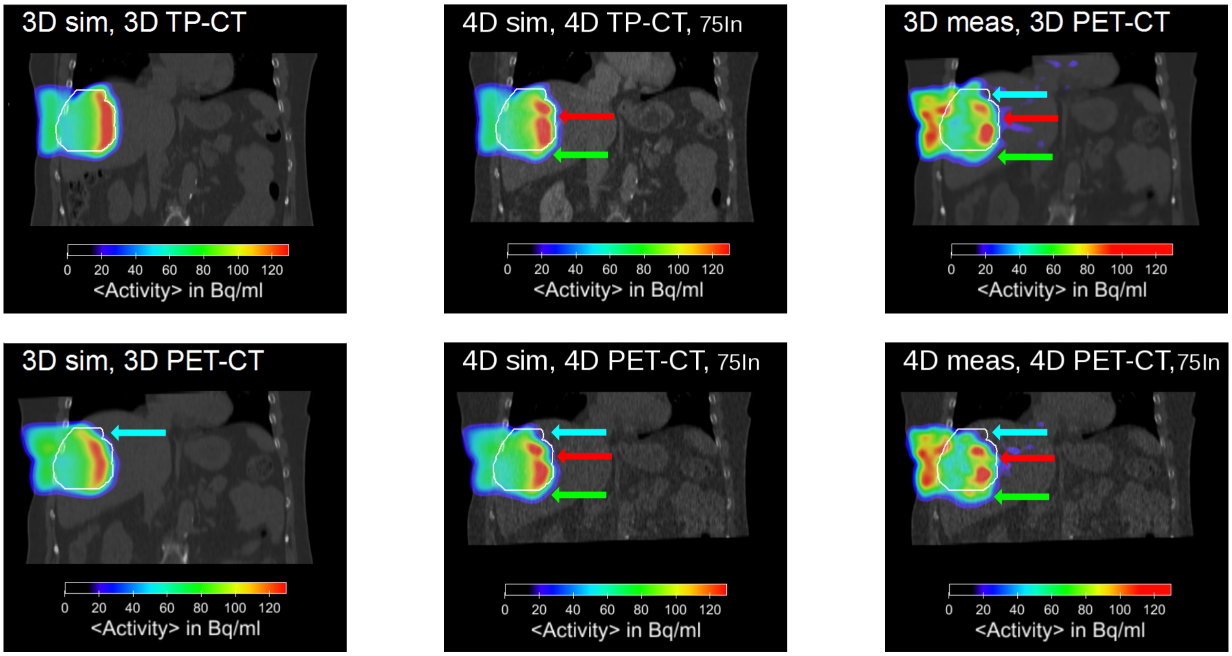

Figure 6.5: 2D activity distributions and corresponding CTs for patient L2. The 3D and 4D activity calculations on the basis of the 3D and 4D TP-CT, respectively (top row, left and middle), are compared to the 3D and 4D simulations on the basis of the 3D and 4D PET-CT data (bottom row, left and middle) and the measured data after the second treatment fraction reconstructed in 3D (top, right) and motion-compensated in 4D (bottom, right). Due to deviations in the absolute activity quantification, a different scaling of the color-wash display has been applied to the measured data. All 4D data-sets are given in the 75% inhale phase. Consideration of organ motion introduces a visible interplay pattern in the distal PTV region (red arrow) and a slight caudal shift of the calculated activity distribution (green arrow), which can be identified in the measurement, as well. The PET-CT-based calculations exhibit a shorter range, particularly in the cranial part of the PTV (light blue arrow), due to changes in the patient external contour, and match more accurately the measurement.

interplay effects could be recovered with reduced blurring in the SI direction by the 4D motion-compensated image reconstruction of the measured data, a notably enhanced agreement to the 4D simulations with respect to the static PET reconstruction has not been found. Besides, the motion-compensated reconstruction is subject to additional uncertainties by the required DIR and, in particular, by the enhanced level of uncertainty in the underlying single-phase PET images, which suffer from a reduced (by a factor of 8) number of true coincidences. Unfavourable effects, such as an increased activity outside the irradiated area due to inaccuracies in the scatter correction (as shown in the previous chapter), are hence expected to be enhanced in the 4D PET image with respect to the 3D PET image. Consequently, an advantageous performance of motion-compensated 4D gated PET imaging in the context of post-irradiation treatment verification could not be conclusively demonstrated for this patient.

Besides the motion-related interplay effects, the irradiation-induced activity has also been found to be slightly shifted towards the caudal direction in the 4D simulations with respect to the static calculations (for the TP-CT and for the PET-CT data), as indicated by the green arrow in figure 6.5. This finding can be attributed to the fact that the 3D TP-CT, on which the actual 3D RTplan has been optimised, represents a motion state close to the maximum inhale. Consequently, during the irradiation, the liver is located in a more cranial position most of the time, and the activity is induced further caudal in the depicted 75% inhale reference phase than actually planned on the 3D TP-CT. In a similar way, this caudal shift with respect to the static simulations has been observed in the corresponding PET measurement. Overall, the 4D activity calculations were found to be in a notably better agreement with the acquired post-irradiation data than the 3D simulations, thus demonstrating the potential advantages of considering organ motion at least in the calculation of the expected activity distributions for offline PET-based treatment monitoring.

However, although the shape of the activity distribution in simulated and measured data was found in reasonably good agreement, a limited accuracy in terms of absolute activity quantification has been observed for this patient. While the measured activity is typically about $10-20\%$ higher in the fatty tissue close to the patient skin, it is approximately $10-40\%$ smaller in the distal part of the PTV. This level of inaccuracy is clearly above the expected uncertainties in the simulation of the induced β^+-emitter distribution. Also in terms of activity quantification by the PET/CT scanner, where additional uncertainties with respect to the static imaging study discussed in chapter 5 might be introduced by the comparably large motion amplitude in the PTV region, inaccuracies of below 10% are expected (based on the results of the *LineMult* phantom irradiation study in section 4.1.2.3 at a comparable number of true coincidences and an even enhanced motion amplitude and level of inhomogeneity of the induced activity pattern). As a consequence, the observed deviations are mainly attributed to inaccuracies in the modelling of the biological washout when post-processing the simulated data. In comparison, considerably smaller deviations in the absolute activity, concerning particularly the ratio of induced activity in the subcutaneous fatty tissue and the distal region of the PTV, have been found for patient L1 (cf. figure 6.3), which suggests a high inter-patient variability of the biological clearance. Up to present, this is not considered in the applied washout model, which relies on the same set of tissue washout parameters (fraction of the slow biological decay component and biological decay constant) for every patient.

When comparing the simulations based on the TP-CT and the PET-CT data, a considerably reduced range in the cranial part of the PTV has been observed for the simulations on the PET-CT data (cf. light blue arrow in figure 6.5). This shorter range has been found to be in better agreement with the reconstructed measured data, as can also be seen from the 2D range deviation maps in figure 6.6: while the measured data shows a considerably reduced range with respect to the 3D TP-CT simulation in the cranial PTV region (blue areas in figure 6.6 (b)) and an average distal PET range deviation of almost 6 mm, a considerably improved agreement to the measurement is provided by the 3D PET-CT simulation, exhibiting an average deviation of below 1 mm. This finding can directly be explained by the observed differences in the patient CT contour between the 3D TP-CT and the 3D PET-CT (figure 6.6 (a)), which provoke the observed differences in the 3D TP-CT simulation with respect to the post-irradiation PET acquisition. Comparing the PET-based ranges deduced from 3D and 4D simulations, very small differences have been found for the investigated TP-CT data, except from a constant shift of the 4D simulation by about 1 mm to smaller depths due to the already mentioned injected contrast agent. For the PET-CT data, the mean range difference between 3D and 4D simulations is even smaller (0.2 mm), as no contrast agent has been applied. However, in the most cranial part of

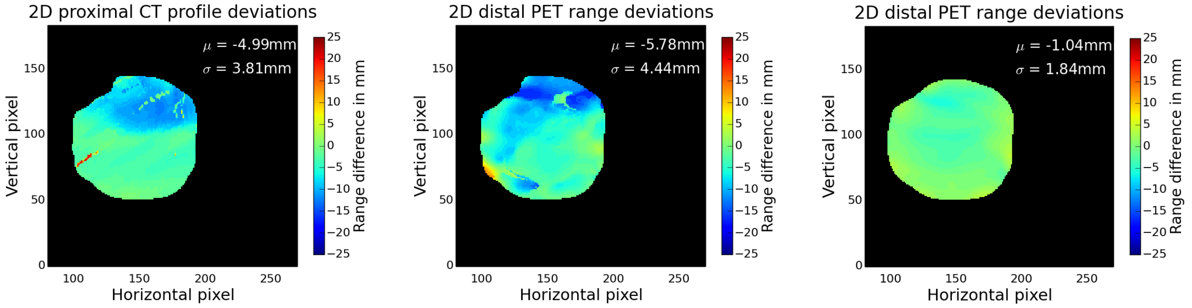

(a) 3D TP-CT vs. 3D PET-CT (b) 3D TP-CT sim vs. 3D meas (c) 3D sim vs. 4D sim, TP-CT

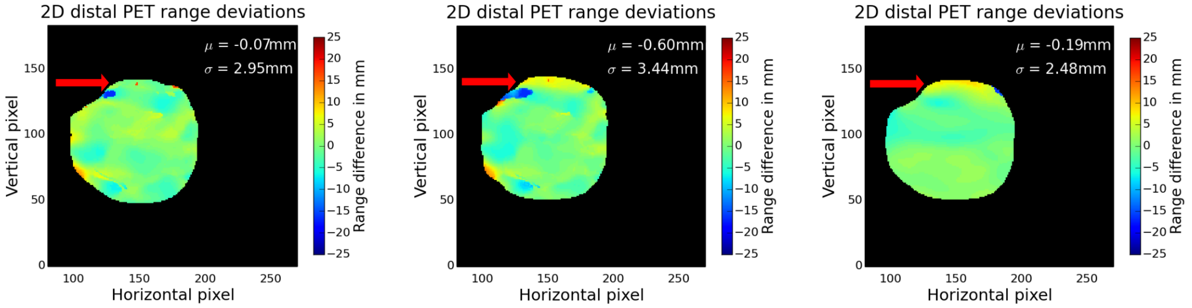

(d) 4D PET-CT sim vs. 3D meas (e) 3D PET-CT sim vs. 3D meas (f) 3D sim vs. 4D sim, PET-CT

Figure 6.6: Results of the range verification for patient L2. In comparison to the 3D TP-CT simulation (top, middle), the 3D PET-CT simulation exhibits notably less deviations with respect to the measured data (bottom, middle), as these have mainly been attributed to differences in the proximal patient CT contour (top, left). Differences between 3D and 4D simulations are overall small for the TP-CT (top, right), as well as for the PET-CT (bottom, right) data-sets. Still, the 4D PET-CT simulation has been observed to best agree with the measurement (bottom, left) due to an enhanced PET-based range in the cranial PTV region (indicated by the red arrow).

the PTV (indicated by the red arrow in the bottom row of figure 6.6), a $5 - 10\,\mathrm{mm}$ higher range of the 4D simulation has been identified, leading to an further improved agreement with the measured data (figure 6.6 (d)). Still, due to the relatively central position of the lesion within the homogeneous liver tissue, respiratory motion generally only results in small changes of the WEPL and herewith of the particle beam range, in agreement with the findings for patient L1. Eventually, it should be mentioned that when using the 4D motion-compensated reconstruction of the measured data, a generally increased level of uncertainty in the determined PET range deviations, corresponding to a notably increased inhomogeneity of the retrieved 2D range deviation maps, has been encountered. Moreover, a slightly reduced agreement to the 4D PET-CT simulation (mean range deviation approximately 1.5 mm) has been observed. This finding should, however, be handled with care due the previously discussed increased level of uncertainty in the motion-compensated image on the basis of a gated 4D PET image reconstruction of the acquired data.

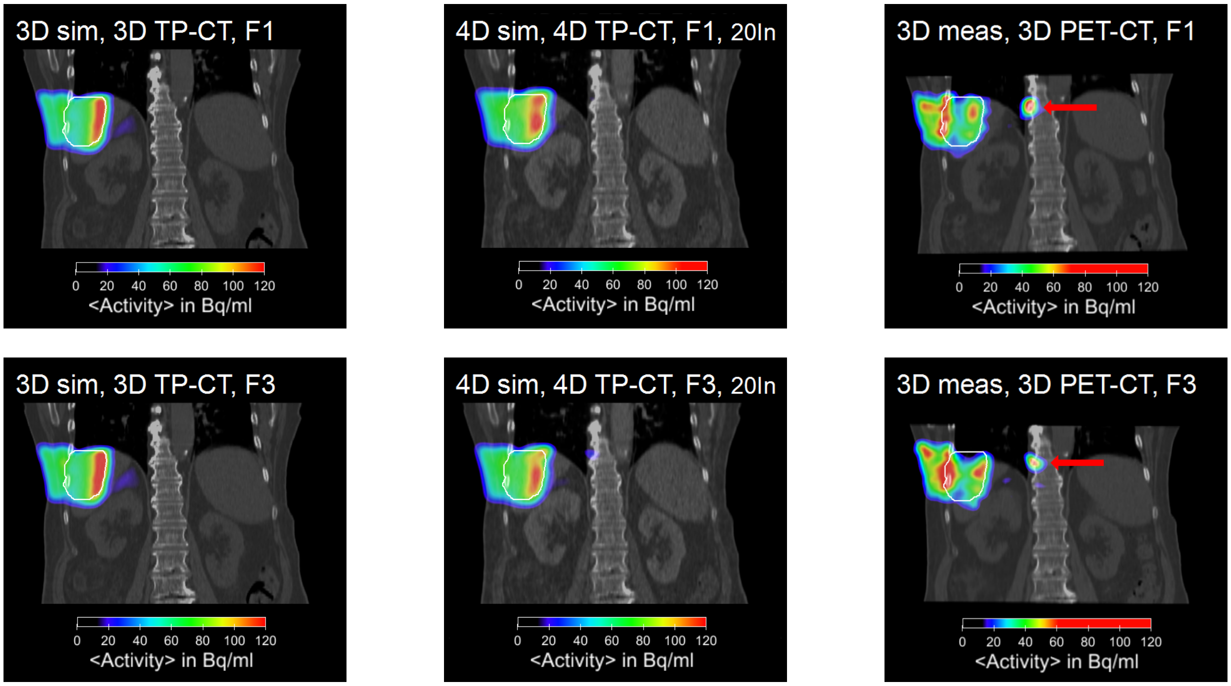

Figure 6.7: 2D activity distributions and corresponding CTs for patient L3. The 3D TP-CT simulation, post-processed according to the timing structures of fractions one (top, left) and three (bottom, left), is compared to the 4D TP-CT simulations (depicted in the 20% inhale reference phase) on the basis of the state RTplans of fraction one (top, middle) and fraction three (bottom, middle), as well as to the corresponding measurements after fraction one (top, right) and three (bottom, right). Due to differences in the absolute amount of induced activity, a different scaling has been applied to the measured data. The 4D simulations exhibit a notable interplay pattern, which has, however, been found to be hardly detectable in the corresponding measured data which suffer from high image noise due to the low counting statistics. An activation of the vertebral bone that has been observed in both measurements (red arrow) could not be reproduced by the 4D TP-CT simulations.

6.2.3 Patient L3

The activity distributions considered in the analysis of patient L3 are shown for a central coronal plane through the irradiated PTV in figure 6.7. The 3D simulation on the basis of the 3D TP-CT, post-processed according to the timing structure of the first (F1) and the third treatment fraction (F3), is compared to the 4D TP-CT simulations (depicted in the 20% inhale reference phase) using the state RTplan sets of fraction one and three as well as to the corresponding 3D PET images acquired after the respective fractions. A simulation based on the fraction-specific 4D PET-CT data and the generation of a motion-compensated 4D PET image have not been feasible for this patient, as no post-irradiation 4D CT scan has been acquired.

In the comparison of 3D and 4D activity calculations, the relatively large SI motion amplitude of approximately 14 mm (see table 6.1) has been found to lead to the formation of motion-related interplay patterns in the distal region of the PTV, in agreement with the findings for patient L2, who was subject to a comparably large SI motion. Comparing the 4D calculations on the basis of the two considered state RTplan sets of fractions one and three, clear differences due to inter-fractional variations in the irregular respiratory motion of the patient have been noted. In general, a higher fraction of the irradiation-induced activity has been found in a further caudal location in the 4D simulation of treatment fraction three.

This slight caudal redistribution has also been observed in the corresponding 3D PET images acquired after the two regarded treatment fractions. In general, however, a very limited agreement of measurement and simulation has been found for patient L3. Due to the (by about 30%) reduced number of true coincidences for patient L3 with respect to patient L2, a considerably enhanced image noise level has been encountered, which particularly limits the detectability of motion-related interplay effects within the irradiated PTV. Although differences in the interplay patterns after fractions one and three are visible in the simulated data, an identification of the calculated interplay patterns and a clear distinction between the two fractions on the basis of the two reconstructed 3D PET images was found to not be feasible. Further challenges are posed by the strongly limited accuracy of the isotope washout modelling: while an agreement within about 10% between measurement and calculated expectation in the subcutaneous fatty tissue has been determined, the calculated activity in the PTV was found to be about twice as high as in the measured data, hinting on a significant underestimation of the biological clearance, even if considering an increased level of uncertainty in the activity quantification by the PET/CT scanner in the presence of organ motion. Particularly in the caudal region of the PTV, a strong isotope washout has been observed in both PET measurements, resulting in a further degradation of the ability to detect the expected interplay patterns.

Nevertheless, another motion-related implication could clearly be recovered in the measured post-irradiation PET data, namely a substantial overshoot in the region of the diaphragm, leading to the activation of the vertebral bone distal to the liver (see red arrow in figure 6.7). With respect to the previously discussed patients, suffering from central lesions within the liver, the more cranial location of the PTV close to the diaphragm makes the irradiation substantially more prone to range deviations by respiratory motion: during inspiration, the liver shifts further caudal and is replaced by low-density lung tissue, in which the beam has a significantly larger range. In the performed 4D simulations on the available 4D TP-CT, this overshoot has also been observed, but at a significantly reduced activity level. The reason could be found in the fact that the simulated activation is not directly located in the vertebral bone, but in the muscle tissue slightly cranial to the spot of activation in the measurement, such that it is subject to a remarkably larger biological clearance. The cranial shift of the activation itself can be explained by the fact that the patient 4D TP-CT, on which all 4D calculations have been based, does not fully cover the respiratory motion amplitude during the two regraded fractions due to inter-fractional variations in the patient breathing cycle. A deeper inhalation than actually represented by the 4D TP-CT phases directly results in a more caudal activation (within the low-perfused vertebral bone) than observed in the presented simulations. After treatment fractions two and four (not shown here), no activation of the vertebral column has been detected. These findings further indicate the variability of the respiratory motion for this patient, as well as the sensitivity of the applied treatment to such alterations and, consequently, the importance of using consistent 4D CT data of the treatment day for the prediction of motion-induced interplay patterns and range deviations.

In the determined distal PET range deviations between simulation and measurement, the observed overshoot has been identified as well (cf. deep red area indicated by the red arrow on

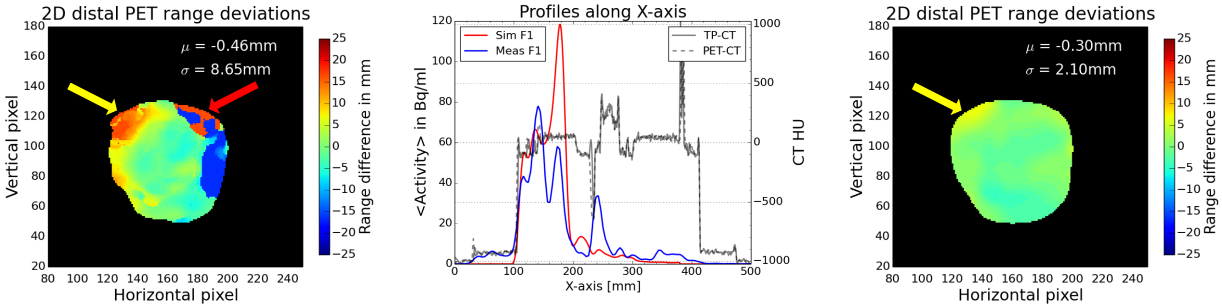

(a) 3D sim vs. 3D meas, F1 (b) 3D sim vs. 3D meas, F1 (c) 3D sim vs. 4D sim, F1

Figure 6.8: Results of the range verification for patient L3. Although the vertebral activation has been identified as over-range in the comparison of 3D simulation and measurement after fraction 1 (left, deep red region indicated by the red arrow), the range analysis is undermined by the inaccurate washout modelling, leading to considerably distorted 1D profiles along the beam axis (x-axis, middle) and herewith an incorrect determination of range deviations (left, dark blue regions). Differences between 3D and 4D simulations (right) have been observed to be generally small, with some exception in the cranial PTV region (cf. yellow arrow in the right plot), which is more sensitive to anatomical changes. The measured data, however, exhibits significantly larger range deviations in the same region (cf. yellow arrow in the left plot) due to the above-mentioned deeper inhalation than actually represented by the 4D TP-CT. For the same reason, the vertebral bone activation is not modelled correctly in the 4D calculation.

---

the top right of the 2D range deviation map depicted in figure 6.8 (a)). The inaccurate washout modelling has, however, been found to unacceptably spoil the retrieved range verification results for this patient and to introduce artificial range deviations, reaching values of up to 25 mm (cf. deep blue areas in figure 6.8 (a)), due to the substantially different shapes of the analysed 1D profiles along the beam axis, as depicted for an exemplary case in figure 6.8 (b). Range differences between 3D and 4D simulations are generally small, with an average deviation of below 0.5 mm due to the applied contrast agent, except from a small region in the most cranial part of the PTV (indicated by the yellow arrow in figure 6.8 (c)). Here, deviations amount to $5-10$ mm due to the higher sensitivity of the primary beam range to anatomical changes, introduced by the large density gradients in this region (similar to the findings for patient L2). Although the identified range deviations lead to a slightly enhanced agreement with the measured data, the latter still exhibits significantly larger over-ranges in this cranial PTV region (yellow arrow in figure 6.8 (a)) because of the above-mentioned deeper inhalation during the irradiation than represented by the 4D TP-CT. Finally, it should be remarked that the observed overshoot did not represent a clinically relevant hazard for the patient, as the beam was stopped in the outer vertebral bone, but did not hit the radiation sensitive spinal cord.

6.2.4 Patient L4

The investigated activity patterns for the first gating patient irradiated at HIT, L4, are depicted in figure 6.9. Besides the 3D simulations based on the 3D TP-CT and the 3D PET-CT acquired after the first treatment fraction, the 4D simulation on the basis of the 4D TP-CT, inherently

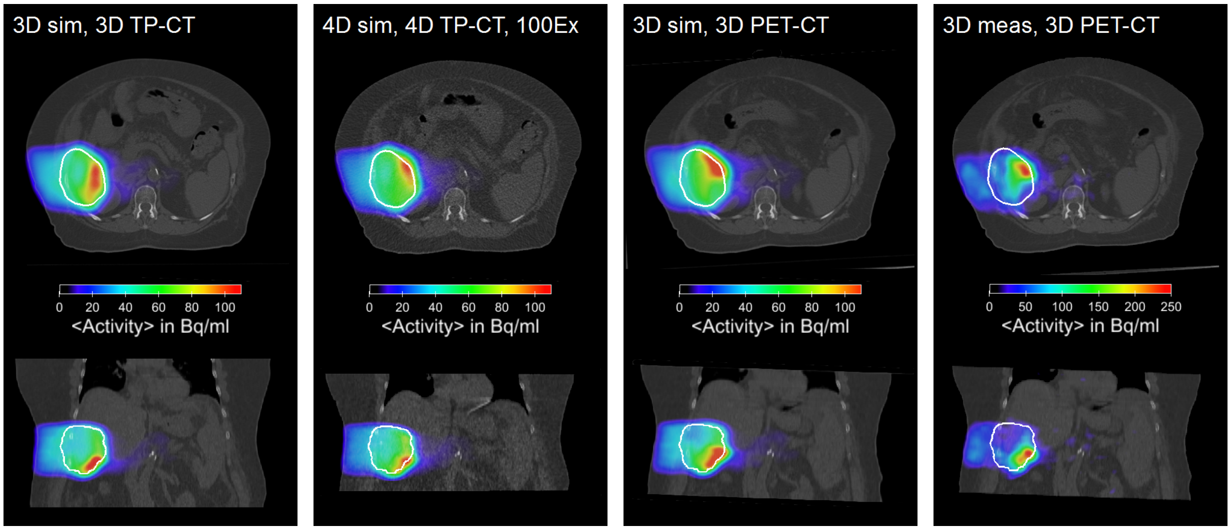

Figure 6.9: 2D activity distributions for patient L4. The 3D (left) and 4D (second from left) TP-CT simulations are shown next to the 3D PET-CT simulation (second from right) and the corresponding 3D PET image (right) after the first treatment fraction. The 4D simulation is depicted in the 100% exhale reference phase. A different scaling is applied to the measured data in order to account for inaccuracies in the washout modelling. Due to the extreme inhale position of the PTV region in the 3D TP-CT, while the irradiation has been gated on the end-exhale phase, considerable deviations between the 3D TP-CT simulation and the 3D PET measurement, representing a time-averaged distribution close to the end-exhale position as well, have been found. Consequently, the 3D simulation on the free-breathing 3D PET-CT, representing a respiratory state of about 20% exhale, and also the 4D TP-CT simulation, providing the correct anatomy in each of the considered motion states, have been found in a better agreement with the measurement. For a more coherent comparison to the measurement, the 4D TP-CT simulation should be warped to the 20% exhale phase, as shown in appendix B.

accounting for the gated beam delivery by the used state RTplans of fraction one, and the corresponding 3D PET measurement are shown. The 4D simulation study is depicted in the reference phase of 100% exhale, i.e., close to maximum inhalation (see figure 6.1). Although the 3D TP-CT had been intended as end-exhale (i.e., 0% relative motion amplitude) breath-hold CT (cf. section 2.6.5), only the upper part of the liver, close to the diaphragm, has been found close to this motion state, while the caudal region of the liver, where the irradiated PTV has actually been located, was found to match best the 100% exhale state of the 4D TP-CT. Probably, this artefact has to be attributed to an unwanted inspiration by the patient during the 3D TP-CT acquisition. Also for this patient, no coherent 4D CT data from the day of the treatment has been available.

Due to the considerably prolonged irradiation time by the gated beam delivery in combination with the extremely irregular respiratory motion of the regarded patient, the activity induced within the liver tissue and also within the right kidney has been found to be washed out for the most part in the acquired post-irradiation PET scan. Only in the abdominal fatty tissue surrounding liver and kidney, a considerable amount of irradiation-induced activity could be detected. Qualitatively, the same observation has been made in the corresponding activity simulations. However, while the amount of induced activity could be reproduced with an accuracy of

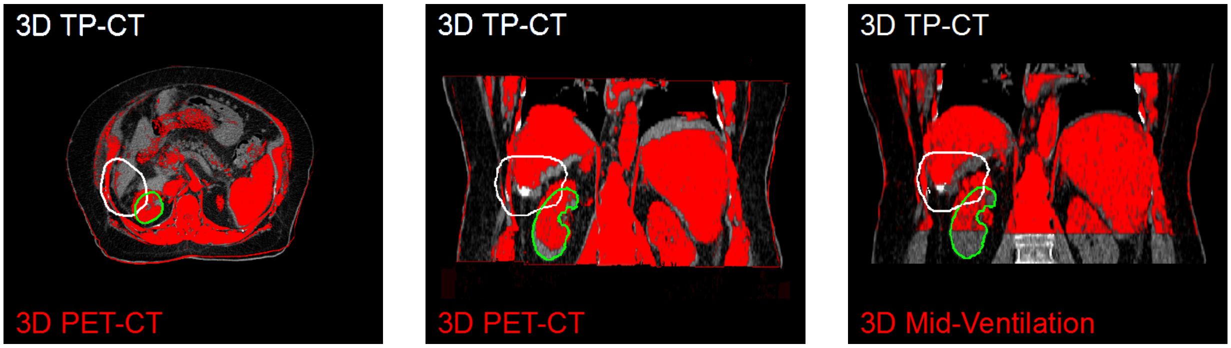

Figure 6.10: Comparison of different 3D CT images of patient L4. The 3D TP-CT is shown as greyscale and overlayed by the rigidly registered 3D PET-CT (red) in the transaxial (left) and coronal (middle) plane, as well as by the calculated 4D TP-CT-based mid-ventilation CT (red, right). In the region of the PTV (white contour) and the right kidney (green contour), the TP-CT represents a phase of significantly deeper inspiration, close to 100% exhale. PTV and kidney are thus shifted caudally with respect to the 3D PET-CT and the mid-ventilation CT, which both show a comparable motion state near 20% exhale in the PTV region.

---

about 10% in the liver, the simulation significantly overestimated the activity in the kidney, while it underestimated the activity in the abdominal fatty tissue by about 50% (see figure 6.9). Due to the high gradients in biological clearance in the caudal PTV region, the calculated activity distribution is highly sensitive to the position of the kidney, the liver and the fatty tissue in the underlying CT scan. As a consequence, rather large differences between the 3D simulations based on the TP-CT and on the PET-CT have been observed (cf. figure 6.9) due to the clearly deviating anatomies represented by these two scans, as shown in figure 6.10. While the 3D TP-CT represents a motion state close to the maximum inspiration in the caudal PTV region, where most of the activity has been detected, the 3D PET-CT corresponds to a motion state of about 20% exhale, i.e., liver and kidney are shifted in the cranial direction with respect to the TP-CT.

Compared to the measured data, a notably higher agreement has been found for the 3D simulation based on the 3D PET-CT with respect to the 3D TP-CT simulation. The reason for this has been identified in the more representative position of the kidney and the caudal edge of the liver in the 3D PET-CT, as confirmed by a comparison to the calculated *mid-ventilation* CT [Wolthaus et al., 2008] (see figure 6.10). The latter CT represents a time-averaged motion state of the patient and was found close to the respiratory state of PET-CT scan in the PTV region. As irradiation has also been performed with gating around end-exhale (i.e., 0% relative amplitude), and herewith in a motion state considerably closer to the mid-ventilation CT and the PET-CT, and since the 3D PET image also represents a time-averaged distribution of the induced activity, a high agreement of measurement and PET-CT simulation could be found. Similarly, an enhanced agreement of the 4D TP-CT simulation to the measurement has been observed, as the calculation is inherently based on the presumably correct, phase-specific CT image and patient geometry.

In the 4D TP-CT simulations of the physical dose, only slight interplay effects have been noticed, thus demonstrating an effective motion mitigation by the gated beam delivery and confirming the finding that differences between 3D TP-CT and 4D TP-CT simulations are predom-

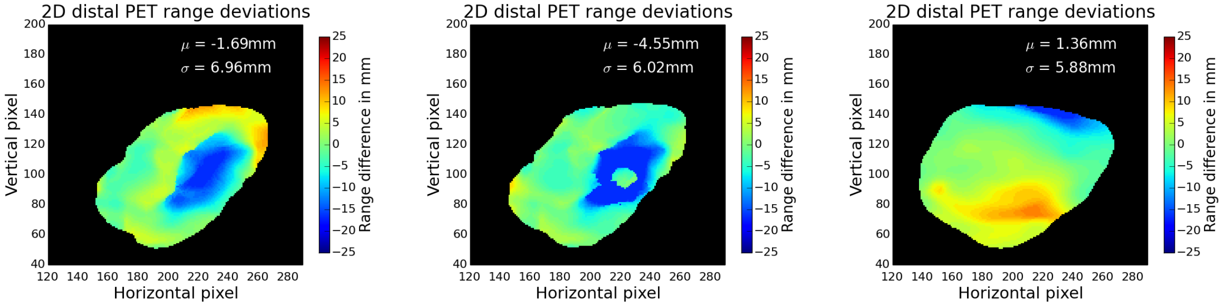

(a) 3D TP-CT sim vs. 3D meas (b) 3D PET-CT sim vs. 3D meas (c) 3D sim vs. 4D sim, TP-CT

Figure 6.11: Results of the range verification for patient L4. The underestimated biological clearance in the kidney leads to an apparent under-range in the measurement with respect to the 3D TP-CT (left) and the 3D PET-CT (middle) simulations (cf. deep blue regions). Except from these range differences, an enhanced agreement can be achieved by using the PET-CT, as differences between TP-CT simulation and measurement are partially attributed to deviations in the CT contour. The mean distal PET range deviation decreases from −1.7 mm for the TP-CT to −4.6 mm for the PET-CT simulation, as range deviations in the kidney region are no longer compensated by over-ranges in the upper part of the depicted range map on the left. Due to the discrepancy of the motion phases used for gating (50% around 0% exhale) and represented by the TP-CT (100% exhale) remarkable deviations between 3D and 4D TP-CT simulations have been found (right).

---

inantly caused by the previously described discrepancy of the 3D TP-CT motion state and the average patient motion state, being close to the anticipated patient anatomy within the applied gating window. Still, an enhanced agreement of the 4D TP-CT simulation to the measurement with respect to the 3D PET-CT simulation has not been observed, even when being warped to a coherent phase close to the mid-ventilation phase of the PET image (see appendix B). Probably, this is due to remaining inter-fractional differences in the patient anatomy, as have been observed in the comparison of the proximal CT contours in the performed range verification (cf. figure B.2 in appendix B).

These deviations in the patient contour have been found to enhance the overall agreement of PET-based range estimations in the measurement and the 3D PET-CT simulation with respect to the 3D TP-CT simulation, as illustrated in figure 6.11. Still, although the position of the kidney is more representative in the 3D PET-CT, the significant underestimation of the biological clearance in the kidney has been identified to provoke a severe over-range in the simulated data, leading to an apparent under-range in the measurement (cf., dark blue areas in figures 6.11 (a) and (b)). In contrast to the other patients, it has also been noted that the determined PET-based range of the 4D simulation remarkably depends on the actually regarded motion state. For a coherent comparison to the time-averaged 3D PET measurement, the 4D calculated activity distribution has thus been warped to the 20% exhale phase, close to the mid-ventilation position (see appendix B), and a similar agreement as observed for the 3D TP-CT simulation (see figure 6.11 (a)) has been determined. However, this does not allow for the conclusion that 3D and 4D TP-CT simulations exhibit similar ranges, as the 3D TP-CT does not represent the considered 20% exhale motion state in the PTV region. For a coherent comparison of these two data-sets, the 4D TP-CT simulation in the 100% exhale phase, as described by the 3D TP-CT, has to be considered (cf. figure 6.11 (c)). Here, substantial differences in the distal PET ranges have been found, which can be mainly attributed to the fact that the irradiation has been gated on end-exhale, as considered in the 4D simulation, while the 3D TP-CT was found to represent a motion state close to maximum inhale in the PTV region. As a consequence, the induced activity is shifted to the caudal direction in the 4D TP-CT simulation, which introduces the observed range differences with respect to the (3D) planned treatment. Although these range deviations with respect to the 3D planning are clinically not critical, they might have been avoided, if the 3D TP-CT had represented a motion state close to the end-exhale position, as originally intended. This would have lead to coherent phases of 3D TP-CT, the applied GW and the post-irradiation 3D PET measurement, herewith diminishing range-differences due to the phase-mismatch of GW and 3D TP-CT, and enabling an easier, more straightforward analysis of the data. In conclusion, these investigations show that even if gating efficiently mitigates motion-related interplay effects, the comparably large motion amplitude has to be carefully considered at the (3D) planning stage and for data evaluation.

6.3 Discussion and conclusion

To the best knowledge of the author, this chapter presented the first application of PET-based treatment verification to clinical cases under consideration of the patient respiratory motion. While 3D (static) PET-based treatment monitoring has already been investigated in clinical scenarios for in-beam, in-room, as well as offline PET acquisition systems (cf. section 3.3), investigations on the potential of extending this method to moving targets have, up to present, been restricted to simplified moving phantom experiments (see section 4.1). In this chapter, four of the first HCC patients treated with scanned ^{12}C ion beams at HIT have been studied in detail to infer feasibility and performance of 4D offline PET-based treatment verification under considerably more challenging clinical conditions.

For patients L1 and L4 with comparably small (residual) SI motion amplitudes of 2 and 5 mm, respectively, hardly any motion-related interplay effects were noticed in the 4D physical dose and activity simulations, in agreement with the findings reported in [Richter et al., 2014] for analytical 4D dose reconstructions of HCC patient irradiation at HIT. In the case of patient L1, tumour motion could effectively be diminished due to the location of the target volume close to the abdominal press and the inclusion of the organ motion into the offline PET-based treatment monitoring workflow did not result in a gain of knowledge. Hence, a 3D analysis of irradiation and post-therapeutic PET measurement is deemed sufficient for patients with comparably small motion amplitudes. In the case of patient L4, a somewhat different situation has been encountered, as the tumour motion has been mitigated by beam gating during the irradiation, while the CTV mean motion amplitude itself still amounted to more than 7 mm. As a consequence, the underlying 3D TP-CT is affected by imaging artefacts and does not represent one coherent motion state. In particular, the PTV region was found in a state of extreme inhale, so that beam gating around the end-exhale plateau lead to a phase-mismatch between planning and irradiation and herewith to an overall limited agreement (without clinically relevant implications) of 3D calculated PET expectation and measurement. Improved agreement with the measured irradiation-induced activity could be achieved by using the 4D TP-CT data and the corresponding set of state RTplan files for simulating the expected activity. Due to the overall small motion amplitude within the GW, it has, however, been found that results similar to the 4D calculation can be achieved by a 3D simulation on a 3D CT image close to the average respiratory state of the patient, and herewith to the respiratory phase within the GW (applied around the stable end-exhale position) and the time-averaged 3D PET image. Still, even though a 3D approach might be sufficient for these kind of gating patients, it is mandatory to account for the target motion in the selection of the used 3D data-sets, which have to exhibit a coherent respiratory state for conclusive comparison of treatment planning data, simulation and post-irradiation PET measurement.

In contrast to patients L1 and L4, patients L2 and L3 are both subject to a significantly larger respiratory motion amplitude of about 10 mm in SI direction. In both cases, the inclusion of organ motion in the performed simulations lead to the formation of interplay patterns in the distal PTV region. Particularly for patient L2, the calculated interplay pattern could be detected in the corresponding post-irradiation measurements as well, thus indicating the advantages of incorporating target motion into the PET-based treatment verification workflow. The potential benefits of 4D motion-compensated PET image reconstruction were studied for this patient, too, but could not be finally concluded due to the enhanced level of uncertainty in the 4D PET image, introduced by the reduced number of true coincidences in the underlying 4D gated PET image reconstruction, as well as by the required DIR. Moreover, the predicted interplay pattern could be detected in the 3D PET image without significant loss of information due to motion-induced blurring, as well. For patient L3, an identification of the expected interplay effects in the reconstructed measured data was considerably more challenging, due to the by about 30% reduced number of true coincidences with respect to patient L2. The comparison of 4D simulations and measurements especially showed that a distinction of the expected different interplay patterns after the two regarded treatment fractions is hindered by the high noise level in the reconstructed images, even though the optimised reconstruction scheme deduced in chapter 5 has been applied. In general, the small number of true counts and the resulting high noise level are seen as one of the main challenges in 4D offline PET-based treatment verification, since the image noise might exceed the inhomogeneity level of motion-related interplay patterns and thus prevent their detection. A further reduction of the image noise would be feasible by enhancing the post-reconstruction Gaussian filter, which would, however, directly lead to the blurring of small-scale interplay effects. Hence, a compromise between image granularity and image noise has to be carefully made.

Additional uncertainties in 4D offline PET monitoring, particularly affecting the MC calculation of the expected activity pattern, are introduced by uncertainties in the time alignment of the beam delivery sequence and the respiratory motion signal (lately eliminated by the use of a dedicated EtherCAT system for synchronous data recording [Richter et al., 2014]), by possible irregular breathing motion, by inter-fractional variations of the respiratory motion, by changes in the correlation of the external motion surrogate and the internal motion with respect to the 4D TP-CT acquisition and by the limited accuracy of the used DIR. While the DIR uncertainties are considered less crucial with respect to the limited spatial resolution and the high noise level in the acquired PET images, variations in the breathing motion have been found to lead to substantial deviations between 4D activity prediction and measurement. In particular, the vertebral bone activation observed for patient L3 due to a significant over-shoot in the cranial PTV region, could not be reproduced in the 4D calculations on the basis of the 4D TP-CT data, which does not cover motion states of comparably deep inhalation as presumably encountered during the beam application. Probably, these uncertainties could be limited by acquiring 4D CT data on the actual treatment day, though at the drawback of an additional radiation exposure to the patient. A future alternative to handle potential breathing irregularities and variations during the actual beam application might be provided by the construction of an extended 4D CT data-set on the basis of 4D MRI imaging [Boye et al., 2013]. MRI imaging is dose-free and thus allows for repeated, prolonged imaging and studying of breathing irregularities and variations. DIR maps retrieved from the time-resolved MRI data can then be used for warping of a 3D (breath-hold) CT to form a 4D CT data-set which covers a considerably wider range of respiratory states than a conventional 4D CT scan. Direct tracking of internal structures in absolute coordinates during 4D imaging and beam application, as potentially provided by the US tracking device investigated in section 4.2 [Schwaab et al., 2014], might additionally be employed for an improved identification of the actual respiratory motion state.

The observed overshoot for patient L3 is, however, also directly related to the location of the PTV close to the diaphragm, which is prone to range uncertainties due to the large density gradients between lung and liver tissue. For more central lesions within the liver (cases L1 and L2) a substantially smaller impact of the target motion on the beam range could be identified. In the case of patient L4, changes in the WEPL due to respiratory motion are expected to be small as well, but due to the activity localisation in the fatty tissue caudal to the liver, a dependence of the 4D calculated range on the respiratory reference state in the 4D simulation has been found. Thus, for similar cases a coherent phase of simulation and PET measurement has to be ensured for proper range validation and comparison.

In two (L3 and L4) of the four studied patients, considerable deviations in the determined distal PET ranges were found to be introduced by inaccuracies in the modelling of the biological clearance, leading to severe differences in the shape of the analysed 1D activity profiles along the beam axis and hindering a thorough range comparison. In general, the modelling of the isotope washout was identified as a second major challenge in 4D offline PET-based treatment verification, besides the inaccuracies in the PET image reconstruction due to the low amount of detected true coincidences. In particular, a large inter-patient variability in the liver has been found. Also in the abdominal fatty tissue, large discrepancies ($> 50\%$) in the absolute amount of activity between measurement and prediction could be detected. Moreover, in the study of patient L3, a space-dependency of the isotope washout within the irradiated PTV has been observed, which further undermines a proper identification and quantification of irradiation-induced interplay patterns.

Summarising the results of this chapter, the feasibility of 4D offline PET-based treatment verification under clinical conditions has been shown and the major challenges have been identified. For the particular cases of patients exhibiting small motion amplitudes, not exceeding a size of about 5 mm, a static (3D) analysis of the post-irradiation data and comparison to a static FLUKA calculation is deemed to be sufficient. In the case of SI motion amplitudes in the order of 10 mm and above, however, interplay patterns due to respiratory motion have been detected in the calculated 4D activity distributions, thus indicating a potential gain of knowledge for offline PET-based treatment verification by taking organ motion into account. In one case, with comparably high counting statistics (about $700,000$ true counts), the expected interplay pattern could be detected with high agreement in the measured data, as well. If going to lower numbers of true coincidences (around $400,000$) the considerable image noise, however, substantially challenges the detection of the expected interplay patterns in the measured data and herewith limits the sensitivity of PET monitoring to motion-related deviations from the planned treatment application. Dedicated image reconstructions algorithms with improved noise robustness are presently under investigation, with a special focus on 4D motion-compensated PET imaging. Here, potential benefits with respect to the currently applied 4D gated image reconstruction are anticipated by 4D MLEM algorithms [Stützer et al., 2013], as well as by the so-called sinogram warping technique [Gianoli et al., 2014]. Both methods make used of the full amount of detected true coincidences in each of the reconstructed motion states, and thus reduce uncertainties in the reconstructed single-phase 4D PET images. Besides the low amount of induced activity, a main restriction in the potential of 4D offline PET-based treatment verification is imposed by uncertainties in the modelling of the biological clearance. As a consequence, PET-based treatment verification, up to present, has to be considered as a qualitative tool for in-vivo dose monitoring. In particular, a reliable quantification, i.e., with uncertainties of few percent, of over- and under-dosage due to motion-related interplay effects cannot be ensured. Further improvements in this context can be achieved by implementing patient-specific washout models for post-processing of the simulated data, which should thus be addressed in future investigations, or by dedicated instrumentation allowing for in-room or in-beam PET imaging, being considerably less sensitive to washout processes [Helmbrecht et al., 2013].

The presented results are still based on a small number of exemplary patient cases. In order to draw conclusions on the potential of 4D offline PET-based treatment verification with high confidence, a careful analysis of further patient data-sets is of need. In particular, these cases should exhibit motion amplitudes of above 10 mm, a high enough ($> 600,000$) number of true coincidences and provide 4D CT data of the treatment day. Up to present, beyond the presented case of patient L2, such data-sets are not available.

Chapter 7

Conclusion and outlook

Over the last decades, tumour therapy with proton and heavy ion beams has become an emerging alternative to conventional radiation therapy with photons. The accessible steep dose gradients in ion beam therapy enable a highly conformal dose delivery to arbitrarily shaped tumour volumes, a low exposure of close-by organs at risk and a reduced integral dose to normal tissue with respect to photon therapy. On the other hand, they are accompanied by an enhanced sensitivity to uncertainties, e.g., in patient positioning or due to changes in the patient anatomy. Hence, it is highly desirable to thoroughly monitor the actually applied treatment in order to fully exploit the anticipated advantages of ion beam therapy. Up to present, the only clinically implemented approach of monitoring the delivery of single treatment fractions close in time to the actual irradiation is based on PET imaging of the irradiation-induced β^+-emitter within the patient. This method is also being pursued at HIT, using a commercial full-ring TOF PET/CT scanner installed next to the treatment rooms for post-irradiation patient imaging.

Additional uncertainties in ion beam therapy are introduced by inter- and intra-fractional motion. Particularly intra-fractional motion, mostly related to the respiration of the patient, might introduce severe changes in the particle beam range on a time-scale of seconds and herewith during the actual beam application. In the case of scanned ions beams, as used at HIT, interference effects between the dynamic beam delivery and the respiratory motion can additionally lead to distortions of the applied dose distribution and the formation of regions of over- and under-dosage. However, despite the increased level of uncertainty, the application of heavy ion beams to moving tumours is of high interest, since e.g., HCC patients, which have been investigated in the scope of this work, have been shown to significantly benefit from irradiation with ^{12}C ions in clinical trials at NIRS, Japan. Although motion can be mitigated by techniques like beam gating or by abdominal compression, the residual tumour motion, the questionable correlation between the required external motion surrogate and the internal tumour movement, as well as variations in the breathing trajectory evoke a strong need for verification of the actually applied treatment under consideration of the actual organ motion.

In this work, the feasibility and potential of 4D offline PET-based treatment verification with a commercial full-ring TOF PET/CT device, taking into consideration the target motion during the beam application, as well as during the subsequent PET acquisition, have been investigated for the first time. A dedicated moving phantom irradiation study at a comparably high number of true coincidences not only demonstrated the feasibility of the pursued 4D offline PET-based treatment monitoring approach, but also highlighted the potential of this technique under laboratory conditions: the different investigated set-ups coherently showed that sub-millimetre accuracy and precision can be achieved in the determination of the ion beam range as well as in the detection of distortions introduced by interplay effects between the dynamic beam delivery and the phantom motion. The sensitivity of the pursued 4D PET monitoring approach was underlined by 4D simulation studies on potential time shifts between the recorded surrogate motion signal and the beam delivery sequence, which could be determined with an accuracy of about 50 ms on the basis of the post-irradiation PET measurement. One major limitation for the achievable precision, accuracy and sensitivity to motion-related interplay patterns was identified in the low amount of irradiation-induced activity and the resulting high image noise level. Particularly in the pursued 4D gated PET image reconstruction, which is presently the only implemented time-resolved reconstruction technique on the used Biograph mCT scanner, the reconstructed images of the single motion states suffer from considerably reduced statistics due to the subdivision of the acquired LM data into the single phases. Improvements are foreseen by 4D MLEM and sinogram warping image reconstruction algorithms, which inherently consider the full amount of events for image reconstruction within each motion state, and are currently under investigation. In the case of irregular breathing patterns, as typically encountered in post-irradiation patient PET imaging, an improved performance might moreover be achieved by enhancing the reliability of sorting the acquired data into the reconstructed motion states. In this context, one promising approach is the direct tracking of internal structures in absolute coordinates by ultrasound imaging. First steps for an integration of this tracking technique in time-resolved PET imaging have been presented in this work, as well: in a simplified set-up with moving point sources, an equivalent performance to the certified ANZAI gating system could be demonstrated in terms of motion mitigation. Investigations with a static point-source arrangement also proved that the degradation of the acquired PET images due to the presence of the US probe within the FOV is negligible, as long as a minimum distance between measured activity and US probe of few centimetres is kept. Further studies with decoupled motion trajectories in more than one dimension and under conditions closer to clinical scenarios, however, still have to demonstrate the anticipated superiority of US-based motion tracking.

Besides possible future improvements in 4D PET imaging by new reconstruction algorithms and tracking devices, this work also showed that optimisation of the applied image reconstruction scheme, considering only reconstruction options already provided by the used commercial PET/CT device, can enhance the imaging performance in low count scenarios, as particularly encountered in time-resolved gated PET imaging. In a dedicated phantom imaging study, an improved geometrical fidelity, as well as an up to 50% reduced image noise could be achieved by reducing the number of iterations and increasing the size of the post reconstruction Gaussian filter with respect to the originally used settings at HIT, which had been inspired by typical settings in nuclear medicine imaging at significantly higher counting statistics. Under poor statistical conditions, the inclusion of a scanner resolution model (PSF) and TOF information in the reconstruction algorithm were found to enhance the imaging performance and to allow for an accurate activity quantification down to less than $80,000$ true coincidences at random fractions of above 95%. The performed measurements and corresponding simulations also helped to identify the low number of true coincidences as the limiting factor in terms of geometrical fidelity and image noise in low-statistics PET-based treatment verification, as long as PSF and TOF information are considered during reconstruction. The high LSO-related random background, on the other hand, was found to mainly lead to an increased background activity which can be neglected in the context of treatment monitoring, where the approximate position of the beam is known. A more critical issue was found in the build up of spurious activity within the imaged object due to an inaccurate scatter correction at very low true numbers (below $100,000$). This effect can, however, be limited by the application of PSF and TOF information and a reduced number of iterations. The analysis of exemplary 3D post-irradiation patient PET scans confirmed a reduction of the image noise by about 50% when using the optimised reconstruction scheme derived in the phantom imaging study at an equivalent or even improved geometrical performance in terms of beam range verification. Consequently, the retrieved optimal reconstruction scheme is presently in clinical use for all post-irradiation PET imaging studies at HIT.

Following the results of the characterisation of the PET/CT scanner performance under extremely low counting statistics, the feasibility of 4D offline PET-based treatment verification has eventually been studied on the basis of four exemplary HCC patients irradiated at HIT, representing the first attempt to extend the technique of PET-based treatment monitoring to moving targets under clinical conditions. In comparison to the above-mentioned phantom irradiation study, patient cases typically exhibit further challenges due to a reduced number of true counts emerging from a less confined region of activation, irregular respiratory motion and activity washout due to biological processes. Nevertheless, the feasibility of 4D offline PET-based treatment verification under clinical conditions could be shown. Based on the investigated small patient cohort, a benefit by taking into account the target motion is anticipated particularly for patient cases with comparably high numbers of true counts (above $600,000$) and SI motion amplitudes in the order of $10\,\mathrm{mm}$. Still, improvements have mainly been noticed on the side of the calculated prediction of the induced activity, while a gain of knowledge by 4D motion-compensated PET imaging could not be finally concluded due to the underlying uncertainties in the 4D gated PET image reconstruction, despite using the optimised reconstruction scheme. At reduced numbers of true counts (about $400,000$), image noise increases and a reliable detection of motion-induced interplay patterns is deemed not feasible at present. Additional challenges are imposed by inaccuracies in the modelling of activity washout. Variations from patient to patient or even within a single target volume are presently not considered in the applied washout model, but might further impede an accurate quantification of motion-induced interplay effects. As a consequence, 4D offline PET-based treatment verification can, up to now, only be considered as a qualitative tool for monitoring the treatment of moving targets. For a reliable statement on the potential of 4D offline PET-based treatment monitoring under clinical conditions, more patient data-sets with large enough motion amplitudes and counting statistics, as well as coherent 4D CT data of the treatment day, are still of need. Additionally, irradiation studies with anthropomorphic moving phantoms are considered of high interest for closing the gap between the presented simplified homogeneous phantom cases and the substantially more complex patient irradiation. Future studies should particularly aim at the development of dedicated noise-robust image reconstruction algorithms and an improved patient-specific washout model.

The two main limiting factors, namely the low number of acquired true coincidences and the inaccurately modelled biological clearance, might, however, also be tackled by dedicated in-beam PET implementations, which inherently offer the ability to detect a higher number of counts [Shakirin et al., 2011; Parodi et al., 2008b] and are less prone to washout processes due to the significantly shorter delay between formation and detection of the β^+-emitter [Helmbrecht et al., 2013]. Over the last years, various studies on the optimal geometrical design of dedicated in-beam PET cameras, including Open-PET [Yamaya et al., 2008; Tashima et al., 2012], partial-ring detectors [Surti et al., 2011; Robert et al., 2013] and C-shaped [An et al., 2013] arrangements, have been conducted and demonstrated a high potential for improvement with respect to presently operating in-beam cameras. Moreover, the development of detector systems with new crystals like $LaBr_3$ (Lanthanum(III) bromide) and read-out by (digital) silicon photomultiplier (SiPM) promises advances in the accessible TOF resolution [Moses, 2007; Schaart et al., 2010] in the near future, which will strongly enhance the imaging performance of partial ring PET detector systems that suffer from truncated projections and the related limited angle artefacts [Crespo et al., 2007; Surti et al., 2011]. Beyond that, improvements are foreseen by the implementation of depth-of-interaction (DOI) PET detectors [Shao et al., 2013], by dedicated reconstruction algorithms [Cabello et al., 2013], as well as the feasibility of increasing the number of detected coincidences by acquiring PET data also during the beam application, and not only within the spill pauses [Sportelli et al., 2014]. Taking into consideration these on-going developments, a clear benefit for PET-based treatment verification can be expected from dedicated TOF in-beam PET cameras within the next years and might further push the potential of 4D in-vivo treatment monitoring. For commercial full-ring PET/CT scanner, advances by an increased TOF resolution, implementation of DOI detectors and noise-robust image reconstruction algorithms are anticipated as well, but in the case of offline imaging, the number of detectable true coincidences still remains limited and the sensitivity to biological clearance increased with respect to in-beam solutions. In this context, in-room PET imaging with commercial full-ring PET devices might be considered as further option to foster 4D PET-based treatment monitoring. The reduced time-delay between irradiation and PET acquisition allows for imaging at higher true coincidence rates and provides a reduced sensitivity to biological washout with respect to offline imaging. Compared to in-beam implementations, however, washout still plays an increasingly important role and has been observed to degrade the results of in-room PET-based treatment verification if not being modelled correctly [Zhu et al., 2011].

Alternative approaches for in-vivo range and treatment verification beyond PET imaging, such as prompt-γ [Testa et al., 2009; Smeets et al., 2012] or interaction vertex imaging [Henriquet et al., 2012; Gwosch et al., 2013], both relying on the detection of prompt irradiation products (γ-rays, protons, ions) emitted on a time-scale of $10^{-21} - 10^{-16}$ s in nuclear reactions, are presently under investigation, too. In contrast to PET-based treatment monitoring, these techniques are insensitive to washout processes, but they are still at an experimental stage and a careful evaluation of their potential under clinical conditions, particularly in the presence of organ motion, is of need. Many of the computational methods developed in the scope of this work, concerning in particular the inclusion of organ motion in the underlying MC simulations, could, however, be applied to these techniques, as well.

Appendix A

Additional results of the moving phantom studies

A.1 *Line Mono* irradiation study

The results retrieved in the range-analysis of the *Line Mono* irradiation study are given in table A.1. The PET-based range differences DR_i presented in section 4.1.2.2 have been calculated on the basis of these range data with respect to $\mathrm{R}_{\mathrm{PET},4}$. The determined absolute ranges in table A.1 should not be compared to the ranges determined in the *Square* study evaluation, because of the different shapes of the integrated ADP and herewith the inconsistent position of A_5 in both studies.

Table A.1: Results of the range analysis of the *Line Mono* irradiation study for all investigated data-sets. The used PMMA fence leads to the formation of four different range values, which have been analysed separately in terms of mean value and standard deviation.

Study	$\mathrm{R}_{\mathrm{PET},1}$[mm]	$\mathrm{R}_{\mathrm{PET},2}$ [mm]	$\mathrm{R}_{\mathrm{PET},3}$[mm]	$\mathrm{R}_{\mathrm{PET},4}$[mm]
Line Mono, static	58.2 ± 0.1	62.9 ± 0.3	68.6 ± 0.7	75.4 ± 0.5
Line Mono G50, 3D	57.8 ± 0.2	63.3 ± 0.3	69.1 ± 0.6	75.0 ± 1.1
Line Mono G50, 4D	57.3 ± 0.1	62.8 ± 0.3	68.1 ± 0.5	74.9 ± 0.5
FLUKA, static	58.5 ± 0.1	63.5 ± 0.1	68.9 ± 0.6	75.8 ± 0.4
FLUKA G50, 4D	58.2 ± 0.1	63.3 ± 0.2	68.7 ± 0.8	75.5 ± 0.6

A.2 *Line Mult* irradiation study

All results obtained in the profile analysis of the *Line Mult* irradiation study data-sets are given in table A.2. The determined PET-based ranges are not suited for a direct comparison to the ranges of the two other studies (*Square* and *Lino Mono*) because the PMMA fence has not been taken into account in the data analysis and the position of A_5 slightly varies with the particular shape of the ADP for each investigated geometry.

Table A.2: Results of the *Line Mult* irradiation study. A high agreement (within 1 mm) of all considered data-sets in terms of R_{PET}, $FWHM_y$ and P_y has been found. For the direction of motion, results are notably less accurate and precise, which can mainly be attributed to the significant distortion of the shape of the analysed lateral profiles by the target motion and the resulting interplay effects, particularly in the case of the G50 study.

Study	R_{PET}[mm]	$FWHM_y$[mm]	$FWHM_z$[mm]	P_y[mm]	P_z[mm]
Line Mult, static	52.6 ± 0.6	19.7 ± 0.7	142.6 ± 0.9	8.7 ± 0.4	11.3 ± 0.9
Line Mult G50, 3D	52.8 ± 0.4	20.2 ± 0.7	141.8 ± 1.9	8.5 ± 0.6	24.3 ± 4.2
Line Mult G50, 4D	52.2 ± 0.5	19.8 ± 1.2	138.6 ± 2.3	7.9 ± 1.1	20.5 ± 10.2
Line Mult G20, 3D	52.9 ± 0.6	20.1 ± 0.9	146.8 ± 1.6	8.6 ± 0.4	16.7 ± 2.0
Line Mult G20, 4D	52.2 ± 0.6	19.9 ± 1.0	143.1 ± 0.6	8.1 ± 0.5	10.1 ± 2.7
FLUKA, static	52.7 ± 0.3	20.4 ± 0.3	145.1 ± 0.1	8.8 ± 0.2	9.4 ± 0.2
FLUKA G50, 4D	52.7 ± 0.3	20.1 ± 0.3	140.1 ± 0.9	8.8 ± 0.6	26.8 ± 15.0
FLUKA G20, 4D	52.5 ± 0.3	20.4 ± 0.2	144.9 ± 0.1	8.8 ± 0.1	9.6 ± 0.1

Besides, single motion phases as retrieved within the 4D gated PET reconstruction have been analysed in a similar way as the motion-compensated 4D PET images to infer the accuracy and precision under a reduced number of true coincidences. Each single phase contains only 1/8 of the total number of coincidences, leading to a significantly decreased SNR. The results of the single phases are presented in table A.3 and compared to the results of the registered, and hereby smoothed, 4D motion-compensated images.

Table A.3: Results of the *Line Mult* irradiation study for a single phase (number 5) of the gated 4D PET images. In comparison to the motion compensated images, a considerably reduced precision can be noticed. In the G20 study, the penumbra in the direction of motion cannot be recovered correctly.

Study	R_{PET}[mm]	$FWHM_y$[mm]	$FWHM_z$[mm]	P_y[mm]	P_z[mm]
L. Mult G50, 4D	52.2 ± 0.5	19.8 ± 1.2	138.6 ± 2.3	7.9 ± 1.1	20.5 ± 10.2
L. Mult G50, 4D, ph 5	52.4 ± 1.1	19.1 ± 2.3	133.9 ± 4.4	8.5 ± 1.4	19.9 ± 7.7
L. Mult G20, 4D	52.2 ± 0.6	19.9 ± 1.0	143.1 ± 0.6	8.1 ± 0.5	10.1 ± 2.7
L. Mult G20, 4D, ph 5	53.0 ± 1.7	18.9 ± 1.8	137.0 ± 4.2	8.4 ± 1.1	24.6 ± 11.0

Appendix B

Additional results of the 4D patient data analysis

B.1 Patient L4

In addition to the 2D activity distributions for patient L4 shown in section 6.2.4, the 4D TP-CT simulation data, warped to the 20% exhale phase, is shown in figure B.1. This phase was found close to the mid-ventilation phase and is thus best suited for comparison to the acquired time-averaged 3D PET data. Indeed, the 4D TP-CT simulation warped to the 20% exhale phase shows an enhanced agreement to the measured 3D PET data with respect to the 4D TP-CT simulation in the reference phase of 100% exhale, particularly in terms of the beam range (indicated by the red arrow in figure B.1). For comparison to the 3D TP-CT simulation, however, the 4D TP-CT simulation in the reference phase of 100% exhale, as represented by the 3D TP-CT in the PTV region, should be considered. Here, an over-ranges in the 4D TP-CT simulation due to the phase-mismatch between 3D TP-CT and gating window could be noticed (cf. section 6.2.4).

In addition to the distal PET range deviations between the statically reconstructed measurement after the first treatment fraction and the 3D TP-CT and the 3D PET-CT simulation, as shown in section 6.2.4, figure B.2 additionally shows the determined proximal CT profile deviations for patient L4. As can be seen, the determined PET-based range differences between measurement and 3D TP-CT simulation are partially attributed to deviations in the proximal CT contour on the treatment day. Consequently, an enhanced agreement of 3D PET-CT simulation and 3D measurement has been found outside the region which is affected by the incorrectly modelled washout in the kidney (deep blue region in the 2D range deviation maps).

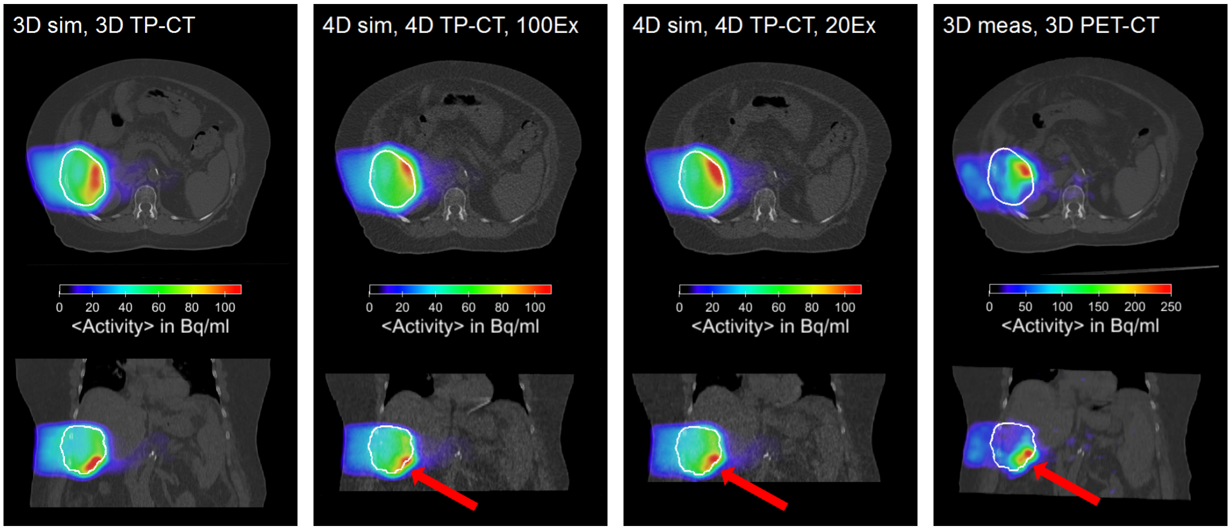

Figure B.1: 2D activity distributions for patient L4. The 3D (left) and 4D TP-CT simulations, once in the 100% exhale reference phase (second from left) and once in the 20% exhale phase (second from right) are shown next to the corresponding 3D PET image (right) after the first treatment fraction. While the 100% exhale phase corresponds to the phase of the 3D TP-CT in the PTV region, the 20% exhale phase is close to the mid-ventilation phase, and herewith the phase of the time-averaged PET image. Consequently, the 20% exhale 4D TP-CT simulation is best suited for the comparison to the 3D PET acquired after the first treatment fraction. Compared to the 3D TP-CT simulation and also to the 4D TP-CT simulation in the 100% exhale phase, the 4D TP-CT simulation in the coherent 20% exhale phase exhibits an improved agreement with the measured data. Particularly the beam range matches better with the measurement in the 20% exhale than in 100% exhale representation (cf. red arrows).

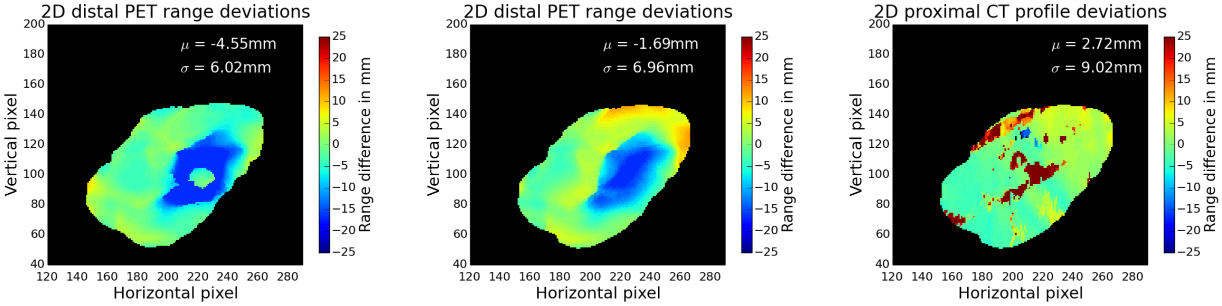

(a) 3D PET-CT sim vs. 3D meas (b) 3D TP-CT sim vs. 3D meas (c) 3D TP-CT vs. 3D PET-CT

Figure B.2: Additional results of the range verification for patient L4. Except from the range differences due to the inaccurately modelled isotope washout in the kidney (deep blue region), an enhanced agreement to the measurement is achieved by the 3D PET-CT simulation (left), as differences between TP-CT simulation and measurement (middle) are partially attributed to deviations in the CT contour (right). The dark red regions in the CT contour deviation map are attributed to a mis-identification of the vacuum mattress as outer patient contour in the CT profile analysis and are thus not of concern.

Bibliography

Ahlen, S. P. (1980). Theoretical and experimental aspects of the energy loss of relativistic heavily ionizing particles. *Rev. Mod. Phys.*, 52(1):121–173.

An, S. J., Beak, C.-H., Lee, K., and Chung, Y. H. (2013). A simulation study of a C-shaped in-beam PET system for dose verification in carbon ion therapy. *Nucl. Instrum. Meth. A*, 698(0):37–43.

Arkeryd, L. (1972). On the Boltzmann equation. *Arch. Ration. Mech. An.*, 45:1–16.

Barkas, W. H. & Evans, D. A. (1963). *Nuclear research emulsions.* Academic Press New York.

Battistoni, G., Cerutti, F., Fasso, A., Ferrari, A., Muraro, S., Ranft, J., Roesler, S., and Sala, P. R. (2007). The FLUKA code: description and benchmarking. *AIP Conference Proceedings*, 896:31–49.

Bauer, J., Unholtz, D., Kurz, C., and Parodi, K. (2013a). An experimental approach to improve the Monte Carlo modelling of offline PET/CT-imaging of positron emitters induced by scanned proton beams. *Phys. Med. Biol.*, 58(15):5193–5213.

Bauer, J., Unholtz, D., Sommerer, F., Kurz, C., Haberer, T., Herfarth, K., Welzel, T., Combs, S. E., Debus, J., and Parodi, K. (2013b). Implementation and initial clinical experience of offline PET/CT-based verification of scanned carbon ion treatment. *Radiother. Oncol.*, 107(2):218–226.

Bert, C. and Durante, M. (2011). Motion in radiotherapy: particle therapy. *Phys. Med. Biol.*, 56(16):R113–R144.

Bert, C., Gemmel, A., Saito, N., Chaudhri, N., Schardt, D., Durante, M., Kraft, G., and Rietzel, E. (2010). Dosimetric precision of an ion beam tracking system. *Radiat. Oncol.*, 5(1):61–70.

Bert, C., Gemmel, A., Saito, N., and Rietzel, E. (2009). Gated Irradiation With Scanned Particle Beams. *Int. J. Radiat. Oncol. Biol. Phys.*, 73(4):1270–1275.

Bert, C., Gräzinger, S. O., and Rietzel, E. (2008). Quantification of interplay effects of scanned particle beams and moving targets. *Phys. Med. Biol.*, 53(9):2253.

Bert, C., Saito, N., Schmidt, A., Chaudhri, N., Schardt, D., and Rietzel, E. (2007). Target motion tracking with a scanned particle beam. *Med. Phys.*, 34(12):4768–4771.

Bethe, H. A. (1930). Zur Theorie des Durchgangs schneller Korpuskularstrahlen durch Materie. *Ann. Phys.*, 397:325–400.

Bhagat, N., Fidelman, N., Durack, J. C., Collins, J., Gordon, R. L., LaBerge, J. M., and Kerlan Jr., R. K. (2010). Complications Associated with the Percutaneous Insertion of Fiducial Markers in the Thorax. *Cardiovasc. Inter. Rad.*, 33(6):1186–1191.

Bichsel, H., Hiraoka, T., and Omata, K. (2000). Aspects of fast-ion dosimetry. *Radiat. Res.*, 153(2):208–219.

Bloch, F. (1933). Bremsvermögen von Atomen mit mehreren Elektronen. *Z. Phys. A-Hadron. Nucl.*, 81:363–376.

Bohr, N. (1940). Scattering and stopping of fission fragments. *Phys. Rev.*, 58(7):654–655.

Boye, D., Lomax, T., and Knopf, A. (2013). Mapping motion from 4D-MRI to 3D-CT for use in 4D dose calculations: A technical feasibility study. *Med. Phys.*, 40(6).

Bragg, W. and Kleeman, R. (1905). On the alpha particles of radium and their loss of range in passing through various atoms and molecules. *Philos. Mag.*, 10:318–340.

Brasse, D., Kinahan, P. E., Lartizien, C., Comtat, C., Casey, M., and Michel, C. (2005). Correction Methods for Random Coincidences in Fully 3D Whole-Body PET: Impact on Data and Image Quality. *J. Nucl. Med.*, 46(5):859–867.

Brooks, R. A. and Di Chiro, G. (1975). Theory of Image Reconstruction in Computed Tomography. *Radiology*, 117(3):561–572.

Bush, D. A., Slater, J. D., Shin, B. B., Cheek, G., Miller, D. W., and Slater, J. M. (2004). Hypofractionated proton beam radiotherapy for stage I lung cancer. *Chest*, 126(4):1198–1203.

Byrne, C. (1998). Accelerating the EMML algorithm and related iterative algorithms by rescaled block-iterative methods. *IEEE T. Image Process.*, 7(1):100–109.

Cabello, J., Torres-Espallardo, I., Gillam, J., and Rafecas, M. (2013). PET Reconstruction From Truncated Projections Using Total-Variation Regularization for Hadron Therapy Monitoring. *IEEE T. Nucl. Sci.*, 60(5):3364–3372.

Case, R. B., Moseley, D. J., Sonke, J. J., Eccles, C. L., Dinniwell, R. E., Kim, J., Bezjak, A., Milosevic, M., Brock, K. K., and Dawson, L. A. (2010). Interfraction and Intrafraction Changes in Amplitude of Breathing Motion in Stereotactic Liver Radiotherapy. *Int. J. Radiat. Oncol. Biol. Phys.*, 77(3):918–925.

Casey, M. E. (2007). Point spread function reconstruction in PET. *Siemens white paper.*

Casey, M. E. (2008). Improving PET With HD-PET + Time of Flight. *Siemens white paper.*

Castro, J. R., Quivey, J. M., Lyman, J. T., Chen, G. T. Y., Phillips, T. L., Tobias, C. A., and Alpen, E. L. (1980). Current status of clinical particle radiotherapy at Lawrence Berkeley laboratory. *Cancer*, 46(4):633–641.

Chen, Q.-S., Weinhous, M. S., Deibel, F. C., Ciezki, J. P., and Macklis, R. M. (2001). Fluoroscopic study of tumor motion due to breathing: Facilitating precise radiation therapy for lung cancer patients. *Med. Phys.*, 28(9):1850–1856.

Chen, W., Unkelbach, J., Trofimov, A., Madden, T., Kooy, H., Bortfeld, T., and Craft, D. (2012). Including robustness in multi-criteria optimization for intensity-modulated proton therapy. *Phys. Med. Biol.*, 57(3):591–608.

Cheng, J.-C., Blinder, S., Rahmim, A., and Sossi, V. (2010). A Scatter Calibration Technique for Dynamic Brain Imaging in High Resolution PET. *IEEE T. Nucl. Sci.*, 57(1):225–233.

Chu, W. T., Ludewigt, B. A., and Renner, T. R. (1993). Instrumentation for treatment of cancer using proton and light-ion beams. *Rev. Sci. Instrum.*, 64(1):2055–2122.

Combs, S., Habermehl, D., Ganten, T., Schmidt, J., Edler, L., Burkholder, I., Jakel, O., Haberer, T., and Debus, J. (2011). Phase i study evaluating the treatment of patients with hepatocellular carcinoma (HCC) with carbon ion radiotherapy: The PROMETHEUS-01 trial. *BMC Cancer*, 11(1):67–75.

Comtat, C., Bataille, F., Michel, C., Jones, J., Sibomana, M., Janeiro, L., and Trebossen, R. (2004). OSEM-3D reconstruction strategies for the ECAT HRRT. In *Nuclear Science Symposium Conference Record, 2004 IEEE*, volume 6, pages 3492–3496.

Conti, M. (2011). Why is TOF PET reconstruction a more robust method in the presence of inconsistent data? *Phys. Med. Biol.*, 56(1):155–168.

Conti, M., Bendriem, B., Casey, M., Chen, M., Kehren, F., Michel, C., and Panin, V. (2005). First experimental results of time-of-flight reconstruction on an LSO PET scanner. *Phys. Med. Biol.*, 50(19):4507–4526.

Crespo, P., Shakirin, G., and Enghardt, W. (2006). On the detector arrangement for in-beam PET for hadron therapy monitoring. *Phys. Med. Biol.*, 51(9):2143–2163.

Crespo, P., Shakirin, G., Fiedler, F., Enghardt, W., and Wagner, A. (2007). Direct time-of-flight for quantitative, real-time in-beam PET: a concept and feasibility study. *Phys. Med. Biol.*, 52(23):6795–6811.

Debus, J., Haberer, T., Schulz-Ertner, D., Jäkel, O., Wenz, F., Enghardt, W., Schlegel, W., Kraft, G., and Wannenmacher, M. (2000). Bestrahlung von Schädelbasistumoren mit Kohlenstoffionen bei der GSI Erste klinische Ergebnisse und zukünftige Perspektiven. *Strahlenther. Onkol.*, 176(5):211–216.

deKemp, R. A. and Nahmias, C. (1994). Attenuation correction in PET using single photon transmission measurement. *Med. Phys.*, 21(6):771–778.

Durante, M. and Löffler, J. S. (2010). Charged particles in radiation oncology. *Nat. Rev. Clin. Oncol.*, 7(1):37–43.

Elsässer, T., Gemmel, A., Scholz, M., Schardt, D., and Krämer, M. (2009). The relevance of very low energy ions for heavy-ion therapy. *Phys. Med. Biol.*, 54(7):101–106.

Enghardt, W. (2005). *In-beam PET for ion therapy monitoring (Positronen-Emissions-Tomographie für die Qualitätssicherung der Ionenstrahl-Therapie von Tumoren).* Habilitation, University of Technology Dresden.

Enghardt, W., Crespo, P., Fiedler, F., Hinz, R., Parodi, K., Pawelke, J., and Pönisch, F. (2004a). Charged hadron tumour therapy monitoring by means of PET. *Nucl. Instrum. Meth. A*, 525(1-2):284–288.

Enghardt, W., Debus, J., Haberer, T., Hasch, B., Hinz, R., Jäkel, O., Krämer, M., Lauckner, K., Pawelke, J., and Pönisch, F. (1999). Positron emission tomography for quality assurance of cancer therapy with light ion beams. *Nucl. Phys. A*, 654(1, Supplement 1):1047c–1050c.

Enghardt, W., Parodi, K., Crespo, P., Fiedler, F., Pawelke, J., and Pnisch, F. (2004b). Dose quantification from in-beam positron emission tomography. *Radiother. Oncol.*, 73, Supplement 2(0):S96–S98.

Fano, U. (1963). Penetration of protons, alpha particles, and mesons. *Ann. Rev. Nucl. Sci.*, 13(1):1–66.

Ferrari, A., Sala, P. R., Fassò, A., and Ranft, J. (2005). *FLUKA: A multi-particle transport code (program version 2005).* CERN-2005-10, INFN/TC_05/11, SLAC-R-773 .

Frey, K., Unholtz, D., Bauer, J., Debus, J., Min, C. H., Bortfeld, T., Paganetti, H., and Parodi, K. (2014). Most-likely-shift method for an automated range analysis with uncertainty evaluation in PET-based in-vivo treatment verification. *Phys. Med. Biol.* under review.

Furukawa, T., Inaniwa, T., Sato, S., Shirai, T., Mori, S., Takeshita, E., Mizushima, K., Himukai, T., and Noda, K. (2010). Moving target irradiation with fast rescanning and gating in particle therapy. *Med. Phys.*, 37(9):4874–4879.

Furukawa, T., Inaniwa, T., Sato, S., Tomitani, T., Minohara, S., Noda, K., and Kanai, T. (2007). Design study of a raster scanning system for moving target irradiation in heavy-ion radiotherapy. *Med. Phys.*, 34(3):1085–1097.

Gates, V. L., Esmail, A. A., Marshall, K., Spies, S., and Salem, R. (2011). Internal Pair Production of 90Y Permits Hepatic Localization of Microspheres Using Routine PET: Proof of Concept. *J. Nucl. Med.*, 52(1):72–76.

Gianoli, C., Kurz, C., Riboldi, M., Bauer, J., Baroni, G., and Parodi, K. (2014). Motion compensated reconstructions in PET-based ion beam treatment verification for moving target. In *International Conference on Translational Research in Radio-Oncology and Physics for Health in Europe, ICTR-PHE 2014.*

Goertzen, A. L., Suk, J. Y., and Thompson, C. J. (2007). Imaging of Weak-Source Distributions in LSO-Based Small-Animal PET Scanners. *J. Nucl. Med.*, 48(10):1692–1698.

Goldhaber, A. S. and Heckman, H. H. (1978). High Energy Interactions of Nuclei. *Annu. Rev. Nucl. Part. Sci.*, 28:161–205.

Goodhead, D. T. (1994). Initial events in the cellular effects of ionizing radiations: clustered damage in DNA. *Int. J. Radiat. Biol.*, 65(1):7–17.

Graeff, C., Durante, M., and Bert, C. (2012). Motion mitigation in intensity modulated particle therapy by internal target volumes covering range changes. *Med. Phys.*, 39(10):6004–6013.

Grezes-Besset, L., Nuyts, J., Boellard, R., Buvat, I., Michel, C., Pierre, C., Costes, N., and Reilhac, A. (2007). Simulation-based evaluation of NEG-ML iterative reconstruction of low count PET data. In *Nuclear Science Symposium Conference Record, 2007 IEEE*, volume 4, pages 3009–3014.

Grözinger, S. O., Rietzel, E., Li, Q., Bert, C., Haberer, T., and Kraft, G. (2006). Simulations to design an online motion compensation system for scanned particle beams. *Phys. Med. Biol.*, 51(14):3517–3531.

Gunzert-Marx, K., Iwase, H., Schardt, D., and Simon, R. S. (2008). Secondary beam fragments produced by 200 MeV/u 12 C ions in water and their dose contributions in carbon ion radiotherapy. *New J. Phys.*, 10(075003):1–21.

Gwosch, K., Hartmann, B., Jakubek, J., Granja, C., Soukup, P., Jäkel, O., and Martisikova, M. (2013). Non-invasive monitoring of therapeutic carbon ion beams in a homogeneous phantom by tracking of secondary ions. *Phys. Med. Biol.*, 58(11):3755–3773.

Haberer, T., Becher, W., Schardt, D., and Kraft, G. (1993). Magnetic scanning system for heavy ion therapy. *Nucl. Instrum. Meth. A*, 330(1-2):296–305.

Haberer, T., Debus, J., Eickhoff, H., Jäkel, O., Schulz-Ertner, D., and Weber, U. (2004). The heidelberg ion therapy center. *Radiother. Oncol.*, 73:186–190.

Habermehl, D., Debus, J., Ganten, T., Ganten, M.-K., Bauer, J., Brecht1, I. C., Brons, S., Haberer, T., Härtig, M., Jäkel, O., Parodi, K., Welzel, T., and Combs, S. E. (2013). Hypofractionated carbon ion therapy delivered with scanned ion beams for patients with hepatocellular carcinoma feasibility and clinical response. *Radiat. Ocol.*, 8(59).

Harpen, M. D. (2004). Positronium: Review of symmetry, conserved quantities and decay for the radiological physicist. *Med. Phys.*, 31(1):57–61.

Hashimoto, T., Tokuuye, K., Fukumitsu, N., Igaki, H., Hata, M., Kagei, K., Sugahara, S., Ohara, K., Matsuzaki, Y., and Akine, Y. (2006). Repeated proton beam therapy for hepatocellular carcinoma. *Int. J. Radiat. Oncol.Biol.Phys.*, 65(1):196–202.

Helmbrecht, S., Enghardt, W., Parodi, K., Didinger, B., Debus, J., Kunath, D., Priegnitz, M., and Fiedler, F. (2013). Analysis of metabolic washout of positron emitters produced during carbon ion head and neck radiotherapy. *Med. Phys.*, 40(9).

Helmbrecht, S., Santiago, A., Enghardt, W., Kuess, P., and Fiedler, F. (2012). On the feasibility of automatic detection of range deviations from in-beam PET data. *Phys. Med. Biol.*, 57(5):1387–1397.

Henriquet, P., Testa, E., Chevallier, M., Dauvergne, D., Dedes, G., Freud, N., Krimmer, J., Létang, J. M., Ray, C., Richard, M.-H., and Sauli, F. (2012). Interaction vertex imaging (IVI) for carbon ion therapy monitoring: a feasibility study. *Phys. Med. Biol.*, 57(14):4655–4669.

Highland, V. (1975). Some practical remarks on multiple scattering. *Nucl. Instrum. Methods*, 129(2):497–499.

Hof, H., Herfarth, K. K., Mnter, M., Hoess, A., Motsch, J., Wannenmacher, M., and Debus, J. (2003). Stereotactic single-dose radiotherapy of stage I nonsmall-cell lung cancer (NSCLC). *Int. J. of Radiat. Oncol. Biol. Phys.*, 56(2):335–341.

Hoisak, J. D., Sixel, K. E., Tirona, R., Cheung, P. C., and Pignol, J.-P. (2004). Correlation of lung tumor motion with external surrogate indicators of respiration. *Int. J. Radiat. Oncol.*, 60(4):1298–1306.

Hudson, H. and Larkin, R. (1994). Accelerated image reconstruction using ordered subsets of projection data. *IEEE T. Med. Imaging*, 13(4):601–609.

Hüfner, J. (1985). Heavy fragments produced in proton-nucleus and nucleus-nucleus collisions at relativistic energies. *Phys. Rep.*, 125:129–185.

ICRU (1993a). *Prescribing, Recording, and Reporting Photon Beam Therapy.* ICRU Report N. 50.

ICRU (1993b). *Quantities and Units in Radiation Protection Dosimetry.* ICRU Report N. 51.

ICRU (1994). *Stopping Powers and Ranges for Protons and Alpha Particles.* ICRU Report N. 49.

ICRU (1999). *Prescribing, Recording, and Reporting Photon Beam Therapy.* ICRU Report N. 62.

Inaniwa, T., Furukawa, T., Nagano, A., Sato, S., Saotome, N., Noda, K., and Kanai, T. (2009). Field-size effect of physical doses in carbon-ion scanning using range shifter plates. *Med. Phys.*, 36(7).

Ionascu, D., Jiang, S. B., Nishioka, S., Shirato, H., , and Berbeco, R. I. (2003). Internal-external correlation investigations of respiratory induced motion of lung tumors. *Med. Phys.*, 34(10):3893–3903.

Jäkel, O., Jacob, C., Schardt, D., Karger, C. P., and Hartmann, G. H. (2001a). Relation between carbon ion ranges and x-ray ct numbers. *Med. Phys.*, 28:701–703.

Jäkel, O., Krämer, M., Karger, C. P., and Debus, J. (2001b). Treatment planning for heavy ion radiotherapy: clinical implementation and application. *Phys. Med. Biol.*, 46(4):1101–1116.

Jakoby, B. W., Bercier, Y., Conti, M., Casey, M. E., Bendriem, B., and Townsend, D. W. (2011). Physical and clinical performance of the mCT time-of-flight PET/CT scanner. *Phys. Med. Biol.*, 56(8):2375–2389.

Kaatsch, P., Spix, C., Hentschel, S., Katalinic, A., Luttmann, S., Stegmaier, C., Caspritz, S., Cernaj, J., Ernst, A., Folkerts, J., Hansmann, J., Kranzhöfer, K., Krieghoff-Henning, E., Kunz, B., Penzkofer, A., Treml, K., Wittenberg, K., Baras, N., Barnes, B., Bertz, J., Buttmann-Schweiger, N., Dahm, S., Franke, M., Haberland, J., Kraywinkel, K., Wienecke, A., and Wolf, U. (2013). *Krebs in Deutschland 2009/2010*. Robert Koch-Institut und Gesellschaft der epidemiologischen Krebsregisterin Deutschland e.V.

Kato, H., Tsujii, H., Miyamoto, T., etsu Mizoe, J., Kamada, T., Tsuji, H., Yamada, S., Kandatsu, S., Yoshikawa, K., Obata, T., Ezawa, H., Morita, S., Tomizawa, M., Morimoto, N., Fujita, J., and Ohto, M. (2004). Results of the first prospective study of carbon ion radiotherapy for hepatocellular carcinoma with liver cirrhosis. *Int. J. Radiat. Oncol.*, 59(5):1468 – 1476.

Keall, P. J., Starkschall, G., Shukla, H., Forster, K. M., Ortiz, V., Stevens, C. W., Vedam, S. S., George, R., Guerrero, T., and Mohan, R. (2004). Acquiring 4D thoracic CT scans using a multislice helical method. *Phys. Med. Biol.*, 49(10):2053–2067.

Kinahan, P. E., Townsend, D. W., Beyer, T., and Sashin, D. (1998). Attenuation correction for a combined 3D PET/CT scanner. *Med. Phys.*, 25(10):2046–2053.

Kitamura, K., Shirato, H., Seppenwoolde, Y., Shimizu, T., Kodama, Y., Endo, H., Onimaru, R., Oda, M., Fujita, K., Shimizu, S., and Miyasaka, K. (2003). Tumor location, cirrhosis, and surgical history contribute to tumor movement in the liver, as measured during stereotactic irradiation using a real-time tumor-tracking radiotherapy system. *Int. J. of Radiat. Oncol. Biol. Phys.*, 56(1):221–228.

Knopf, A.-C. and Lomax, A. (2013). In vivo proton range verification: a review. *Phys. Med. Biol.*, 58(15):R131–R160.

Knopf, A.-C., Parodi, K., Paganetti, H., Bortfeld, T., Daartz, J., Engelsman, M., Liebsch, N., and Shih, H. (2011). Accuracy of Proton Beam Range Verification Using Post-Treatment Positron Emission Tomography/Computed Tomography as Function of Treatment Site. *Int. J. Radiat. Oncol. Biol. Phys.*, 79(1):297–304.

Koch, N., Liu, H., Starkschall, G., Jacobson, M., Forster, K., Liao, Z., Komaki, R., and Stevens, C. W. (2004). Evaluation of internal lung motion for respiratory-gated radiotherapy using MRI: Part Icorrelating internal lung motion with skin fiducial motion. *Int. J. Radiat. Oncol.*, 60(5):1459–1472.

Krämer, M., Jäkel, O., Haberer, T., Kraft, G., Schardt, D., and Weber, U. (2000). Treatment planning for heavy-ion radiotherapy: physical beam model and dose optimization. *Phys. Med. Biol.*, 45(11):3299–3317.

Krämer, M., Weyrather, W. K., and Scholz, M. (2003). The increased biological effectiveness of heavy charged particles: from radiobiology to treatment planning. *Technol. Cancer Res. Treat.*, 2(5):427–436.

Kumazaki, Y., Akagi, T., Yanou, T., Suga, D., Hishikawa, Y., and Teshima, T. (2007). Determination of the mean excitation energy of water from proton beam ranges. *Rad. Meas.*, 42(10):1683–1691.

Kupelian, P. A., Langen, K. M., Willoughby, T. R., Zeidan, O. A., and Meeks, S. L. (2008). Image-Guided Radiotherapy for Localized Prostate Cancer: Treating a Moving Target. *Sem. Radiat. Oncol.*, 18(1):58 – 66.

Kurz, C., Mairani, A., and Parodi, K. (2012). First experimental-based characterization of oxygen ion beam depth dose distributions at the heidelberg ion-beam therapy center. *Phys. Med. Biol.*, 57(15):5017–5034.

Lambert, J., Suchowerska, N., McKenzie, D. R., and Jackson, M. (2005). Intrafractional motion during proton beam scanning. *Phys. Med. Biol.*, 50(20):4853–4862.

Lhommel, R., Elmbt, L., Goffette, P., Eynde, M., Jamar, F., Pauwels, S., and Walrand, S. (2010). Feasibility of 90Y TOF PET-based dosimetry in liver metastasis therapy using SIR-Spheres. *Eur. J. Nucl. Med. Mol. I.*, 37(9):1654–1662.

Liu, C., Pierce II, L. A., Alessio, A. M., and Kinahan, P. E. (2009). The impact of respiratory motion on tumor quantification and delineation in static PET/CT imaging. *Phys. Med. Biol.*, 54(24):7345–7362.

Liu, H. H., Balter, P., Tutt, T., Choi, B., Zhang, J., Wang, C., Chi, M., Luo, D., Pan, T., Hunjan, S., Starkschall, G., Rosen, I., Prado, K., Liao, Z., Chang, J., Komaki, R., Cox, J. D., Mohan, R., and Dong, L. (2007). Assessing Respiration-Induced Tumor Motion and Internal Target Volume Using Four-Dimensional Computed Tomography for Radiotherapy of Lung Cancer. *Int. J. Radiat. Oncol. Biol. Phys.*, 68(2):531–540.

Low, D. A., Harms, W. B., Mutic, S., and Purdy, J. A. (1998). A technique for the quantitative evaluation of dose distributions. *Med. Phys.*, 25(5):656–661.

Lujan, A. E., Larsen, E. W., Balter, J. M., and Ten Haken, R. K. (1999). A method for incorporating organ motion due to breathing into 3D dose calculations. *Med. Phys.*, 26(5):715–720.

Mairani, A., Brons, S., Cerutti, F., Fass, A., Ferrari, A., Krmer, M., Parodi, K., Scholz, M., and Sommerer, F. (2010). The FLUKA Monte Carlo code coupled with the local effect model for biological calculations in carbon ion therapy. *Phys. Med. Biol.*, 55(15):4273–4289.

Malone, S., Crook, J. M., Kendal, W. S., and zanto, J. S. (2000). Respiratory-induced prostate motion: quantification and characterization. *Int. J. Radiat. Oncol. Biol. Phys.*, 48(1):105–109.

Melcher, C. and Schweitzer, J. S. (1992). Cerium-doped lutetium oxyorthosilicate: a fast, efficient new scintillator. *IEEE T. Nucl. Sci.*, 39(4):502–505.

Min, C.-H., Kim, C. H., Youn, M.-Y., and Kim, J.-W. (2006). Prompt gamma measurements for locating the dose falloff region in the proton therapy. *Appl. Phys. Lett.*, 89(18):183517.

Min, C. H., Zhu, X., Winey, B. A., Grogg, K., Testa, M., Fakhri, G. E., Bortfeld, T. R., Paganetti, H., and Shih, H. A. (2013). Clinical Application of In-Room Positron Emission Tomography for In Vivo Treatment Monitoring in Proton Radiation Therapy. *Int. J. Radiat. Oncol. Biol. Phys.*, 86(1):183–189.

Minohara, S., Kanai, T., Endo, M., Noda, K., and Kanazawa, M. (2000). Respiratory gated irradiation system for heavy-ion radiotherapy. *Int. J. Radiat. Oncol. Biol. Phys.*, 47(4):1097–1103.

Miyamoto, T., Baba, M., Yamamoto, N., Koto, M., Sugawara, T., Yashiro, T., Kadono, K., Ezawa, H., Tsujii, H., Mizoe, J.-E., Yoshikawa, K., Kandatsu, S., and Fujisawa, T. (2007). Curative treatment of Stage I nonsmall-cell lung cancer with carbon ion beams using a hypofractionated regimen. *Int. J. Radiat. Oncol. Biol. Phys.*, 67(3):750–758.

Mizuno, H., Tomitani, T., Kanazawa, M., Kitagawa, A., Pawelke, J., Iseki, Y., Urakabe, E., Suda, M., Kawano, A., Iritani, R., Matsushita, S., Inaniwa, T., Nishio, T., Furukawa, S., Ando, K., Nakamura, Y. K., Kanai, T., and Ishii, K. (2003). Washout measurement of radioisotope implanted by radioactive beams in the rabbit. *Phys. Med. Biol.*, 48(15):2269–2281.

Molière, G. (1948). *Theorie der Streuung schneller geladener Teilchen I - Einzelstreuung am abgeschirmten Coulomb-Feld.* Z. Naturforsch. 3a.

Mori, S., Hara, R., Yanagi, T., Sharp, G. C., Kumagai, M., Asakura, H., Kishimoto, R., Yamada, S., Kandatsu, S., and Kamada, T. (2009a). Four-dimensional measurement of intrafractional respiratory motion of pancreatic tumors using a 256 multi-slice CT scanner . *Radiother. Oncol.*, 92(2):231 – 237.

Mori, S., Lu, H.-M., Wolfgang, J. A., Choi, N. C., and Chen, G. T. Y. (2009b). Effects of Interfractional Anatomical Changes on Water-Equivalent Pathlength in Charged-Particle Radiotherapy of Lung Cancer. *J. Radiat. Res.*, 50(6):513–519.

Moses, W. W. (2007). Recent advances and future advances in time-of-flight PET. *Nucl. Instrum. Meth. A*, 580(2):919–924.

Moses, W. W. (2011). Fundamental limits of spatial resolution in PET. *Nucl. Instrum. Meth. A*, 648, Supplement 1(0):S236–S240.

Murray, I., Kalemis, A., Glennon, J., Hasan, S., Quraishi, S., Beyer, T., and Avril, N. (2010). Time-of-flight PET/CT using low-activity protocols: potential implications for cancer therapy monitoring. *Eur. J. Nucl. Med. Mol. I.*, 37(9):1643–1653.

Nagaki, A., Onoguchi, M., and Matsutomo, N. (2011). Patient WeightBased Acquisition Protocols to Optimize 18F-FDG PET/CT Image Quality. *J. Nucl. Med. Technol.*, 39(2):72–76.

Negoro, Y., Nagata, Y., Aoki, T., Mizowaki, T., Araki, N., Takayama, K., Kokubo, M., Yano, S., Koga, S., Sasai, K., Shibamoto, Y., and Hiraoka, M. (2001). The effectiveness of an immobilization device in conformal radiotherapy for lung tumor: reduction of respiratory tumor movement and evaluation of the daily setup accuracy. *Int. J. Radiat. Oncol. Biol. Phys.*, 50(4):889–898.

Nehmeh, S. A., Erdi, Y. E., Ling, C. C., Rosenzweig, K. E., Squire, O. D., Braban, L. E., Ford, E., Sidhu, K., Mageras, G. S., Larson, S. M., and Humm, J. L. (2002). Effect of respiratory gating on reducing lung motion artifacts in PET imaging of lung cancer. *Med. Phys.*, 29(3):366–371.

Nihei, K., Ogino, T., Ishikura, S., and Nishimura, H. (2006). High-dose proton beam therapy for Stage I nonsmall-cell lung cancer. *Int. J. Radiat. Oncol. Biol. Phys.*, 65(1):107–111.

Nishio, T., Miyatake, A., Ogino, T., Nakagawa, K., Saijo, N., and Esumi, H. (2010). The Development and Clinical Use of a Beam ON-LINE PET System Mounted on a Rotating Gantry Port in Proton Therapy. *Int. J. Radiat. Oncol. Biol. Phys.*, 76(1):277–286.

Nuyts, J., Stroobants, S., Dupont, P., Vleugels, S., Flamen, P., and Mortelmans, L. (2002). Reducing Loss of Image Quality Because of the Attenuation Artifact in Uncorrected PET Whole-Body Images. *J. Nucl. Med.*, 43(8):1054–1062.

Ollinger, J. M. (1996). Model-based scatter correction for fully 3D PET. *Phys. Med. Biol.*, 41(1):153–176.

Ollinger, J. M. and Fessler, J. A. (1997). Positron Emission Tomography. *IEEE Signal Proc. Mag.*, (Jan. 1997):43–55.

Paganetti, H. (2002). Nuclear interactions in proton therapy: dose and relative biological effect distributions originating from primary and secondary particles. *Phys. Med. Biol.*, 47(5):747–764.

Paganetti, H. (2012). Range uncertainties in proton therapy and the role of Monte Carlo simulations. *Phys. Med. Biol.*, 57(11):R99–R117.

Paganetti, H., Niemierko, A., Ancukiewicz, M., Gerweck, L. E., Goitein, M., Loeffler, J. S., and Suit, H. D. (2002). Relative biological effectiveness (RBE) values for proton beam therapy. *Int. J. Radiat. Oncol. Biol. Phys.*, 53(2):407–421.

Pan, T., Ting-Yim, L., Rietzel, E., and Chen, G. T. Y. (2004). 4D-CT imaging of a volume influenced by respiratory motion on multi-slice CT. *Med. Phys.*, 31(2):333–340.

Parodi, K. (2004). *On the feasibility of dose quantification with in-beam PET data in radiotherapy with* ^{12}C *and proton beams*. PhD thesis, Technische Universität Dresden, Germany.

Parodi, K., Bortfeld, T., Enghardt, W., Fiedler, F., Knopf, A., Paganetti, H., Pawelke, J., Shakirin, G., and Shih, H. (2008a). PET imaging for treatment verification of ion therapy: Implementation and experience at GSI Darmstadt and MGH Boston. *Nucl. Instrum. Meth. A*, 591(1):282–286.

Parodi, K., Bortfeld, T., and Haberer, T. (2008b). Comparison Between In-Beam and Offline Positron Emission Tomography Imaging of Proton and Carbon Ion Therapeutic Irradiation at Synchrotron- and Cyclotron-Based Facilities. *Int. J. Radiat. Oncol. Biol. Phys.*, 71(3):945–956.

Parodi, K., Crespo, P., Eickhoff, H., Haberer, T., Pawelke, J., Schardt, D., and Enghardt, W. (2005a). Random coincidences during in-beam PET measurements at microbunched therapeutic ion beams. *Nucl. Instrum. Meth. A*, 545(1-2):446 – 458.

Parodi, K., Ferrari, A., Sommerer, F., and Paganetti, H. (2007a). Clinical CT-based calculations of dose and positron emitter distributions in proton therapy using the FLUKA Monte Carlo code. *Phys. Med. Biol.*, 52(12):3369–87.

Parodi, K., Mairani, A., Brons, S., Hasch, B. G., Sommerer, F., Naumann, J., Jäkel, O., Haberer, T., and Debus, J. (2012). Monte Carlo simulations to support start-up and treatment planning of scanned proton and carbon ion therapy at a synchrotron-based facility. *Phys. Med. Biol.*, 57(12):3759–3784.

Parodi, K., Mairani, A., and Sommerer, F. (2013). Monte carlo-based parametrization of the lateral dose spread for clinical treatment planning of scanned proton and carbon ion beams. *J. Radiat. Res.*, 54(Suppl 1):i91–i96.

Parodi, K., Paganetti, H., Cascio, E., Flanz, J. B., Bonab, A. A., Alpert, N. M., Lohmann, K., and Bortfeld, T. (2007b). PET/CT imaging for treatment verification after proton therapy: A study with plastic phantoms and metallic implants. *Med. Phys.*, 34(2):419–435.

Parodi, K., Paganetti, H., Shih, H. A., Michaud, S., Loeffler, J. S., DeLaney, T. F., Liebsch, N. J., Munzenrider, J. E., Fischman, A. J., Knopf, A., and Bortfeld, T. (2007c). Patient Study of In Vivo Verification of Beam Delivery and Range, Using Positron Emission Tomography and Computed Tomography Imaging After Proton Therapy. *Int. J. Radiat. Oncol. Biol. Phys.*, 68(3):920–934.

Parodi, K., Ponisch, F., and Enghardt, W. (2005b). Experimental study on the feasibility of in-beam PET for accurate monitoring of proton therapy. *IEEE T. Nucl. Sci.*, 52(3):778–786.

Parodi, K., Saito, N., Chaudhri, N., Richter, C., Durante, M., Enghardt, W., Rietzel, E., and Bert, C. (2009). 4D in-beam positron emission tomography for verification of motion-compensated ion beam therapy. *Med. Phys.*, 36(9):4230–4243.

Pedroni, E., Bacher, R., Blattmann, H., Bhringer, T., Coray, A., Lomax, A., Lin, S., Munkel, G., Scheib, S., Schneider, U., and Tourovsky, A. (1995). The 200MeV proton therapy project at the Paul Scherrer Institute: Conceptual design and practical realization. *Med. Phys.*, 22(1):37–53.

Phelps, M. E., Hoffman, E. J., Mullani, N. A., and Ter-Pogossian, M. M. (1975). Application of Annihilation Coincidence Detection to Transaxial Reconstruction Tomography. *J. Nucl. Med.*, 16(3):210–224.

Phillips, M. H., Pedroni, E., Blattmann, H., Boehringer, T., Coray, A., and Scheib, S. (1992). Effects of respiratory motion on dose uniformity with a charged particle scanning method. *Phys. Med. Biol.*, 37(1):223–234.

Prall, M., Kaderka, R., Saito, N., Graeff, C., Bert, C., Durante, M., Parodi, K., Schwaab, J., Sarti, C., and Jenne, J. (2014). Ion beam tracking using ultrasound motion detection. *Med. Phys.*, 41(4).

PTCOG (2013). Patient statistics, http://ptcog.web.psi.ch/.

Qi, J. and Leahy, R. M. (2006). Iterative reconstruction techniques in emission computed tomography. *Phys. Med. Biol.*, 51(15):R541–R578.

Rao, M., Yang, W., Chen, F., Sheng, K., Ye, J., Mehta, V., Shepard, D., and Cao, D. (2010). Comparison of Elekta VMAT with helical tomotherapy and fixed field IMRT: Plan quality, delivery efficiency and accuracy. *Med. Phys.*, 37(3):1350–1359.

Remouchamps, V. M., Vicini, F. A., Sharpe, M. B., Kestin, L. L., Martinez, A. A., and Wong, J. W. (2003). Significant reductions in heart and lung doses using deep inspiration breath hold with active breathing control and intensity-modulated radiation therapy for patients treated with locoregional breast irradiation. *Int. J. Radiat. Oncol. Biol. Phys.*, 55(2):392–406.

Richter, D. (2013). *Treatment planning for tumors with residual motion in scanned ion beam therapy.* PhD thesis, Technische Universität Darmstadt Germany.

Richter, D. (2014). Private communication.

Richter, D., Saito, N., Chaudhri, N., Härtig, M., Ellerbrock, M., Jäkel, O., Combs, S. E., Habermehl, D., Herfarth, K., Durante, M., and Bert, C. (2014). Four-Dimensional Patient Dose Reconstruction for Scanned Ion Beam Therapy of Moving Liver Tumors. *Int. J. Rad. Oncol.*, 89(1):175–181.

Richter, D., Schwarzkopf, A., Trautmann, J., Krämer, M., Durante, M., Jäkel, O., and Bert, C. (2013). Upgrade and benchmarking of a 4D treatment planning system for scanned ion beam therapy. *Med. Phys.*, 40(5).

Rietzel, E., Schardt, D., and Haberer, T. (2007). Range accuracy in carbon ion treatment planning based on CT-calibration with real tissue samples. *Radiat. Oncol.*, 2(1):14.

Robert, C., Fourrier, N., Sarrut, D., Stute, S., Gueth, P., Grevillot, L., and Buvat, I. (2013). PET-based dose delivery verification in proton therapy: a GATE based simulation study of five PET system designs in clinical conditions. *Phys. Med. Biol.*, 58(19):6867–6885.

RPTC (2012). Das deutsche Protonen Therapie-Zentrum Dritter Jahresbericht Leading Proton Cancer Therapy In Europe.

Saito, N., Bert, C., Chaudhri, N., Gemmel, A., Schardt, D., Durante, M., and Rietzel, E. (2009). Speed and accuracy of a beam tracking system for treatment of moving targets with scanned ion beams. *Phys. Med. Biol.*, 54(16):4849–4862.

Schaart, D. R., Seifert, S., Vinke, R., van Dam, H. T., Dendooven, P., Löhner, H., and Beekman, F. J. (2010). $LaBr_3$:Ce and SiPMs for time-of-flight PET: achieving 100 ps coincidence resolving time. *Phys. Med. Biol.*, 55(7):N179–N189.

Schardt, D., Elsässer, T., and Schulz-Ertner, D. (2010). Heavy-ion tumor therapy: Physical and radiobiological benefits. *Rev. Mod. Phys.*, 82(1):383–425.

Schardt, D., Steidl, P., Krämer, M., Weber, U., Parodi, K., and Brons, S. (2008). Precision Bragg-curve measurements for light-ion beams in water. *GSI-Report 2008-1 (GSI Scientific Report 2007)*, page 373.

Schneider, W., Bortfeld, T., and Schlegel, W. (2000). Correlation between CT numbers and tissue parameters needed for Monte Carlo simulations of clinical dose distributions. *Phys. Med. Biol.*, 45(2):459–478.

Scholz, M. (2003). Effects of Ion Radiation on Cells and Tissue. *Adv. Polym. Sci.*, (162):95–155.

Scholz, M. and Elsässer, T. (2007). Biophysical models in ion beam radiotherapy. *Adv. Space Res.*, 40(9):1381–1391.

Scholz, M. and Kraft, G. (1994). Calculation of Heavy Ion Inactivation Probabilities Based on Track Structure, X Ray Sensitivity and Target Size. *Radiat. Prot. Dosim.*, 52(1-4):29–33.

Scholz, M. and Kraft, G. (1996). Track structure and the calculation of biological effects of heavy charged particles. *Adv. Space Res.*, 18(12):5–14.

Schulz-Ertner, D., Karger, C. P., Feuerhake, A., Nikoghosyan, A., Combs, S. E., Jäkel, O., Edler, L., Scholz, M., and Debus, J. (2007). Effectiveness of carbon ion radiotherapy in the treatment of skull-base chordomas. *Int. J. Radiat. Oncol. Biol. Phys.*, 68(2):449 – 457.

Schulz-Ertner, D., Nikoghosyan, A., Thilmann, C., Haberer, T., Jäkel, O., Karger, C., Kraft, G., Wannenmacher, M., and Debus, J. (2004). Results of carbon ion radiotherapy in 152 patients. *Int. J. Radiat. Oncol. Biol. Phys.*, 58(2):631–640.

Schwaab, J., Brons, S., Fieres, J., and Parodi, K. (2011). Experimental characterization of lateral profiles of scanned proton and carbon ion pencil beams for improved beam models in ion therapy treatment planning. *Phys. Med. Biol.*, 56(24):7813–7827.

Schwaab, J., Prall, M., Sarti, C., Kaderka, R., Bert, C., Kurz, C., Parodi, K., Günther, M., and Jenne, J. (2014). Ultrasound tracking for intra-fractional motion compensation in radiation therapy. *Phys. Medica*.

Seiler, P. G., Blattmann, H., Kirsch, S., Muench, R. K., and Schilling, C. (2000). A novel tracking technique for the continuous precise measurement of tumour positions in conformal radiotherapy. *Phys. Med. Biol.*, 45(9):N103–N110.

Seppenwoolde, Y., Shirato, H., Kitamura, K., Shimizu, S., van Herk, M., Lebesque, J. V., and Miyasaka, K. (2002). Precise and real-time measurement of 3d tumor motion in lung due to breathing and heartbeat, measured during radiotherapy. *Int. J. Radiat. Oncol. Biol. Phys.*, 53(4):822–834.

Serber, R. (1947). Nuclear reactions at high energies. *Phys. Rev.*, 72(11):1114–1115.

Shackleford, J. A., Kandasamy, N., and Sharp, G. C. (2010). On developing B-spline registration algorithms for multi-core processors. *Phys. Med. Biol.*, 55(21):6329–6351.

Shakirin, G., Braess, H., Fiedler, F., Kunath, D., Laube, K., Parodi, K., Priegnitz, M., and Enghardt, W. (2011). Implementation and workflow for PET monitoring of therapeutic ion irradiation: a comparison of in-beam, in-room, and off-line techniques. *Phys. Med. Biol.*, 56(5):1281–1298.

Shao, Y., Sun, X., Lou, K., Zhu, X., Mirkovic, D., Poenisch, F., and Grosshans, D. (2013). WEG50003: In-Beam PET Imaging with Depth-Of-Interaction Measurement for Accurate Proton Beam-Range Verification. *Med. Phys.*, 40(6):503–503.

Shepp, L. and Vardi, Y. (1982). Maximum Likelihood Reconstruction for Emission Tomography. *Medical Imaging, IEEE Transactions on*, 1(2):113–122.

Shirato, H., Seppenwoolde, Y., Kitamura, K., Onimura, R., and Shimizu, S. (2004). Intrafractional tumor motion: lung and liver. *Semin. Radiat. Oncol.*, 14(1):10–18.

Shirato, H., Shimizu, S., Kitamura, K., Nishioka, T., Kagei, K., Hashimoto, S., Aoyama, H., Kunieda, T., Shinohara, N., Dosaka-Akita, H., and Miyasaka, K. (2000). Four-dimensional treatment planning and fluoroscopic real-time tumor tracking radiotherapy for moving tumor. *Int. J. Radiat. Oncol. Biol. Phys.*, 48(2):435–442.

Smeets, J., Roellinghoff, F., Prieels, D., Stichelbaut, F., Benilov, A., Busca, P., Fiorini, C., Peloso, R., Basilavecchia, M., Frizzi, T., Dehaes, J. C., and Dubus, A. (2012). Prompt gamma imaging with a slit camera for real-time range control in proton therapy. *Phys. Med. Biol.*, 57(11):3371–3405.

Sonke, J.-J., Lebesque, J., and van Herk, M. (2008). Variability of four-dimensional computed tomography patient models. *Int. J. Radiat. Oncol. Biol. Phys.*, 70(2):590–598.

Sportelli, G., Belcari, N., Camarlinghi, N., Cirrone, G. A. P., Cuttone, G., Ferretti, S., Kraan, A., Ortuo, J. E., Romano, F., Santos, A., Straub, K., Tramontana, A., Guerra, A. D., and Rosso, V. (2014). First full-beam PET acquisitions in proton therapy with a modular dual-head dedicated system. *Phys. Med. Biol.*, 59(1):43–60.

Stützer, K., Bert, C., Enghardt, W., Helmbrecht, S., Parodi, K., Priegnitz, M., Saito, N., and Fiedler, F. (2013). Experimental verification of a 4D MLEM reconstruction algorithm used for in-beam PET measurements in particle therapy. *Phys. Med. Biol.*, 58(15):5085–5111.

Surti, S., Karp, J., Muehllehner, G., and Raby, P. (2002). Investigation of lanthanum scintillators for 3D PET. In *Nuclear Science Symposium Conference Record, 2002 IEEE*, volume 2, pages 1177–1181.

Surti, S., Zou, W., Daube-Witherspoon, M. E., McDonough, J., and Karp, J. S. (2011). Design study of an in situ PET scanner for use in proton beam therapy. *Phys. Med. Biol.*, 56(9):2667–2685.

Tashima, H., Yamaya, T., Yoshida, E., Kinouchi, S., Watanabe, M., and Tanaka, E. (2012). A single-ring OpenPET enabling PET imaging during radiotherapy. *Phys. Med. Biol.*, 57(14):4705–4718.

Ter-Pogossian, M. M., Phelps, M. E., Hoffman, E. J., and Mullani, N. A. (1975). A Positron-Emission Transaxial Tomograph for Nuclear Imaging (PETT). *Radiology*, 114(1):89–98.

Testa, E., Bajard, M., Chevallier, M., Dauvergne, D., Foulher, F. L., Freud, N., Létang, J., Poizat, J., Ray, C., and Testa, M. (2009). Dose profile monitoring with carbon ions by means of prompt-gamma measurements. *Nucl. Imstrum. Meth. B*, 267(6):993 – 996.

Tobias, C. A., Lawrence, J. H., Born, J. L., McCombs, R. K., Roberts, J. E., Anger, H. O., Low-Beer, B. V. A., and Huggins, C. B. (1958). Pituitary Irradiation with High-Energy Proton Beams A Preliminary Report. *Cancer Res.*, 18:121–134.

Tsujii, H., Mizoe, J., Kamada, T., Baba, M., Tsujii, H., Kato, H., Kato, S., Yamada, S., Yasuda, S., Ohno, T., Yanagi, T., Imai, R., Kagei, K., Kato, H., Hara, R., Hasegawa, A., Nakajima, M., Sugane, N., Tamaki, N., TAkagi, R., Kandatsu, S., Yoshikawa, K., Kishimoto, R., and Miyamoto, T. (2007). Clinical Results of Carbon Ion Radiotherapy at NIRS. *J. Radiat. Res.*, 48(Suppl.A):A1–A13.

Unholtz, D., Sommerer, F., Bauer, J., van Straaten, D., Haberer, T., Debus, J., and Parodi, K. (2011). Post-therapeutical beta+-activity measurements in comparison to simulations towards in-vivo verification of ion beam therapy. In *Nuclear Science Symposium and Medical Imaging Conference (NSS/MIC), 2011 IEEE*, pages 2273–2276.

Unkelbach, J., Bortfeld, T., Martin, B. C., and Soukup, M. (2009). Reducing the sensitivity of IMPT treatment plans to setup errors and range uncertainties via probabilistic treatment planning. *Med. Phys.*, 36(1):149–163.

van Herk, M., Bruce, A., Kroes, A. G., Shouman, T., Touw, A., and Lebesque, J. V. (1995). Quantification of organ motion during conformal radiotherapy of the prostate by three dimensional image registration. *Int. J. Radiat. Oncol. Biol. Phys.*, 33(5):1311–1320.

van Velden, F. H., Kloet, R. W., van Berckel, B. N., Lammertsma, A. A., and Boellaard, R. (2009). Accuracy of 3-Dimensional Reconstruction Algorithms for the High-Resolution Research Tomograph. *J. Nucl. Med.*, 50(1):72–80.

Vedam, S. S., Keall, P. J., Kini, V. R., Mostafavi, H., Shukla, H. P., and Mohan, R. (2003a). Acquiring a four-dimensional computed tomography dataset using an external respiratory signal. *Phys. Med. Biol.*, 48(1):45–62.

Vedam, S. S., Kini, V. R., Keall, P. J., Ramakrishnan, V., Mostafavi, H., and Mohan, R. (2003b). Quantifying the predictability of diaphragm motion during respiration with a noninvasive external marker. *Med. Phys.*, 30(4):505–513.

Verel, I., Visser, G. W., and van Dongen, G. A. (2005). The Promise of Immuno-PET in Radioimmunotherapy. *J. Nucl. Med.*, 46(1 suppl):164S–171S.

Verhaeghe, J. and Reader, A. J. (2010). AB-OSEM reconstruction for improved Patlak kinetic parameter estimation: a simulation study. *Phys. Med. Biol.*, 55(22):6739–6757.

Walker, M. D., Asselin, M.-C., Julyan, P. J., Feldmann, M., Talbot, P. S., Jones, T., and Matthews, J. C. (2011). Bias in iterative reconstruction of low-statistics PET data: benefits of a resolution model. *Phys. Med. Biol.*, 56(4):931–949.

Watson, C. (2000). New, faster, image-based scatter correction for 3D PET. *IEEE T. Nucl. Sci.*, 47(4):1587–1594.

Watson, C., Casey, M., Michel, C., and Bendriem, B. (2004). Advances in scatter correction for 3D PET/CT. In *Nuclear Science Symposium Conference Record, 2004 IEEE*, volume 5, pages 3008–3012.

Watson, C., Newport, D., and Casey, M. (1996). A Single Scatter Simulation Technique for Scatter Correction in 3D PET. In *Three-Dimensional Image Reconstruction in Radiology and Nuclear Medicine*, volume 4 of *Computational Imaging and Vision*, pages 255–268. Springer Netherlands.

Webb, S. (2003). The physical basis of IMRT and inverse planning. *Br. J. Radiol.*, 76(910):678–689.

Weyrather, W. K., Ritter, S., Scholz, M., and Kraft, G. (1999). RBE for carbon track-segment irradiation in cell lines of differing repair capacity. *Int. J. Radiat. Biol.*, 75(11):1357–1364.

Whitfield, G., Jain, P., Green, M., Watkins, G., Henry, A., Stratford, J., Amer, A., Marchant, T., Moore, C., and Price, P. (2012). Quantifying motion for pancreatic radiotherapy margin calculation. *Radiother. Oncol.*, 103(3):360 – 366.

Wilson, R. R. (1946). Radiological use of fast protons. *Radiology*, 47:487–491.

Winkelmann, T., Cee, R., Haberer, T., Naas, B., Peters, A., and Scheloske, S. (2010). Experience at the ion beam therapy center (HIT) with two years of continuous ECR ion source operation. *Proceedings of ECRIS08, Chicago, IL USA*.

Wolthaus, J. W. H., Sonke, J.-J., van Herk, M., and Damen, E. M. F. (2008). Reconstruction of a time-averaged midposition CT scan for radiotherapy planning of lung cancer patients using deformable registrationa. *Med. Phys.*, 35(9):3998–4011.

Wood, M. L. and Henkelman, R. M. (1984). MR image artifacts from periodic motion. *Med. Phys.*, 12(2):143–151.

Wunderink, W., Romero, A. M., de Kruijf, W., de Boer, H., Levendag, P., and Heijmen, B. (2008). Reduction of Respiratory Liver Tumor Motion by Abdominal Compression in Stereotactic Body Frame, Analyzed by Tracking Fiducial Markers Implanted in Liver. *Int. J. Radiat. Oncol. Biol. Phys.*, 71(3):907–915.

Yamamoto, S., Horii, H., Hurutani, M., Matsumoto, K., and Senda, M. (2005). Investigation of single, random, and true counts from natural radioactivity in LSO-based clinical PET. *Ann. Nucl. Med.*, 19(2):109–114.

Yamaya, T., Inaniwa, T., Minohara, S., Yoshida, E., Inadama, N., Nishikido, F., Shibuya, K., Lam, C. F., and Murayama, H. (2008). A proposal of an open PET geometry. *Phys. Med. Biol.*, 53(3):757–773.

Zenklusen, S. M., Pedroni, E., and Meer, D. (2010). A study on repainting strategies for treating moderately moving targets with proton pencil beam scanning at the new Gantry 2 at PSI. *Phys. Med. Biol.*, 55(17):5103–5121.

Zhang, T., Keller, H., O'Brien, M. J., Mackie, T. R., and Paliwal, B. (2003). Application of the spirometer in respiratory gated radiotherapy. *Med. Phys.*, 30(12):3165–3171.

Zhang, X., Günther, M., and Bongers, A. (2010). Real-Time Organ Tracking in Ultrasound Imaging Using Active Contours and Conditional Density Propagation. In *Medical Imaging and Augmented Reality*, volume 6326 of *Lecture Notes in Comput. Sci.*, pages 286–294. Springer Berlin Heidelberg.

Zhang, Y., Boye, D., Tanner, C., Lomax, A. J., and Knopf, A. (2012). Respiratory liver motion estimation and its effect on scanned proton beam therapy. *Phys. Med. Biol.*, 57(7):1779–1795.

Zhu, X., Espaa, S., Daartz, J., Liebsch, N., Ouyang, J., Paganetti, H., Bortfeld, T. R., and Fakhri, G. E. (2011). Monitoring proton radiation therapy with in-room PET imaging. *Phys. Med. Biol.*, 56(13):4041–4057.

Acknowledgements

At first, I would like to thank Prof. Katia Parodi for giving me the opportunity to pursue my PhD in her group at the Heidelberg Ion-Beam Therapy Center and for supervising this thesis. She always followed my progress with great interest and supported this work with enthusiasm and all her scientific expertise. I am also very grateful to her for giving me the chance to visit interesting conferences and to spent three months at the Siemens Molecular Imaging headquarters in Knoxville, TN.

I want to thank Prof. Jan Wilkens for taking the time to review this thesis as second referee.

Of course, a heartfelt thanks goes to my present and former co-workers for the enjoyable working atmosphere and for all their support: Julia Bauer, Ilaria Rinaldi, Andrea Mairani, Daniel Unholtz, Chiara Gionoli, Kathrin Frey, Meret Hildebrandt, Wenjing Chen and Thomas Tessonnier. In particular, I would like to thank Daniel Unholtz for supporting the 4D-extension of the SimInterface, Chiara Gionoli for sharing her expertise in motion-compensated PET imaging and, last but not least, Julia Bauer for all her useful advice, the interest in my work and the manifold fruitful discussions which have been of great benefit for this thesis.

I also want to express my gratitude to the HIT medical physicist team around Prof. Oliver Jäkel for their help in preparing the moving phantom irradiation studies and Prof. Thomas Haberer for kindly providing the beam-time to carry out these studies. Many thanks are moreover addressed to the Heidelberg University Hospital medical staff, i.e., to the physicians around Prof. Jürgen Debus, as well as to the MTRA team around Marliese Schenk, for supporting the post-irradiation PET verification measurements of the patient cases discussed within this work.

Moreover, I want to acknowledge the constructive collaboration with the colleagues from *mediri*, especially Julia Schwaab and Jürgen Jenne. They did not only provide the US tracking device used in this work, but also offered great help in designing, carrying out and evaluating the presented experiments on US-based 4D PET imaging.

Furthermore, thanks to the colleagues from GSI, in particular to Daniel Richter, who enabled the presented 4D MC simulations by generating the required state-raster files in TRiP4D and who had to answer countless questions on 4D dose calculation and image registration. I also thank Nami Saito for providing her *plastimatch* registration scripts and Prof. Christoph Bert for his help in designing the moving phantom irradiation studies. Beyond, I want to mention Kristin Stützer from OncoRay, Dresden, who gave valuable input for planning the phantom experiments and helped in acquiring the data.

I also thank the colleagues from Siemens Molecular Imaging: Frederic Schoenahl for sharing detailed information on the acquired LM data and, in particular, Maurizio Conti for his supervision and support during my stay in Knoxville, for sharing his expertise in PET imaging and for making me feel comfortable in Knoxville.

Last, but not least, I would like to deeply thank my family, in particular my parents and my sister, for all their love and support throughout the past years. I know I can always rely on them.

This work has been supported by the European FP7 project ENVISION (Grant Agreement N. 241851).

Erklärung:

Ich versichere, dass ich diese Arbeit selbstständig verfasst habe und keine anderen als die angegebenen Quellen und Hilfsmittel benutzt habe. Diese Dissertation hat in gleicher oder ähnlicher Form keiner anderen Prüfungskommission vorgelegen.

München, den 12.06.2014

. . . .

(Christopher Kurz)

Publications related to this work

Peer-reviewed articles

Seravalli, E, Robert, C, Bauer, J, Stichelbaut, F, Kurz, C, Smeets, J, Van Ngoc Ty, C, Schaart, DR, Buvat, I, Parodi, K and Verhaegen, F, (2012). Monte Carlo calculations of positron emitter yields in proton radiotherapy. *Phys. Med. Biol.* , 57(6):1659–1673.

Robert, C, Dedes, G, Battistoni, G, Böhlen, TT, Buvat, I, Cerutti, F, Chin, MPW, Ferrari, A, Gueth, P, Kurz, C, Lestand, L, Mairani, A, Montarou, G, Nicolini, R, Ortega, PG, Parodi, K, Prezado, Y, Sala, PR, Sarrut, D and Testa, E (2013). Distributions of secondary particles in proton and carbon-ion therapy: a comparison between GATE/Geant4 and FLUKA Monte Carlo codes. *Phys. Med. Biol.* , 58(9):2879–2899.

Bauer, J, Unholtz, D, Sommerer, F, Kurz, C, Haberer, T, Herfarth, K, Welzel, T, Combs, SE, Debus, J and Parodi, K (2013). Implementation and initial clinical experience of offline PET/CT-based verification of scanned carbon ion treatment. *Radiother. Oncol.* , 107(2):218–226.

Bauer, J, Unholtz, D, Kurz, C and Parodi, K (2013). An experimental approach to improve the Monte Carlo modelling of offline PET/CT-imaging of positron emitters induced by scanned proton beams. *Phys. Med. Biol.* , 58(15):5193–5213.

Frey, K, Bauer, J, Unholtz, D, Kurz, C, Krämer, M, Bortfeld, T and Parodi, K (2014). TPS_{PET} - A TPS-based approach for in vivo dose verification with PET in proton therapy. *Phys. Med. Biol.* , 59(1):1–21.

Schwaab, J, Prall, M, Sarti, C, Kaderka, R, Bert, C, Kurz, C, Parodi, K, Günther, M and Jenne, J (2014). Ultrasound tracking for intra-fractional motion compensation in radiation therapy. *Phys. Medica*, 30(5):578–582.

Gianoli, C, Riboldi, M, Kurz, C, de Bernardi, E, Bauer, J, Fontana, G, Ciocca, M, Parodi, K and Baroni, G (2014). PET-CT scanner characterization for PET raw data use in biomedical research. *Comput. Med. Imag. Grap.* , 38(5), 358–368.

Knopf, A, Nill, S, Yohannes, I, Graeff, C, Dowdell, S, Kurz, C, Sonke, JJ, Biegun, A, Lang, S, McClelland, J, Champion, B, Fast, M, Wölfelschneider, J, Gianoli, C, Rucinski, A, Baroni, G, Richter, C, van de Water, S, Grassberger, C, Weber, D and Bert, C (2014). Challenges of radiotherapy: Report on the 4D treatment planning workshop 2013. *Phys. Medica*, in press.

Ammar, C, Frey, K, Bauer, J, Melzig, C, Chiblak, S, Hildebrandt, M, Unholtz, D, Kurz, C, Brons, S, Debus, J, Abdollahi, A and Parodi, K (2014). Comparing the biological washout of β^+-activity induced in mice brain after ^{12}C-ion and proton irradiation. *Phys. Med. Biol.*, tentatively accepted, revision required.

Gianoli, C, Riboldi, M, Kurz, C, Fontana, G, Parodi, K and Baroni, G (2014), A sinogram warping strategy for pre-reconstruction 4D PET optimization. *Med. Biol. Eng. Comput.*, submitted.

Schwaab, J, Kurz, C, Sarti, C, Zhang, X, Bongers, A, Schoenahl, F, Bert, C, Debus, J, Parodi, K and Jenne, J (2014). First steps towards ultrasound motion compensation for imaging and therapy: calibration with an optical system and 4D PET imaging. *Z. Med. Phys.*, submitted.

ENVISION Collaboration (2014). ENVISION: imaging secondary particles to improve dose conformality of proton and ion therapy. *Med. Phys.*, to be submitted.

Two more publications (first author) in preparation. These will cover the feasibility studies on 4D offline PET-based treatment verification and the characterisation of the Biograph mCT scanner performance under extremely low counting statistics discussed in the scope of this thesis.

Clinical study protocols

Combs, SE, Bauer, J, Unholtz, D, Kurz, C, Welzel, T, Habermehl, D, Haberer, T, Debus, J and Parodi, K (2012). Monitoring of patients treated with particle therapy using positron-emission-tomography (PET): the MIRANDA study. *BMC CANCER*, 12:133.

Conference contributions and proceedings

Kurz, C, Bauer, J, Bert, C, Jenne, J, Schoenahl, F, Unholtz, D and Parodi, K (2012). First Steps towards 4D Offline PET-Based Treatment Verification at the Heidelberg Ion Beam Therapy Center. *ICTR-PHE 2012*, Geneva, Switzerland. Oral presentation. *Radiother. Oncol.*, 102:S55–S56.

Kurz, C, Bauer, J, Unholtz, D, Richter, D, Bert, C, Kaderka, R, Laube, K and Parodi, K (2013). On the feasibility of 4D off-beam PET-based treatment verification in ion beam therapy. *PTCOG 52, 2013*, Essen, Germany. Poster presentation.

Kurz, C, Bauer, J, Guerin, L, Conti, M, Eriksson, L and Parodi, K (2013). Investigating the Limits of PET/CT Imaging at Very Low True Count Rates in Ion-Beam Therapy Monitoring. *IEEE NSS-MIC 2013*, Seoul, South Korea. Oral presentation. *IEEE NSS-MIC 2013 Conference Record*, M07-3.

Kurz, C, Bauer, J, Unholtz, D, Combs, SE, Debus, J, Richter, D, Kaderka, R, Bert, C, Stützer, K, Gianoli, C, Baroni, G and Parodi, K (2013). Current Status of 4D Offline PET-Based Treatment Verification at the Heidelberg Ion-Beam Therapy Center. *IEEE NSS-MIC 2013*, Seoul, South Korea. Oral presentation. *IEEE NSS-MIC 2013 Conference Record*, HT3-4 & M21-12.

Kurz, C, Bauer, J, Unholtz, D, Frey, K, Gianoli, C, Baroni, G, Combs, SE, Debus, J and Parodi, K (2013). Offline PET-based Treatment Verification at the Heidelberg Ion-Beam Therapy Center: Clinical Experience and On-Going Research. *PIPA 2013*, Yokohama, Japan. Oral presentation.

Kurz, C, Bauer, J, Unholtz, D, Combs, SE, Debus, J, Richter, D, Kaderka, R, Bert, C, Stützer, K, Gianoli, C, Baroni, G and Parodi, K (2013). Current Status of 4D Offline PET-Based Treatment Verification at the Heidelberg Ion-Beam Therapy Center. *4D Treatment Planning Workshop 2013*, Villigen, Switzerland. Poster presentation.

Seravalli, E, Bauer, J, Robert, C, Stichelbaut, F, Kurz, C, Smeets, J, Schaart, DR, Buvat, I, Parodi, K and Verhaegen, F (2012). Comparison of Monte Carlo positron-emitter yield calculations in proton radiotherapy. *ICTR-PHE 2012*, Geneva, Switzerland. *Radiother. Oncol.*, 103:S320.

Bauer, J, Unholtz, D, Sommerer, F, Kurz, C, Haberer, T, Debus, J and Parodi, K (2012). Experimental validation of simulated positron emitter yields and refined tissue classification for improved Monte Carlo modeling towards offline PET/CT-based verification of proton therapy. *Third European Workshop on Monte Carlo Treatment Planning of the European Workgroup on MCTP*, Sevilla, Spain.

Bauer, J, Unholtz, D, Sommerer, F, Kurz, C, Haberer, T, Combs, SE, Welzel, T, Herfarth, K, Debus, J and Parodi, K (2012). First clinical experience with offline PET/CT-based in-vivo verification of scanned carbon ion irradiation. *31th Meeting of the European Society for Therapeutic Radiology and Oncology (ESTRO)*, Barcelona, Spain.

Parodi, K, Bauer, J, Sommerer, F, Unholtz, D, Kurz, C, Haberer, T, Welzel, T, Herfarth, K, Combs, SE and Debus, J (2012). Post-therapeutic PET/CT-based verification of scanned proton and carbon ion therapy at the Heidelberg Ion Beam Therapy Center. *World Congress on Medical Physics and Biomedical Engineering*, Beijing, China.

Schwaab, J, Sarti, C, Kurz, C, Zhang, X, Bongers, A, Parodi, K and Jenne, J (2012). Calibration of an ultrasound tracking system for moving organs in heavy ion therapy. *Extended abstract of the 43rd DGMP annual meeting*, Jena, Germany.

Gianoli, C, Bauer, J, Kurz, C, Riboldi, M, Parodi, K and Baroni, G (2013). A Clinical Study on 4D PET Optimization and Quantification in Off-line Treatment Verification. *PTCOG 52, 2013*, Essen, Germany.

Bauer,J, Unholtz, D, Kurz, C, Combs, SE, Welzel, T, Debus, J and Parodi, K (2013). MRI-based brain tissue classification for an improved MC modelling of post-therapeutic PET/CT-based treatment verification.*PTCOG 52, 2013*, Essen, Germany.

Frey, K, Bauer, J, Unholtz, D, Kurz, C, Krämer, M, Bortfeld, T and Parodi, K (2013). TPS$_{\mathrm{PET}}$ A new approach for TPS-based calculation of proton-irradiation induced position emitter distributions for in-vivo dose verification with PET. *PTCOG 52, 2013*, Essen, Germany.

Parodi, K, Bauer, J, Kurz, C, Unholtz, D, Sommerer, F, Frey, K, Haberer, T, Herfarth, K, Welzel, T, Combs, SE and Debus, J (2013). Offline PET/CT imaging of scanned proton and carbon ion beams: initial clinical experience for different tumour sites. *AAPM 2013*, Indianapolis, USA. *Med. Phys.* 40, 504.

Bauer, J, Hildebrandt, M, Unholtz, D, Kurz, C and Parodi K (2013). On the Modelling of Facility-Specific PET Imaging for Proton Treatment Verification: Experimental Validation and Inter-Facility Comparison. *AAPM 2013*, Indianapolis, USA. *Med. Phys.* 40, 548.

Frey, K, Bauer, J, Unholtz, D, Kurz, C, Krämer, M, Bortfeld, T and Parodi, K (2013). TPS$_{\mathrm{PET}}$ - A TPS-Based Approach for In-Vivo Dose Verification with PET in Proton Therapy. *AAPM 2013*, Indianapolis, USA. *Med. Phys.* 40, 547.

Schwaab, J, Sarti, C, Prall, M, Kaderka, R, Bert, C, Kurz, C, Parodi, K, Günther, M and Jenne, J (2013). Ultrasound tracking for intra-fractional motion compensation in radiation therapy. *44. Jahrestagung der Deutschen Gesellschaft für Medizinische Physik*, Cologne, Germany . *Abstractband*, p175 - 6.

Gianoli, C, Kurz, C, Riboldi, M, Bauer, J, Baroni, G, and Parodi, K (2014). Motion compensated reconstructions in PET-based ion beam treatment verification for moving target. *ICTR-PHE 2014*, Geneva, Switzerland.

Bauer, J, Kurz, C, Unholtz, D, Frey, K, Combs, SE, Debus, J and Parodi, K (2014). PET/CT-based verification of scanned proton and carbon ion treatment at HIT – an overview. *ICTR-PHE 2014*, Geneva, Switzerland.

Other publications

Laube, K, Bert, C, Fiedler, F, Helmbrecht, S, Kaderka, R, Kurz, C, Parodi, K, Saito, N, Tian, Y and Enghardt, W (2013). Gated phantom irradiation for 4D in-beam and 4D off-beam PET comparison. *GSI Scientific Report for 2012.*

Publications beyond this work

Kurz, C, Mairani, A and Parodi, K (2012). First experimental-based characterization of oxygen ion beam depth dose distributions at the Heidelberg Ion-Beam Therapy Center. *Phys. Med. Biol.* , 57(15):5017–34. *medicalphysicsweb*, http://medicalphysicsweb.org/cws/article/research/50539.